Gerold M. Rangger

Modeling of metal-organic interfaces for improving state-of-the-art organic electronic devices.

Dissertation

zur Erlangung des akademischen Grades Doktor der technischen Wissenschaften

Betreuer:

Ao.Univ.-Prof. Dipl.-Ing. Dr.techn. Egbert Zojer

Institut für Festkörperphysik

Graz, Februar 2010

Für meine Eltern und meine Frau Karina.

Acknowledgments

First of all, I want to thank my parents who made all this possible. They have been supporting me along my way. Thanks for carrying, supporting and loving.

Secondly, I want to express my deepest gratitude to my wife Karina who supported me throughout the last years. Thanks for pushing me forward, encouraging me and listening.

Last but not least, I want to thank my brothers for their continuous support.

I would like to express profound gratitude to my supervisor, Prof. Egbert Zojer, for his invaluable support, encouragement, supervision and useful suggestions throughout this research work. Thanks to all the current/former members of the "Egbert" group, Anna for being patient with us - "fly my helicopter fly" and for sharing the desk at the beginning of our time here, Oliver for his chemist-wisdom and patience while drawing chemical structures for me over and over again, Fördi - please do not correct anything when being hungry any more, Lukas, Peter, Simon, Marco, Mulla and Piet. Thanks guys for answering all my questions and for discussions. Their support and continuous guidance enabled me to complete my work successfully.

Some people need to be mentioned explicitly. Lorenz for introducing the magic of VASP and SIESTA and for continuous support throughout the last years. You're the "projection master" and program king. I am glad that it did not bother you too much to look over my programs and help me in locating errors. Georg for showing me some special tricks of his own, suggesting the MOOP, for fruitful discussions and for letting me stay at his place some time during my research stay in Atlanta. He taught me the magic of how to obtain XPS, IR and STM results in *VASP*. We also had great fun climbing in the area and thanks for taking me with you to my first and probably last "Boulder Competition". At that point I want to acknowledge Jean-Luc Brédas for hosting me at the Georgia Institute of Technology. It was a pleasant time there, thanks to all who made this possible.

I want to express my gratitude to Prof. Zhigang Shuai for giving me the opportunity to stay in Beijing at his group. Thanks to all the members of his group there for hosting me that gentile. Special thanks to "Xiao Wang" for the endless discussions, his patience with my poor Chinese, the great time we had exploring Beijing and the Great Wall. Thanks "Xiao Niu" for teaching me Chinese and the art of table tennis and the great time at the Great Wall. Next time we meet I want a rematch. "Xiao Ma", Liping Chen and David Beljonne for their patience with my Chinese and for showing me the Chinese cuisine.

Finally I want to thank everyone else who offered their assistance and support along the way.

Deutsche Fassung:
Beschluss der Curricula-Kommission für Bachelor-, Master- und Diplomstudien vom 10.11.2008
Genehmigung des Senates am 1.12.2008

EIDESSTATTLICHE ERKLÄRUNG

Ich erkläre an Eides statt, dass ich die vorliegende Arbeit selbstständig verfasst, andere als die angegebenen Quellen/Hilfsmittel nicht benutzt, und die den benutzten Quellen wörtlich und inhaltlich entnommene Stellen als solche kenntlich gemacht habe.

Graz, am ……. ……..
(Unterschrift)

Englische Fassung:

STATUTORY DECLARATION

I declare that I have authored this thesis independently, that I have not used other than the declared sources / resources, and that I have explicitly marked all material which has been quoted either literally or by content from the used sources.

……. ……..
date (signature)

Abstract for
PhD Thesis

Modeling of metal-organic interfaces for improving state-of-the-art organic electronic devices.

Gerold Rangger
Insitute of Solid State Physics, University of Technology, Graz
8010 Graz, Austria

Organic electronics is a quick growing branch in today's economy and include organic light-emmitting diodes, organic field-effect-transistors and organic photovoltaic cells. Despite their different functionalities, all of them have interfaces between electrodes and conjugated organic materials in common. To improve the interface energetics has attracted reasonable interest in recent years and is of crucial importance for the device performance. This work deals with the theoretical modelling of (i) self assembled monolayers and (ii) flat lying molecules as isolated quantities and the interfaces formed when put onto a metal surface. This is done with state-of-the-art computational methods.

Abstrakt
Doktorarbeit

Modeling of metal-organic interfaces for improving state-of-the-art organic electronic devices.

Gerold Rangger
Institut für Festkörperphysik, Technische Universität Graz
8010 Graz, Austria

Organische Elektronik ist ein schnell wachsender Markt. Alle elektronischen Bauteile in diesem Bereich haben eines gemeinsam und zwar eine Grenzschicht zwischen Elektroden und organischem Material. Die Funktionsweise hängt sehr stark von dieser Grenzschicht und den Molekülen ab. Eine Verbesserung der Bauteile durch Modifikation dieser Grenzschicht mit einer Zwischenschicht, die einerseits aus sich selbst-assemblierenden stehenden Molekülen oder auch aus flach liegenden Molekülen bestehen kann, ist erstrebenswert. Die vorliegende Arbeit beschäftigt sich mit der theoretischen Beschreibung solcher Grenzschichten und von Molekülen, die eine Modifikation dieser erlauben. Dazu werden moderne Konzepte der Quantenchemie und der theoretischen Festkörperphysik verwendet.

Contents

1 Introduction

In recent years the need for understanding interfaces between electrodes and organic materials has attracted more and more interest in the interdisciplinary field of physics, chemistry and material science. It is hoped to improve charge-carrier injection in a systematic way and hence, in the end, to decisively improve organic electronic devices.

This thesis deals with molecules being especially promising candidates of such interface modifications. These molecules and the interfaces formed between these molecules and metals are analyzed from a theoretical perspective using state-of-the-art computational methods. Hereby, molecular properties are calculated with the quantum-chemistry package GAUSSIAN and all interfaces are studied with the band-structure codes VASP and SIESTA.

In the following, I will give a short overview of the contents of this thesis describing in detail also the contributions of all collaborators to the present work.

In a first part of the thesis, the analyzed systems were investigated in collaboration with international groups. Thereby, the focus was twofold.

(i) In chapter 3, the effect of self-assembled monolayers (SAMs) with different head-groups on Ag(111) is studied. The work was published by Gerold M. Rangger, Lorenz Romaner, Georg Heimel, and Egbert Zojer, in Ref. [1] and is reproduced in this thesis. The investigated systems within this publication were inspired through previous work of Georg Heimel who intensively studied SAMs on Au(111).

The next two chapters 4 and 5 are based on a collaboration with the group of Prof. Shuai Zhigang of the Chinese Academy of Science in Beijing (currently also at the Department of Chemistry, Tsinghua University, Beijing). Here, the work was conducted in close collaboration with Dr. LinJun Wang. This lead to my research stay at the Chinese Academy of Science as we discovered that the influence of internal coordinate optimization on his results was crucial for the conclusions. I worked intensively with LinJun Wang on the issue of SAMs with different backbone polarizability bearing different head-groups. I showed him how to perform internal optimizations in VASP. As a consequence of the importance of these optimizations on the results, we redid all his Cartesian optimizations for all his systems and re-interpreted the results.

Here, it needs to be mentioned that to the best of my knowledge, “first of its kind” optimizations of SAMs on metals based on internal coordinates in VASP were performed with the GADGET tool. This was made available to us by a collaboration with the VASP group in Vienna in particular Dr. Tomáš Bučko. The contact is mangaged by Ferdinand Rissner of our group.

During our study, Linjung Wang and I additionally identified the importance of the “H-effect” in the definition of the bond-dipole emerging upon adsorption and studied it in great detail (chapter 5). As a result two publications emerged. The first one is about differently polarizable backbones by LinJun Wang, Gerold M. Rangger, Lorenz Romaner, Georg Heimel, Tomáš Bučko, ZhongYun Ma, QiKai Li, Zhigang Shuai, and Egbert Zojer Ref. [2]. The second one is about the “H-effect”, bond-dipole by LinJun

Wang, Gerold M. Rangger, ZhongYun Ma, QiKai Li, Zhigang Shuai, Egbert Zojer, and Georg Heimel in Ref. [3].

(ii) The second big part of the thesis deals with flat lying molecules on metal surfaces. The aim of the European Commission project "ICONTROL", as part of which these studies were conducted, was to come up with strong electron accepting and donating molecules in order to modify the interface-energetics. Thereby, chemists of the Max Planck Institute (MPI) for Polymer Research in Mainz synthesized materials, experimental physicists of the Institute of Physics of the Humboldt University in Berlin tested their impact on metal surfaces and in the end their device performance was investigated at the TNO-Holst center in Eindhoven. Our role in that process was to quickly screen suggestions of the chemistry department in terms of acceptor and donor strength and then furthermore to calculate electronic properties of the molecules on surfaces.

First, chapter 6, deals with an in the mean-time prototypical strong organic acceptor 2,3,5,6-tetrafluoro-7,7,8,8-tetracyanoquinodimethane (F_4TCNQ) on the (111) surfaces of Ag, Au and Cu. The results were published by Rangger Gerold M., Hofmann Oliver T., Romaner Lorenz, Heimel Georg, Bröker, Benjamin, Blum Ralf-Peter, Johnson Robert L., Koch Norbert, and Zojer, Egbert in Ref. [4]. This work builds on the work of Lorenz Romaner who first, theoretically characterized F_4TCNQ on Cu(111).

In the next chapter on this topic, 7, an improved acceptor 3,5-difluoro-2,5,7,7,8,8-hexacyanoquinodimethane (F_2HCNQ) is analyzed on Ag(111). This molecule came into consideration due to intensive discussion with Benjamin Bröker during which we were focusing on how to improve F_4TCNQ. The results have recently been submitted by Rangger Gerold M., Bröker, Benjamin, and Zojer, Egbert.

The next family of molecules (pyrenetetraone (PyT), bromo-pyrenetetraone (Br-PyT) and nitro-pyrenetetraone (NO_2-PyT)) was suggested by the chemistry group around Prof. Müllen of the Max Planck Institute (MPI) for Polymer Research in Mainz. They are described in great detail in chapter 8. The ultra-violet photoemission spectroscopy (UPS) and x-ray photoelectron spectroscopy (XPS) experiments using these molecules were carried out by Benjamin Bröker of the Humboldt University in Berlin and the synthesis as well as cyclic voltammetry measurements were made by by Ralph Rieger of the MPI-Mainz. Benjamin Bröker is currently preparing a publication. My part was to theoretically investigate the molecules on Ag(111) and Au(111). The corresponding chapter of this thesis (8) was written by me using experimental data and figures of Benjamin Bröker's first draft. In the summary contained in this thesis, the focus lies on the theoretical modeling.

Chapter, 9, deals with the simulation of physical quantities such as scanning tunneling microscopy (STM) and XPS using F_4TCNQ and F_2HCNQ as molecules. This chapter is a result of my research stay at the Georgia Institute of Technology in Atlanta in the group of Jean-Luc Brédas. Dr. Georg Heimel taught me how to model these quantities. Hereby, whenever possible comparisons with experiments are made.

The last part of my thesis, chapter 10, reintroduces an old chemical tool to analyze bonding at surfaces. This tool, the crystal orbital overlap population (COOP) was brought to my attention by Prof. Michael G. Ramsey during a lecture at the Karl Franzens University Graz. Unfortunately, this way of analyzing the bond did not become

as popular as I think it should be. Here, this method was used for the analysis of the bond between the strong acceptor F_4TCNQ on Ag(111), see 10.1, and the strong donor 1H,1'H-[4,4']bipyridinylidene (HV0) on Au(111), see 10.2. An additional development of this method was suggested by Dr. Georg Heimel and is based on work of Dr. Lorenz Romaner. This is the molecular orbital overlap population (MOOP) and was also applied to the two molecules mentioned above. The two parts, subchapters 10.1 and 10.2, should serve as a first draft for upcoming publications.

Prior to the theoretical results, the concepts, the basic idea behind the COOP and MOOP and the fundamental equations which are solved by the programs are introduced in chapter 2. For that purpose the output of the atomic orbital band-structure code SIESTA is used as input for Fortran programs which evaluate the COOP and the MOOP. The program for evaluation of the COOP was written by me; for calculating the MOOP, programs written by Romaner Lorenz were used.

A current list of my publications follows this introduction and the papers largely reproduced within this thesis are highlighted (publication year is written bold). These papers have been chosen either because I am the main author or because significant contributions of mine are included. The latter is the case for two joint publications with LinJun Wang and one upcoming publication with Benjamin Bröker.

Scientific Work - Publications

2010 *"A particularly strong organic acceptor for tuning the hole-injection barriers in modern organic devices."*
Rangger, Gerold M. and Hofmann, Oliver T., and Bröker, Benjamin, and Zojer, Egbert
submitted to Synthetic Metals

2010 *"Simultaneously Understanding the Geometric and Electronic Structure of Anthraceneselenolate on Au(111): A Combined Theoretical and Experimental Study"*
Track, Anna M. and Rissner, Ferdinand and Heimel, Georg and Romaner, Lorenz and Bashir, Asif and Rangger, Gerold M. and Hofmann, Oliver T. and Bučko, Tomáš and Witte, Gregor and Zojer, Egbert
Physical Chemistry C
DOI: 10.1021/jp9102756

2010 *"Is there a Au-S bond dipole in self-assembled monolayers on gold?"*
Wang, LinJun and Rangger, Gerold M. and Ma, ZhongYun and Li, QiKai and Shuai, Zhigang and Zojer, Egbert and Heimel, Georg
Physical Chemistry Chemical Physics
DOI: 10.1039/B924306

2010 *"Self-assembled monolayers of polar molecules on Au(111) surfaces: distributing the dipoles"*
Egger, David A. and Rissner, Ferdinand and Rangger, Gerold M. and Hofmann, Oliver T. and Wittwer, Lukas and Heimel, Georg and Zojer, Egbert
Physical Chemistry Chemical Physics
DOI: 10.1039/b924238b

2009 *"Understanding the Electronic Structure of Metal/SAM/OrganicSemiconductor Heterojunctions"*
Rissner, Ferdinand and Rangger, Gerold M. and Hofmann, Oliver T. and Track, Anna M. and Heimel, Georg and Zojer, Egbert
ACS Nano, 3, 3513-3520
DOI: 10.1021/nn9010494

Scientific Work - Publications

2009 *Electronic Structure of Self-Assembled Monolayers on Au(111) Surfaces: The Impact of Backbone Polarizability*
Wang, LinJun and Rangger, Gerold M. and Romaner, Lorenz and Heimel, Georg and Bučko, Tomáš and Ma, ZhongYun and Li, QiKai and Shuai, Zhigang and Zojer, Egbert
Advanced Functional Materials, 19, 3766 - 3775
DOI:10.1002/adfm.200901152

2009 *"F4TCNQ on Cu, Ag, and Au as prototypical example for a strong organic acceptor on coinage metals"*
Rangger, Gerold M. and Hofmann, Oliver T. and Romaner, Lorenz and Heimel, Georg and Bröker, Benjamin and Blum, Ralf-Peter and Johnson, Robert L. and Koch, Norbert and Zojer, Egbert
Physical Review B, 79, 165306-165318
DOI: 10.1103/PhysRevB.79.165306

2008 *"Reducing the Metal Work Function beyond Pauli Pushback: A Computational Investigation of Tetrathiafulvalene and Viologen on Coinage Metal Surfaces"*
Rangger, Gerold M. and Romaner, Lorenz and Heimel, Georg and Zojer, Egbert
The Journal of Physical Chemistry C, 112, 20357-20365
DOI: 10.1021/jp806834g

2008 *"Understanding the properties of interfaces between organic self-assembled monolayers and noble metals - a theoretical perspective"*
Rangger, Gerold M. and Romaner, Lorenz and Heimel, Georg and Zojer, Egbert
Surface and Interface Analysis, 40, 371-378
DOI: 10.1002/sia.2645

2 Theory

2.1 Density functional theory (DFT)

(used literature throughout this section: [5–10])

In order to get a first idea of what density functional theory (DFT) is about, it is useful to take a step back and recall some elementary quantum mechanics. In quantum mechanics all information we can possibly have about a given system is contained in the system's Hamiltonian, which is the central quantity for any theoretical treatment. [5] In solid state physics as well as in chemistry, the only fundamental interaction dealing with is the electrostatic one. [5] Thereby, relativistic effects are usually neglected if only valence electrons are considered. The system of nuclei and electrons is described by the time-independent, non relativistic Schrödinger equation

$$\hat{H}\,\Psi \;=\; E\,\Psi, \tag{1}$$

were, $\hat{H}$ is the Hamiltonian operator and Ψ is a set of solutions, or eigenstates, of the Hamiltonian. The Hamiltonian has the well-defined form

$$\hat{H} = \hat{T}_{\text{nucl}} + \hat{T}_{\text{el}} + \hat{V}_{\text{nucl}-\text{nucl}} + \hat{V}_{\text{nucl}-\text{el}} + \hat{V}_{\text{el}-\text{el}} \tag{2}$$

with $\hat{T}_{\text{nucl}}$ and $\hat{T}_{\text{el}}$ being the kinetic energy of the nuclei and the electrons, respectively. [5,7] The other terms describe the electrostatic interaction between the positively charged nuclei and the electrons. The separate parts of the Hamiltonian of an atom-electron system are given by

$$\hat{T}_{\text{nucl}} \;=\; -\sum_{I}^{L} \frac{\hbar^2}{2M_I}\nabla_I^2 \tag{3}$$

$$\hat{T}_{\text{el}} \;=\; -\sum_{i}^{N} \frac{\hbar^2}{2m}\nabla_i^2 \tag{4}$$

$$\hat{V}_{\text{nucl}-\text{nucl}} \;=\; \frac{1}{2}\sum_{I\neq J} \frac{Z_I Z_J e^2}{|\mathbf{R}_I - \mathbf{R}_J|} \tag{5}$$

$$\hat{V}_{\text{nucl}-\text{el}} \;=\; \sum_{i,I} \frac{Z_i e^2}{|\mathbf{R}_I - \mathbf{r}_i|} \tag{6}$$

$$\hat{V}_{\text{el}-\text{el}} \;=\; \frac{1}{2}\sum_{i\neq j} \frac{e^2}{|\mathbf{r}_i - \mathbf{r}_j|}\,. \tag{7}$$

Here atoms are numbered by capital letter indices. Z_i represents the charge of the I-th nuclei. [5] The factor $\frac{1}{2}$ ensures that the interactions between the same pairs of particles are not counted twice. [5] M_I and m are the masses of the I-th nuclei and of the electron and $\hbar$ is related with the Plank constant (h) by $\hbar = \frac{h}{2\pi}$.

Unfortunately, the solution of the Schrödinger equation (1) with the Hamiltonian

(2) in a closed form is in general not possible.[5] Therefore, approximations have to be made. The first one is the so-called Born-Oppenheimer approximation.[11] The central idea underlying this approximation is the separation in the time scale of processes involving electrons and atoms due to the large mass mismatch of electrons and nuclei.[5] In practice, one splits up the full Hamiltonian and defines the electronic Hamiltonian $\hat{H}_{\mathrm{el}}$ for fixed nuclear coordinates $\{\mathbf{R}\}$ as:[5]

$$\hat{H}_{\mathrm{el}} = \hat{T}_{\mathrm{el}} + \hat{V}_{\mathrm{nucl-nucl}} + \hat{V}_{\mathrm{nucl-el}} + \hat{V}_{\mathrm{el-el}}. \tag{8}$$

Important in that context is that the nuclei coordinates are parameters now. In the Born-Oppenheimer approximation the eigenenergy $E_{\mathrm{el}}(\mathbf{R})$ of the electronic Schrödinger equation is then taken to be the potential for the nuclear motion.[5] Here, quantum effects are often neglected and the classical equation of motion is solved.

$$M_I \frac{\partial^2}{\partial t^2}\mathbf{R}_I = -\frac{\partial}{\partial \mathbf{R}_I} E_{\mathrm{el}}(\mathbf{R}) \tag{9}$$

As a result the force acting on the atoms can be conveniently evaluated using the Hellmann-Feynman theorem[12,13]

$$\mathbf{F}_I = -\frac{\partial}{\partial \mathbf{R}_I} E_{\mathrm{el}}(\mathbf{R}) = < \Psi(r, \{\mathbf{R}\}) | \frac{\partial}{\partial \mathbf{R}_I} \hat{H}_{\mathrm{el}}(\{\mathbf{R}\}) | \Psi(r, \{\mathbf{R}\}) > \tag{10}$$

Employing the Born-Oppenheimer approximation means first of all to solve the electronic structure problem for fixed nuclei positions. Hence, the positions of the nuclei determine the external electrostatic potential in which the electrons move. In fact the Born-Oppenheimer approximation is very successful in the theoretical description of processes at surfaces.

In order to determine the total energies of particular systems, necessary as prerequisite for a theoretical treatment of any property or process at surfaces, the Schrödinger equation (1) has to be solved.[5] The two most important characteristics of the ground state electronic structure are the electron density distribution $n(\mathbf{r})$ and the total energy E, for given locations $\mathbf{R}_I$ of the nuclei.[10] Historically, two different fields, wave-function and electron density based methods, emerged. Despite their methodological differences both branches have one common starting point, namely the Born-Oppenheimer approximation.

A wide field of modern quantum chemistry methods are based on the expansion of the wave function in terms of Slater determinants.[14] An advantage of such methods is that one can generate results that systematically approach the exact solution of the Schrödinger equation by using more sophisticated methods.[6] Nonetheless, traditional multiparticle wave-function methods are rather limited to a small number of atoms when applied to systems of many particles without symmetries.[15] This is due to the fact that the wave-function for an N electron system contains $4N$ variables, three spatial

and one spin coordinate for each electron.[6]

On the other end of the spectrum, back in 1964 Hohenberg and Kohn proposed a new way of solving a given problem by moving from the wave functions to the ground state electron density as core variable of the Schrödinger equation. As a result the multi-dimensional wave-function based problem $\Psi(\mathbf{r}_1, \mathbf{r}_2, ..., \mathbf{r}_N)$ is reduced to a three dimensional $n(\mathbf{r})$.

This approach became increasingly successful as it in fact became the most commonly applied method for obtaining ground-state properties of given systems over the past decades. Nevertheless, the most serious shortcoming of this approach is the need for an approximation of the exchange-correlation functional, *vide infra*. Here, regardless of the ever increasing computational power and the immense research still no unique exchange-correlation functional exists for all the different systems. In DFT there is no systematic approach to improve the result towards the exact solution.[6]

2.1.1 Basic idea

In the following the fundamental ideas of DFT[i] together with the approximations necessary are briefly revised as all calculations presented in this thesis are within this framework.

DFT is based on the famous Hohenberg-Kohn theorems:[19]

"*The ground-state density n(r) of a system of interacting electrons in an external potential uniquely determines this potential.*"

This theorem states that a functional of the electron density exists that can be used to solve the Schrödinger equation (1) but it however does not say anything about how this functional actually looks like. Nevertheless, a second theorem of Hohenberg-Kohn defines an important property of this functional:[19]

"*The electron density that minimizes the energy of the overall functional is the true electron density corresponding to the full solution of the Schrödinger equation.*"

Hence, DFT in a way is in principle an exact theory, i.e., if we knew the true form of the functional, we would get the exact ground state electron density by varying it until the energy is minimized. Nonetheless, the exact form of this functional is yet unknown and therefore DFT is based on approximations to this functional. Therefore, despite of its popularity it needs to be stressed that results and conclusions drawn merely on the basis of DFT are not the ultimate truth. Hence, in this thesis, wherever possible, the theoretical results were compared with experimental data.

[i] Historically DFT is the successor of the Thomas Fermi theory.[16–18] Hence, the idea of taking the density for describing a quantum system is older than DFT.

2.1.2 Kohn-Sham equations

Hohenberg and Kohn first proved that there is a one-to-one relationship of the ground state charge density and the external potential.[19] Hence the Hamiltonian and consequently all properties derivable from $\hat{H}$ such as the ground-state wave function $\Psi_0(\mathbf{r}_1, \ldots, \mathbf{r}_N)$ is **uniquely** determined (to within a physically irrelevant additive constant) by the knowledge of the ground-state density $n(\mathbf{r})$:[10]

$$n(\mathbf{r}) \rightarrow V_{\text{ext}}(\mathbf{r}) \tag{11}$$

This is true whether the ground-state is degenerate or not. A proof can be found in basically any textbook dealing with DFT such as in Refs. [10 and 5].

Using the Rayleigh-Ritz minimization principle the exact ground-state energy can be determined by the minimization of the energy functional $E[n]$ with respect to the density n.[5,10] As a consequence the ground-state energy is a unique functional of n_0

$$E_0 = \underset{n(\mathbf{r})}{min}(T[n(\mathbf{r})] + V_H[n(\mathbf{r})] + V_{\text{ext}}[n(\mathbf{r})] + E_{\text{xc}}[n(\mathbf{r})]) = \underset{n(\mathbf{r})}{min}\, E[n(\mathbf{r})], \tag{12}$$

where $E[n(\mathbf{r})]$ is given by the sum of a kinetic energy functional, T, for non-interacting electrons, a functional of the classical electrostatic interaction energy, corresponding to the Hartree energy, V_{H}, the functional of the external potential, V_{ext}, and the unknown exchange correlation functional, E_{xc}, a purely quantum mechanical interaction.[5] The energy minimization is normally done in an iterative way until self-consistency is reached.[20] Instead of using the many-body quantum-mechanic wave function now only the density has to be varied in order to get the ground state properties. In practice, however, no direct variation of the density is made.[5] The density is expressed as sum of N independent basis functions[5]

$$n(\mathbf{r}) = \sum_{i}^{N} |\phi_i(\mathbf{r})|^2 . \tag{13}$$

Here, the basis functions ϕ_i are chosen in a way that they are orthonormal to each other, i.e. $< \phi_i|\phi_j >= \delta_{ij}$. Inserting this expansion in equation (12) under the constraint of normalization leads to a set of Kohn-Sham equations,[5]

$$\left[-\frac{\hbar^2}{2m}\nabla^2 + v_{\text{eff}}(\mathbf{r})\right]\phi_i(\mathbf{r}) = \epsilon_i\phi_i(\mathbf{r}), \tag{14}$$

where m is the mass of an electron and ϵ_i are the eigenvalues of the Kohn-Sham equations. In that context it is important to state that all quantities of the Kohn-Sham equations (14), i.e., the eigenstates ϕ_i and eigenvalues ϵ_i do not have any real physical meaning. Nevertheless, they are essential for obtaining the electron density.

The advantage of these Kohn-Sham equations is that it is a self-consistent, one-particle Schrödinger equation with an effective single-particle potential that can be expressed as:[5,10]

$$v_{\text{eff}}[n(\mathbf{r})] = v_{\text{ext}}[n(\mathbf{r})] + v_{\text{H}}[n(\mathbf{r})] + v_{\text{xc}}[n(\mathbf{r})]. \tag{15}$$

Hereby, the unknown exchange-correlation potential $v_{\mathrm{xc}}[n(\mathbf{r})]$ is given by the functional derivative of the exchange-correlation energy with respect to the electron density [5,10]

$$v_{\mathrm{xc}}(\mathbf{r}) = \frac{\delta E_{\mathrm{xc}}[n(\mathbf{r})]}{\delta n(\mathbf{r})}. \tag{16}$$

To solve the Kohn-Sham equations, in reality, one starts with an initial guess for the electron density. [9] Then the eigenfunctions ϕ_i are obtained as a solution of the Kohn-Sham equations (14). [9] The resulting density is mixed to a certain extend with the initial one and with this new density the whole iterative process is repeated until self-consistency is reached, i.e. the old and the new densities are virtually the same. [9] This in the end leads to the the ground state energy via following equation

$$E[n(\mathbf{r})] = \sum_{i=1}^{N} \epsilon_i - \frac{1}{2} \int d\mathbf{r}\, d\mathbf{r}' \, \frac{n(\mathbf{r})\, n(\mathbf{r}')}{|\mathbf{r} - \mathbf{r}'|} - \int d\mathbf{r}\, v_{\mathrm{xc}}(\mathbf{r})\, n(\mathbf{r}) + E_{\mathrm{xc}}[n(\mathbf{r})], \tag{17}$$

where it was taken into account that by simply summing up the single-particle Kohn-Sham eigenvalues the classical electron-electron interactions are counted twice and hence needed to be removed once. [7,10]

In real life one must content oneself with approximations for E_{xc}. [10] Hereby, one can choose out of a wide pool of different functionals, all of them having their own advantages and disadvantages. In the following subsection the most common approaches are shortly revised.

2.1.3 Exchange-correlation functionals

In the following two prominent approximations to the exchange-correlation functional are shortly revised.

The most prominent approximation is the so called local density approximation (LDA)

$$E_{\mathrm{xc}}^{\mathrm{LDA}}[n(\mathbf{r})] = \int n(\mathbf{r}) \epsilon_{\mathrm{xc}}^{\mathrm{LDA}}(n(\mathbf{r}))\, \mathrm{d}\mathbf{r} \tag{18}$$

where $\epsilon_{\mathrm{xc}}^{\mathrm{LDA}}(n(\mathbf{r}))$ is the exchange-correlation energy per electron of a **uniform** electron gas of density n. [5,7,10] The latter is known from independent studies of the uniform electron gas. [7] The corresponding exchange-correlation potential v_{xc} is, by equation (16), given by [5,10]

$$v_{\mathrm{xc}}(\mathbf{r}) \;=\; n(\mathbf{r})\, \frac{\partial \epsilon_{\mathrm{xc}}^{\mathrm{LDA}}(n)}{\partial n}\bigg|_{n=n(\mathbf{r})} + \epsilon_{\mathrm{xc}}^{\mathrm{LDA}}(n(\mathbf{r})). \tag{19}$$

Several LDA approximations exist - commonly abbreviated with the initials of the authors, sometimes including the years. Examples are the following:

- Vosko-Wilk-Nusair (VWN) [21]
- Perdew-Zunger (PZ81) [22]

- Cole-Perdew (CP) [23]
- Perdew-Wang (PW92) [24]

Typically LDA underestimates the correlation part of the energy but overestimates the exchange part. [5,7] In the end, it often results in reasonably good values for the total exchange-correlation energy ϵ_{xc}. Hence, LDA has been surprisingly successful in a wide range of bulk and surface problems. [20] This is up to now not fully understood and it is attributed to the fortunate cancellation of opposing errors in the exchange and correlation part of LDA. [5] Usually LDA tends to result in over-binding, i.e. binding and cohesive energies turn out to be too large compared to experiments. [5] This additionally results in too small lattice constants and bond length. [5]

Any real system is spatially inhomogeneous, i.e., it has a spatially varying density $n(\mathbf{r})$. Therefore, it is useful to somehow include information on the variation of the density in the functional. The easiest way for doing so is including gradient-corrections of the form $|\nabla n(\mathbf{r})|$ to LDA.[ii] Functionals of the form

$$E_{\mathrm{xc}}^{\mathrm{GGA}}[n(\mathbf{r})] = \int n(\mathbf{r})\epsilon_{\mathrm{xc}}(n(\mathbf{r}), |\nabla n(\mathbf{r})|)\mathrm{d}\mathbf{r} \tag{20}$$

are known as generalized gradient approximation (GGA) functionals and are increasingly popular since the late 1980th. [25] A selection of the most popular functionals are given below:

- Perdew, Burke and Ernzerhof (PBE) [26]
- revised Perdew, Burke and Ernzerhof (revPBE) [27]
- Perdew-Wang 1991 (PW91) [28]

Some of the failures of GGA include (a) the lack of properly describing van der Waals forces, (b) insufficient electron affinities for negative ions, (c) underestimation of cohesive energies, (d) overestimations of distances, including bonding distances of molecules on surfaces, (e) wrong long-range effective one-particle potential. [5] Bearing all these shortcomings in mind, nevertheless, results based on GGA are quite successfully used in describing quantum mechanical systems. Hence, all the surface problems reported in the thesis have been calculated using GGA mostly with the PW91 and the PBE exchange correlation functional.

Before choosing a functional in the calculations, it is important to understand the similarities and differences between the various exchange-correlation functionals available. [9] An useful classification of functionals has been described by Perdew et. al. [29], where they compared the search of the universal exchange correlation functional to the Biblical account of Jacob's ladder (Genesis 28). [9] Hereby LDA represents the

[ii] Higher order corrections of the form $|\nabla n(\mathbf{r})|^{\alpha}$ or $\nabla^{\beta} n(\mathbf{r})$ with $\alpha, \beta > 2$ are exceedingly difficult and costfully to calculate and are usually not performed.

lowest rung followed by GGA, Meta-GGA, Hyper-GGA all advancing a step higher towards the "perfect" method without approximation.[29] Hereby, Becke, Lee, Yang and Parr (B3LYP),[30,31] also used in this thesis for calculations of molecular properties of isolated molecules, count to semiempirical hyper-GGA's, that mix a fixed fraction of exact exchange to GGA-exchange.[29]

2.1.4 Plane waves and basis set

DFT is a very valuable method in solid state physics if one deals with periodic structures.[5,8] The periodicity of solid crystals is utilized via Bloch's theorem. It effectively reduces the infinite number of electrons to a finite number of electrons within a single primitive unit cell. The natural basis to describe such periodic systems are plane waves[5]

$$\Psi_{\mathbf{k}}^{\mathbf{G}}(\mathbf{r}) = \frac{1}{\sqrt{V}} e^{i(\mathbf{k}+\mathbf{G})\mathbf{r}}. \tag{21}$$

Plane waves satisfy the Bloch condition,

$$\Psi_{\mathbf{k}}(\mathbf{r}) = e^{i\mathbf{k}\cdot\mathbf{r}} u_{\mathbf{k}}(\mathbf{r}). \tag{22}$$

with $u_{\mathbf{k}}(\mathbf{r}+\mathbf{R}) = u_{\mathbf{k}}(\mathbf{r})$ for any lattice vector $\mathbf{R}$. In equation (21) $\mathbf{G}$ is a reciprocal lattice vector and $\mathbf{k}$ lies in the first Brillouin zone.[5] Within a periodic external potential, i.e., for instance a crystal, a linear combination of plane waves with the periodicity of the lattice are taken as wave functions:[32]

$$\Psi_{\mathbf{k}} = \sum_{\mathbf{G}} C_{\mathbf{k}-\mathbf{G}} e^{i(\mathbf{k}-\mathbf{G})\mathbf{r}}. \tag{23}$$

Due to computational costs the amount of planewaves taken at each $\boldsymbol{k}$-point is limited.[32] Therefore, one has to use an energy-cutoff:[32]

$$E_{\text{cutoff}}(\mathbf{k}-\mathbf{G}) = \hbar^2(\mathbf{k}-\mathbf{G})/(2m). \tag{24}$$

The quality of the calculations can yet be controlled by the amount of planewaves taken into consideration, i.e. the value of the cutoff energy.

In order to obtain the total energy of a crystal a summation over the lowest eigenvalues of the Kohn-Sham equation has to be performed.[5] For an infinite periodic system this leads to replacing the sum over the eigenvalues by an integral over the first Brillouin zone

$$\sum_i \epsilon_i \longrightarrow \sum_{\text{bands,j}} \frac{V}{(2\pi)^3} \int_{\text{BZ}} d^3\mathbf{k}\epsilon_j(\mathbf{k}), \tag{25}$$

summing over all occupied energy bands within the first Brillouin zone into account.[5] This integral can accurately be approximated by a sum over a finite set of $\boldsymbol{k}$-points.[5] There are several ways to obtain such sets of $\boldsymbol{k}$-points. A popular one, also used throughout the thesis, is attributed to Monkhorst and Pack.[33] Here, a set of equally spaced $\boldsymbol{k}$-points is used. The number of $\boldsymbol{k}$-points is inverse proportional to the unit cell size in real space, i.e. the larger the unit cell in one direction the less $\boldsymbol{k}$-points are required in that direction. Note that for accurate calculations of metals for instance, more $\boldsymbol{k}$-points

than for insulator calculations are required to describe the Fermi surface.[32]

Throughout this thesis the Monkhorst-Pack $\boldsymbol{k}$-point generation was used. Thereby the number of subdivisions N_i in each direction of the reciprocal space, with $\mathbf{b}_i$ being the reciprocal lattice vectors, need to be specified. Note that $\boldsymbol{k}$-point grids, with even subdivisions are shifted of the Γ-point in *VASP* automatically[32]

$$\mathbf{k} = \mathbf{b}_1 \frac{n_1 + 1/2}{N_1} + \mathbf{b}_2 \frac{n_2 + 1/2}{N_2} + \mathbf{b}_3 \frac{n_3 + 1/2}{N_3}, \tag{26}$$

with $n_1 = 0, ..., N_1 - 1$, $n_2 = 0, ..., N_2 - 1$ and $n_3 = 0, ..., N_3 - 1$.

To improve the accuracy of such a discrete approximation to the Brillouin zone integration and to overcome convergence issues, broadening methods based on finite temperature approaches are used such as the Methfessel-Paxton[34] smearing, mainly used throughout the thesis, or linear interpolation schemes including weighting factors such as the tetrahedron Blöchl method.[35]

When facing surface problems, the 3D periodicity is disturbed. This is due to the fact that the surface breaks symmetry in one dimension. Assuming that the surface is infinitely extended in x and y direction, the z-direction does not possess translational symmetry. To overcome this problem the so called repeated slab approach is used. Here, the metal is representend by a finite number of atoms, 5 rows in this thesis, where the top two metal rows are allowed to relax accounting for surface reconstructions and the bottom rows are kept fixed representing the metal bulk. On top of this metal slab the molecules are adsorbed. The unit cell is then artificially repeated in z-direction with a sufficient amount of vacuum separating successive slabs. Additionally, a dipole-sheet is inserted within this vacuum area accounting for the different potentials of the slab in z-direction. A typical setup is shown in Figure 2 where two successive slabs are shown. Additionally the dipole-sheet as well as the unit cell are indicated.

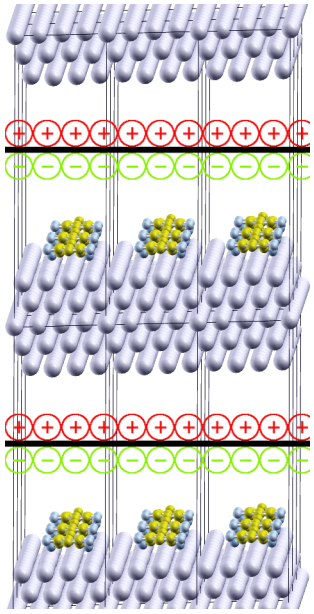

Figure 2: Representation of an infinitely extented slab of an acceptor molecule adsorbed on Ag(111). The unit cells and the inserted dipole layer are indicated as well.

Inserting the wave functions (21) into the Kohn-Sham equations (14) leads to a set of linear equations,

$$[E - E(\mathbf{k}-\mathbf{G})]C_{\mathbf{k}-\mathbf{G}} = \sum_{\mathbf{G}'} C_{\mathbf{k}-\mathbf{G}'} V_{\mathbf{G}-\mathbf{G}'} \tag{27}$$

where $V_{\mathbf{G}}$ is the Fourier component of the periodic lattice potential $V(\mathbf{r})$. This way the problem is reduced to solving a set of algebraic equations.[iii] The computational costs of the calculation is determined by the chosen energy cutoff and is already quite large for small systems.

All surface problems described in this thesis are based on calculations with the plane wave DFT-code *VASP*.[32,37–39] Using *VASP* the electronic ground state is obtained with the following algorithms. The computational framework of *VASP* consists of an outer loop in which the charge-density is optimized, and an inner loop in which the wave-functions are optimized.[32] In short this works as follows: The input charge density and wave functions are treated as independent quantities.[32] Within each selfconsistency loop the charge density is used to set up the Hamiltonian, then the wave functions are optimized iteratively, in a way that they approach the exact wave functions of this Hamiltonian.[32] Out of these optimized wave functions a new charge density is created, which is mixed with the old input-charge density. For the mixing of the charge density an efficient Broyden/Pulay mixing scheme[40,41] is used.

The conjugate gradient (CG)[42,43] or the or a residual minimization method (RMM)[40,44]

[iii] This is discussed in greater detail in chapter 7 of Ref. [36] among others.

do not recalculate the exact Kohn-Sham eigenfunctions but an arbitrary linear combination of the lowest eigenfunctions. Therefore it is necessary to diagonalize the Hamiltonian in the subspace spanned by the trial wave functions.[32] This is done until a predefined charge-density convergence criteria is reached.

Geometry optimizations in *VASP* are based on the Hellmann-Feymann theorem (10). Using this theorem *VASP* calculates the force $\mathbf{F}_I$ on an ion at position $\mathbf{R}_I$ and optimizes the structure until the remaining forces are below a certain threshold. For updating the ions several methods exist. Here, usually an update scheme depending on damped molecular dynamics was used in this thesis. This is especially recommended for bad initial guesses.[32] Hereby, a damped second order equation of motion is used to update the ionic degrees of freedom allowing to control the damping factor and the step size.[32]

2.1.5 Atomic orbitals and basis set

SIESTA[45,46] is a DFT program based on numerical atomic orbitals as basis functions. Hereby, one advantage is that computational costs scale linearly with the number of atoms $\mathcal{O}(N)$.[45,47] Throughout this thesis it is used for a single electronic relaxation step on-top of pre-geometry optimized structures.

The main advantage of atomic orbitals is their efficiency. Fewer orbitals are needed per electron for similar precision as for plane-wave based solution methods of the Kohn-Sham equations (14).[45,47] In *SIESTA* there are no constraints either on the radial shape of these orbitals or on the size of the basis.[45] Hence multiple-ζ, polarization, off-site, contracted and diffuse orbitals can in principle be used.[6,48] The main disadvantage of atomic orbitals is the lack of systematics for optimal convergence, an issue that quantum chemists have been working on for many years.[48–50]

It is essential for $\mathcal{O}(N)$-codes such as *SIESTA* that the Hamiltonian and overlap matrices are sparse.[45] This however requires that small matrix elements are neglected or the use of strictly confined basis orbitals.[45] The latter implies that the basis orbitals are strictly zero outside a certain radius.[51] Within this radius, the atomic basis orbitals are products of a numerical radial function and a spherical harmonic.[45,47] For an atom I at position $\mathbf{R}_I$ this leads to

$$\phi_{Ilmn}(\mathbf{r}) = \phi_{Iln}(\mathbf{r}_I)Y_{lm}(\hat{\mathbf{r}}_I), \tag{28}$$

where $\mathbf{r}_I = \mathbf{r} - \mathbf{R}_I$ and l, m represent the angular momentum and n labels the orbital index.[45]

A multiple-ζ basis is usually referred to several orbitals (different n-s) with the same angular but different radial dependence.[45] A Double Zeta (DZ) type basis hence doubles all basis functions, i.e., hydrogen would be described with two s-functions (1s and 1s').[6] An further improvement would be DZ-split valence basis sets.[6] This implies that only the basis functions for the valence electrons are doubled as a doubling of the core electron functions is in practice rarely considered.[iv]

A next better basis set is a Triple Zeta (TZ) basis set, now containing three times as many functions as the minimum basis set, i.e., 3 s-functions for hydrogen.[6] Again if

[iv] The term DZ is used to cover both cases.

only the valence orbitals are tripled, it is called a TZ split-valence basis set.[v]

A next improvement is to include higher angular momentum functions, usually denoted as polarization functions.[6] As a result p-orbitals introduce a polarization in s-orbitals, d-orbitals are used to polarize p-orbitals and so on. Using a double-zeta basis set with polarization functions would be denoted as double-zeta-polarized (DZP); using two polarization functions as (DZ2P); a triple-zeta basis with polarization functions - TZP and so on.

Practically, in *SIESTA* each radial function can have a different cutoff radius and within this radius it can have a completely free shape.[45] *SIESTA* provides an automatic procedure to generate sufficiently good basis sets. All of them are based on the split-valence method.[48]

In that method, the first-ζ basis orbitals are fixed linear combinations of Gaussians, determined either variationally or by fitting numerical atomic eigenfunctions.[45] The second-ζ orbital is one of the Gaussians, which is split from the contracted combination and the same procedure could be repeated for higher order ζ orbitals.[45]

SIESTA adapts the split-valence method for the numerical orbitals.[45] Following that method, the second-ζ orbital $\phi_l^{2\zeta}(\mathbf{r})$ in *SIESTA* has the same tail as the first-ζ orbitals $\phi_l^{1\zeta}(\mathbf{r})$ but it changes to a polynomial behavior inside a split-radius $\mathbf{r}_l^s$.[45]

$$\phi_l^{2\zeta}(\mathbf{r}) = \begin{cases} \mathbf{r}^l(a_l - b_l\mathbf{r}^2) & \text{if } \mathbf{r} < \mathbf{r}_l^s \\ \phi_l^{1\zeta}(\mathbf{r}) & \text{if } \mathbf{r} \geqslant \mathbf{r}_l^s \end{cases} \tag{29}$$

Here, a_l and b_l are determined by imposing the continuity of value and slope at $\mathbf{r}_l^s$.[45] The characteristics of such orbitals is that they combine the decay of the atomic eigenfunctions with a smooth and featureless behavior inside $\mathbf{r}_l^s$.[45]

In order to obtain well converged results it is useful to include polarization orbitals as well into the description to account for the deformation induced by bond formation.[45] Within this thesis, calculations in *SIESTA* used the double-ζ polarized (DZP) basis set as it usually leads to good results and a fair balance between computational time and preciseness of the calculations.

2.1.6 Pseudopotentials

For most of the physical and chemical quantities of interest it is sufficient to treat the valence electrons as core electrons hardly participate in any chemical interaction.[5] Especially for the description of core electrons within a plane-wave basis a large energy cutoff including plane waves that oscillate on short length scales in real space is necessary.[5,9] This however increases the computational costs without being necessary from a physical point of view.[9] Therefore, from the earliest developments of plane-wave methods the advantage to approximate the collective impact of the core electrons and hence to reduce the number of plane waves necessary to do the calculations was realized.[9]

The basic idea behind a norm-conserving (*vide infra*) pseudopotential approach, being a quite "old" invention of Hamann, Schlüter and Chiang[52] 1979, is that one defines a

[v] The term TZ is used to cover both cases.

cutoff radius r_c. For all $r > r_c$ the pseudopotential wave function, $\chi(\mathbf{r})$, and the real wave function, $\psi(\mathbf{r})$, should be identical

$$\chi(\mathbf{r}) = \psi(\mathbf{r}) \qquad \text{if} \qquad r > r_c. \tag{30}$$

This also implies that their potentials are identical. Furthermore, the real wave function ψ and the pseudopotential wave function χ possess the same norm-conserving integral [8] within a sphere of the radius r_c[vi]

$$\int_{|\mathbf{r}|\leqslant r_c} d^3|\chi(\mathbf{r})|^2 = \int_{|\mathbf{r}|\leqslant r_c} d^3|\psi(\mathbf{r})|^2. \tag{31}$$

The latter ensures that the pseudopotential wave function is a quantum mechanically correct approximation of the real wave function. [8] Outside the core region defined by, r_c, the pseudopotential and the pseudo-wave function are identical to the all-electron potential and wave function. Within that region however, the radial nodes of the wave function are removed while maintaining the norm of the wave functions and the scattering properties. [8]

"Roughly speaking" a pseudopotential approach replaces the charge density for a chosen set of core electrons with a smoothened density in a way that the important physical properties of the core electrons and mathematical properties of the core density are preserved. [9] In all calculations the core electrons are fixed at their position, i.e. the frozen core approximation is used. Calculations not applying this approximation are called all-electron calculations.[vii]

For the frozen core approximation, the projector augmented wave (PAW) method originally introduced by Blöchl [53] was adapted for *VASP* by Kresse and Joubert. [54] They performed an extensive study comparing ultra-soft pseudopotentials (USPPs) based on the work by Vanderbilt [55] with PAW and both with all electron calculations for small molecules. [54] Their study showed that PAW gives basically the same result as USPPs. [54] Both are in reasonably good agreement with all electron calculations. [54] However, PAW potentials are slightly more accurate than the USPP in a way that PAW gives more reliable results for magnetic materials and atoms with large differences in electronegativity. [54]

This is why throughout this thesis whenever *VASP* calculations were made, PAW pseudopotentials were used. For most of the elements used several PAW versions exist; two of them were used. Almost all calculations were made with the *soft* pseudopotentials. Only for a few special calculations the so called *hard* pseudopotentials were used. *Soft* pseudopotentials work with a cutoff energy for the planewaves in the range of 250 to 280 eV. [32] The *hard* pseudopotentials, cutoff energy around 700 eV, give results essentially identical to the "best" DFT calculations presently available but at increased computational costs. [32]

SIESTA also uses norm-conserving pseudopotentials based on the Troullier-Martins

[vi] This is why this approach is called norm-conserving.

[vii] WIEN2K is such an all electron code developed in Vienna in the group of P. Blaha, K. Schwarz, G. Madsen, D. Kvasnicka and J. Luitz.

scheme.[56,57] For *SIESTA*, I had to built some pseudopotentials. Therefore, calculations including relativistic effects were made using LDA with Ceperly Adler(CA) flavor. In the following, the generation of a pseudopotential file for Br is explained as an example. The pseudopotential files for *SIESTA* are generated with the *ATOM* [58] code. This code can be found in the util-directory of the *SIESTA* package. It contains also a manual with the detailed description for generating pseudopotentials.[58] Based on that manual 58, the following will explicitly state the essential steps including the output and discuss the important parameters on the way towards a pseudopotential generation.

Pseudopotential generation in SIESTA. Within this part a detailed step-by-step instruction of how to construct a Br-pseudopotential file for *SIESTA* is given. This can be done with the *ATOM*-program. The *ATOM* [58] input file for the relativistic Br pseudopotential generation (pg) looks as follows using an improved Troullier-Martins scheme ($tm2$) with a critical radius of $r_c = 3.00\,\text{Bohr}$. Hereby, the $4s^2$, $4p^5$, $4d^0$, and the $4f^0$ are the 4 valence electrons sets, and the $1s^2$, $2s^2$, $2p^6$, $3s^2$, $3p^6$ and $3d^{10}$ are the 6 core electrons sets.

```
%define NEW_CC
  pg Br TM2 Pseudopotencial GS ref
       tm2     3.00
  Br   pbr
        0
   6    4              # norbs_core, norbs_valence
   4    0      2.00    # 4s2
   4    1      5.00    # 4p2
   4    2      0.00    # 4d0
   4    3      0.00    # 4f0
     1.40      1.50      1.85      1.40      1.50      0.00
#
# Last line (above):
# rc(s) rc(p) rc(d) rc(f) rcore_flag rcore #
#
1234567890123456789012345678901234567890123456789012345678901234567890      Ruler
```

In that calculation the pseudopotential core radii, all given in Bohr, are 1.40 for the s, 1.50 for the p, 1.85 for the d, 1.40 for the f channel and 1.50 for the core correction as they produced the best result. For a detailed description refer to the *ATOM* manual.[58]

In a second step, an all-electron (ae) calculation for Br has to be made.[viii] To test the quality of the obtained pseudopotential (PS) one has to compare the all electron (AE) with the PS eigenvalues (4th column). This is done by executing "`grep '& v' OUT`". The output looks as follows:

[viii] The corresponding input file is not explicitly shown here as only minor changes have to be made. Refer to the *ATOM* manual[58] for the correct keywords.

```
 ATM 3.2.2  4-APR-08   Br TM2 Pseudopotencial GS ref                    &v&d
 4s   0.5    2.0000      -1.47593076       0.00000000     -55.58128530  &v
 4p  -0.5    1.6667      -0.60225909       0.00000000     -44.78941134  &v
 4p   0.5    3.3333      -0.56596215       0.00000000     -43.66659679  &v
 4d  -0.5    0.0000       0.00000000       0.00000000      -0.70020938  &v
 4d   0.5    0.0000       0.00000000       0.00000000      -0.70020938  &v
 4f  -0.5    0.0000       0.00000000       0.00000000      -0.66926886  &v
 4f   0.5    0.0000       0.00000000       0.00000000      -0.66926885  &v
---------------------------- &v
 4s   0.5    2.0000      -1.47593365       0.95136379      -8.09749804  &v
 4p  -0.5    1.6667      -0.60222230       1.36189714      -7.21871372  &v
 4p   0.5    3.3333      -0.56595342       1.30113618      -7.06965747  &v
 4d  -0.5    0.0000       0.00000000       0.00112687      -0.13871218  &v
 4d   0.5    0.0000       0.00000000       0.00112687      -0.13871218  &v
 4f  -0.5    0.0000       0.00000000       0.00215193      -0.13367562  &v
 4f   0.5    0.0000       0.00000000       0.00215193      -0.13367562  &v
---------------------------- &v
```

The AE and PS eigenvalues are not exactly identical because the pseudopotentials are changed slightly to make them approach their limit tails faster.[58] The values in the

As first test, the AE and PS charge densities are compared to get a feeling for its quality. This can be conveniently done with the help of a provided gnuplot-script. In a next step the wave functions, their logarithmic derivatives, the real-space pseudopotential as well as the Fourier transformed pseudopotential are compared using again a provided gnuplot-script to produce the figures. First of all the charge densities are analyzed in Figure 3.

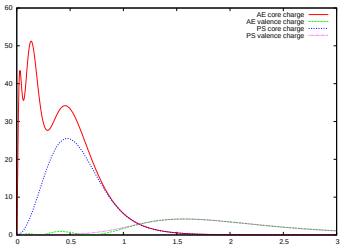

Figure 3: Comparison of the *AE* and the *PS* charge densities of Br. Here, explicitly the valence and the core charge densities for both calculations are shown.

Here it is important that the pseudo-charge density equals the true all-electron charge density for the valence electrons, i.e. outside the critical radius r_c, and that they are "identical" at r_c. Note that the pseudo-charge density of the core electrons does not possess any nodes at $r < r_c$ as stated above. In the next Figure 4 the output of the second gnuplot-script for testing purposes is shown for the Br 4s, 4p, 4d and 4f states, respectively.

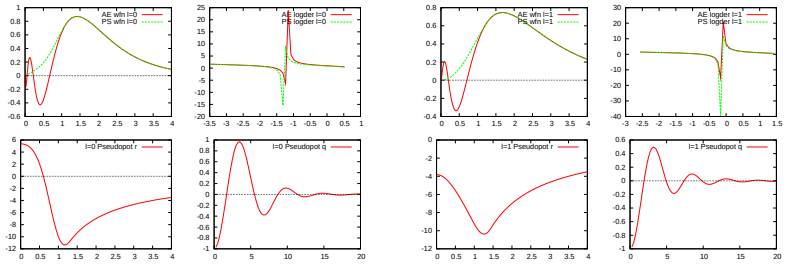

(a) Br 4s

(b) Br 4p

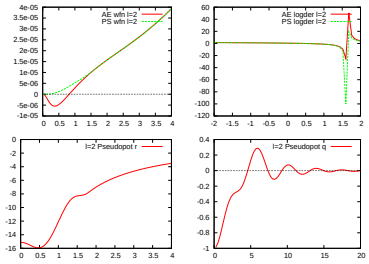

(c) Br 4d

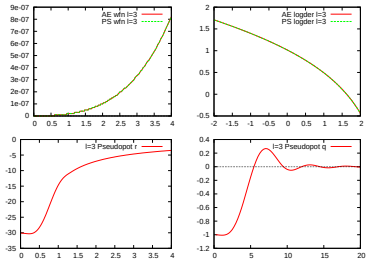

(d) Br 4f

Figure 4: All panels contain a comparison of the AE and PS wave functions (top left), the AE and PS logarithmic derivatives (top right), the real-space pseudopotential (bottom left) and the Fourier-transformed pseudopotential times q^2/Z_{ps} (bottom right) as obtained from the gnuplot-script. In a) the Br 4s electronic properties are shown, in b) the 4p, in c) the 4d and in d) the 4f.

Figure 4 allows a quick screening whether the chosen parameters are suitable. It is important that the wave functions of both calculations are identical at $r > r_c$ and that the Fourier-transformed pseudopotential is smooth at large r. Hence, screening of the top left and bottom right panels for each shell is practically sufficient.

In the end of the day, however, there is no substitute for a proper transferability testing.[58] A pseudopotential with good transferability will reproduce the all-electron energy levels and wave functions in arbitrary environments, i.e., also in the presence of charge transfer, which always takes place when forming solids and molecules.[58] An advantage of norm conservation is that it guarantees a certain degree of transferability. Nevertheless, we can get a better assessment by performing all-electron and 'pseudo'-calculations on the same series of atomic configurations, and comparing the eigenvalues and excitation energies.[58] Therefore, test calculations containing the concatenation of 6 jobs were made and afterwards the command "`grep '& d' OUT`" was executed for comparison of the energies and "`grep '& v' OUT`" for comparison of the eigenvalues. Here, the first three are input parameters of the all-electron (ae) and the last three of the pseudopotential test (pt) runs for the same configurations. The input file for the

different configurations read as follows:

```
ae Br TM2 Pseudopotencial GS ref
Br   pbr
      0
 6    4
 4    0      2.00
 4    1      5.00
 4    2      0.00
 4    3      0.00
ae Br TM2 Pseudopotencial GS ref
Br   pbr
      0
 6    4
 4    0      2.00
 4    1      5.50
 4    2      0.00
 4    3      0.00
ae Br TM2 Pseudopotencial GS ref
Br   pbr
      0
 6    4
 4    0      2.00
 4    1      4.00
 4    2      1.00
 4    3      0.00
pt Br TM2 Pseudopotencial GS ref
Br   pbr
      0
 6    4
 4    0      2.00
 4    1      5.00
 4    2      0.00
 4    3      0.00
pt Br TM2 Pseudopotencial GS ref
Br   pbr
      0
 6    4
 4    0      2.00
 4    1      5.50
 4    2      0.00
 4    3      0.00
pt Br TM2 Pseudopotencial GS ref
Br   pbr
      0
 6    4
 4    0      2.00
 4    1      4.00
 4    2      1.00
 4    3      0.00

12345678901234567890123456789012345678901234567890123456789012345678901234567890      Ruler
```

The configurations differ in the promotion of electrons from one level to another (exciting electrons), where in the second configuration only a fraction of an electron was transferred. Hence, the first calculation corresponds to a neutral Br-atom calculation. In the second configuration half an electron was added to the 4p2 shell, and in the last configuration an electron of the 4p2 shell was transferred to the 4d0 shell. The output for checking the corresponding energies is shown below:

```
 ATM 3.2.2 13-MAR-08   Br TM2 Pseudopotencial GS ref                    &v&d
 ATM 3.2.2 13-MAR-08   Br TM2 Pseudopotencial GS ref                    &v&d
```

```
 ATM 3.2.2 13-MAR-08   Br TM2 Pseudopotencial GS ref                    &v&d
 &d total energy differences in series
 &d          1        2        3
 &d  1    0.0000
 &d  2   -0.2097   0.0000
 &d  3    0.7833   0.9929   0.0000
*----- End of series ----* spdfg &d&v
 ATM 3.2.2 13-MAR-08   Br TM2 Pseudopotencial GS ref                    &v&d
 ATM 3.2.2 13-MAR-08   Br TM2 Pseudopotencial GS ref                    &v&d
 ATM 3.2.2 13-MAR-08   Br TM2 Pseudopotencial GS ref                    &v&d
 &d total energy differences in series
 &d          1        2        3
 &d  1    0.0000
 &d  2   -0.2097   0.0000
 &d  3    0.7832   0.9929   0.0000
*----- End of series ----* spdfg &d&v
```

Comparison shows that the results agree well and hence the *Br* pseudopotential is suitable. The same excellent agreement can be found when comparing the eigenvalues (4th column) of the pt-run (first three parts) and the ae-run (last three parts) as the following output shows.

```
 ATM 3.2.2 13-MAR-08   Br TM2 Pseudopotencial GS ref                    &v&d
 4s   0.5    2.0000      -1.47593076       0.00000000     -55.58128530  &v
 4p  -0.5    1.6667      -0.60225909       0.00000000     -44.78941134  &v
 4p   0.5    3.3333      -0.56596215       0.00000000     -43.66659679  &v
 4d  -0.5    0.0000       0.00000000       0.00000000      -0.70020938  &v
 4d   0.5    0.0000       0.00000000       0.00000000      -0.70020938  &v
 4f  -0.5    0.0000       0.00000000       0.00000000      -0.66926886  &v
 4f   0.5    0.0000       0.00000000       0.00000000      -0.66926885  &v
---------------------------- &v
 ATM 3.2.2 13-MAR-08   Br TM2 Pseudopotencial GS ref                    &v&d
 4s   0.5    2.0000      -1.14227023       0.00000000     -55.06775715  &v
 4p  -0.5    1.8333      -0.28843770       0.00000000     -43.34271613  &v
 4p   0.5    3.6667      -0.25471233       0.00000000     -42.11221843  &v
 4d  -0.5    0.0000       0.00000000       0.00000000      -0.62911175  &v
 4d   0.5    0.0000       0.00000000       0.00000000      -0.62911141  &v
 4f  -0.5    0.0000       0.00000000       0.00000000      -0.62837674  &v
 4f   0.5    0.0000       0.00000000       0.00000000      -0.62837626  &v
---------------------------- &v
 ATM 3.2.2 13-MAR-08   Br TM2 Pseudopotencial GS ref                    &v&d
 4s   0.5    2.0000      -1.91342069       0.00000000     -56.81412282  &v
 4p  -0.5    1.3333      -0.99950954       0.00000000     -47.25732562  &v
 4p   0.5    2.6667      -0.95831191       0.00000000     -46.23170673  &v
 4d  -0.5    0.4000      -0.04702773       0.00000000     -12.29033820  &v
 4d   0.5    0.6000      -0.04668128       0.00000000     -12.17117544  &v
 4f  -0.5    0.0000       0.00000000       0.00000000      -0.66954383  &v
 4f   0.5    0.0000       0.00000000       0.00000000      -0.66954383  &v
---------------------------- &v
*----- End of series ----* spdfg &d&v
 ATM 3.2.2 13-MAR-08   Br TM2 Pseudopotencial GS ref                    &v&d
 1s   0.5    2.0000      -1.47606902       0.95132777      -8.09752375  &v
 2p  -0.5    1.6667      -0.60225992       1.36203111      -7.21895055  &v
 2p   0.5    3.3333      -0.56598436       1.30125932      -7.06988192  &v
 3d  -0.5    0.0000       0.00000000       0.00112687      -0.13871218  &v
 3d   0.5    0.0000       0.00000000       0.00112687      -0.13871218  &v
 4f  -0.5    0.0000       0.00000000       0.00215193      -0.13367562  &v
 4f   0.5    0.0000       0.00000000       0.00215193      -0.13367562  &v
---------------------------- &v
 ATM 3.2.2 13-MAR-08   Br TM2 Pseudopotencial GS ref                    &v&d
 1s   0.5    2.0000      -1.14250170       0.92890881      -8.05564929  &v
 2p  -0.5    1.8333      -0.28848806       1.28029376      -7.04724179  &v
 2p   0.5    3.6667      -0.25477896       1.21535469      -6.88306282  &v
 3d  -0.5    0.0000       0.00000000       0.00982843      -0.12581974  &v
```

```
 3d   0.5    0.0000        0.00000000        0.00982843       -0.12581974  &v
 4f  -0.5    0.0000        0.00000000        0.01079635       -0.12566962  &v
 4f   0.5    0.0000        0.00000000        0.01079635       -0.12566962  &v
---------------------------- &v
 ATM 3.2.2 13-MAR-08   Br TM2 Pseudopotencial GS ref                    &v&d
 1s   0.5    2.0000       -1.91326726        1.00330621       -8.18751478  &v
 2p  -0.5    1.3333       -0.99919052        1.50710096       -7.48542710  &v
 2p   0.5    2.6667       -0.95801555        1.44944468       -7.34950944  &v
 3d  -0.5    0.4000       -0.04700482        0.30305740       -2.38705210  &v
 3d   0.5    0.6000       -0.04666473        0.29718125       -2.36551762  &v
 4f  -0.5    0.0000        0.00000000        0.00215150       -0.13373027  &v
 4f   0.5    0.0000        0.00000000        0.00215150       -0.13373027  &v
---------------------------- &v
*----- End of series ----* spdfg &d&v
```

A graphical representation of the all-electron and the pseudopotential wave function underlines the found agreement, Figure 5.

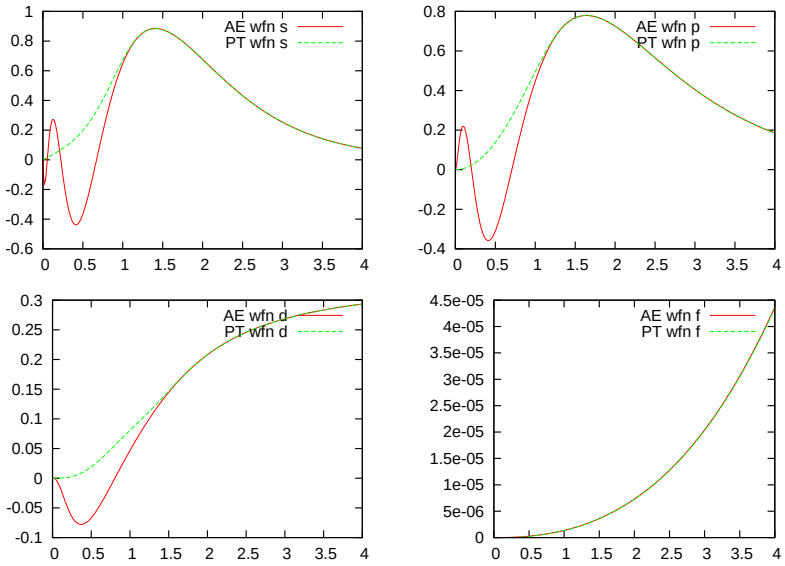

Figure 5: Comparison of the valence all-electron (ae) and pseudo-wavefunctions (pt) of Br for the different orbitals (top: s and p; bottom: d and f).

In the end, *SIESTA* needs pseudopotential files with the extention **.psf*. Throughout my thesis I constructed relativistic pseudopotentials for *Ag.psf, Au.psf, B.psf, Br.psf, Cl.psf, C.psf, H.psf, Na.psf, N.psf, O.psf, Se.psf and S.psf.*

2.2 Physical and chemical analysis of surface properties

The following subsection deals with a brief introduction of the basic analysis methods used for the surface problems investigated in this thesis. Some of the properties can be

compared to experimental data and others are valuable theoretical tools to investigate bonding of molecules to surfaces.

2.2.1 Density of states and projections

In a solid or on the surface, there are a very large number of levels or states. A way to characterize them is to look at all the levels in a given energy interall. The density of states (DOS) of a system describes the number of states as a function of energy. The integral of the DOS up to the Fermi level gives the total number of occupied levels. Multiplied by two it gives the total number of electrons. Hence, the DOS plots the distribution of electrons in energy in real space. It can usually be obtained in a straightforward way from the DFT calculations. Hereby, the calculated bandstructure is summed up in $\boldsymbol{k}$-space over the first Brillouin zone.[ix]

$$N(E) = \sum_{i=1}^{\infty} \delta(E - \epsilon_i) \tag{32}$$

Here, the sum is extended over all eigenstates of the Kohn-Sham Hamiltonian, equation (14). As we are dealing with a finite number of eigenstates this distribution has to be smeared out. Hereby, several techniques exist. Most of the time, a first order Methfessel-Paxton smearing was used in this thesis.[34] Sometimes a Gaussian smearing[59] and in case of accurate representation of the DOS the so called tetrahedron method with Blöchl corrections was used.[35][x]

Upon contact with the metal surface, molecular bands hybridize and shift in energy. When analyzing the DOS it is highly interesting where in energy a specific atomic species contribute or where in energy specific molecular orbitals contribute. An explicit way for calculating these effects for metal-organic interfaces is to project the DOS onto the molecule or the molecular orbitals.[60–64] Such a projection of the density of states, projected density of states (PDOS), can be defined in the following way:

$$n_\alpha(E) = \sum_{i=1}^{\infty} | < \phi_\alpha | \varphi_i > |^2 \delta(E - \epsilon_i). \tag{33}$$

Equation (33) is a general projection of the density of states (PDOS) where ϕ_α is a localized state and φ_i represents Bloch states. If ϕ_α is a position state $|\mathbf{r}>$ the so called local density of states (LDOS) is obtained which has been used for scanning tunneling microscopy (STM) simulations, see subsection 2.2.4.

For a more detailed description of the PDOS I want to refer to the PhD thesis of Lorenz Romaner[65] where different projection techniques, also used throughout this thesis, are explained in great detail. For our purpose it is important to keep in mind that whenever projections onto the molecular orbitals of the isolated monolayer in its adsorption position are made the quantity will be called molecular orbital density of

[ix] Note that for periodic systems integrals in real space are replaced by finite integrals over the first Brillouin zone in $\boldsymbol{k}$-space, which are approximated by a summation.

[x] "The main drawback of the tetrahedron Blöchl method is that it is not variational with respect to partial occupancies. Therefore, the calculated forces might be wrong by a few percent." For further details see Ref. [32].

states (MODOS). When the contributions onto the whole molecular region is analyzed the term molecular density of states (MDOS) will be used instead of the more general term PDOS.

2.2.2 Population analysis based on basis functions

It is of uppermost interest to get a feeling how the electrons rearrange when an electrically neutral atom bonds to another neutral atom that is more electronegative, or to a surface. Hereby, electrons are partially redistributed. This is due to the hybridization of the molecular orbitals with the metal bands, and as a result the electrons are "shared" between the metal and the molecule. This in the end leads to fractional or partial occupancies. Hence, partial charges are created due to the asymmetric distribution of electrons in chemical bonds. The information gained out of such an analysis are often used for a qualitative understanding of the structure and reactivity of molecules. Although it is quantum-mechanically not possible to strictly associate electrons of a multi-atomic system with individual atoms several partitioning schemes exist. Commonly there are three conceptually different approaches used for assigning a charge to a given atom.[6]

1. Partitioning the wave functions in terms of the basis functions.
2. Fitting schemes.
3. Partitioning the electron density into atomic domains.

Population analysis schemes falling within the first point are the *Mulliken*[66] population analysis, used in this thesis and described for a simple example below, and the *Löwdin*[67,68] method.[6] The *ElectroStatic Potential* (ESP) method, for instance, belongs to point two and the perhaps most rigorous way of dividing a molecular volume into atomic subspaces, the *Atoms In Molecules* (AIM) method of Bader[69,70] falls under point three.[6] Further methods within this point are the *Natural Atomic Orbital* and *Natural Bond Orbital* analysis developed by F. Weinholt and co-workers.[71] For a brief introduction to all of them I want to refer to the chapter about wave-function analysis in the book of Jensen et al. [6].

I would like to take a simple example to illustrate the way how the Mulliken population analysis works. This is taken from a textbook by Roald Hoffmann.[72] Let us consider a two-center molecular orbital:

$$\Psi = c_1\chi_1 + c_2\chi_2 \tag{34}$$

Hereby, χ_1 is centered at atom one and χ_2 at atom two. χ_1 and χ_2 are normalized but not orthogonal. The distribution of an electron in this molecular orbital (MO) is then given by $|\Psi|^2$. $|\Psi|^2$ should be normalized in a way that

$$\int |\Psi|^2 d\tau = \int |c_1\chi_1 + c_2\chi_2|^2 d\tau = c_1^2 + c_2^2 + 2c_1c_2S_{12} \stackrel{!}{=} 1 \tag{35}$$

where S_{12} is the overlap integral between χ_1 and χ_2. It describes the electron distribution in Ψ. Obviously c_1 belongs to atom 1 and c_2 to two. $2c_1c_2S_{12}$, however, is a quantity that is somehow associated with both atoms, i.e., includes their interaction. It is called the overlap population. As there is no unambiguous way to decide where the electrons belong Mulliken suggested a democratic solution, splitting $2c_1c_2S_{12}$ equally between both atoms, which is an arbitrary but unbiased choice. Nevertheless, due to the normalization condition this assignment guarantees that the sum of the electron density for atom one and two is 1.

In a next step we generalize this simple example. Common within the framework of wave function based partitioning schemes is that somehow the overlap matrix **S** and the density matrix **D** are involved.[6] The Mulliken analysis is based on partitioning the $\mathbf{D} \cdot \mathbf{S}$ matrix product.[66] A diagonal element $D_{\alpha\alpha}S_{\alpha\alpha}$, hereby represents the number of electrons of the α-th atomic orbital (AO). An off-diagonal element $D_{\alpha\beta}S_{\alpha\beta}$ is split equally between the AOs of α and β. Such a partitioning scheme obviously comes along with some errors. Some common problems within this type of partitioning are:[6]

- The diagonal elements of the matrix may be larger than two. This implies more than two electrons can be in one orbital, violating the Pauli principle.
- The off-diagonal elements may become negative. This implies a negative number of electrons between two basis functions, which clearly is physically impossible.
- There is no objective reason for dividing the off-diagonal contributions equally between the two orbitals. This partitioning clearly does not properly consider the electronegativity effect.
- Basis functions centered, e.g., on atom A may have a small exponent, such that they effectively describe the wave function far from atom A. Nevertheless, the electron density is counted as only belonging to A.
- The dipole, quadrupole, etc., moments are in general not conserved, i.e. a set of population atomic charges does not reproduce the original multipole moments.

Nonetheless, with all its shortcomings this Mulliken population analysis was used throughout my thesis as it is conveniently accessible in *SIESTA* and the conclusions drawn here are not affected by slight changes of the population.

2.2.3 COOP and MOOP

"The detective work of tracing molecule-surface interactions"[72] can be partially answered with the help of decompositions and projections of the DOS, *vide supra*. Nonetheless, the important question, where within a molecule the bonds establish cannot be answered that way. Therefore, the idea of an overlap population (see example within 2.2.2) needs to be extended to the crystal and in the end of the day to the surface. Hereby, the characteristic term for bonding $2c_1c_2S_{12}$ represents the bond order:[xi] it is

[xi] This is correct if the overlap integral is taken as positive, what can be made [72]

bonding if c_1 and c_2 have the same sign and anti-bonding if they are of opposite sign. The magnitude depends on their size and the extent of the overlap. It is highly desirable to have a comparably analysis method for extended systems as well. Hughbanks and Hoffmann introduced such a tool named crystal orbital overlap population (COOP) in the early 1980s.[64,73]

Within this thesis I follow the process described in Refs. [64,73] for the analysis of the COOP. The COOP is defined as

$$COOP_{X,Y}(E) = \sum_{m\in X, l\in Y, i, \mathbf{k}} c^*_{im\mathbf{k}}\, c_{il\mathbf{k}}\, S_{ml\mathbf{k}}\, \delta(E - \epsilon_{i\mathbf{k}}) \tag{36}$$

Here, X and Y denote a set of atomic orbitals, the $c_{il\mathbf{k}}$ correspond to the linear combination of atomic orbitals (LCAO)-coefficients and the $S_{ml\mathbf{k}}$ is the overlap matrix. This definition resolves the bonding (positive) and anti-bonding (negative) contributions of specific atomic orbitals on the energy scale. It enables us to investigate the role of specific atoms within the adsorption process and even allows analyzing the impact of geometric distortions and charge transfer.

In order to familiarize myself with that kind of analysis and to test the programs I took several molecules as example including H_2, N_2, H_2O, HCl among others. Here, I want to use N_2 in analogy to Ref. [64,72] to introduce the advantages of this method. Figure 6a shows the molecular orbital diagram of N_2. There, the atomic orbitals of the isolated N-atoms are indicated as well. The shape of the arising molecular orbitals formed through interaction out of the isolated orbitals are additionally shown. The lowest atomic orbitals, the $1s$ orbitals, are not shown because their molecular orbital (the σ_g and σ_u) pair will contribute little in terms of bonding as their overlap will be negligible. The gerade combination of the $2s$ orbitals, σ, will be strongly bonding. The ungerade combination, σ^*, is expected to be anti-bonding. π_{xy} is expected to be strongly bonding. σ' is expected to be slightly bonding and π^*_{xy} to be strongly anti-bonding.[xii] Using the COOP to trace down bonding, Figure 6b characterizes bonding for N_2 at one glance. There the DOS, dotted lines, as well as the COOP is shown. It is easily seen that maximal bonding occurs for 7 electron pairs, including the 2 pairs of the nitrogen $1s$ combination. More or fewer electrons will hence weaken the overlap population.
In Figure 6b the expected slightly bonding contribution of σ' is anti-bonding. Considering the relative size it is however essentially "non-bonding" as Hoffmann puts it for the same combination in his book[72] and his review article.[64]

[xii] The results in Figure 6a were obtained with *SIESTA*1.3 using GGA and the PBE exchange-correlation functional. Test calculations, however, varying the exchange correlation (XC) functional and the distance, show that the σ' combination as well as the σ^*, both best characterized as lone-pair combinations, can be either slightly bonding or anti-bonding. Nevertheless, they are essentially non-bonding.

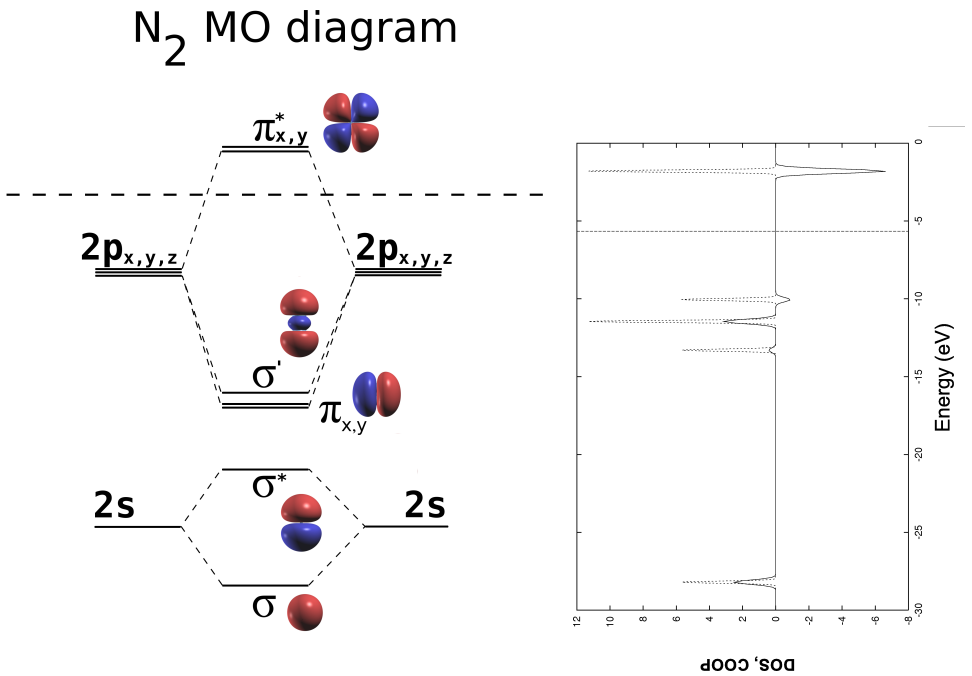

(a) (b)

Figure 6: Molecular orbital diagram of N_2. The representation of the molecular orbitals as obtained from an isolated molecule calculation as well as the individual atomic orbitals are shown in (a). In (b) the DOS of N_2 (dashed lines) as well as the COOP in (b). The vertical line in (b) indicates the Fermi energy.

Conceptually, the basis set in which the COOP is evaluated is not restricted to AOs. The same analysis can be carried out also in the basis of MOs to see where, on the energy scale, a specific MO gives bonding or anti-bonding contributions. Hence, in agreement with previous work,[1], another complete basis set $\{|M_{m\mathbf{k}}|\}$ was chosen. It includes all molecular orbitals $\left\{|\tilde{M}_{m\mathbf{k}}|\right\}$ and all metallic atomic orbitals $\{|A_{g\mathbf{k}}|\}$.[xiii] In analogy to the LCAO-coefficients we can calculate the linear combination of molecular orbitals (LCMO)-coefficients.[1,65] Hence, the molecular orbital overlap population (MOOP) can be calculated as:

$$MOOP_{X,Y}(E) = \sum_{m\in X, l\in Y, i,k} c^{M*}_{im\mathbf{k}}\, c^{M}_{il\mathbf{k}}\, S^{M}_{ml\mathbf{k}}\, \delta(E-\epsilon_{i\mathbf{k}}) \tag{37}$$

Hereby, $S^{M}_{ml\mathbf{k}}$ is the overlap matrix of the molecular orbitals.

Note that positive areas in the COOP and MOOP curves represent bonding and negative areas anti-bonding interactions. Additionally, for both quantities one can define a total overlap population (ToP) as integration up to the Fermi energy. This reflects the bonding strength and theoretically scales with the bond order.[72]

[xiii] Note that for the latter also the Bloch states of the metal could have been chosen. However, as the only interesting aspect is where on the energy scale a specific orbital is bonding or antibonding with respect to all the metallic states, the difference does not matter.

2.2.4 STM, XPS and IR

STM, X-ray photoelectron spectroscopy (XPS) and Infrared (IR) are three surface characterization methods. All require expensive equipment as well as highly idealized circumstances, i.e. ultra high vacuum, clean surfaces. Therefore, it is highly desired to quickly obtain simulated results. *VASP* offers the opportunity to simulate all three of them. The basic concepts are highlighted in this chapter.

STM is a quite "new" theory, invented in the early 80s by Gerd Binning and Heinrich Rohrer,[74–76] who were awarded the Nobel Prize in Physics in 1986. A brief introduction can be found for instance in Refs. [77,78]. Roughly spoken a conducting tip is brought in close vicinity to the surface. Then a bias is applied between the tip and the surface allowing electrons to tunnel through the vacuum. Hence, electrons are moving and a current is emerging. This tunneling current can be measured as a function of tip position, the applied voltage and the local density of states of the sample at the position of the tip.[79] Hence, the STM image represents the tunneling probability density map of electronic states near the Fermi level. The tunneling current in Bardeen's formalism[80] is given by

$$I = \frac{2\pi e}{\hbar} \sum_{\mu,\nu} f(E_\nu)\left[1 - f(E_\nu + eV)\right] |M_{\mu\nu}|^2 \delta(E_\mu - E_\nu) \tag{38}$$

where $f(E_\nu)$ is the Fermi function at the energy E_ν, V is the applied voltage, $M_{\mu\nu}$ is the tunneling matrix element between states ψ_μ of the probe and ψ_ν of the surface, and E_μ is the energy of state ψ_μ in the absence of tunneling.[81] Here, the tunneling matrix element $M_{\mu\nu}$, is the crucial element. It is given by:

$$M_{\mu\nu} = \frac{\hbar^2}{2m} \int dS(\psi_\mu^* \nabla\psi_\nu - \psi_\nu^* \nabla\psi_\mu) \tag{39}$$

where the integral is taken over any surface lying completely within the vacuum (barrier) region separating two sides.[81] In the case of small applied voltage and low temperature equation (38) can be simplified to:[81]

$$I = \frac{2\pi}{\hbar} e^2 V \sum_{\mu,\nu} |M_{\mu\nu}|^2 \delta(E_\nu - E_F)\delta(E_\mu - E_F) \tag{40}$$

In the early 1980th Tersoff and Hamann[79,81] developed a theoretical model where the surface is exactly represented while the wavefunction at the tip is assumed to have spherical symmetry (i.e. s-orbital), centered at the apex atom of the tip at position r_t. In that case, the tunneling current simplyfies to[81]

$$I \approx \sum_{\nu} |\psi_{rt}|^2 \delta(E_\mu - E_\nu) = \varrho(r_t, E_F), \tag{41}$$

where $\varrho(r_t, E_F)$ is the tunneling conductance.[81] The crucial approximation in that case was the evaluation of the matrix element only for a s-wave tip wave function.[79] Although the Tersoff-Hamann model is quite a drastic simplification inclusion of higher angular momenta for tip states or the use of a more realistic model for the tip structure

does not lead to significantly improved results. Additionally, one assumes that the electric field does not influence the electronic structure. Nonetheless, the simple Tersoff-Hamann approach leads to the most important features of STM images[82,83] and was used in my work.
Experimentally, there are five main variable parameters in STM.[78] These are the lateral coordinates, x and y, the height z, the bias voltage V, and the tunneling current I. Three main modes of STM operation are existing, depending on the manner in which these parameters are varied:

- *Constant-current mode*: I and V are kept constant, the tip scans x and y while z is measured.
- *Constant-height mode*: z and V are kept constant, the tip scans x and y while I is measured.
- *Scanning tunneling spectroscopy (STS)*: the tip position in x, y and z is kept constant while V is varied and current I is measured.

VASP offers the possibility to simulate the first two STM operation modes. Hereby, the local density of states at the tip position as a function of "applied voltage", i.e. the integrated local density of states between the tip bias and the Fermi level, is visualized either at a constant height or "current". Theoretically, constant height images translate to a cut through the averaged (*vide infra*), energy-integrated LDOS at a specific height and the constant-current mode translates to a representation of the iso-surface of the LDOS integrated between the Fermi energy and the tip biased at a specified voltage.[83] For both choices a smoothing of the very dense real-space grid is necessary as without it an unphysical resolution of about 0.1 $\mathring{A}$ is obtained resulting in unrealistic STM images as the tip could penetrate to the substrate between the adsorbates.[83] In order to take the finite size and shape of the tip into account the LDOS is averaged over the surface of either 56 or 69 points.[83] The modeled tips are shown in Figure 2.2.4.[83]

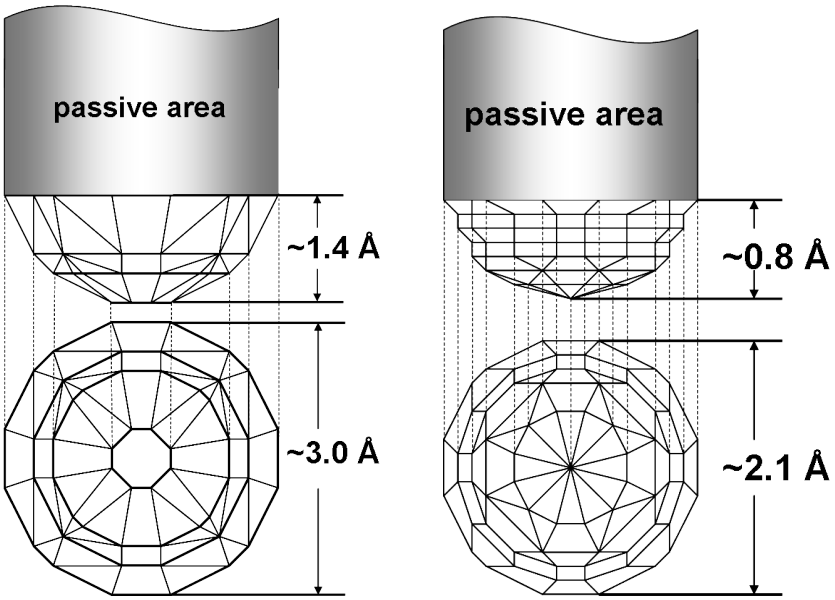

Figure 7: a) Side and bottom view on the model of the STM tip with 56 points. b) Side and bottom view on the model of the STM tip with 69 points. Indicated are the diameter and the height of the tips.

In that way, each point of the real-space grid is replaced by the average over the surface of the spherical tips with their apex being at that point of space.[83]

XPS XPS allows analyzing the elemental compostion within the probed material and the chemical environment of a given element. XPS spectra are obtained using a beam of X-rays by irradiating a material while simultaneously measuring the kinetic energy and the number of electrons leaving the sample. It is surface sensitive as it detects the top 1 to 10 nm and it requires ultra high vacuum (UHV) conditions. In the following a short description of the experiment is given and then the possibilities of obtaining XPS-spectra in *VASP* are shortly revised.

The energy that is required to remove a core electron from an atom is called core-level binding energy.[84] Experimentally, this energy is obtained via measuring the energy difference of the core-level electrons, excited via X-ray photons, and the Fermi energy.

There does not exist a detailed description of how *VASP* calculates XPS. The following follows Ref. [84], a publication of the *VASP*-group. This is to the best of my knowledge the most detailled description of the theoretical background of how *VASP* calculates XPS shifts. They do refer to unpublished work therein but up to now this work has not been published.

In *VASP* core level binding energies can be calculated either in the *initial* or the *final* state approximation using a modified PAW method.[84] In both cased it is assumed that the core hole remains entirely localized at the excited atom, which is usually a quite reasonable assumption.[84]

In the *initial* state approximation the core electron is removed without changing the potential of the valence electrons and using the frozen core approximation (Koopman's theorem).[84] Hence, electronic screening is totally neglected.[84] The core electron binding energy, Equation 42, is calculated directly out of the Kohn-Sham eigenvalues of the investigated core state ε_C and the Fermi level ε_F.[84,85]

$$E_{CL}^{\text{initial}} = \varepsilon_C - \varepsilon_F. \tag{42}$$

Here, only self-consistency for the core electrons is desired as the electron density of the valence electrons of the undisturbed systems enters as constraint. The result of initial state calculations is an absolute value for the core-level shift.

In the *finial* state approximation the valence electrons are allowed to relax as a consequence of the hole left by the removed core-electron.[84] This hole is rapidly screened by the valence electrons. As this happens in reality as well this approximation is expected to better fit to experiments. For the *final* state approximation, a single core electron is excited to the valence band.[84] Thereby, screening of the other core electrons is neglected as they are kept frozen at their original positions for which the potential was generated.[84] That this frozen core approach is suitable is shown in Ref.[85 and 84]. However, screening of the valence electrons is included.[84]

It is important to know that using this approach no absolute values for the core level binding energies can be calculated.[84] Rather core level shifts can be analyzed and compared to the experiment. They, however, show a relative sophisticated consistency and are within $20 - 50\,meV$.[84]

For the initial state shift the keyword ICORELEVEL=1 needs to be set in the INCAR file. For the final state shift the keyword ICORELEVEL=2 as well as the detailled parameters determining what electron is removed need to be specified in the INCAR file. The atom of interest needs to be specified in the POSCAR file as well and the POTCAR file needs to be updated accordingly. The corresponding tags are:

- CLNT = 1, 2, ... defines for which atomic species the electron is removed[xiv]
- CLN = 1, 2, ... defines the main quantum number of the electron
- CLL = 0, 1, 2, ... defines the angular momentum quantum number
- CLZ = 1.0 number of electrons to be removed; should be 1.0

Köhler and Kresse [84] validated the approach used in *VASP* through comparison with calculations based on "conventional" core excited ionic PAW potentials.

IR spectroscopy is based on the fact that molecules have specific frequencies corresponding to discrete energy levels, i.e. vibrational modes, at which they vibrate. They are determined by the shape of the molecular potential energy surfaces, the masses of the atoms and, by the associated vibronic coupling, i.e. roughly spoken the spring constant.

$$\tilde{\nu} = \frac{1}{2\pi c}\sqrt{\frac{k}{\mu}} \tag{43}$$

[xiv] This is determined with the ordering of the atomic species in the POSCAR file.

where k is the spring constant representing the bond, c is the speed of light, and μ is the reduced mass of the system. Generally, in order to be IR-active the vibrational mode must be associated with changes in the permanent dipole moment. On metal surfaces, only modes with a transition dipole moment perpendicular to the surface are IR active, as dipoles parallel to the surface are compensated by their mirror images in the far field. The resonant frequencies can be in a first approach related to the strength of the bond, and the mass of the atoms at either end of it. Thus, the frequency of the vibrations can be associated with a particular bond type.

VASP allows to calculate the Hessian matrix. The Hessian matrix contains the first derivatives of the force acting on atoms with respect to the atomic positions, equivalent to the second derivatives of the energy with respect to the atomic position. To calculate the Hessian the finite difference method is used.[xv] This means that each ion is displaces along Cartesian coordinates ($\pm\Delta x$, $\pm\Delta y$, $\pm\Delta z$). Hereby, Δ corresponds to the magnitude of the displacement, which can be specified with the POTIM tag in the INCAR file, and x, y, z to the Cartesian vectors. From the induced forces the interatomic force constants and in the end the Hessian matrix can be obtained. Diagonalization of the Hessian yields the eigenmodes and eigenfrequencies of the investigated system. In that context it is useful to recall that *VASP* performs a single electronic relaxation step for every displacement. At each displacement the dipole moment perpendicular to the surface is calculated, which is used to obtain the IR-intensities as the derivative of the dipole moment along the normal coordinate of the specific mode to the power of two. This whole procedure is very time-consuming. As a consequence the substrate is normally frozen, i.e. only the atoms of the adsorbate are displaced due to the large mass of the substrate in comparison to the masses of the atoms of the molecule.

To get familiarized, test calculations for *CO* on *Cu*(111) were made where up to 3 metal layers were displaced using soft and hard pseudopotentials. The quality of the calculation does, however, not really depend on the number of metal rows allowed to move. On the other hand the choice of the pseudopotential, i.e. soft versus hard pseudopotentials, can quite significantly influence the result. In the end of the day, one has to make a compromise between accuracy and computational costs.[xvi] The corresponding values for *CO* on *Cu*(111) can be found in the internal *VASP*-manual[86]. Table 1 lists the wavenumbers of all vibrations and their intensities for the different calculations made for *CO* on *Cu*(111). Note, that in order to obtain reliable results the pre-optimized geometries with tight convergence criteria must be used and the self-consistent field (SCF)-cycles of the singlepoints for the IR-calculations have to be made with tight convergence criteria as well.[86]

[xv] In *VASP* the parameter NFREE in the the INCAR file determines how many displacements are used for each ion and direction.

[xvi] For the IR-spectra of 2,3,5,6-tetrafluoro-7,7,8,8-tetracyanoquinodimethane (F_4TCNQ), a molecule intensively studied throughout my thesis, soft pseudopotential calculations, where only the molecule was displaced, were performed due to computational reasons.

Table 1: Results of the IR-spectrum of CO on Cu(111), comparing different settings. Hard pseudopotential calculations are compared to soft pseudopotential calculations and to calculations where metal rows were displaced as well. Thereby, **soft** PP_{om} (**hard** PP_{om}) corresponds to soft (hard) pseudopotential calculations with only the molecule displaced; **soft** PP_{1m} (**hard** PP_{1m}) corresponds to soft (hard) pseudopotential calculations with the molecule and 1 metal row displaced; **soft** PP_{3m} corresponds to soft pseudopotential calculations with the molecule and 3 metal rows displaced; The first column lists the wavenumbers in cm^{-1}, the following three columns the intensities in x,y and z direction and the last column the total intensity as one third of the sum of the three separate parts.

wavenumber	**Intensity**$_x$	**Intensity**$_y$	**Intensity**$_z$	**Intensity**$_{\text{total}}$
2020.10718	0.0	0.0	7.83297345	7.83297345
337.24928	0.0	0.0	0.03069460	0.03069460
265.18871	0.0	0.0	0.00005116	0.00005116
264.81694	0.0	0.0	0.00000983	0.00000983
11.67869	0.0	0.0	0.00027743	0.00027743
35.14877	0.0	0.0	0.00016298	0.00016298
soft PP_{1m}				
2020.42143	0.0	0.0	7.84398671	7.84398671
401.92971	0.0	0.0	0.03642325	0.03642325
266.44145	0.0	0.0	0.00009762	0.00009762
266.05292	0.0	0.0	0.00002580	0.00002580
188.22332	0.0	0.0	0.00000001	0.00000001
188.17802	0.0	0.0	0.00000172	0.00000172
187.33022	0.0	0.0	0.00000076	0.00000076
187.30316	0.0	0.0	0.00000001	0.00000001
151.13065	0.0	0.0	0.00000000	0.00000000
147.82506	0.0	0.0	0.00071617	0.00071617
108.21098	0.0	0.0	0.00080936	0.00080936
76.04297	0.0	0.0	0.00000043	0.00000043
74.95054	0.0	0.0	0.00000127	0.00000127
12.55605	0.0	0.0	0.00024218	0.00024218
35.71273	0.0	0.0	0.00013001	0.00013001
soft PP_{3m}				
2020.42144	0.0	0.0	7.84399880	7.84399880
402.08260	0.0	0.0	0.03632116	0.03632116
267.26654	0.0	0.0	0.00009384	0.00009384
266.88610	0.0	0.0	0.00002632	0.00002632
215.29851	0.0	0.0	0.00033985	0.00033985
206.58338	0.0	0.0	0.00000019	0.00000019
206.55561	0.0	0.0	0.00000007	0.00000007
202.55417	0.0	0.0	0.00000049	0.00000049
194.89948	0.0	0.0	0.00000593	0.00000593
194.84556	0.0	0.0	0.00000010	0.00000010
192.83122	0.0	0.0	0.00014343	0.00014343
179.60368	0.0	0.0	0.00000022	0.00000022
179.55539	0.0	0.0	0.00000002	0.00000002
148.24889	0.0	0.0	0.00000025	0.00000025
148.20273	0.0	0.0	0.00000183	0.00000183
133.93750	0.0	0.0	0.00000014	0.00000014
119.50315	0.0	0.0	0.00122719	0.00122719
100.34609	0.0	0.0	0.00000238	0.00000238
99.04847	0.0	0.0	0.00000544	0.00000544
82.77911	0.0	0.0	0.00004263	0.00004263
55.90044	0.0	0.0	0.00000075	0.00000075
54.68954	0.0	0.0	0.00000214	0.00000214
14.97489	0.0	0.0	0.00024353	0.00024353
36.35406	0.0	0.0	0.00013180	0.00013180
hard PP_{om}				
2108.53087	0.0	0.0	10.1624461	10.1624461
306.77587	0.0	0.0	0.03759357	0.03759357
280.60983	0.0	0.0	0.00002613	0.00002613
277.53823	0.0	0.0	0.00009946	0.00009946
66.02412	0.0	0.0	0.00025098	0.00025098
48.25135	0.0	0.0	0.00042110	0.00042110
hard PP_{1m}				
2108.70577	0.0	0.0	10.17154893	10.17154893
374.68458	0.0	0.0	0.04457549	0.04457549
281.99573	0.0	0.0	0.00003336	0.00003336
279.07192	0.0	0.0	0.00012572	0.00012572
182.20829	0.0	0.0	0.00000127	0.00000127
181.79924	0.0	0.0	0.00000673	0.00000673
180.86263	0.0	0.0	0.00000001	0.00000001
180.79385	0.0	0.0	0.00000004	0.00000004
142.02727	0.0	0.0	0.00000001	0.00000001
139.77475	0.0	0.0	0.00103632	0.00103632
85.83989	0.0	0.0	0.00151308	0.00151308
66.57261	0.0	0.0	0.00011253	0.00011253
57.77484	0.0	0.0	0.00000138	0.00000138
57.37063	0.0	0.0	0.00001421	0.00001421
48.10332	0.0	0.0	0.00034114	0.00034114

3 Understanding the properties of interfaces between organic self-assembled monolayers and noble metals - a theoretical perspective.

3.1 Foreword

Highly-ordered, self-assembled monolayers (SAMs) on (noble) metal surfaces are of particular importance for both the emerging field of single-molecule electronics as well as for improving the characteristics of more conventional organic (opto)electronic devices. In the first part within this section, a microscopic description of electrode work-function modification induced by SAMs and the alignment of molecular states relative to the states in the metal is given. The focus will be on the Ag(111) surface and biphenyl SAMs involving different donor/acceptor head-group substituents. The impact of different docking groups will also be discussed and the results will be compared to previous findings (primarily) for SAMs on Au(111). The second part of this chapter deals with an in-depth description of charge rearrangements and the hybridization between molecular and metal states by projecting the electronic states of the combined system onto the orbitals of the isolated molecules. Furthermore, the sulfur-silver bond is analyzed by means of the crystal orbital overlap population (COOP).[87]

This part is a reproduction of the publication Rangger et al. [1]. A copy of the head of the paper is shown in Figure 8.

Research Article

SURFACE and INTERFACE ANALYSIS

Received: 14 August 2007 Revised: 17 October 2007 Accepted: 17 October 2007 Published online in Wiley Interscience: 9 January 2008

(www.interscience.com) DOI 10.1002/sia.2645

Understanding the properties of interfaces between organic self-assembled monolayers and noble metals – a theoretical perspective

Gerold M. Rangger,[a] Lorenz Romaner,[a] Georg Heimel[b] and Egbert Zojer[a]*

Figure 8: Copy of the head of the paper showing all contributing authors. This chapter is largely identical to this paper.

Hereby, the fact that geometry optimizations based on Cartesian coordinates lead to very different optimum structures as they often got stuck in saddle points or local minima, was not accounted for. The here studied systems on Ag were inspired by work of Dr. Georg Heimel who investigated such systems on Au.[83,88,89]

3.2 Introduction

Over the past decades, SAMs of organic molecules chemisorbed on different substrates have attracted significant attention [90–95] due to their wide range of possible applications in the field of plastic and molecular electronics. The ease of preparation and the high structural order of SAMs make them promising candidates for modifying macroscopic surface properties such as wetting or corrosion resistance [96,97] and a variety of applications has been explored including, e.g., nanolithography and chemical sensing. [98,99] Furthermore, for the fabrication of organic electronic devices such as organic field-effect-transistors (OFETs) the usefulness of controlling the interface energetics by means of SAMs is well acknowledged. [88] In particular, the modification of the substrate work function (Σ) allows for tuning of charge carrier injection barriers. [100,101] Also for the field of single-molecule electronics the use of π-conjugated molecules on noble metal electrodes is of great interest. [102–104] In such devices the molecule itself represents the active element and the energetic alignment of the metal Fermi level (EF) with respect to the frontier molecular orbitals (MOs) governs the transport characteristics.

It has been shown that the chemical structure [83,88,89] of the π-conjugated molecules forming the SAMs (in particular electron-rich and electron-poor substituents [89] and the nature of the docking group [88]) affects the level alignment and the modification of the substrate work function in a decisive way. While in the above mentioned studies much emphasis was laid on SAMs on Au(111) substrate, [83,88,89] here, we focus on Ag(111) surface. Hence, we address the influence of the metal.

The following subsections provide an analyzes of the electronic structure of a number of biphenyls with different head and docking groups. First, the situation for the isolated monolayer will be discussed; subsequently, the bond formation occurring due to adsorption and the corresponding charge rearrangements are described in real space; this then allows to develop a consistent picture of the parameters governing level alignment and the total work-function modification.

In the second part, a charge conserving way of projecting the density of states (DOS) onto individual MOs, of the monolayer, molecular orbital density of states (MODOS), will be described and applied to a SAM on Ag(111); finally, the COOP as introduced in the theory part 2.2.3 is used to analyze bonding and anti-bonding contributions related to the S-Ag bond.

3.3 Methodology

The calculations were performed using density functional theory (DFT) based band-structure calculations. The repeated-slab approach was used where the metal substrate was represented by 5 layers of Ag atoms and the SAM was put on one side of the metal. A vacuum gap (>20 $\mathring{A}$) was introduced between the uppermost atom of the molecule and the next slab atoms. As a reference system, we chose the 4-mercaptobiphenyl on Ag(111) as this allows us to directly compare our results with previous calculations on Au(111). The considered head-group substitutions included an *amine* (-NH2), a *cyano* (-CN), and a *thiol* (-SH) group. The latter was chosen to access the case of

the symmetric molecule. Moreover, an isocyanate (-NC) docking group was considered as well to address the docking group influence on Ag(111). To describe the various SAMs, we will use the following nomenclature: (docking group|2P|substituent).[88] The molecules were arranged in a $p(\sqrt{3} \times 3)$ herringbone structure on the substrate as shown in Figure 9a. Figure 9b highlights the tilt angle of the adsorbed molecules with respect to the surface normal. For all substituents the same arrangement and docking group was assumed to ensure comparability, although it cannot be excluded that electrostatic repulsion[89] somewhat limits the packing density for the two polar end groups -NH2 and -CN. Upon adsorption, the thiols are converted into thiolates with the sulfur atoms bonded to the surface. We hence follow the widely used theoretical approach that the SAMs adsorbs upon hydrogen removal. This issue is analyzed in a later section 5. As previously suggested we take the fcc-hollow (slightly shifted to the bridge) site as the favorable absorption site.[105,106]

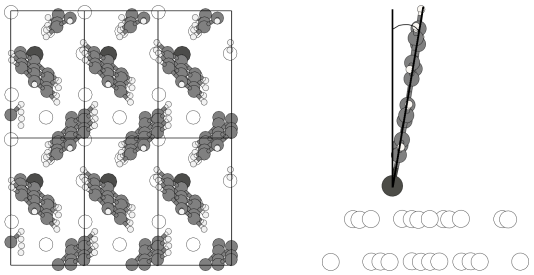

(a) (b)

Figure 9: a) Top view of the S|2P|H system. The herringbone structure is well resolved, and the $p(\sqrt{3} \times 3)$ unit cell is indicated by the black rectangles. Only the top metal layer is shown for reasons of clarity. b) Side view indicating the tilt of the molecules relative to the surface normal. For the various substituents, the inter-ring twist varies between 3° and 5°. The relatively small value can be rationalized by the about 5% higher lateral packing density on the Ag(111) surface compared to the bulk crystal. Only the top two metal rows are shown.

Most calculations were done with *VASP*,[37,38,107,108] using the Perdew-Wang 1991 (PW91) exchange-correlation functional. A plane-wave basis set with a cutoff energy of 20 Ryd was used. For the valence-core electron interaction the projector augmented wave (PAW) method as explained within Refs. [[53,54]] was applied, which allowed for the low kinetic energy cutoff for the plane-wave basis set. For all SAM-calculations, we used a $(8 \times 5 \times 1)$ Monkhorst-Pack grid[33] of **k**-points for the self-consistent field calculations together with a first order Methfessel-Paxton occupation scheme[34] (broadening of 0.2 eV). All calculations were done in a non spin-polarized manner as no significant changes were observed in spin-polarized test calculations on similar SAMs on Au(111).[89] All atoms of the molecule as well as of the two upper metal layers were fully relaxed using a damped molecular dynamics scheme until the remaining forces were smaller than $0.01 eV/\mathring{A}$. The molecular density of states (MDOS) in *VASP* was determined by projection of each Kohn-Sham orbital onto spherical harmonics inside spheres around each atom and weighing the contribution of that atomic orbital to the DOS accordingly. To obtain the DOS projected onto the SAM the MDOS, all non-metallic contributions were summed up.

SIESTA[45] calculations were performed as described in Ref. [109]. These calculations are required for obtaining the COOP and the MODOS as discussed in the theory part 2.2.3. In spite of the methodological differences between *VASP* and *SIESTA*, the deviations between the obtained DOS of the whole system are negligible. This applies also to the respective projections onto the molecular regions projected density of states (PDOS), which justifies the use of two conceptionally slightly different computational approaches within this thesis. The big advantage of *SIESTA* is that as a result of the atomic orbital (AO) type basis set, the calculation of the COOP and the MODOS becomes much more straightforward. Also here, all calculations were done in a non spin-polarized manner. Due to the fact that there are two molecules per unit cell, this is expected to provide a reasonable description of the situation also when considering the non-saturated monolayer.

All $3D$ graphical representations of the system were produced using XCrysden.[110]

3.4 Results and Discussion

Upon adsorption of a SAM on a metal substrate, the electronic structure of the metal and the SAM are modified. This gives rise to (i) a modification of the work function ($\Delta\Phi$), (ii) a change in the relative alignment of the molecular states relative to the metal Fermi level (sections 3.4.1, 3.4.2 and 3.4.3). This is concomitant with a change in the occupation of the MOs of the monolayer (section 3.4.4) and a modification of the bonding/anti-bonding character between the S-H and S-Ag bonds as analyzed by the COOP.

3.4.1 Isolated SAM

The conceptional aspects concerning the electronic structure of the SAM on the metal can be best derived from a gedankenexperiment: The first step is the formation of an isolated saturated monolayer (consisting only of the molecules, which are already in the geometry they will adopt upon adsorption on the metal; in the case of the thiol docking groups, the S atoms are terminated with H). Figure 10 shows the plane-averaged electrostatic potential of the layer consisting of the saturated molecule (HS|2P|H) together with the DOS. One can identify the energy levels corresponding to the highest occupied molecular orbital (HOMO) and lowest unoccupied molecular orbital (LUMO). The vacuum levels to the left and right of the potential well differ by ΔE_{vac} as the molecules possess an intrinsic dipole moment. Consequently, there are also left and right electron affinities (EAs) and ionization potentials (IPs), as indicated in Figure 10. In the non-interacting Schottky-Mott limit, ΔE_{vac}, represents the adsorbate-induced work-function modification.

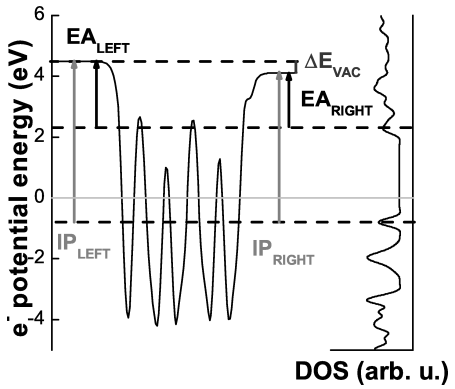

Figure 10: Left: Plane-averaged electron potential energy of the (HS|2P|H) monolayer. The different values for IP_{left}, EA_{left} and IP_{right}, EA_{right} as well as ΔE_{vac} are indicated. On the right side, the DOS of the monolayer is shown clearly revealing the peaks associated with the HOMO and the LUMO.

Interestingly, although the molecules with different head-group substitutions have significantly different molecular IPs and EAs,[89] their left IPs in the monolayer are virtually identical (see Table 2). This behavior is reflected by the fact that the potential distributions in the region of the molecular cores are basically identically for all molecules, i.e., the head-group substitutions influence the plane-averaged potential only in the immediate vicinity of the substituent.[89] Consequently, in the non-interacting Schottky-Mott limit, the positions of the HOMOs relative to the metal Fermi level are the same for (HS|2P|H), (HS|2P|SH), (HS|2P|CN), and (HS|2P|-NH2). In contrast, changing the docking group primarily affects the 'left' quantities, while the 'right' ones hardly change,[88] as can be seen for the examples of (HS|2P|H) and (CN|2P|H) in Table 2.

Table 2: H-saturated SAM: Potential step across the infinite molecular layer (ΔE_{vac} in eV). Ionization potentials (IP_{left}, IP_{right}) and electron affinities (EA_{left} and EA_{right}) of the (saturated) 2D infinite layer of molecules in eV.

Isolated monolayer	ΔE_{vac}	IP_{left}	IP_{right}	EA_{left}	EA_{right}
HS|2P|H	-0.38	5.28	4.90	2.20	1.82
HS|2P|NH2	-1.48	5.11	3.63	2.20	0.72
HS|2P|CN	3.84	5.18	9.02	2.35	6.19
HS|2P|SH[i]	0.20	5.08	5.28	2.21	2.41
CN|2P|H	-3.47	8.53	5.06	5.45	1.98

[i]The observation that also the nominally symmetric (HS|2P|SH) system has a non-vanishing ΔE_{vac}, is a result of using the final geometry of the adsorbed monolayer with a slightly distorted geometry for the present considerations

3.4.2 Bond formation

In the next step of the gedankenexperiment, the molecular layer is bonded to the Ag surface. For the thiol docking groups, this corresponds to replacing the bond between S and H by a bond between S and three Ag atoms. For the isocyanate docking group a new bond between the C atoms and the Ag atoms is formed.

The corresponding (plane averaged) charge rearrangements upon bonding are obtained by subtracting the charge densities of the non-interacting systems, i.e., the Ag slab ($\rho_{\mathrm{Ag(111)}}$) and the monolayer (ρ_{mono}) (all in their final geometries), from those where the monolayer and the metal interact, i.e., where the charge density of the full system is calculated self-consistently. In the case of thiol docking groups, the isolated monolayer has been saturated with H, which then also needs to be taken into account yielding (M denotes the number of molecules in the unit cell):

$$\Delta\,\rho_{bond}(\boldsymbol{r}) \;=\; \frac{1}{M}\,\left[\,\rho(\boldsymbol{r}) \;-\; \left(\,\rho_{Ag(111)}(\boldsymbol{r}) \;+\; \rho_{mono}(\boldsymbol{r}) \;-\; \rho_{H}(\boldsymbol{r})\right)\right] \tag{44}$$

The in the x-y plane integrated charge density rearrangements $\Delta\,\rho_{\mathrm{bond}}(z)$ for (Ag|S|2P|NH2) are shown in Figure 11.

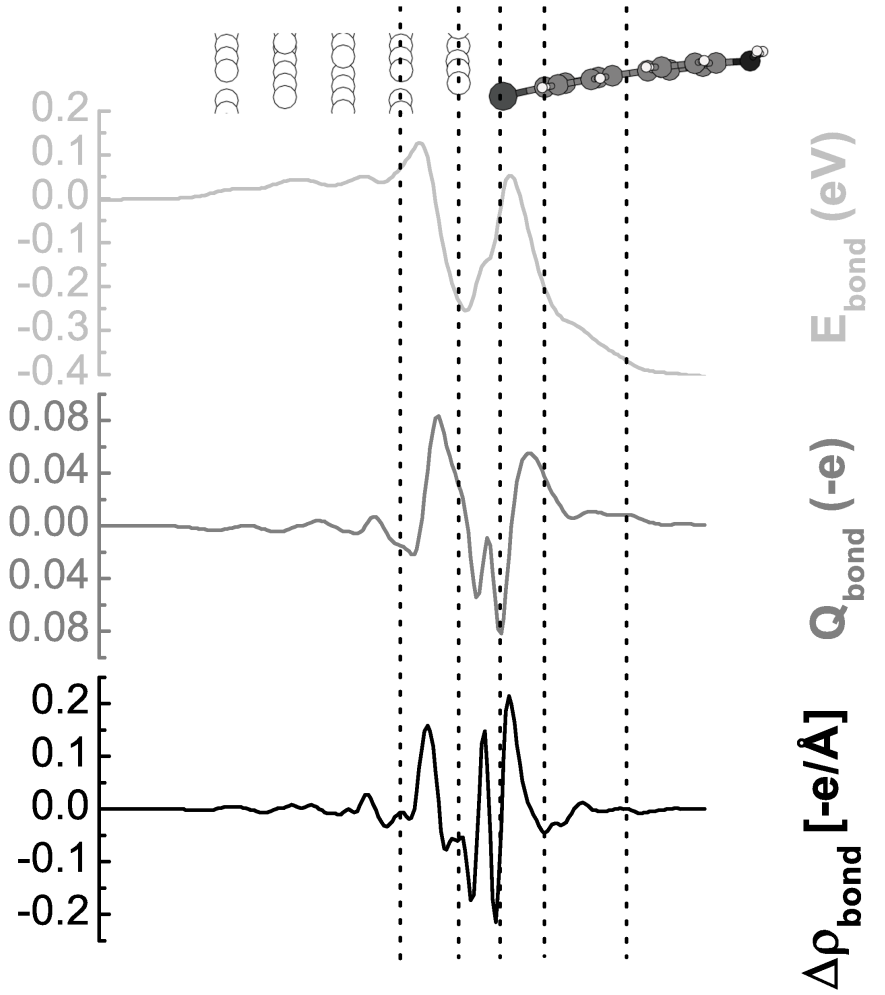

Figure 11: The in the x-y plane integrated charge rearrangements, $\Delta\,\rho_{bond}$, and total charge transferred, Q_{bond}, per molecule as well as the resulting (plane-integrated) electron potential energy change, E_{bond}, for the (S|2P|NH2) system.

One can clearly see that all charge rearrangements are confined to the immediate interface region (i.e., the top two Ag layers, as well as the S and the adjacent C atom). In order to assess the amount of charge transferred upon adsorption, $Q_{\rm bond}(z)$, we integrate the plane integrated $\Delta\,\rho_{\rm bond}$ over z' from a position below the slab to a certain position z.

$$Q_{\rm bond}(z) \;=\; \int_{-\infty}^{z} \Delta\,\rho_{\rm bond}(z')\,dz' \tag{45}$$

The fact that $Q_{\rm bond}$ is approximately zero in the region between the top Au layer and the S atom shows that there is virtually no net charge transfer between the metal and the molecular region. This is in sharp contrast to SAMs at reduced packing densities

where a pronounced maximum of Q_{bond} is observed in that regions. Nevertheless, the charge rearrangements will change the electron potential energy landscape accordingly. Such a modification of the electrostatic potential upon bond formation, $E_{\mathrm{bond}}(\boldsymbol{r})$, can be obtained by solving the Poisson equation. Here, θ denotes the packing density.

$$\nabla^2 E_{\mathrm{bond}}(\boldsymbol{r}) = \frac{\theta\, e}{\epsilon_0} \Delta\, \rho_{\mathrm{bond}}(\boldsymbol{r}) \tag{46}$$

The plane integrated values for $E_{\mathrm{bond}}(z)$ are also shown in Figure 11. The net change of the potential resulting from the bond is $0.4\, eV$ and will in the following be referred to as bond dipole (BD). As there is no net long range charge transfer, its appearance can be associated with the charge fluctuations represented by acting like a series of (small) local dipoles. The BD values for the different substituents are summarized in Table 3 and are all found to be very similar. They are consistently smaller by a factor of more than 2 compared to bonding the same molecules to a Au(111) surface.11 For the isocyanate docking group, a much larger BD is obtained, which is even pointing in the opposite direction, which is again consistent with the observations on Au. [88]

3.4.3 The combined system: conjugated SAM on Ag(111)

Owing to the strong localization of $\Delta\, \rho_{\mathrm{bond}}(z)$ in the densely packed system, the potential distribution for the combined system (metal substrate + SAM) can, in a first approximation, be regarded as a the potential of the bare Ag slab plus the potential from the molecular layer shifted by BD. The actual, self-consistently in the x-y plane-integrated potential of the system is shown in Figure 12 for the (Ag|S|2P|H) system. Again, the positions of the states in the SAM can be derived from the corresponding MDOS. The assignment of MDOS features to individual MO is, however, not always straightforward in the interacting case. [89] Therefore, the terms highest occupied π-state (HOPS) and lowest occupied π-state (LUPS) will be used for the first peaks of the MDOS below and above the Fermi level. The latter characterizes the energy up to which the states in the metal slab are filled. Consequently, the energy differences between EF and the HOPS (ΔE_{HOPS}) and LUPS (ΔE_{LUPS}) correspond to the hole- and electron-injection barriers into the monolayer.

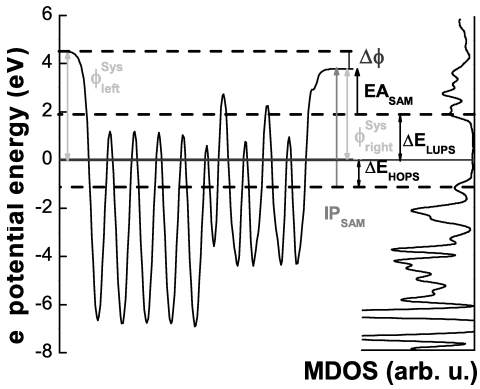

Figure 12: Left: Plane-averaged electron potential energy of the combined system (Ag|S|2P|H). Right: The molecular DOS of the SAM; the positions of the HOPS and the LUPS are indicated by the dashed lines. The IP and EA of the molecular layer (IP_{SAM} and EA_{SAM}), the left and right side work functions (ϕ_{left} and ϕ_{right}), the work-function modification ($\Delta\phi$) as well as the hole- and electron-injection barriers (ΔE_{HOPS} and ΔE_{LUPS}) are shown as well. The energy sacale is given relative to E_F

From the above considerations (in particular the definition of $\Delta\,\rho_{\mathrm{bond}}(\boldsymbol{r})$), it becomes clear that the over-all modification of the work function resulting from covering the Ag(111) surface with a SAM is obtained as a combination of the effect due to the molecular dipole moments expressed by ΔE_{vac} and the bond dipole BD:[100,101,111]

$$\Delta\phi = BD + \Delta E_{\mathrm{vac}} \tag{47}$$

The calculated values of $\Delta\phi$ together with the work functions of the SAM covered Ag substrate (ϕ_{right}) obtained with the employed methodology are listed in Table 3. The high values obtained for $\Delta\phi$ can be regarded as an upper limit to the actual (experimental) situation considering the high degree of order and uniformity in the SAM assumed here, which might be difficult to achieve experimentally considering the relatively large molecular dipole moments (*vide supra*).

Table 3: Combined SAM/Ag(111) system: Work function, ϕ_{right}, of the SAM covered Ag(111) surface; work-function modification induced by the SAM, $\Delta\Phi$; bond dipole, BD; ionization potential and electron affinity of the molecular layer, IP_{SAM} and EA_{SAM}; energy corrections for the frontier MOs resulting from adsorption, $E_{\mathrm{corr}}^{\mathrm{HOMO}}$ and $E_{\mathrm{corr}}^{\mathrm{LUMO}}$; and positions of the frontier π and π^* states of the SAM relative to the Fermi level, ΔE_{HOPS} and ΔE_{LUPS}. All quantities are given in eV.

System	ϕ_{right}	$\Delta\Phi$	BD	IP_{SAM}	EA_{SAM}	$E_{\mathrm{corr}}^{\mathrm{HOMO}}$	$E_{\mathrm{corr}}^{\mathrm{LUMO}}$	ΔE_{HOPS}	ΔE_{LUPS}
Ag|S|2P|H	3.71	-0.73	-0.39	4.88	1.77	0.01	0.40	-1.17	1.93
Ag|S|2P|NH2	2.58	-1.87	-0.38	3.61	0.64	0.03	0.10	-1.03	1.94
Ag|S|2P|CN	7.93	3.48	-0.35	9.00	6.13	0.03	0.07	-1.07	1.80
Ag|S|2P|SH	4.28	-0.18	-0.37	n.a.	n.a.	n.a.	n.a.	n.a.	n.a
Ag|CN|2P|H	2.85	-1.64	1.82	5.26	2.41	-0.19	-0.43	-2.41	0.44

Amongst the investigated systems, the largest work function decreases are obtained

for (Ag|S|2P|NH2) and (Ag|CN|2P|H), where in the former case a large negative ΔE_{vac} and the *BD* are additive, while in the latter case a particularly large ΔE_{vac} is partly compensated by the *BD* of the isocyanate docking group. The resulting ϕ_{right} in those two cases are already smaller than $3\,eV$, but in principle a further significant reduction of the system work function by combining the CN- docking group with a donating substituent like -NH2 can be expected (however, potentially with additional film forming constraints). The opposite trend in ϕ_{right} is observed for the -CN end group substitution, where the SAM results in a potential increase of the system work function to nearly $8\,eV$.

An interesting observation is that when comparing the values of ϕ_{right} for the Ag(111) surface in Table 3 with those that can be extracted for Au (111) from Ref. [88] one finds that they are within approx. $0.2\,eV$ in spite of the fact that the calculated work function of the bare Au(111) surface is $0.7\,eV$ larger than that of Ag(111);
$\phi_{Au(111)} = 5.2\,eV$; $\phi_{Ag(111)} = 4.5\,eV$
This is because the larger work function of Au is compensated by the equally larger bond dipole (see also discussion for the H terminated case in Ref. [88]). The *BD* also plays a crucial role for the relative alignment between the highest occupied states in the metal at EF and the molecular levels, as ΔE_{HOPS} is given by:

$$\Delta E_{\text{HOPS}} = \phi_{Au(111)} - IP_{\text{left}}^{\text{SAM}} + BD + E_{\text{corr}} \tag{48}$$

The origin of the (typically relatively small) correction factor, E_{corr}, is the slight modification of the potential in the molecular region close to the interface. This results in a small change in the energetic positions of the 'molecular states'. E_{corr} can also be independently calculated from the differences of the 'right' IPs of the isolated monolayers and the layers adsorbed onto the metal.

As far as the level alignment is concerned, it turns out that, in the case of the thiol docking group, the frontier molecular π and π^* states (HOPS and LUPS) are found at virtually the same energetic positions $(-1.1 \pm 0.1)\,eV$ for the HOPS and $(1.9 \pm 0.1)\,eV$ for the LUPS, independent of whether an electron-rich or an electron-poor substituent is attached to the far end of the molecule. This is analogous to the situation observed for Au(111),[89] although the variations in ΔE_{HOPS} are somewhat larger here. As can be understood from Equation 48, this is a direct consequence of the nearly identical IP_{lefts} and *BD*'s obtained for the various end group substitutions, which result from the strongly localized potential modifications induced by the substituents and from the also local nature of the charge redistributions at the interface (*vide supra*). In contrast, the large positive *BD* of the isocyanate docking group increases ΔE_{HOPS} by nearly $1.3\,eV$.

Consequently, at least in the densely packed monolayer, an end-group substitution can be used only to control the overall work function of a SAM-covered substrate. Modifying the docking group, however, changes *BD*, which enters Equation 64 and Equation 48 and, therefore, allows tuning of both, the level alignment as well as the work-function modification. After developing this 'general' picture, the following two sections will be dedicated to a more in depth analysis of molecular orbital rearrangements and their

contributions to metal-molecule bonding.

3.4.4 Molecular orbital density of states (MODOS)

When molecules adsorb onto metallic surfaces, interactions occur between the metallic states and the molecular orbitals. These interactions cause the molecular orbitals to broaden and shift. An explicit way to calculate these effects for the metal-organic interface is to project the DOS onto the molecular orbitals.[60–62,64,73,112,113] In this work, this projected DOS will be called the MODOS. It identifies the contributions to the total DOS arising from a specific MO, or more precisely, from the band formed by an MO in the isolated monolayer.

The energetic position of the maximum of the MODOS allows determining how a particular MO is aligned with respect to the Fermi level and the broadening of the MODOS is a measure for the hybridization of the corresponding molecular state. It is a measure for the coupling between that particular orbital with the metallic states. Another purpose of the projection is that, by integrating the MODOS up to the Fermi level, it is possible to assign a nominal occupation to each molecular orbital, which allows analyzing the bonding-induced charge transfer for each individual orbital.

The occupation of each molecular orbital can be calculated by integrating the MODOS up to the Fermi level yielding the occupation O_m of the MO.

$$O_m = \int_{-\infty}^{E_f} MODOS_m(E)\, dE \tag{49}$$

The charge associated with each molecular orbital then equals $2 \cdot O_m \cdot (-e)$.

As a model case, the MODOS for (S|2P|H) on Ag(111) will be discussed. Here, to illustrate the potential of the MODOS for analyzing bonding between a metal and an organic layer, we will primarily describe the situation when considering the non-saturated (S|2P|H) as the 'reference system'. This provides a more instructive picture, as attaching this layer to the metal results in the formation of a new bond, while in the case discussed in 3.4.1, when considering a monolayer saturated with hydrogen, one only deals with replacing one bond (S-H) with another (S-Au).

In the isolated monolayer, O_m is for all 'occupied MOs' 100 %, with the exception of the singly unoccupied molecular orbital (SOMO), for which it is 50% filled. After adsorption, this occupation pattern is changed as is shown in Figure 13. (Note: As there are two molecules per unit cell, always two points in the plot correspond to a certain molecular orbital). Major changes are observed for the SOMO-6, the SOMO-1, and the SOMO, for which we also observe a particularly strong hybridization with the metallic states, as illustrated by the corresponding MODOS plots in Figure 14 (the MODOS associated with the SOMO-2 is shown for comparison). The contributions of the SOMO-6 and SOMO-1 above the Fermi level (which is set to zero in Figure 14) cause these orbitals to loose about 0.12 electrons and 0.37 electrons, respectively. The SOMO, on the other hand, gains 0.72 electrons due to the dominant contributions below the Fermi level (i.e., its maximum being shifted to clearly below the Fermi level as a result of the interaction).

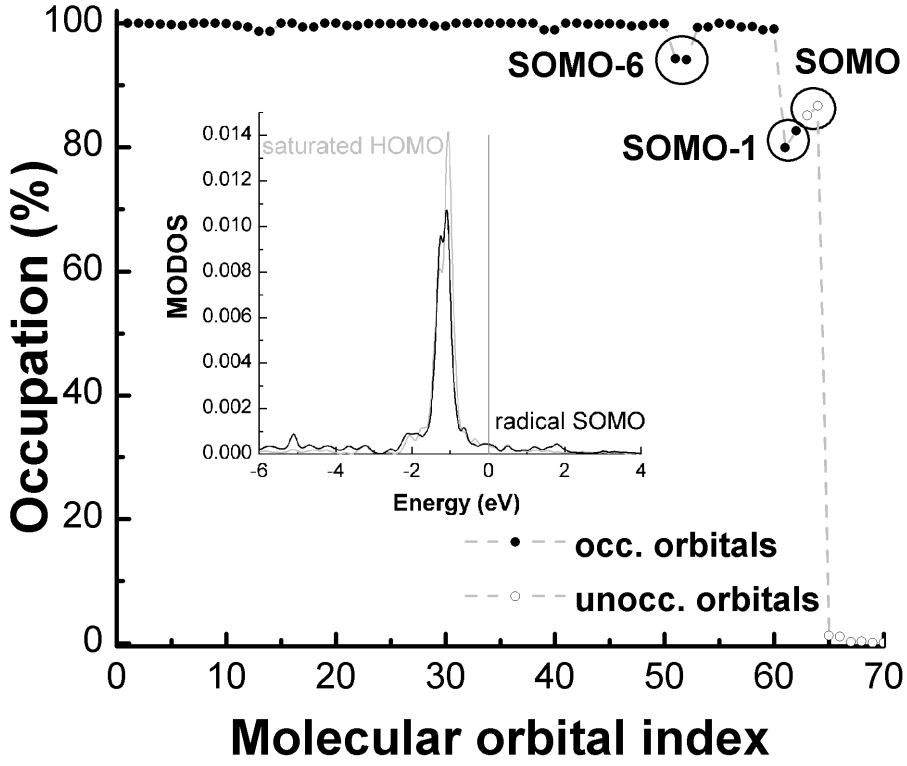

Figure 13: Occupation of the molecular orbitals in the SAM/metal system with the unsaturated monolayer taken as the reference. The full (open) circles correspond to the orbitals that are occupied (unoccupied) in the isolated monolayer. The inset compares the MODOS associated with the SOMO (unsaturated monolayer as reference) and the SOMO (saturated monolayer as reference); details see text.

When choosing the monolayer with the sulfur moieties saturated with hydrogen atoms as a reference, no clear trends in the charge redistribution picture can be derived. Rather, all orbitals (including the HOMO, which for this reference system is doubly occupied) loose a varying amount of electrons. This is a consequence of the conceptional problem, that, when now calculating the MODOS, the hydrogen related coefficients need to be dropped (as the H atoms are removed upon adsorption). This then results in the 'truncated' MOs becoming linearly dependent. Nevertheless, the resulting MODOS associated with the HOMO in the saturated case is nearly identical to the MODOS of the SOMO in the non-saturated (i.e., radical) calculations as shown in the inset of Figure 13.

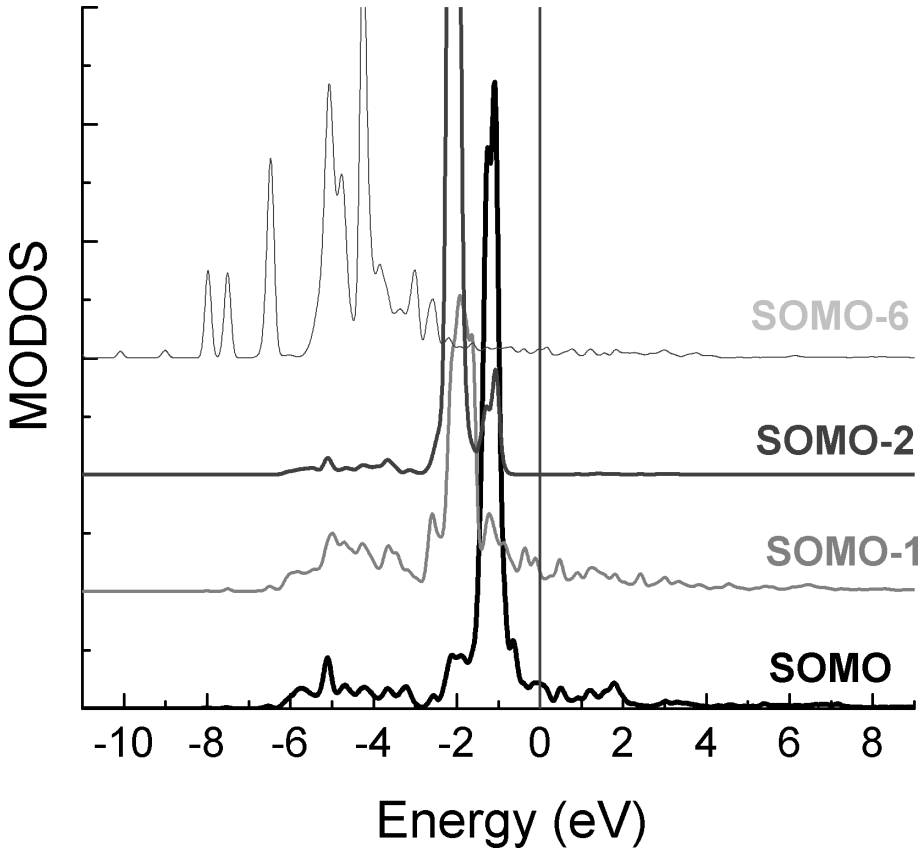

Figure 14: MODOS associated with the strongly interacting SOMO-6, SOMO-1 and SOMO orbitals with the unsaturated monolayer taken as the reference. Of each pair of orbitals (resulting from the two molecules in the unit cell of the reference layer; see text), the one at higher energy is plotted. The lower energy one looks very similar. The curves were shifted in y-direction for the sake of clarity. The position of the Fermi energy is taken from the self-consistent *SIESTA* calculations.

3.4.5 The crystal orbital overlap population (COOP)

As a final step, S-Ag bond is analyzed by means of the COOP as described in Refs. [73 and 64] . This quantity resolves bonding and anti-bonding contributions to the DOS on the energy scale and is defined as,

$$COOP_{X,Y} = \sum_{m\in X, I\in Y, i, \boldsymbol{k}} c^*_{im\boldsymbol{k}}\, c_{il\boldsymbol{k}}\, S_{ml\boldsymbol{k}}\, \delta(E-\epsilon_{i\boldsymbol{k}}) \tag{50}$$

where X and Y denote a set of AOs, typically the AOs belonging to an atom or to a set of atoms (note: as in the case of the MODOS, also the COOP is calculated using *SIESTA*, which relies on an atomic orbital type basis set). The $c_{il\boldsymbol{k}}$ are the corresponding linear combination of atomic orbitals (LCAO) coefficients and $S_{ml\boldsymbol{k}}$ is the overlap matrix.

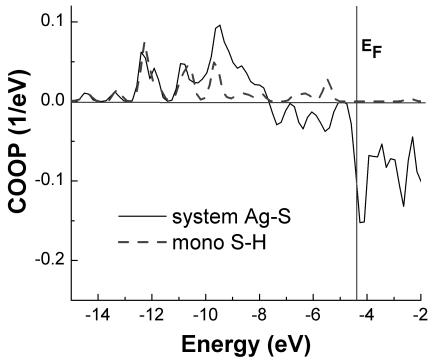

Figure 15: COOP(E) between S and all Ag atoms (solid line; combined SAM/metal system) and between S and H (dashed line; saturated monolayer). The postion of the Fermi energy is taken from the self-consistent SIESTA calculations and was aligned.

Figure 15 compares the COOP for the S-Ag bond (X=AOs of all Ag atoms and Y=AOs of the two S atoms in the unit cell) and the S-H bond (X=AOs of saturating hydrogen and Y=AOs of the sulfur). While at large negative energies the two curves are fully bonding and very similar, differences between the curves arise around the Fermi level of the system. Here the S-Ag bond shows pronounced anti-bonding contributions, whereas the S-H bond is still bonding. A closer analysis shows that these contributions largely stem from the overlap between sulfur s-orbitals and the metal states. The total overlap population is obtained via integrating the S-Ag and the S-H COOP up to the Fermi energy. It is an indicator of the strength of a bond. We obtain values of 1.03 and 1.57, respectively; i.e., the S-Ag bond is weaker than the S-H bond due to the anti-bonding contributions in the energy range up to $3\,eV$ below EF. Interestingly, the so obtained ratio between the two bonds (S-Ag/S-H) 0.65 compares well with the ratio of the bond enthalpies of Ag-S ($217\,\frac{kJ}{mol}$) and S-H ($344\,\frac{kJ}{mol}$).[114]

3.5 Summary and conclusions

In summary, we discussed the microscopic origin of the work-function modification induced by a self assembled monolayer chemically bound to a coinage metal, as well as the alignment between the molecular and metal states. The former is determined by the sum of the bond dipole and the vacuum level change related to the intrinsic dipole moments of the molecules forming the monolayer; the latter is given by the work function of the isolated monolayer on the side on which it will be attached to the metal plus, again, the bond dipole. Effects resulting from end group substitution as well as the charge rearrangements following the bonding of the molecules to the surface are strongly localized. Consequently, end group substitution will only affect the work-function modification, while changing the docking group also allows tuning the level alignment. Interestingly, for all investigated SAMs, the work functions for the SAM covered Ag(111) surfaces are very similar to those for and Au(111) described in Ref. [89]. Moreover, charge rearrangements and hybridization were analyzed on an 'orbital' level by projecting the density of states of the combined molecule/metal system onto the molecular states; the bonding and anti-bonding overlap populations of the S-Ag

and S-H bonds are compared.

4 The influence of the backbone polarizability on the interface energetics of self-assembled monolayers on Au(111).

4.1 Foreword

Modifying metal electrodes with the help of self-assembled monolayers (SAMs) attracts more and more interest in the field of organic and molecular electronics. The two key parameters in that context are the modification of the electrode work function due to SAM adsorption and the alignment of the SAM conducting states relative to the metal Fermi level. In order to evaluate the influence of different backbones, especially different polarizabilities of the backbones a joint study with the group of Prof. Shuai of the Chinese Academy of Science (currently also at the Tsinghua university) was made.

This section summarizes the most important results of the paper by LinJun Wang recently published in Advanced Materials.[2] A copy of the head of the paper is shown in Figure 16. I am second author of this paper and the whole study was decisively pushed forward during a research stay of mine at the Chinese Academy of Science. We discovered the influence of geometry optimizations based on internal coordinates on the results of LinJun Wang's Cartesian optimizations. We then redid all his optimizations using the new internal optimization technique (vide supra) and summarized the new results.

ADVANCED FUNCTIONAL MATERIALS
www.afm-journal.de
Materials Views
www.MaterialsViews.com

Electronic Structure of Self-Assembled Monolayers on Au(111) Surfaces: The Impact of Backbone Polarizability

By *LinJun Wang, Gerold M. Rangger, Lorenz Romaner, Georg Heimel, Tomas Bučko, ZhongYun Ma, QiKai Li, Zhigang Shuai,* and Egbert Zojer**

Figure 16: Copy of the head of the paper showing all contributing authors. This chapter is largely identical to this paper.

This study provides a solid theoretical basis for the fundamental understanding of SAMs and significantly improves the understanding of structure-property relationships needed for the future development of functional organic interfaces.

4.2 Introduction

In modern organic (opto)electronic devices the charge- carrier injection efficiencies between organic semiconductors and metals depends on their contacts and is of crucial importance for the device performance.[115–118] One of the most attractive and promising ways of surface treatments to improve charge injection is to modify the metal electrodes using SAMs.[119–123] Hereby the effective tuning of the work function of the electrode

is enabled due to the SAM sandwiched between the metal electrode and the active organic material. This allows control of the charge-injection barriers between the electrode Fermi level (EF) and the frontier electronic states in the organic semiconductor. [120] At the same time however, an additional tunneling resistance determined by the alignment of the electronic states within the SAM relative to EF is introduced. The latter also plays a decisive role in molecular electronics, where the SAM itself becomes the active component of the device. [102–104,124–126]

Therefore, as a matter of fact the induced electrode work-function modification and the alignment of the SAM states with respect to the metal Fermi level constitute the two most important electronic quantities in the context of organic and molecular electronics. Hence a complete and thorough understanding of all factors determining these parameters is highly desired.

A SAM can be divided into three parts (i) the head-group, (ii) the backbone and (iii) the docking group, cf. Figure 17. Each of them can be separately altered to tune the electronic properties. In a previous chapter of this thesis I discussed the effect of head-group substituents and the choice of the docking group on the work-function modification and the level alignment on Ag(111), cf. 3. Further investigations on the effect of different head-group substituents and docking groups can be found in Refs. [1,88,89,127] The main conclusion out of all studies is that the head-group substituents only affect their end of the SAM, i.e. the work-function modification for close packed systems. On the other end, different docking groups affect the level alignment of the SAM states with the metal Fermi level and hence the electron/hole injections.

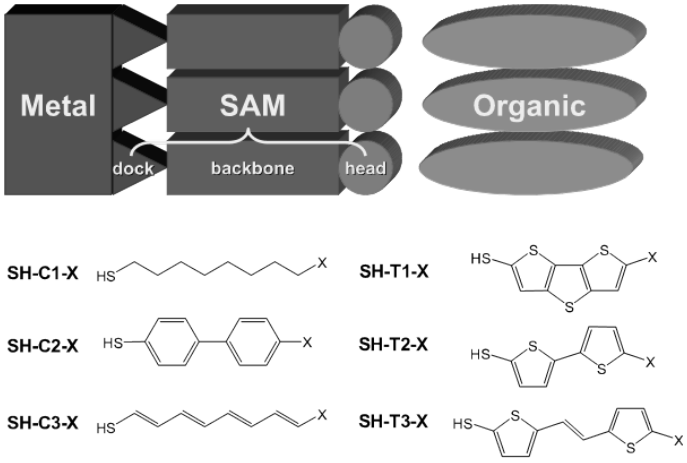

Figure 17: Top: Schematic illustration of a SAM-modified interface between a metal and an organic semiconductor. The three SAM components namely the docking group, the backbone, and the head group are indicated. Bottom: Chemical structures of the studied molecules, where X denotes the head group substituents, -NH2 and -CN. Accordingly, when only referring to the backbones, the abbreviations C1, C2, C3, T1, T2, and T3 are used. The substituted molecules are denoted as backbone-substituent, the thiols as SH-backbone-substituent, and the molecules forming the SAM as S-backbone-substituent.

The aim of the present part is to illustrate the effect of the backbone and there

precisely the influence of different polarizabilities on the two key-parameters. Additionally, the impact of either electron-rich (donor) or electron-poor (acceptor) head-groups in conjunction with different backbone polarizabilities is studied as different polarizabilities should allow different impacts of e.g. head-group substituents on the level alignment. In other words "communication channels" between the head-group and the docking-group/metal are expected to open as a function of polarizability of the backbone. This thought of a "communication channel" is backed up as it was shown that the packing-density in that context influences the level alignment between SAMs and the metal due to significant depolarization of dipolar molecules in monolayers.[111,128] This is attributed to the dipole moments of neighboring molecules.[111,128]

Thus, we employed slab-type band-structure calculations following Ref. [83]. The calculations are based on density functional theory (DFT). Thereby a systematic series of SAMs on Au(111) is studied with the focus on the impact of the backbone. Furthermore, we are interested in i) whether the chemical nature and the polarizability of the backbone qualitatively changes the impact of donor/acceptor head-group substitutions on the level alignment, ii) the impact of the backbone itself on the level alignment, and iii) the influence of the backbone on the work-function modification.

In order to deal with these points, first of all the implications of different head-groups in conjunction with different polarizable backbones on the isolated molecules is studies. Then issues regarding the structure of the SAMs are analyzed followed by the level alignment and the work-function modification. In the end the issue of packing density is touched as well.

4.3 Computational Methodology

All calculations are based on DFT, using generalized gradient approximation (GGA). The *VASP*[38,39] code version 4.6 with a plane-wave basis set at an energy cutoff of 20 Ryd was used. The Perdew-Wang 1991 (PW91)[53,54] exchange correlation functional together with the projector augmented wave (PAW) method to describe the valence-core interactions. A Monkhorst-Pack[33] k-point grid of (8x5x1) was applied at full coverage for the self-consistent field (SCF) calculations in connection with a second order Methfessel-Paxton[34] occupation scheme for the density of states (DOS) with a broadening of 0.2 eV. All calculations were carried out non-spin polarized. Reduced coverage calculations followed the guidelines of Ref. [111], enlarging the surface unit cell and removing molecules. Their geometries, however, were not allowed to relax as we were interested in the effect of polarization.

To obtain a 3D periodic system the repeated slab approach was employed with 5 metal rows representing the Au(111) surface. Thereby, the top two rows as well as the molecules were allowed to relax until the remaining forces were below $0.01\frac{eV}{\mathring{A}}$. For the geometry optimizations, a recently developed scheme relying on internal coordinates was employed[129] in order to describe the tilt angles of the long molecular axis relative to the surface better. Geometry optimizations based on Cartesian coordinates lead to very different optimum structures as they often got stuck in saddle points or local minima.[i]

[i] Thereby, structures differing by only a few hundredth of eV lead to significant different tilt/twist angles. This can lead to variations of up to 1.60 eV for S-C1-NH2.

To identify the highest occupied π-state (HOPS) being fully delocalized along the backbone the local density of states (LDOS) of the first peak in the molecular density of states (MDOS) was evaluated. Following this procedure for all backbones except C1 the first peak provided such a narrow transport channel along the backbone. For C1 the third peak showed this feature.

The isolated molecular properties were calculated with Gaussion 03 Rev.E.01.[130] The PW91/PW91 exchange correlation functional was used for reasons of consistency together with a 6-31G** basis set. The molecular properties were optimized with planar backbones, which is reasonable as all backbones within the SAM are planar. Test calculations with Becke, Lee, Yang and Parr (B3LYP) and diffuse basis functions yielded similar trends.

4.4 The investigated systems

4.4.1 The investigated systems

The investigated molecules are depicted in the bottom part of Figure 17 (see figure caption for naming conventions). For each backbone, we considered a donor- (X = -NH2) and an acceptor- (X = -CN) substituted version. In addition to the aromatic biphenyl backbone (C2) as the reference system,[1,83,88,89,111,128,131–134] we studied a non conjugated alkane (C1) and a fully π-conjugated alkene (C3). Additionally, thiophene-based molecules (T1, T2, and T3) were considered as intrinsically more electron-rich, fully conjugated, but non-aromatic backbones. All of the considered backbones have similar length With the exception of T3.

Table 4 summarizes the key parameters of the isolated molecules. Note that here the values belong to the backbones alone, i.e. without head- and docking-group unless otherwise stated.

Table 4: Molecular electronic properties of all investigated backbones. Values are reported for the unsubstituted backbones bearing neither substituent nor an -SH docking group. Exceptions are ΔE_{H-NH2} and ΔE_{H-CN}, where -NH2/-CN substituents were added. IP (EA) are the vertical ionization potentials (electron affinities).[a] $E/_{rmHOMO}$ is the energy of the highest occupied molecular orbital for the unsubstituted backbone, α_{zz} is the zz component of the polarizability tensor, with z being the long molecular axis defined as connecting the two terminal C atoms. ΔE_{H-NH2} (ΔE_{H-CN}) is the change of the HOMO energy upon substitution with an -NH2 (-CN) head group.[b] μ_{CN} (μ_{NH2}) is the total dipole moment of the CN- (NH2-) substituted molecule and φ_{CN} and φ_{NH2} are the respective angles between the dipole moments and the long molecular axes. All dipole moments are given in Debye (D); a positive sign refers to the dipole moment pointing from the backbone towards the substituent.

Backbone	IP (eV)	EA (eV)	Hardness (eV)	E_{HOMO} (eV)	α_{zz} (Bohr^3)	ΔE_{H-CN} (eV)	ΔE_{H-NH2} (eV)	μ_{CN} (D)	φ_{CN} (°)	μ_{NH2} (D)	φ_{NH2} (°)
C1	9.45	-3.66	6.56	-6.99	115	-0.29	2.00(-0.05)	-4.28	32	1.30[c]	35
C2	7.61	-0.56	4.09	-5.30	211	-0.49	0.83	-5.33	0	2.60	23
C3	7.11	0.04	3.53	-4.76	288	-0.54	0.82	-6.02	18	4.58	12
T1	7.30	-0.49	3.90	-4.93	198	-0.55	0.66	-5.69	16	2.51[d]	27
T2	7.21	-0.39	3.80	-4.80	192	-0.57	0.66	-5.52	12	2.57	25
T3	6.74	0.15	3.30	-4.57	327	-0.51	0.55	-6.23	9	3.17	20

[a] Electron affinities are defined here as the total energy of the neutral system minus that of the negatively charged molecule.

[b] Defined as the energy of the HOMO of the substituted system minus the energy of the HOMO of the unsubstituted system.

[c] In the single-molecule optimizations of C1-NH2 a lower energy conformer with a dipole moment of 1.44 D is found; there, the plane of the -NH2 group is perpendicular to the plane of the backbone. This prevents an efficient mixing of the nitrogen lone pair with backbone states so that the -NH2 group largely loses its donating character. This molecular conformation is, however, found to be unfavorable on the surface, where a structure with the -NH2 plane close to coplanar with the backbone is found; therefore, we report here the molecular dipole moment for such a situation.

[d] The fact that the T1 backbone is not centrosymmetric has only a minor impact on the total dipole moment as can be inferred from the unsubstituted molecule having a dipole moment of only 0.48 D.

Not surprisingly, the electronic polarizability (α_{zz}) along the long molecular axis is largest for C3 and T3. Especially for T3 the enhanced polarizability due to the additional vinylene unit which increases the conjugation length can be seen. For the least polarizable backbone C1 the value is by a factor of about 2.5 smaller. The other display intermediate values. The chemical hardness,[135] a measure for the ability of the molecule to resist changes of its electron cloud is a suitable measurement for the potential impact of the different backbones.[ii] Our chosen backbones cover a wide range of chemical hardness and as expected the values decline when the polarizability (α_{zz}) increases.

Adding an either donor or acceptor head-group to our molecules will cause the electron cloud of the backbone to react on the disturbance of balance. When considering the chemical hardness we expect the C1 backbone to hardly react whereas the other backbones should feature a pronounced response. This impact can be estimated by the change in the highest occupied molecular orbital (HOMO) energies prior and after the substitution. Hereby, the accepting -CN group results in a stabilization of the occupied orbitals. It amounts to up to -0.57 eV for T2, whereas as expected it is significantly smaller for C1, -0.29 eV, due to the lack of π-orbitals. Surprisingly in that context is that the change for T3 results to only -0.51 eV despite having the highest long-axis polarizability and the lowest chemical hardness. This is an indication that the overall α_{zz} polarizability might not be the proper quantity to describe the substitution effect. Here, rather the local polarizability in the vicinity of the head-group determines the reaction of the molecule.

Substitution with the π-donor -NH2 destabilizes the occupied orbitals. This effect is smaller for the T-series as a consequence of the already electron-rich backbone. Surprisingly, hereby is that quickly analyzing the effect on C1 results in a destabilization of 2.00 eV, which strongly conflicting with the *vide supra* described properties of the least polarizable backbone. A closer inspection, however, reveals that this is simply a consequence of the HOMO is localized on the substituent. Hence, when considering the response of the backbone, which is the highest σ state, its response is 0.05 eV, perfectly suited. Nonetheless, both values are given in Table 4.

The most striking influence on the magnitude of the SAM-induced work-function modification has the molecular dipole moment, μ_{CN} and μ_{NH2}. They point in opposite directions and differ in absolute values as the -CN dipole is significantly larger. The higher the polarizability the higher the dipole will be. This is confirmed as the dipole moments are largest for the two most polarizable and least chemically hard backbones C3 and T3 and smallest for the least polarizable and chemically hardest backbone C1. This additionally implies a certain charge transfer to/from the backbone depending on the polarizability. This is consistent with the particularly large dipole moment for acceptor substitution, i.e. -CN, of the electron-rich thiophene based backbone.

It is noteworthy that only for C2CN the dipole axis is parallel to the long molecular axis, compare values of φ_{CN} and φ_{NH2} in Table 4. For all other setups there is a significant angle between the long molecular axis and the dipole moment along the z-axis. This effect is most pronounced for C1 and C3 due to their intrinsic zig-zag pattern. The reason why the angle is smaller for C3 is that the dipole is partly located on the

[ii] The chemical hardness is defined as half the difference between IP and EA. [136]

backbone as, due to its large polarizability, charge transfer between head-group and backbone occurred. For the -NH2 head-group the situation is insofar not so straight forward as it features an additional out-of-plane component of the dipole moment due to its slight pyramidal structure.

4.4.2 Structure of the SAMs on the surface

In this study the SAMs are supposed to adsorb upon hydrogen removal from the thiol docking group. This strategy is widely used in literature [83,88,100,131,137] and this adsorption path was also assumed in the previous chapter 3. A later chapter 5 will deal about this issue in greater detail.

For reasons of consistency, the same $p(\sqrt{3} \times 3)$ surface unit cell with two molecules has been assumed for all systems. This surface unit cell is known from alkane thiols (C1) on Au(111).[138,139] Moreover, biphenylthiols are known to assemble in this unit cell on Au(111) in the characteristic herringbone pattern shown for S-C2-CN in Figure 18a.[140]

Figure 18c,d,e show that variations in γ immediately influence the directions of the molecular dipole moments and hence the work-function modification for S-C1-CN, S-C2-CN, and S-C3-CN. As this angle is a very soft degree of freedom even when using the internal optimizer a number of different local-minimum structures are found being separated by only 0.16 eV. Furthermore, for the most loosely packed system S-C3-CN the herringbone pattern vanishes and a layered conformation emerges, cf. 18b. In the following results based on the lowest-energy conformation are reported. Nevertheless, it cannot be excluded that they are the "true" minimum structures.

4.5 Electronic structure of SAMs bonded to the Au(111) surface

4.5.1 Level Alignment

Figure 19 illustrates all the important quantities in connection with surface modification and their interrelation. It shows the plane-averaged electron potential energy for the S-C3-NH2 system on a 5 layer gold slab and the corresponding MDOS. Further indicated are the Fermi energy E_F set to zero, the gold work function ($\phi_{\mathrm{Au}} = E_{\mathrm{vac}}^{\mathrm{left}} - E_F$), the work-function modification ($\Delta\Phi = E_{\mathrm{vac}}^{\mathrm{right}} - E_{\mathrm{vac}}^{\mathrm{left}}$), the highest occupied π-states (HOPS), the energy position of the HOPS with respect to E_F (ΔE_{HOPS}), and the ionization potential of the SAM ($\mathrm{IP_{SAM}} = E_{\mathrm{vac}}^{\mathrm{right}} - \mathrm{HOPS}$). Note that in the case of C1 the HOPS actually referres to the highest delocalized σ-state as the highest π-state is only located at the head-group. In that case the σ-state provides the first continuous transport channel along the molecular backbone.

The most relevant quantities for charge carrier injection into the SAM is ΔE_{HOPS} for the holes and ΔE_{LUPS} for the electrons into the lowest unoccupied π-state. As a matter of fact the latter is not considered in the present study as DFT is known to describe its position poorly.

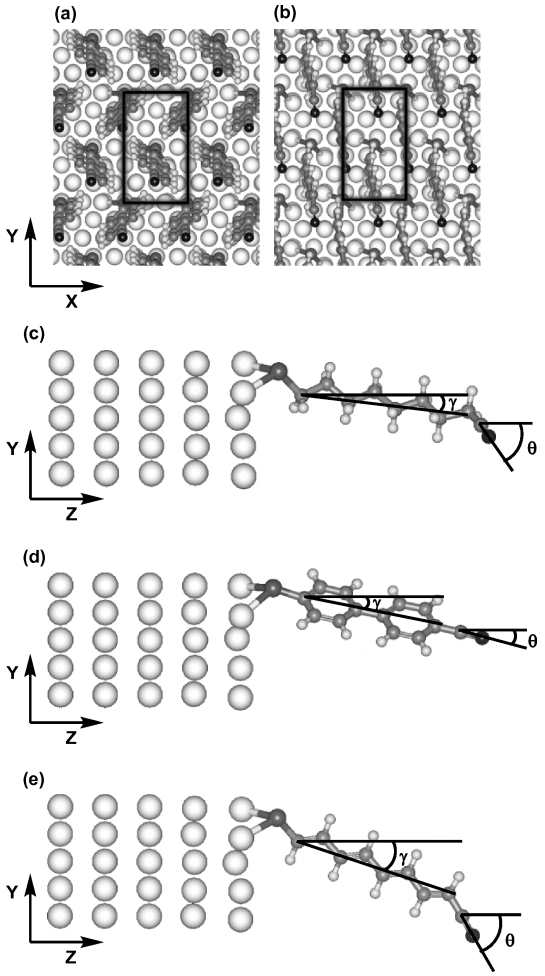

Figure 18: a) Top view of S-C2-CN on Au(111). Two molecules are arranged in the $p(\sqrt{3} \times 3)$ surface unit cell showing the characteristic herringbone pattern. b) Layered conformation identified as the lowest-energy structure for S-C3-CN. c-e0 Side views of S-C1-CN, S-C2-CN, and S-C3-CN on Au(111). Only one molecule is shown for the sake of clarity. The long molecular axis (γ) and the substituent axes (ϕ) are tilted with respect to the surface normal.

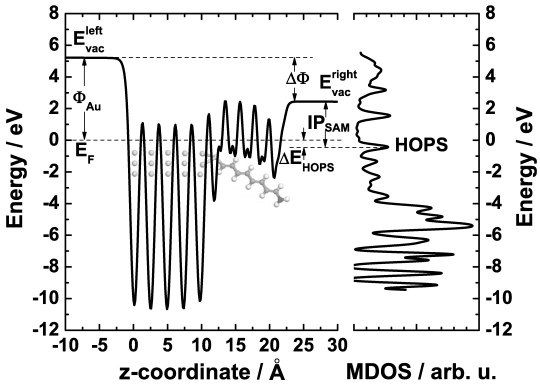

Figure 19: Left: Plane-averaged electron potential energy across a SAM of S-C3-NH2 on a 5-layer Au(111) slab. Right: Corresponding MDOS. The origin of the energy axis is the Fermi level (EF). Also indicated are the left and right vacuum levels (E_{vac}^{left}, E_{vac}^{right}), the gold work function ($\phi_{Au} = E_{vac}^{left} - E_F$), the work-function modification ($\Delta\Phi = E_{vac}^{right} - E_{vac}^{left}$), the highest occupied π-states (HOPS), the energy position of the HOPS with respect to E_F (ΔE_{HOPS}), and the ionization potential of the SAM ($IP_{SAM} = E_{vac}^{right} - HOPS$)

.

Table 5 summarizes the level alignment for all backbones with its substituents. It is found that ΔE_{HOPS} is virtually independent of the substituent. In contrary IP_{SAM} features significant differences between the donor and the acceptor head group. The highest is found for T1 and amounts to 5.42 eV. This behavior is found despite the strongly varying backbone properties including ionization potentials (IPs), HOMO energies, dipole moments, and polarizabilities as well as chemical hardness. Hence, independent of that the substituents only affect the potential landscape in their vicinity and therefore only E_{vac}^{right}. As a result they do not interact with the metal/SAM interface in the densely packed setups. This counterintuitive finding refutes both chemically plausible strategies proposed in the introduction suggesting that it is not a molecular property responsible for the effect. Instead it must be connected with the collective electrostatic effects in the monolayer, as Natan et al.[141] pointed out. They attributed that fact due to the dense arrangement of dipoles arguing that it behaves like a plate capacitor, i.e. the electric field emanating from these dipoles decays on a length scale shorter than the inter-dipole distance and hence the length of the molecules.[141]

Table 5: Electronic properties of the various donor- and acceptor-substituted SAMs on Au(111). ΔE_{HOPS} is the alignment of the HOPS and the Fermi level; $\mathrm{IP_{SAM}}$ is the ionization potential of the SAM; $\Delta\Phi$ is the SAM-induced work-function modification; the angle between the surface normal and the long molecular axes and the substituted axes are denoted as γ, and θ. μ_z is the component of the molecular dipole moment along the surface normal calculated for the substituted backbones in the geometries they assume in the SAM; namely, in the calculation of μ_z, no depolarization effects are considered. β is the angle between the total molecular dipole moment and the surface normal. As there are two non-equivalent molecules in the unit cell, the average values for γ, θ, β and μ_z are noted.

Systems	ΔE_{HOPS} (eV)	$\mathrm{IP_{SAM}}$ (eV)	$\Delta\Phi$ (eV)	γ (°)	θ (°)	β (°)	μ_z (D)
S-C1-NH2	-3.80	7.09	-1.86	11	42	75	0.33
S-C1-CN[iii]	-3.96	10.21	1.02	7	64	51	-2.65
S-C2-NH2	-0.86	3.57	-2.43	17	14	37	1.92
S-C2-CN	-0.93	8.83	2.62	12	15	14	-5.23
S-C3-NH2	-0.43	2.87	-2.68	27	54	38	3.25
S-C3-CN[iii]	-0.43	7.23	1.57	19	62	42	-4.52
S-T1-NH2	-0.51	2.77	-2.86	7	18	33	2.08
S-T1-CN	-0.51	8.19	2.42	6	22	21	-5.29
S-T2-NH2	-0.45	3.01	-2.58	20	35	43	1.94
S-T2-CN	-0.47	7.66	1.95	20	40	31	-4.62
S-T3-NH2	-0.40	2.90	-2.63	23	36	40	2.53
S-T3-CN	-0.39	7.53	1.89	22	41	32	-5.10

What does, however, exert a significant impact on the level alignment is the chemical structure of the backbone itself. Hereby, rather surprisingly it does not depend on the head-group. This trend can be clearly identified in Table 5. ΔE_{HOPS} is largest for the aliphatic backbone C1, intermediate for C2 and smallest for the non-aromatic conjugated systems (C3, T1, T2 and T3).

Thereby, a systematic picture evolves when plotting ΔE_{HOPS} as a function of the HOMO energy of the isolated backbones of Table 4. Figure 20 shows the results for the -CN substituted SAMs. The same evolution can be found when plotting the results of the -NH2 SAMs, not shown here. For both a steady decrease of the hole injection barrier with decreasing E_{HOMO} is found. This trend is only stopped as ΔE_{HOPS} is becoming so small that Fermi level pinning occurs. This happens when the onset of the HOPS crosses E_F and results in a redistribution of the electrons from the HOPS into the metal. As a result the curve levels off and ΔE_{HOPS} gets pinned at about 0.3 - 0.4 eV below the Fermi energy. As we are interested in a continuous transport channel, i.e. a HOPS delocalized over the entire backbone only a small fraction of charge transport already give rise to sizable dipoles resulting in the HOPS peak being pinned.

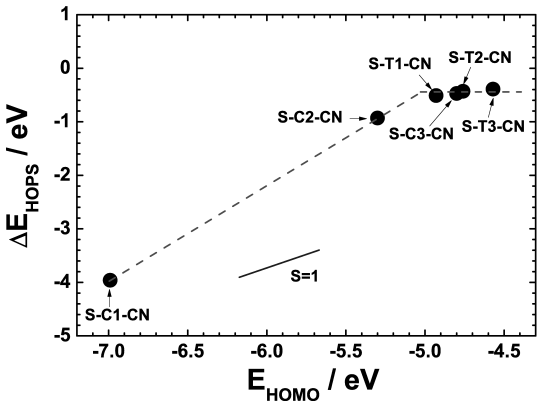

Figure 20: ΔE_{HOPS} as a function of the energy of the highest occupied delocalized molecular orbital of the isolated backbone, E_{HOMO}. The dashed lines are a guide to the eye to better visualize the Fermi-level pinning. For comparison, a solid line with a slope of one is also shown.

An implication of this finding is that the choice of the backbone offers one more possibility to tune the interface in modern opto-electronic devices in a desired way, besides employing different head- and docking-groups. As a result the tunneling barrier from electrodes through the SAM into an active organic material can be adjusted.

A quantity being affected by both, the backbone as well as the head-group is $\mathrm{IP_{SAM}}$ (cf. Table 5). The $\mathrm{IP_{SAM}}$ is connected with the work-function modification $\Delta\Phi$ as well as the work function of the gold Φ_{Au} and ΔE_{HOPS} in the following way. $\Delta\Phi = \mathrm{IP_{SAM}} + \Delta E_{\mathrm{HOPS}} - \Phi_{\mathrm{Au}}$. Therefore, a characteristic dependence of the SAM induced work-function modification is expected.

[iii] Internal-coordinate optimization of these systems results in a slow convergence in the vicinity of a local minima. Based on that geometry a Cartesian optimization was made leading to the local minima.

4.5.2 Work-function modification

Systematically connecting $\Delta\Phi$ to the backbone properties as well as to the substituents leads to a complex picture as $\Delta\Phi$ depends on three interwoven factors.

- *The magnitude of the molecular dipole moments.* This is insofar not straight forward as the magnitude is given by the intrinsic dipole moments of the molecules plus the dipole induced by charge transfer between the backbones and the donor/acceptor head-group. The latter is governed by the local polarizability in the vicinity of the head-group. The macroscopic quantity $\Delta\Phi$ is related to the dipole moment via the Helmholtz equation. It links $\Delta\Phi$ with the dipole moment per surface area.

- *The orientation of the individual molecular dipole moments relative to the surface normal.* This parameter crucially influences the modification properties as only molecular dipole moments perpendicular to the surface contribute. The magnitude is hence normally reduces by the cosine of the derivation in the angle, $\mu_z = \mu \cdot cos(\beta)$. β is the angle between the surface normal and μ. This reduced dipole moment enters the Helmholtz equation and leads to a work-function modification, $\Delta Phi = -e\mu_z/(\epsilon_0 A)$. Here, e is the elementary charge and ϵ_0 the vacuum permittivity.

- *Depolarization effects.* In a 2D arrangements of polarizable dipoles, aligned in a way that all out of plane dipole components are parallel, the dipole moment of each molecule is reduced compared to the isolated case. In the former case all dipoles induce oppositely oriented dipoles in all neighbors. This however, goes in hand with significant packing-induced charge rearrangements located on the head-group as well as throughout the SAM.[128] This results in a net depolarization[141–143] and in the end in a reduced work-function modification.[111] The magnitude of this reduction depends on the polarizability of the backbones. In the end as we have seen priory it more precisely depends on the local polarizability around the head-group as the latter is responsible for the work-function modification.[128]

The work-function modification of all investigated systems is given in Table 5 together with the orientation of the molecules. Therefore, the angles γ between the long molecular axes, β between dipole axes and θ between the substituent axes and for all cases the surface normal are given. Note that here the averaged angle of the two non-equivalent molecules in the surface unit cell is given. To obtain a trend in the evolution of the work-function modification and the molecular dipole moment, $\Delta\Phi$ is plotted as a function of the absolute value (solid black symbols) of μ_{CN} and μ_{NH2} in Figure 21. Hereby, interestingly no trend is observable. The only thing, admitting not surprising, that can be seen is that the CN substitution leads to a collective increase in the work function while NH2 leads to a decrease. The absolute values are rather comparable for both, which might be unexpected at first. Especially, considering the larger molecular dipole moments of CN (Table 4) but it can, however, be explained by the contributions from the thiol docking groups (not considered when calculating the molecular dipole moments) and by the charge rearrangements and their effect on the work-function modification.[89]

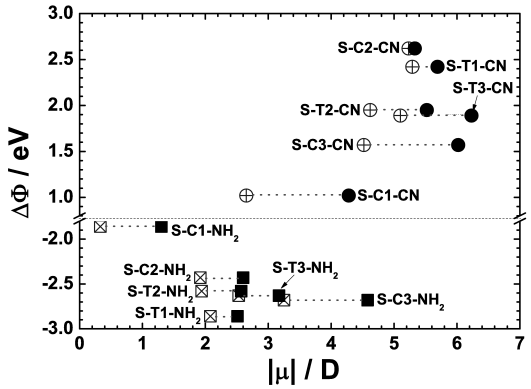

Figure 21: Dependence of $\Delta\Phi$ on the molecular dipole moment, μ. Solid symbols denote $\Delta\Phi$ as a function of the total molecular dipole moments ($|\mu_{\mathrm{CN}}|$ or $|\mu_{\mathrm{NH2}}|$ from Table 4). Crossed symbols denote $\Delta\Phi$ as a function of μ_z, the (average) component of the molecular dipole moment perpendicular to the surface (see caption of Table 5). The dotted lines connect the two data points for each SAM. Note the break in the y axis.

Hence surprisingly hardly any correlation between the total molecular dipole moments (first point from above) and $\Delta\Phi$ at full coverage can be found. No correlation can be found when using the molecular HOMO instead of the dipole moment (Figure not shown). The correlation improves in a way when using the dipole moment perpendicular to the surface, μ_z, instead of the total dipole moment (crossed symbols in Figure 21). By doing so the orientation of the dipole moments is considered (second point from above). Not surprisingly the largest deviation between the value with the total dipole moment and μ_z for our two head-groups is found for the C1 backbone. Not surprisingly in a way that one could expect it from the largest angle between the dipole axes and the long molecular axes.

Surprisingly, the by far clearest trend is found when plotting $\Delta\Phi$ as a function of the cosine of β, the angle between the molecular dipole moments and the surface normal, Figure 22. The latter is calculated for isolated NH2 or CN substituted backbones in the same geometry they adopt in the SAM. A strong near-linear dependence of $\Delta\Phi$ on $\cos(\beta)$ is observed. The dashed lines in Figure 22are linear fits to all data points within the same head-group. This is insofar unexpected as the actual magnitude of the molecular dipole moments is not considered. This leaves the conclusion that the chemical nature of the backbone does not have a direct impact on the work-function modification $\Delta\Phi$. On the other hand importantly the orientation of the molecular dipole moment with respect to the surface normal is the dominant factor for the work-function modification . To ensure that this is not some kind of artifact this was reproduced when taking the Cartesian optimized structures. The resulting values are shown as small open circles in Figure 22.

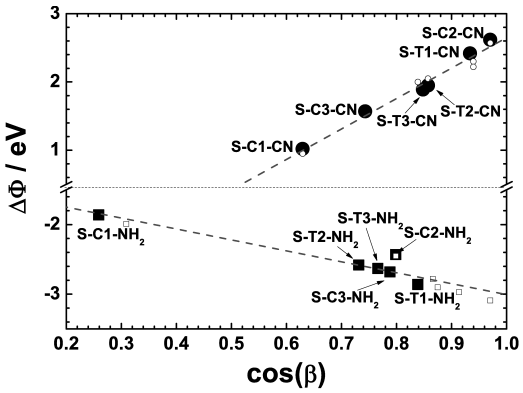

Figure 22: Dependence of $\Delta\Phi$ on the cosine of β with β being the angle between the dipole axes of the individual molecules relative to the surface normal (see caption of Table 5). Note that the averaged angle is denoted as there are two non-equivalent molecules per unit cell. The large solid symbols are based on internal coordinate optimizations and the small open symbols are the results based on pure Cartesian optimization. The dashed linear line is a fit to all data points. Note the break in the y-axis.

In order to understand this finding one has to remember the origin of those variations as well as the last of the above mentioned factors, depolarization. In that context important is to recall that the molecular dipole moments are a combination of intrinsic dipole moments of the molecule itself as well as induced dipole moments due to charge transfer between head-group and backbone. We have seen that the latter increases with increased local backbone polarizability. On the other hand depolarization effects also increase with increased backbone polarizability and hence as a result, the effective dipole moment per molecule in the SAM is large reduced. The data of Figure 22 implies that the component of the molecular dipole, related to induced dipoles due to charge transfer between head-group and backbone, and the counter-dipole due to the electric field generated by all neighboring dipolar molecules (as a result of the substituent and induced dipoles) largely cancel each other in the here studied systems a full coverage. Furthermore, there are still two additional effects hidden in the mechanism just proposed and which can be held responsible for the remaining scatter in $\Delta\Phi$. The first one is the effect of substrate molecule charge transfer upon bond formation [88,89] which exhibits a certain tilt angle dependence.[127] The latter is currently also under consideration within our group and F. Rissner is preparing a paper. The second is the dipole arising from the pinning of the HOPS.

For the design of applications using the SAM to promote charge carrier injection these findings underline that the control of the orientation of the dipolar substituents is vitally important for predictably and reproducible results. Hereby, it has to be kept in mind that the orientation of the backbone structure is not the same as the orientation of the dipolar substituents. Once structural control is achieved, varying the dipole orientation by different backbones opens up the possibility of additionally optimizing the substituents in terms of hydrophobicity/-philicity or (bio)chemical-reactivity. However, it has to be kept in mind that the backbone orientation, γ, and the dipole orientation, β, accordingly, are very soft degrees of freedom. Therefore, significant dynamical

fluctuation of all angles and consequently of $\Delta\Phi$ are expected at finite temperatures.

4.5.3 The impact of coverage

This part will highlight the influence of the packing density on depolarization effects. Especially the impact of the different backbones will be analyzed. This is especially interesting as reduced coverage and imperfections are often encountered in experiments. It has been shown that depolarization leads to a pronounced packing-density dependence of both the work-function modification and the level alignment in biphenyl based SAMs (C2).[111] Following the guidelines of Ref. [111], as a simplified case, the molecules are successively removed from a large supercell.[iv]

Figure 23 shows the packing density dependence of the work-function modification. Hereby, the coverages ranging from full, $\tau = 1$ till $\tau = 1/16$ are analyzed. The quantity $\Delta\Phi(\tau)/\tau$ is an approximate measure for how large the work-function modification would be at full coverage, if there was only the amount of depolarization present that one encounters at coverage τ. Note that the value for $\Delta\Phi(1/16)/(1/16)$ serves as an estimate of how large the work-function modification would be without the effect of depolarization.

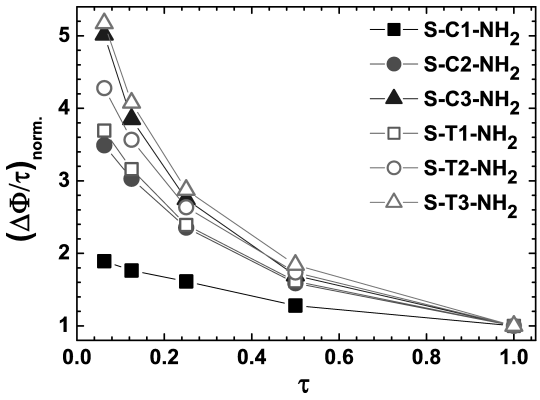

Figure 23: Effective depolarization for the -NH2 substituted SAMs as a function of coverage. The quantity $(\Delta\Phi/\tau)_{\text{norm}}$ is defined as the work-function modification at a particular coverage divided by that coverage and normalized to $\Delta\Phi$ at full coverage $(\tau - 1)$. The plot illustrates how much larger the work-function modification would be without depolarization effects.

It can be seen in Figure 23 that already for the reference system C2 a pronounced effect could be achieved as the work-function modification at full coverage would be around 3.4 times larger in the absence of depolarization. For more polarizable backbones this effect is even more pronounced and is strongest for T3, where this effect would be 5.2 times larger.

These results confirm the importance of depolarization with respect to the achievable work-function modification depending on the backbone polarizability. They addition-

[iv] The geometries at reduced coverage are not re-optimized in order to get the influence of depolarization. Optimizations would also overstretch the limits of the computational capacities and additionally the tilt angle would be increased.

ally, illustrate the sizable impact of static disorder. The latter would reflect itself in deviations from ideally ordered SAMs and would lead to dynamic fluctuations of $\Delta\Phi$.

4.6 Conclusions

The present chapter dealt with the role of the backbone polarizability on the alignment of the SAM states with the metal Fermi level. Especially, the effect of donor/acceptor head-group substitution and the work-function modification was studied. Therefore, a comprehensive first-principles study on SAMs of organic thiols on Au(111) was performed.

For densely packed SAMs, the donor or acceptor character of the head-group has no impact on the level alignment independent of the polarizability of the backbones but it exclusively determines the achievable work-function modification. Different HOMO positions depending on the backbone, however, do significantly affect the level alignment until Fermi level pinning of the HOPS is encountered.

Independent of the backbones, the CN head-group leads to an increase and the NH2 head-group to a decrease of the work-function modification. Surprisingly the orientation of the molecular dipole moments (largely localized on these head-groups) and not the magnitude of the backbone-dependent, induced molecular dipole moments is the dominant factor in terms of achievable work-function modification. This is attributed to canceling of two factors, namely the larger substituent-induced dipole moment in more polarizable backbones and the concurrent increase of depolarization in densely packed SAMs.

Significant dynamic fluctuation of the work-function modification can be expected at finite temperature as the orientation of the molecules relative to the surface normal represents a rather soft degree of freedom. Furthermore, deviations from the ideal SAM structure are shown to affect the work function in a nontrivial manner because of the complex coverage dependence of the involved depolarization phenomena.

In the field of molecular electronics, these findings underline the importance of the chemical structure of the backbone in determining the tunnel barriers through SAMs. Additionally through interrelation between backbone structure and dipole-moment orientation, variation of the backbone allows tuning the charge-injection barriers from electrodes into active organic materials.

5 The controversy of the bond dipole in self-assembled monolayers on gold.

5.1 Foreword

During my research with Wang LinJun of the Chinese Academy of Science about the effect of different polarizable backbones of self-assembled monolayers (SAMs) on the work-function modification, previous chapter, we discovered problems when partitioning the system into a monolayer part and the metal slab. The problem deals with how to obtain the "proper" bond-dipole in thiol-based SAMs. We discovered that both approaches commonly used in literature have their own specific advantages and shortcomings and therefore we intensively studied both systems using our availiable data. This section summarizes the most important results of the accepted paper in Physical Chemistry Chemical Physics. The authors of this paper are Wang LinJun, Rangger Gerold M., Ma ZhongYun, Li QiKai, Shuai Zhigang, Zojer Egbert, and Heimel, Georg. As second author my contribution to this paper was decisive in terms of bringing up this issue in first place and in gathering data for the evaluation of the problem. Together with LinJun Wang, we systematically analyzed both approaches of obtaining the bond-dipole and summarized their impact. Subsections 5.2 to 5.5 follow the accepted paper.

5.2 Introduction

A crucial factor for modern organic (opto)electronic devices are charge-carrier injection efficiencies between organic semiconductors and metals.[115–118] One increasingly important way to tune the charge injection is by modifying metal electrodes using SAMs.[119–123] Hereby, the SAM, sandwiched between the metal electrode and the active organic material, allows tuning of the metal work function. As a result control of the charge-injection barriers between the electrode Fermi level (E_F) and the frontier electronic states in the organic semiconductor can be achieved.[120]

Therefore, as a matter of fact, the induced electrode work-function modification and the alignment of the SAM states with respect to the metal Fermi level constitute the two most important electronic quantities in the context of organic and molecular electronics.

The work function, Φ, of a electrode/metal is defined as the energy difference between its Fermi level, E_F, and the energy of an electron at rest directly outside the metal surface, E_{vac}. The work-function modification, $\Delta\Phi$, is a result of a potential jump introduced by the SAM. Thereby, theoretically in order to compare different molecules regarding the achievable $\Delta\Phi$ the latter is commonly split into two additive components. The first one is due to an intrinsic dipole moment of the SAM layer itself, ΔE_{vac}. The second is a result of the charge rearrangements occurring upon bond formation, E_{BD}.

5.3 Theoretical background

Considering, a perfectly homogeneous SAM, each potential energy step is linked to a corresponding plane-averaged charge (re)distribution, $\rho(z)$, via the Poisson equa-

tion,[83,88,131]

$$\Delta E(z) = -\frac{e}{\epsilon_0}\rho(z). \tag{51}$$

Here, e denotes the elementary charge[i] and ϵ_0 the vacuum permittivity. It is important in that field that only a net dipole moment perpendicular to the surface leads to a non-vanishing $\Delta E(z)$. In that case Equation 51 is commonly replaced by the heuristic Helmholtz equation, where the two contributions to $\Delta\Phi$ are regarded as arising from two laterally homogeneous dipole layers.[83,88,100,101,112,119,131,133,137,144–147]

$$\Delta\Phi = \Delta E_{\text{vac}} + \Delta E_{\text{BD}} = -\frac{en}{\epsilon_0}\left[\frac{|\mu|\cos(\beta)}{\epsilon_{\text{eff}}(n)} + \mu_{\text{BD}}(n)\right] \tag{52}$$

Here, n denotes the molecular packing density, $|\mu|$ is the dipole moment of the free molecule, and β is the angle between the dipole axes of the molecules in the SAM and the surface normal. Generally, the depolarization factor $\epsilon_{\text{eff}}(n)$ and the bond dipole at the Au-S interface, $\mu_{\text{BD}}(n)$, depend on the coverage in a non-trivial manner.[111,128] Therefore, we assume full coverage n for all SAMs considered in this study.

For many adsorbates, the partitioning of $\Delta\Phi$ into a molecular part (first term in Equation 52) and a bonding-induced part (second term in Equation 52) is unambiguously defined.[88] However, for SAMs with thiols, two different partitioning schemes coexist in literature. One considers the saturated R-SH species[83,88,100,131,137] and the second one the radical species R-S·[101,112,119,133,144–147] as molecular contribution in Equation 52, ΔE_{vac}. Here, R denotes the backbone and the head-group of the SAM.

As a result two different adsorption reactions are described, where in the first model the bonding of the SAM to the metal happens upon *replacing* the S-H bonds and where the second is based on *forming* new bonds between the radicals and the metal.

$$R - SH + Au \longrightarrow R - S - Au + \frac{1}{2}H_2 \tag{53}$$

$$R - S\cdot + Au \longrightarrow R - S - Au \tag{54}$$

Naturally, different molecular dipole moments are found for the saturated and the radical species and, consequently, by virtue of Equation 52, also different ΔE_{vac} values. Nonetheless, the final observable $\Delta\Phi$ is identical in both approaches as the final systems are the same, i.e. SAM bond to the Au surface. As a consequence the bonding-induced contribution to the work-function modification, ΔE_{BD},differs accordingly. Theoretically, the latter is obtained by applying Equation 51 to the plane-averaged charge-density differences, ρ_{diff}. The latter are depending on the different reaction pathways, Equation 53 and 54.[83,88,131,145–147]

$$\rho_{\text{diff}}^{\text{sat}} = \rho_{\text{sys}} - \rho_{\text{Au}} - (\rho_{\text{sat}} - \rho_H) \tag{55}$$

$$\rho_{\text{diff}}^{\text{rad}} = \rho_{\text{sys}} - \rho_{\text{Au}} - \rho_{\text{rad}} \tag{56}$$

[i] Note, that e is per definition positive

Here, *sys*, *Au*, *rad*, *sat*, and *H* refer to the entire metal/SAM system, the pristine metal, the free-standing molecular monolayer of radical and H-saturated species, and the layer of saturating H-atoms, respectively. Experimentally, ΔE_{BD} can be extracted from $\Delta\Phi$ measurements on a series of molecules with the aid of their calculated dipole moments and reasonable estimates for all other quantities in Equation 52.[100,112,119,137,144]

Density functional theory (DFT) calculations following the saturated approach have found values of ΔE_{BD} of around -1.2 eV for SAMs of biphenylthiols on Au(111),[83,88,131] while negligible values of -0.01 till 0.08 eV have been reported for SAMs of alkylthiols following the radical scheme.[145–147] Even more strikingly, experimental studies on thiols with an aromatic ring adjacent to the -SH group have reported a ΔE_{BD} values of -0.85 eV when relying on dipole values calculated for saturated molecules,[137] while a ΔE_{BD} between +0.6 and +1.0 eV has been found using dipole values calculated for radicals.[144]

Thus, the bond dipole of thiols to gold appears to depend not only on the chemical structure of the molecular backbone. It, rather unsatisfactorily, also depends on the chosen partitioning scheme. As the purpose of the latter, however, is to permit correlating the chemical structure of the SAM-forming molecules with the achievable $\Delta\Phi$, the question arises which of the two possibilities is better suited to provide a chemically and physically insightful picture of the relevant interfacial processes.

5.3.1 Computational methodology

We computationally investigated a series of functionalized thiols on Au(111) by performing slab-type DFT band-structure calculations, following the methodology as previously described in this thesis in chapter 4.3 and is not revised at that point in great detail. Therefore, the plane-wave DFT code *VASP*[38,39] using the internal-coordinate geometry optimizer *GADGET*,[129] and *XCRYSDEN*.[110] As shown in Figure 24a, each molecule consists of a strong polar head-group and different polarizable backbones. The head-group consists of a strong donor (-NH2) lowering Φ or a strong electron acceptor (-CN) increasing the work function. The role of the SAMs in connection with the electronic properties was studied in a previous chapter 4 and was published in an other joint paper.[2] Note that the total dipole moment of these molecules is composed of the contributions from the head-group on one side and from the thiol docking-group on the other side. The latter is pointing roughly in the direction of the S-H bond (*vide infra*). For the sake of comparability, the same rectangular $p(\sqrt{3} \times 3)$ unit cell is assumed for all monolayers, cf. Figure 24b.

5.4 Results and Discussion

5.4.1 Saturated scenario

In a first step the saturated scenario is analyzed. Thereby, one has to assume the position of the saturating hydrogen atom at the sulfur atom, see Figure 24c when analyzing the free-standing molecular monolayer. The latter is needed to evaluate ΔE_{vac}. Two well-defined and essentially iso-energetic positions can be found for the hydrogen atoms. Thereby, the hydrogen lies in the plane defined by the sulphur and the two

nearest carbon atoms. As the S-C bond is inclined with respect to the surface normal by about 17° for all investigated molecules. The C-S-H bond angle is only around 97°.

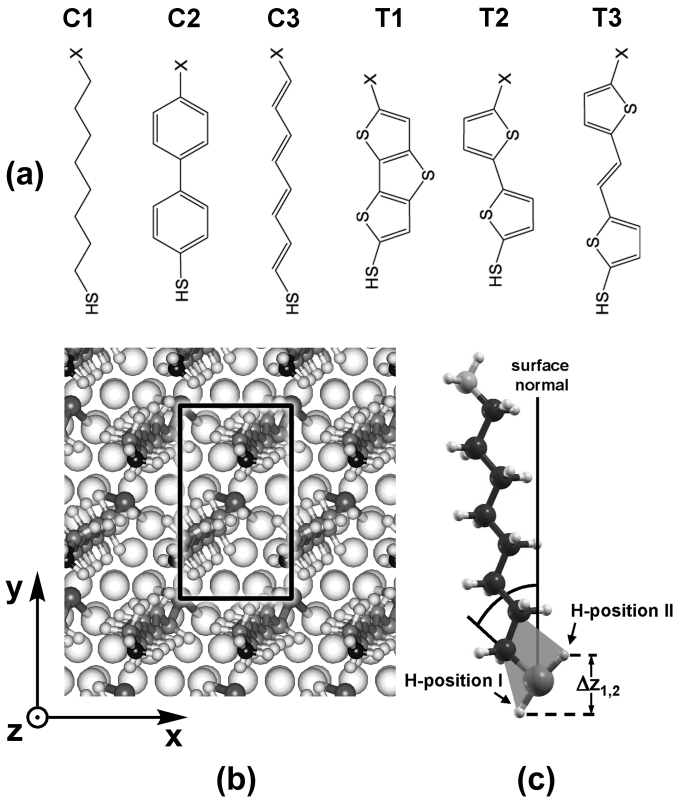

Figure 24: (a) Chemical structures and labels of the investigated thiols; X stands for amino (-NH2) and cyano (-CN) head-group substitutions. (b) Top view of the $p(\sqrt{3} \times 3)$ surface unit cell containing two molecules (shown for C1), which is assumed for all SAMs. (c) Side view of one NH2-substituted C1 molecule in the free-standing H-saturated monolayer indicating the two possible hydrogen positions, the inclination of the S-C bond to the surface normal, and the height difference, $\Delta z_{1,2}$, between the two saturating hydrogen atoms in position I and II.

This results in the hydrogen at position II to lie above the plane of the sulphur atoms, i.e., farther away from where the metal surface will be located once bonding is established, and below the sulphur plane in position I. As ΔE_{BD} clearly should reflect the bonding of sulphur to gold, the latter is obviously a better choice; The ΔE_{BD} values obtained with the hydrogen at position I in the free-standing thiol layer are listed in Table 6. They are all negative and they reflect the local polarizability [2] of the molecular backbone adjacent to the sulphur. Hereby, larger values are observed for more polarizable backbones. [2] Notably, the value for the alkyl backbone C1 is non-zero. Also listed are the ΔE_{BD} values for hydrogen position II.

Table 6: DFT-calculated vertical distance, $\Delta z_{1,2}$, between the saturating hydrogen atoms in positions I and II, left-sided ionization potential, IP_{left}, energy perturbation of the highest occupied delocalized orbitals upon metal-molecule bonding, E_{corr}, and potential energy step due to the bond dipole, ΔE_{BD}, for hydrogen position I as well as ΔE_{BD} for hydrogen position II obtained for the saturated partitioning scheme.

		H-position			
		I			II
Systems	$\Delta z_{1,2}$ ($\AA$)	IP_{left} (eV)	E_{corr} (eV)	ΔE_{BD} (eV)	ΔE_{BD} (eV)
S-C1-NH2	1.1919	7.74	0.03	-1.27	0.16
S-C1-CN	1.880	8.17	-0.01	-1.00	0.13
S-C2-NH2	0.675	5.03	0.14	-1.14	-0.69
S-C2-CN	0.515	5.13	0.17	-1.20	-0.85
S-C3-NH2	1.894	3.89	0.16	-1.87	-0.78
S-C3-CN	2.067	3.74	0.16	-2.06	-0.88
S-T1-NH2	0.821	4.26	0.14	-1.54	-1.01
S-T1-CN	0.788	4.30	0.14	-1.57	-1.07
S-T2-NH2	1.269	4.04	0.12	-1.70	-0.94
S-T2-CN	1.266	4.10	0.13	-1.71	-0.95
S-T3-NH2	1.173	3.99	0.13	-1.70	-0.98
S-T3-CN	1.160	4.01	0.13	-1.72	-1.02

Not only are they very different, but closer inspection of Table 6 reveals that the difference to the H-position I values increases essentially linearly with the height difference, $\Delta z_{1,2}$ of the hydrogens in the two positions (Figure 24c), i.e., with the projection of the local dipole moment around the -SH group onto the surface normal (*vide supra*), shown in Figure 25. This indicates that, using the saturated partitioning scheme, ΔE_{BD} also reflects the orientation of the S-C bond with respect to the surface normal, which somewhat complicates a systematic comparison of different molecules.

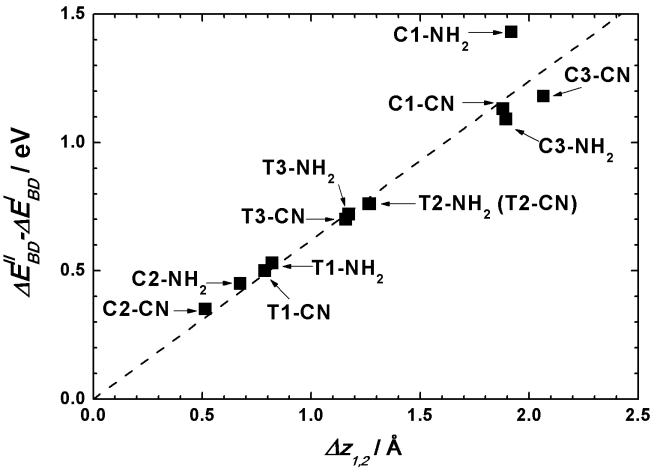

Figure 25: Difference between the E_{BD} values obtained with the saturated partitioning scheme for hydrogen positions I and II as a function of $\Delta z_{1,2}$, the height difference between the saturating hydrogen atoms in position I and II; the dashed line is a linear fit through the origin.

In order to further test the ability of the saturated approach to provide chemically and physically meaningful information, we also examined a different quantity, namely the left-sided, i.e. the side facing the vacuum, ionization potentials (IPs) of the free-standing saturated monolayers. They are defined as the energy difference between its highest occupied, fully delocalized states, usually π-states highest occupied π-state (HOPS)[ii] and ΔE_{vac} on the thiol side.[83,88,131]

Note that the latter obviously differs from E_{vac} above the head-group substituents by ΔE_{vac}. Therefore, also the "right-sided" IPs must differ from their left-sided counterparts by ΔE_{vac}.[83,88,131] Analyzing the IP_{left} values of Table 6 the chemical nature of the backbones is maintained, i.e., lower values are found for structures with smaller energy gaps and more extended conjugation.[2] Nonetheless, also IP_{left} is a function of the inclination of the S-C bond, or rather the projection of the local dipole moment of the S-H group onto the layer normal, as it was shown for ΔE_{BD} previously.

Finally, it has been observed that the right-sided IPs in the free-standing monolayers differ from the IP of the SAM bonded to the metal (reported in Ref. [2] and shown in Table 5) by a small amount. This is due to a perturbation of the molecular electronic structure as a result of the molecule-metal bond, E_{corr}.[83,88,131] Table 6 lists also these correction values and they are typically below 0.2 eV for all investigated systems.

This, however, underlines that replacing the S-H bonds with S-Au bonds has little effect on the energy levels within the SAM. Therefore, the saturated partitioning scheme conserves the chemical information on the nature of the molecular backbone.

[ii] In the case of C1 it corresponds to the highest fully delocalized σ-state.[2]

5.4.2 Radical scenario

In this part we analyze the radical scenario. Hereby, instead of replacing S-H bonds with S-Au bonds, a new bond is formed between the R-S· species (radical) and the gold surface. While the radical is unlikely to actually participate in the process of SAM formation, an obvious advantage is that one does not introduce the artificial H-positioning effect. The results obtained with the radical partitioning scheme are listed in Table 7.

Table 7: DFT-calculated potential energy step due to the bond dipole, ΔE_{BD}, left-sided ionization potential, IP_{left}, and energy perturbation of the highest occupied delocalized orbitals upon metal-molecule bonding, E_{corr}, obtained for the radical partitioning scheme.

Systems	ΔE_{BD} (eV)	IP_{left} (eV)	E_{corr} (eV)
S-C1-NH2	-0.04	8.95	-0.02
S-C1-CN	-0.04	0.07	-0.09
S-C2-NH2	1.11	6.07	-1.11
S-C2-CN	0.96	6.08	-1.08
S-C3-NH2	1.33	6.11	-0.86
S-C3-CN	1.28	6.14	-0.83
S-T1-NH2	1.18	5.89	-1.11
S-T1-CN	1.19	5.88	-1.07
S-T2-NH2	1.22	5.81	-1.07
S-T2-CN	1.17	5.81	-1.08
S-T3-NH2	1.27	5.89	-0.99
S-T3-CN	1.23	5.89	-0.99

Now, noticeable at first glimpse is the vanishing ΔE_{BD} value for the akyl backbone C1. This is in agreement with previous studies following this approach.[145–147] For all other molecular structures, ΔE_{BD} changes sign compared to the saturated scheme, Table 6. As a result, a potential dependence on the orientation of the S-C bond is hard to assess. Further notably is that now the IP_{left} values, Table 7, all are within the narrow range of 5.8-6.1 eV, cf. Ref. [133]. Once again the exception is the akyl backbone C1 as a result of the different nature of the highest occupied delocalized states, i.e. the σ-orbital for C1 vs. π-orbital for the others.[2] Remarkable different are the E_{corr} values. They are around 1 eV for the radical case, yet again with the exception of C1 (*vide infra*). This leads to the conclusions that, in the radical partitioning scheme, chemical information on the nature of the backbone is largely lost. Furthermore this implies that the electronic structure of the free-standing radical layer is significantly perturbed relative to that of the "parent" thiol molecules as well as to the bonded molecule.

The reason for these observations is that the radical character of the -S· termination dominates the docking side. Therefore it determines the docking-sided electronic structure of the free-standing monolayer and, consequently, also the interfacial charge redistributions upon metal-molecule bond formation. Hence, by dealing with the radical

one induces major charge rearrangements on that side of the molecule. The latter can be expressed as $(\rho_{\mathrm{rad}} + \rho_H)$-$\rho_{\mathrm{sat}}$ and are shown in the left panels of Figure 3.

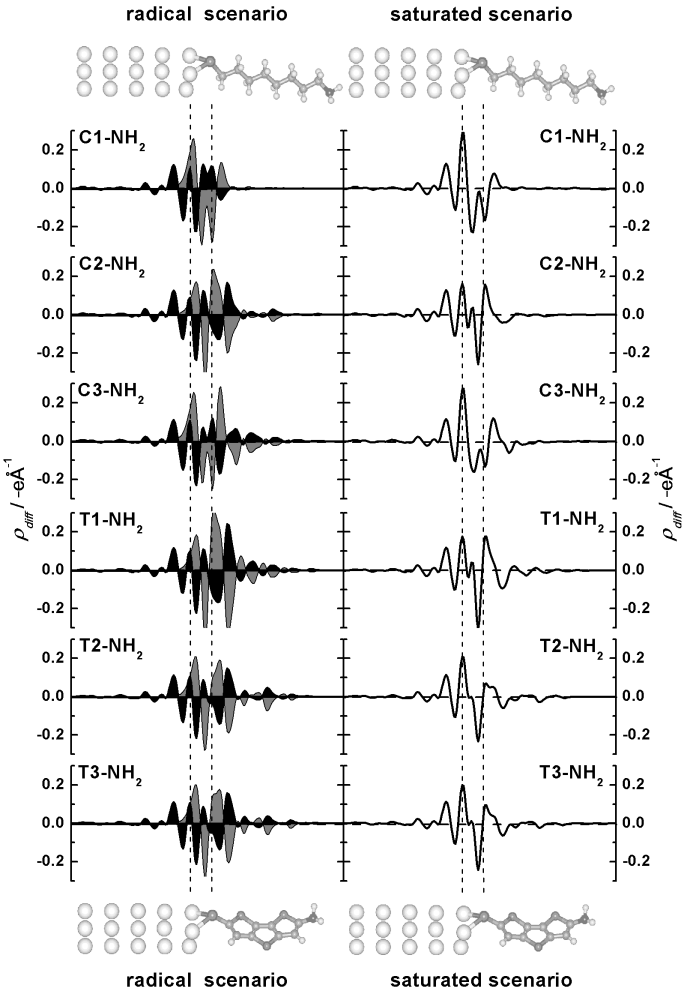

Figure 26: Left column: Plane-integrated charge-density difference per unit-cell area, $(\rho_{\mathrm{rad}} + \rho_H)$-$\rho_{\mathrm{sat}}$, describing the removal of the hydrogen from the thiol (gray) and plane-integrated charge-density difference per unit-cell area, ρ_{diff} after Equation 55, describing the bond formation between radical and metal (black). Right column: Plane-integrated charge-density difference per unit-cell area, ρ_{diff} after Equation 56, describing the bonding of the hydrogen-saturated molecular monolayer to the metal. The curves in the right panels, which describe the actual bonding-induced interfacial charge rearrangements, are also the sum of the two curves in the left panel. The vertical lines indicate the (average) positions of the top-most gold layer and the sulphur atoms. The structure of the C1 system is shown at the bottom as guide to the eye.

For all conjugated systems (C2-T3), the charge redistributions resulting from hydrogen removal reach far onto the molecular backbones. This is a direct consequence to the strong coupling of the sulfur atom to the π-electron system. As usual, a qualitatively

different behavior is observed in the case of the alkylthiol (C1). Here, both the π-system as well as the radical character are strongly localized on the sulphur alone. Therefore, the delocalized σ-states are hardly affected by radical formation. Upon establishing the bond of the radical species and the gold charges are redistributed following Equation 56. Thereby, the molecule is essentially converted back to a closed-shell species and the charge redistributions are largely reversed in the spatial region of the SAM, cf. left panel of Figure 26. As a consequence, the actual chemical and physical information connected with the bond formation lies hidden in the difference between the processes of removing the hydrogen atoms from the sulphur and replacing it with the gold surface. Exactly this difference (right panels in Figure 26), corresponding to ρ_{diff} of the saturated case (Equation 55), is obscured in the radical approach.

5.5 Summary and Conclusions

In this part, we have identified and discussed two distinctly different ways of analyzing the bond formation between thiol-SAMs and the metal, Au(111) in the present study. Thereby, the difference is lying in the Au-S bond dipole.

One approach, the saturated one, where the bond formation is described by replacing the S-H bond with S-Au bonds, conserves information on the chemical structure of the thiols, reflecting the orientation of the S-C bond, and provides insights into the interfacial charge rearrangements that occur upon metal-molecule bonding. In particular, a considerable negative ΔE_{BD} is found for a wide range of molecules, including alkylthiols. The negative side of this approach however, is that it suffers from the positions of the saturating H-atoms in the non-bonded SAM. As a matter of fact they are not unambiguously defined and introduce an additional, not vanishing, dipole moment.

The second approach does not feature this con as thereby the radical species is taken as reference system. However, in such an approach chemical information on the SAM is largely lost and the relevant bonding-related charge redistributions are not accessible. This indicates that the radical approach is of little use when trying to understand the relation between the chemical structures of the SAM-forming molecules and the electronic properties of the interface.

6 F_4TCNQ on Cu, Ag, and Au as prototypical example for a strong organic acceptor on coinage metals.

6.1 Foreword

Metal work-function modification with the help of organic acceptors is an efficient tool to significantly enhance the performance of modern, state-of-the-art organic molecular electronic devices. In this chapter an in the mean-time prototypical organic acceptor, namely 2,3,5,6-tetrafluoro-7,7,8,8-tetracyanoquinodimethane (F_4TCNQ), is characterized on Ag(111), Au(111) and Cu(111) metal surfaces, by means of density-functional theory calculations. Particular attention is paid to charge-transfer processes at the metal-organic interface.

This part is reproduces the publication by Rangger et al., Ref. [4], to a large extend. The slightly modified numbers in the Table for the monolayer calculation of F_4TCNQ are a result of a new singlepoint calculation with higher accuracy and tighter convergence criteria (PREC=Accurate, and EDIFF=1E-6 in the *VASP* input file). This calculation has been made recently in connection with an accurate calculation for 3,5-difluoro-2,5,7,7,8,8-hexacyanoquinodimethane (F_2HCNQ), a different acceptor molecule, discussed in section 7.

A copy of the head of the paper is shown in Figure 27

PHYSICAL REVIEW B **79**, 165306 (2009)

F4TCNQ on Cu, Ag, and Au as prototypical example for a strong organic acceptor on coinage metals

Gerold M. Rangger,[1] Oliver T. Hofmann,[1] Lorenz Romaner,[1,2] Georg Heimel,[3] Benjamin Bröker,[3] Ralf-Peter Blum,[3] Robert L. Johnson,[4] Norbert Koch,[3] and Egbert Zojer[1]
[1]*Institut für Festkörperphysik, Technische Universität Graz, A-8010 Graz, Austria*
[2]*Department of Material Physics, University of Leoben, A-8700 Leoben, Austria*
[3]*Institut für Physik, Humboldt-Universität zu Berlin, D-12389 Berlin, Germany*
[4]*Institut für Expermentalphysik, Universität Hamburg, D-22761 Hamburg, Germany*
(Received 23 December 2008; revised manuscript received 18 February 2009; published 8 April 2009)

Figure 27: Copy of the head of the paper showing all contributing authors. This chapter is largely identical to this paper.

6.2 Introduction

Physical and chemical processes taking place at the interface between metals and organic molecules have attracted considerable attention in recent years[148–154], since such junctions can crucially determine the performance of organic (opto)electronic devices.[116,155–159] Several strategies have been developed to tune the alignment between the metal Fermi level and the molecular states and, thus, to facilitate carrier-injection across metal-organic interfaces. These include the application of polar, covalently bound self-assembled monolayers,[88,119,123,131,144,160–163] redox-doping of the organic layers,[164,165] or the deposition of (sub)monolayers of strong electron acceptors[166–170] (or donors[148,159,171,172]), which form charge transfer complexes with the

underlying metal.[113,168,173–177] The latter are of particular relevance for the present study.

Usually, when apolar molecules physisorb on clean metal surfaces, the respective work functions are reduced by Pauli repulsion.[149] For example, a work-function decrease in the range of 0.38 to 0.42 eV has been reported for the adsorption of the noble gas Ar on the (111) surfaces of Cu, Ag, and Au.[178] The decrease is nearly twice as large for (inert) alkane chains on Au, Ag and Pb.[179] This phenomenon is detrimental for the injection of holes from a metal electrode into an organic semiconductor. It can, however, be avoided by depositing an interfacial (sub-)monolayer consisting of molecules which induce electron transfer from the metal to the organic adsorbate. This can be achieved by depositing strong organic acceptors.[149,166,167,173,175] A particularly potent and in the meantime 'prototypical' example for such an acceptor is F_4TCNQ. It has been shown by photoelectron spectroscopy that charge is transferred from Au,[167] Ag,[170] and Cu surfaces[176] to F_4TCNQ. This could be used to reduce the hole-injection barriers (HIBs) into organic semiconductor molecules deposited on top of the F_4TCNQ monolayers. In fact, even a continuous tuning of the HIB over a wide range could be achieved by changing the F_4TCNQ coverage.[167,170] We have shown recently[176] by a combined theoretical and experimental study for sub-monolayers of F_4TCNQ on Cu(111) that the actual charge redistribution at the interface is much more complex than one might infer merely on the basis of photoelectron data.

Here, we discuss the involved processes in considerably more detail for several related systems. First, we focus on a densely packed F_4TCNQ layer on Ag(111); this substrate metal is chosen as the 'working horse' of the present contribution for reasons discussed below. Moreover, we describe, how changing the packing density of the adsorbate affects the electronic structure of the interface and discuss a possible reason, why depolarization in densely packed F_4TCNQ layers is only of minor significance. Subsequently, the role of the substrate metal for the interfacial charge transfer, energy-level pinning and the resulting work-function change is addressed. Finally, the results of the calculations are compared to experimental data with a focus on new measurements performed on Ag (111) surfaces.

6.3 Methodology

6.3.1 Computational methodology

The calculations presented here are based on density functional theory (DFT), using the generalized gradient approximation (GGA). The plane-wave based code *VASP*[38,39] is applied in the repeated slab approach using the Perdew-Wang 1991 (PW91) functional.[53,54] Two different Monkhorst-Pack[33] k-point grids ($4 \times 4 \times 1$) and ($3 \times 3 \times 1$) are used depending on the size of the unit cells, together with a second order Methfessel-Paxton occupation scheme[34] (broadening of $0.2\,eV$). All calculations were done in a non spin-polarized manner. In all cases discussed here, 5 layers of metal represent the metal substrate and a vacuum gap of more than $20\,\AA$ separates the slabs in z-direction. All atoms of the molecule as well as of the two top metal layers were fully relaxed using a damped molecular dynamics scheme until the remaining forces were smaller than $0.01\frac{eV}{\AA}$. To obtain the density of states (DOS) projected onto the molecular monolayer (molecular density of states (MDOS)), each Kohn-Sham orbital was projected

onto spherical harmonics inside spheres around each atom. Subsequently, the DOS was weighted accordingly to the contributions of that atomic orbital and all non-metallic contributions were summed up.

For the special, charge conserving, projections of the DOS of the system onto the bands derived from the molecular orbitals calculated without the metal, we applied the atomic orbital based code *SIESTA*.[45] A more detailed description of the methodology applied in the *SIESTA* calculations can be found in the Theory part 2.1.5 and in Ref. [109]. Despite the methodological differences between *VASP* and *SIESTA* the deviations between the obtained DOS of the system are negligible.[65]

XCrysDen[110] was used to plot unit cells and 3D charge rearrangements.

Gaussian03[130] was used to obtain the iso-density representations of the molecular orbitals. The double-zeta polarized basis set 6-31G(d,p)[180,181] was employed in conjunction with the Becke, Lee, Yang and Parr (B3LYP)[i] exchange-correlation functional.[30,31]

6.3.2 Structure of the system

The chemical structure of F_4TCNQ is shown in the Figure 28a. It is characterized by four electron withdrawing -CN groups at its extremities and four highly electronegative F atoms attached to the central ring. Moreover, in its charge neutral state, the central ring is distorted towards a quinoidal structure, which is known to further promote charge transfer through aromatic stabilization in the charged state.[182] When adsorbed on the (111) surfaces of Au and Ag, the F_4TCNQ molecules were arranged in two different surface unit cells corresponding to dense (monolayer) and loose (sub-monolayer) packing. The former is shown in Figure 28b and corresponds to a $\begin{pmatrix} 4 & -1 \\ 4 & 0 \end{pmatrix}$ surface unit cell. It has been observed experimentally for a F_4TCNQ monolayer on Au(111) by low temperature scanning tunneling microscopy (STM).[183][ii]

It is at least reasonable to assume a similar structure for densely packed F_4TCNQ on Ag(111), considering the virtually identical dimensions of the surface unit cells of Au(111) and Ag (111). To the best of our knowledge, no low energy electron diffraction (LEED) or low-temperature STM data that would allow an unambiguous determination of the adsorption structure are available for F_4TCNQ on Ag(111). For studying loosely packed layers, a $(3\sqrt{3} \times 5)$ cell as shown in Figure 28c has been chosen. In the densely packed monolayer, the long molecular axes are parallel to the $< 11\bar{2} >$ direction consistent with the above mentioned experiments.[183] In loosely packed layers, the molecular orientation is not known. Therefore, we have first aligned the molecules along the $< 1\bar{1}0 >$ direction[176] and then rotated them in steps of 30 degrees until they pointed in the $< 11\bar{2} >$ direction.[iii] Maximum variations in the induced work-function

[i] Test calculations using the PW91 exchange-correlation functional were made as well. As they do not change the conclusions drawn here only the values for the B3LYP calculations are reported as they are known to be better for isolated molecules.

[ii] That this arrangement is a reasonable one was tested for Au(111) and Ag(111) as there the simulated STM images could be compared to the measured ones. Overall they showed reasonable good agreement. The results are shown in a later section 9.2

[iii] The $< 11\bar{2} >$ direction was fully optimized and single-point calculations on the rotated molecules were performed for the other setups. Moreover comparisons of different fully optimized setups on

change were only around 0.05 eV. Therefore, to ease comparison with the data in Ref. [176], the molecules were aligned parallel to the $< 1\bar{1}0 >$ direction. This setup will be discussed in the following for low coverages.

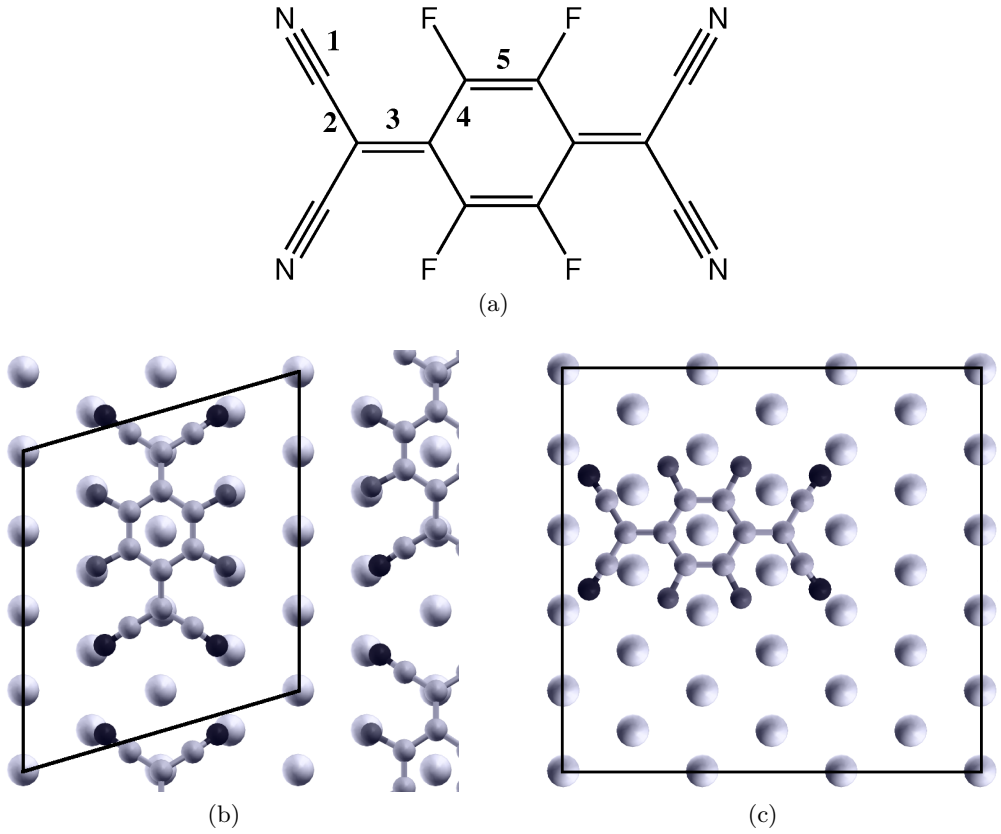

Figure 28: a) Chemical structure of F4TCNQ. b) Experimentally suggested unit cell for F4TCNQ on Au (111), which is used here also on Ag(111). The long molecular axis of F4TCNQ is parallel to the $< 11\bar{2} >$ direction. c) Loosely packed F4TCNQ molecules on Ag(111) in analogy to the structure on Cu(111) as studied in Ref. [176]. The long molecular axis is parallel to the $< 1\bar{1}0 >$ direction. Only the top metal layer and the molecule are shown for reasons of clarity.

For the Cu(111) surface, only the loose-packing geometry is studied, as the Cu lattice constant is by about 14% shorter than that of Ag and Au. This rules out adopting the experimental unit cell found on Au(111) (*vide supra*), as this would result in unrealistically small inter-atomic distances on Cu(111). The nitrogen-nitrogen distance, for example, would be 2.90 $\AA$ which is smaller than the sum of their van der Waals radii (approx. 3.1 $\AA$). Such a situation would lead to a hugely overestimated bending of the molecules and, thus, to an unphysical situation. To the best of our knowledge, the actual surface structure of F_4TCNQ on Cu(111) has not yet been determined, and it is not even known whether a commensurate structure is formed at all.

Cu(111) and Au(111) did not show differences.

6.3.3 Experimental setup

Of primary interest was a photoemission study of F_4TCNQ on Ag(111), as for this system experimental data are scarce.[170] Hence, the experiments presented in the chapter were performed at the *FLIPPER II* end-station at HASYLAB (Hamburg, Germany).[184] The interconnected sample preparation chambers (base pressure $4 \times 10^{-10} mbar$) and analysis chamber (base pressure $2 \times 10^{-10} mbar$) allowed sample transfer without breaking ultrahigh vacuum conditions. The Ag(111) single crystal substrate was cleaned by repeated cycles of annealing (up to $550\,°C$) and Ar-ion sputtering. F_4TCNQ (Fluka) was evaporated using a resistively heated pinhole source, at an evaporation rate of ca. $1\,\frac{Å}{min}$. The film mass thickness was monitored with a quartz-crystal microbalance. For all thickness values reported hereafter, identical sticking coefficients of the molecules on the metal substrate and on the microbalance were assumed. While the former can be expected to be close to unity, the sticking coefficient on the microbalance surface was most likely smaller, as it was pre-covered with other organic molecules from other experiments. This results in an underestimation of the actual F_4TCNQ layer mass-thickness on the metal substrate. Moreover, no detailed information on the growth mode of F_4TCNQ on Ag(111) is available, thus island-growth cannot be excluded, particularly for thicker films. Spectra were recorded with a double-pass cylindrical mirror analyzer with an energy resolution of $200\,meV$. The photon energy was $22\,eV$. The secondary electron cut-off (SECO) was measured with the sample biased at $-3.00\,V$. The errors of all given values of binding energies and SECO positions are estimated to be $\pm 0.05\,eV$.

6.4 Results and discussion

Prior to discussing the packing density dependence of the electronic structure as well as how the choice of the substrate metal affects the interaction, the general scenario encountered for F_4TCNQ adsorption is discussed for a densely packed layer on Ag(111).

6.4.1 Densely packed F4TCNQ on Ag(111): interface energetics

Similar to its precursor 7,7,8,8-tetracyanoquinodimethane (TCNQ)[185], in which all fluorine atoms are replaced by hydrogen atoms, F_4TCNQ is known to adopt a fully planar and quinoidal structure in the gas phase or as a molecular crystal.[186] This situation changes dramatically upon adsorption on Ag(111): F_4TCNQ adopts a bent geometry with the nitrogen atoms $1.23\,Å$ closer to the top metal layer than the π-backbone, which indicates a strong attractive interaction between the -CN substituents and the metal surface.[iv]

The central ring is calculated to be $3.61\,Å$ above the top Ag layer. An equivalent situation is encountered for adsorption on the Au(111) and Cu(111) surfaces; the latter has been confirmed by X-ray standing wave (XSW) experiments albeit with a somewhat smaller bending than in the calculations.[176] Moreover, a distortion of the molecular skeleton from a quinoidal towards an aromatic structure is observed. This aromatic stabilization can be identified when comparing the bond length changes in Table 8.

[iv] This is an important issue which will be analyzed separately later in the chapter about intramolecular changes of F_4TCNQ upon adsorption 10.1.2

The geometric distortions are comparable to those of reduced TCNQ [187] and are a first indication for charging of the molecule.

Table 8: Bond lengths upon adsorption of F4TCNQ on Ag(111) in the dense monolayer setup. The bond length of the *isolated* F4TCNQ molecules and the *adsorbed* F4TCNQ monolayer and their differences are given. The numbering of the bonds listed in the second column is shown in Figure 28a.

Bond	Number	$r_{\text{isolated}}\,/\mathring{A}$	$r_{\text{adsorbed}}\,/\mathring{A}$	$\Delta r\,/\mathring{A}$
$N \equiv N$	1	1.19	1.20	+0.01
$C - C$	2	1.43	1.40	-0.03
$C = C$	3	1.40	1.46	+0.06
$C - C$	4	1.44	1.41	-0.03
$C = C$	5	1.37	1.39	+0.03

The particularly electron affinity (EA) of F_4TCNQ ($3.68\,eV$ for the vertical EA and $3.81\,eV$ for the adiabatic EA)[v] implies that such charge transfer should correspond to filling the lowest unoccupied molecular orbital (LUMO) orbital of F_4TCNQ, which in the non-interacting case would lie below the Fermi level of the metal. Indeed, a more or less complete filling of the LUMO with approximately two electrons has been suggested on the basis of ultra-violet photoemission spectroscopy (UPS) measurements. [167,170] The inconsistency in this picture is, however, that moving two electrons from the top metal layer by about $3\,\mathring{A}$ to the molecular π-system would result in a dipole moment of $6\,e\mathring{A}$, 29 Debye(D), per molecule. According to the Helmholtz equation, this would result in a work function increase by approximately $9\,eV$ for a densely packed layer. This is not only unrealistically large and also inconsistent with the UPS data, but would also shift the energetic levels of F_4TCNQ in a way that the (now filled) LUMO would come to lie significantly above the metal Fermi level - and, thus, should not be occupied at all. These considerations imply that the charge transfer between Ag and F_4TCNQ as well as the resulting work-function modification are significantly more complex than expected and, therefore, deserve a more in-depth investigation.

The actually calculated electron potential energy for the Ag slab prior to (dashed line) and subsequent to F_4TCNQ adsorption (solid line) is shown in the left part of Figure 29.

[v] Both EA values were obtained using *GAUSSIAN03* at the 6-31G(d, p) level. The adiabatic EA allows the structure in the excited level to relax whereas the vertical EA does not take this into account.

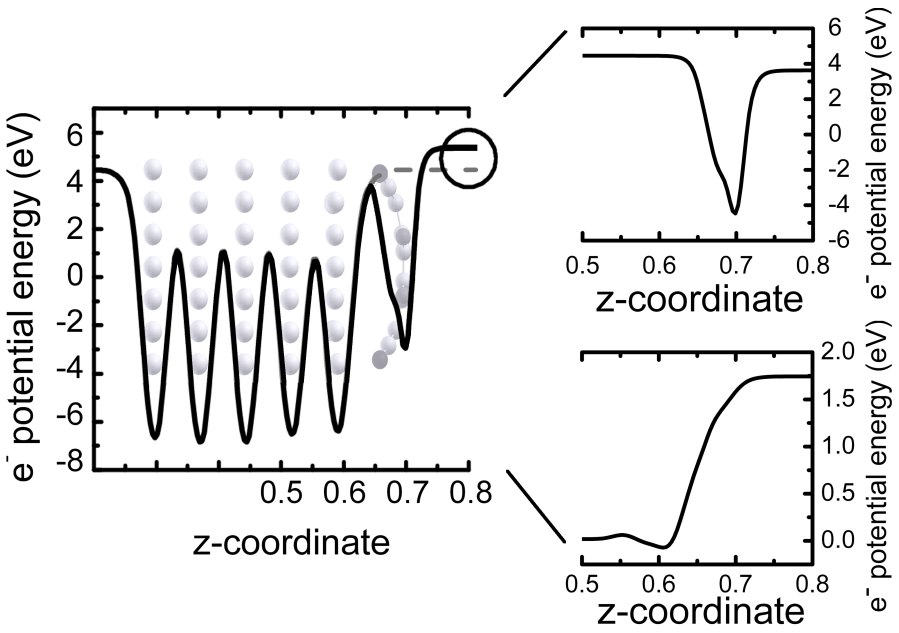

Figure 29: Energetics of the adsorption of F_4TCNQ on Ag(111) as a densely packed monolayer. Left: Plane averaged electron potential energy of the acceptor metal system in its final, fully relaxed structure (solid line) and plane averaged potential energy of the metal slab alone (dashed line). The structure of the system is shown in the background as a guide to the eye. The two energies significantly differ only in the region where the acceptor molecule is adsorbed; in particular, the energy above the slab is shifted by the adsorbate. The circle highlights the work-function modification of upon adsorption of F_4TCNQ. The latter results from a superposition of the effects plotted to the right. Right - Top: Plane averaged electron potential energy of the F_4TCNQ monolayer in its final structure (but without the metal present). Right - Bottom: The effect of the charge rearrangements on the electron potential energy landscape. The z-range in the two right graphs is limited compared to the left plot to ease the comparison of all three figures.

Upon adsorption, an increase of the electron potential energy is clearly visible on the F_4TCNQ side of the slab (as indicated by the circle). This corresponds to a work-function increase of $+0.85\,eV$. In analogy to the situation for thiolate-bonded self-assembled monolayers the work-function modification can be partitioned into a 'molecular' contribution, ΔE_{vac}, and a contribution due to the interfacial charge rearrangement (usually referred to as bond dipole (BD)), compare 47:[89,131]

$$\Delta\phi = BD + \Delta E_{\text{vac}} \tag{57}$$

'Molecular contribution' here means the possible impact of the molecular monolayer that is not associated with charge transfer from/to the metal. When adsorbing (di)polar molecules, it is related to the molecular dipole moment perpendicular to the surface.

Such an (infinitely) extended dipole layer results in a shift of the vacuum level by

$$\Delta E_{\text{vac}} = \frac{1}{\varepsilon_0 A}\mu \tag{58}$$

μ refers to the dipole moment per molecule in the monolayer (including, e.g., depolarization effects),[111,142] ε_0 is the vacuum permittivity, and A is the area per molecule. In the present case, the situation is insofar less straightforward, as isolated F_4TCNQ molecules do not possess any dipole moment (they are centrosymmetric). However, as discussed above, this changes due to adsorption. In the distorted conformation of the monolayer, each individual F_4TCNQ molecule possesses a dipole moment of $-2.62\,D$.[vi] I.e., it points away from the metal surface. ΔE_{vac} can, therefore, be regarded as the contribution to the work-function change that results from the adsorption induced geometric distortion of the F_4TCNQ molecules. However, if it were the only constituent of $\Delta\phi$, F_4TCNQ adsorption would result in a work function decrease by $-0.82\,eV$ on Ag(111). This can also be seen in the top right part of Figure 29, which shows the electron potential energy calculated for the F_4TCNQ monolayer in the absence of the metal but in the geometry the molecules will adopt following adsorption.

In addition to the distortion, the interaction between Ag and F_4TCNQ, however, results in significant interfacial charge rearrangements. They can be extracted from our calculations by subtracting the charge densities of the non-interacting systems, i.e., the Ag slab, $\rho_{Ag(111)}$, and the monolayer, ρ_{mono},[vii] from that of the combined system, ρ.

$$\Delta\,\rho_{\text{bond}}(\boldsymbol{r}) = \rho(\boldsymbol{r}) - \left(\rho_{\text{Ag(111)}}(\boldsymbol{r}) + \rho_{\text{mono}}(\boldsymbol{r})\right) \tag{59}$$

All charge densities are calculated self-consistently for the individual sub-systems in the geometries they eventually adopt in the combined Ag/F_4TCNQ system. As discussed above, the effects resulting from geometry changes of the monolayer are already accounted for in ΔE_{vac}. The resulting charge rearrangements then result in a modification of the potential energy landscape for the electrons that can be derived from the Poisson equation:

$$\nabla^2 E_{\text{bond}}(\boldsymbol{r}) = \frac{e}{\epsilon_0}\,\Delta\,\rho_{\text{bond}}(\boldsymbol{r}) \tag{60}$$

The values integrated over the x-y plane, $E(z)$, are shown in the bottom right part of Figure 29. In this way, the contribution of the interfacial charge rearrangements to the change in the system work function [corresponding to BD in Equation 58] is obtained; it amounts to $+1.68\,eV$. Consequently, the charge rearrangements result in a pronounced increase of the work function, as expected for the adsorption of a strong acceptor like F_4TCNQ. The net effect, i.e., the sum of ΔE_{vac} [Equation 58] and BD [see Equation 58], is a work-function increase by $+0.85\,eV$. Hence, the geometric distortions upon adsorption compensate half of the charge-transfer effect. This implies that geometry changes have to be kept in mind when designing new acceptor materials

[vi] This value is obtained for calculations of the monolayer in its final geometry in the absence of the metal substrate.

[vii] Here, the slab and the monolayer are considered both in their final geometries that they will assume in the combined system; this is necessary, as the impact of the adsorption induced geometric distortions has already been accounted for by ΔE_{vac}.

for surface modifications. Still, both $\Delta\phi$ with $+0.85\,eV$ as well as BD with $+1.68\,eV$, are significantly smaller than the values estimated from simple electrostatic considerations based on doubly occupying the molecular LUMO (*vide supra*). This makes it necessary to investigate the charge rearrangements at the interface in more detail.

6.4.2 Charge rearrangements at the interface

Contour plots of the charge rearrangements upon adsorption calculated using Equation 59 are shown in Figure 30 together with an iso-density representation of the LUMO orbital of the isolated molecule (to avoid confusions, the sign of the wave function is not considered in the latter case).

In Figures 30a and 30b, electrons flow from the dark to the light gray areas. By comparing these charge rearrangements with the shape of the LUMO orbital of the isolated F_4TCNQ molecule in Figure 30c, electron transfer into the LUMO can be unambiguously confirmed. The regions of electron accumulation are concentrated on those bonds that are shortened upon adsorption (cf., Table 8 and Figure 28a). The electron density on the metal is clearly decreased (dark area) - in particular, right underneath the -CN substituents of F_4TCNQ. Moreover, there is also a pronounced electron depletion in the π-system in the -CN regions, whose origin will become clear when discussing changes in the orbital occupation of F_4TCNQ upon adsorption.

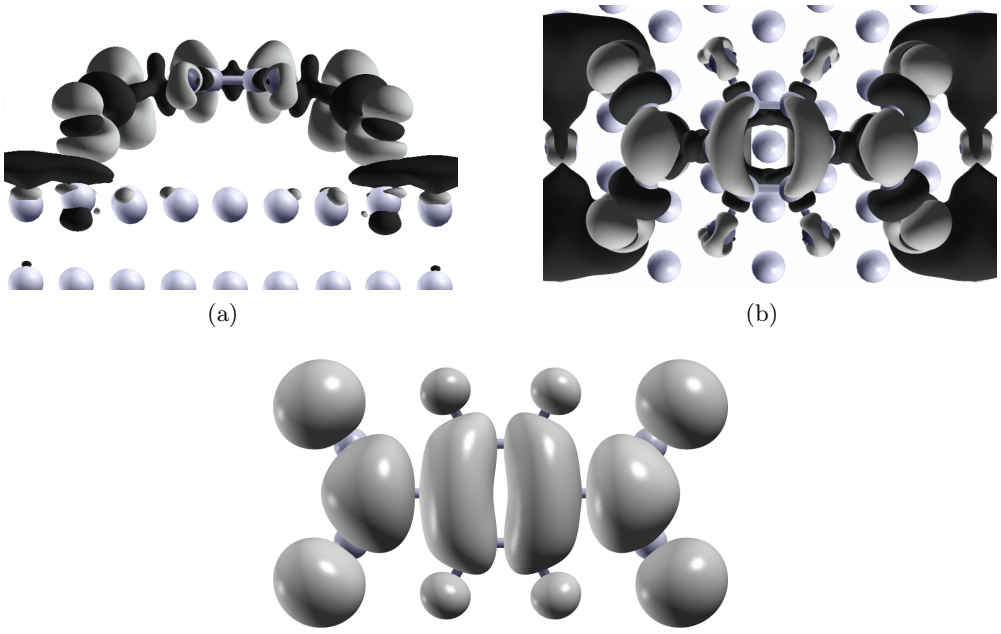

Figure 30: From top to bottom: a) Side and b) top view of the 3-dimensional charge density rearrangements for F4TCNQ adsorption on Ag(111) (dense packing). Electrons flow from the dark gray to the light gray areas. In a) only the top two metal rows are shown; in b) only the top metal layer is shown. In c) the molecular LUMO of F4TCNQ is displayed (note that the unlike usually done when plotting molecular orbitals, no difference in shading is used to denotes the phase of the wave function to avoid confusions). An isovalue of 0.01 electrons per $\mathring{A}^3$ was used for the 3D charge density plots and 0.01 electrons per Bohr^3 for the LUMO representation.

Prior to that, the charge rearrangement integrated over the x-y plane within a unit cell, $\Delta\rho_{\text{bond}}(z)$, needs to be discussed. It provides some additional insight into changes in the charge density and allows an easy comparison of charge rearrangements obtained at different packing densities or for different substrate metals (as discussed in later sections of this paper). First of all, $\Delta\rho_{\text{bond}}(z)$ shown in the top part of Figure 31 confirms the increased electron density in the π-electron region of F_4TCNQ as well as a pronounced electron depletion directly above the top metal layer. The charge rearrangements within the metal slab are confined to the immediate interface region; the electron density in the bottom three layers is virtually unaffected by the presence of the adsorbate. A 'dip' in $\Delta\rho_{\text{bond}}(z)$ in the region of the -CN substituents is also clearly resolved consistent with the decreased π-electron density in that part of the molecule.

To assess the total amount of transferred charge, it is useful to integrate $\Delta\rho_{\text{bond}}(z')$ over z' from below the slab to a certain position z, as done for the self-assembled monolayer (SAM) system previously, compare chapter 3.4.2 equation 45. This gives the quantity $Q_{\text{bond}}(z)$

$$Q_{\text{bond}}(z) = \int_0^z \Delta\,\rho_{\text{bond}}(z')\,dz'\,, \tag{61}$$

which is shown in the bottom part of Figure 31 for a F_4TCNQ monolayer on Ag(111).

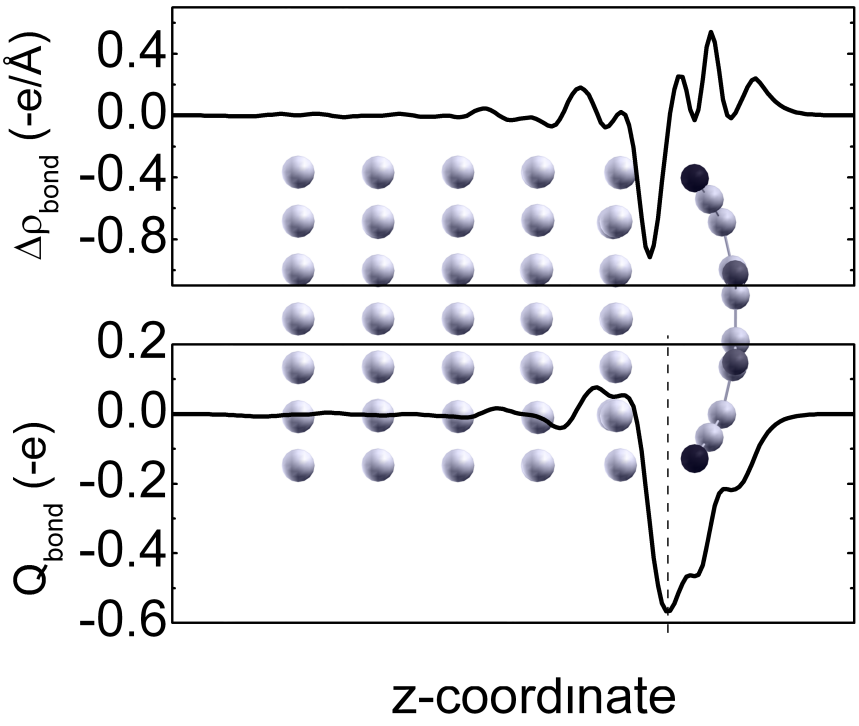

Figure 31: Top: charge density rearrangement, $\Delta, \rho_{\text{bond}}$, upon adsorption of a densely packed F4TCNQ monolayer on a Ag(111) surface integrated over the x-y plane within the unit cell; Bottom: resulting total charge transferred, Q_{bond}. The vertical line denotes the maximum value of Q_{bond} (details see text). The structure of the combined system is shown in the background as a guide to the eye. Note that e corresponds to the (positive) elementary charge. Hence, with the unit of the y-axis being (-e/$\mathring{A}$), positive y-values correspond to electron accumulation (i.e., charge depletion) and negative values to electron depletion (i.e., charge accumulation).

$Q_{\text{bond}}(z)$ gives the charge shifted from the region below a plane at position z to the region above z. It steeply decreases above the metal plane (electron depletion), reaches a minimum (dashed line in Figure 31) and then increases in the region of the molecule (electron accumulation) reaching zero above the molecular layer (as imposed by the condition of overall charge neutrality). It displays the clear signature of electron transfer from the metal to F_4TCNQ. There is no unambiguous way to determine the actual amount of that transfer, as no clear distinction between the spatial region associated with the molecule and the metal is possible. Here, we define the maximum value of $Q_{\text{bond}}(z)$ as the amount of transferred charge. For a monolayer of F_4TCNQ it amounts to 0.55 electrons per molecule. In the following, we will compare that value to the charge transfer obtained from a more conventional (but usually more ambiguous) atomic-orbital

based partitioning scheme.

Alternatively to analyzing the charge rearrangements due to bond formation in real space, one can describe them in a molecular orbital picture. In this way, the question can be addressed which of the molecular orbitals looses or gains electrons as a result of the interaction with the metal. In this context, it is important to point out that such changes in orbital occupation can also be fractional. This is because upon contact with the metal, molecular and metal states hybridize and such hybrid bands can be partially occupied. This is especially expected for states close to the Fermi level. An elegant way to trace down such effects for the metal-organic interface is to project the DOS onto the molecular orbitals of the non-interacting adsorbate layer (i.e. the molecular layer with no metal present).[1,63,64,73,112] This allows assigning contributions to the total DOS to specific molecular orbitals. Here, we use the definition of the molecular-orbital projected DOS (molecular orbital density of states (MODOS)) previously introduced in chapter 3.4.4.

$$\mathrm{MODOS_m(E)} = \sum_{\mathrm{i,l},\boldsymbol{k}} \mathrm{c^M_{i,m,\boldsymbol{k}}}^{*}\, \mathrm{c^M_{i,l,\boldsymbol{k}}}\, \hat{\mathrm{S}}_{\mathrm{m,l},\boldsymbol{k}}\, \delta(\mathrm{E} - \varepsilon_{\mathrm{i},\boldsymbol{k}}) \tag{62}$$

The $c^M_{i,m,\boldsymbol{k}}$ are the linear combination of molecular orbitals (LCMO) coefficients and $\hat{S}_{m,l,\boldsymbol{k}}$ is the overlap matrix of the molecular orbitals (MOs) (for further details see Ref. [1]). The MODOS can, for instance, be used to determine how a particular MO is aligned with respect to the Fermi level even in the case of strong hybridization between metal and molecular states. This is shown for selected MOs in Figure 32 for F_4TCNQ on Ag(111). The molecular part to the total DOS (MDOS) of the system is shown in the bottom curve. In the displayed energy range, it can be partitioned into contributions from the LUMO, the highest occupied molecular orbital (HOMO), and the HOMO-1. One observes that the molecular LUMO is clearly responsible for the peak in the DOS just below the Fermi edge. The broadening of the respective MODOS-features is a measure for the hybridization of the corresponding molecular state with metal orbitals (on top of the 'external' broadening here set to $0.1\,eV$ when plotting the DOS).

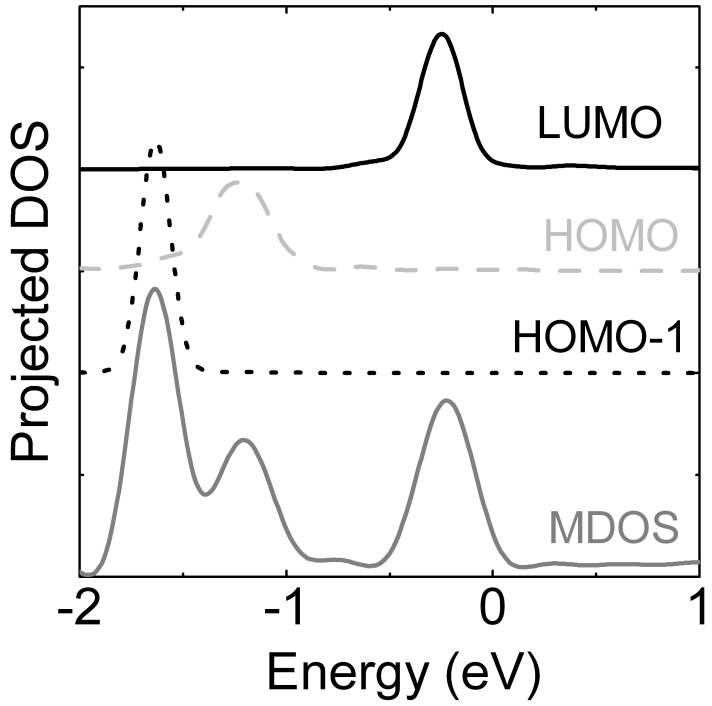

Figure 32: Partitioning of the DOS of F_4TCNQ on Ag(111) into contributions from individual molecular orbitals. From top to bottom: contribution of the molecular LUMO, the molecular HOMO, and the molecular HOMO-1; bottom: MDOS, i.e. the total molecular contribution. The Fermi energy is chosen as the origin of the energy axis.

By integrating the *MODOS* associated with a particular molecular orbital, m, up to the Fermi energy, one can obtain a nominal occupation, O_m, of that orbital, compare equation 49 in chapter 3.4.4.

$$O_m = \int_{-\infty}^{E_f} \mathrm{MODOS_m(E)\,dE} \tag{63}$$

This then allows analyzing the bonding-induced charge transfer for each individual orbital, as shown in Figure 33 for the densely-packed F_4TCNQ monolayer on Ag(111).

One can clearly see that - as a consequence of the interfacial charge transfer - the LUMO is almost completely filled (filling of 89 %, i.e., by approx. 1.8 electrons). This is in agreement with the conclusions drawn before from the real-space charge-transfer picture in Figure 30. At the same time, however, four deeper lying orbitals (HOMO-9 to HOMO-12) have significantly lost electrons. They can be identified as σ-orbitals largely localized on the -CN groups. These orbitals strongly participate in the bonding of the F_4TCNQ molecule to the substrate, as can also be inferred from the bending of the molecule. The reason, why nominally deep lying rather than frontier orbitals are

responsible for that σ-electron transfer lies in their particularly strong hybridization with the metal states.[176] In some sense, one could thus consider the -CN groups as docking groups, strongly linking the F_4TCNQ layer to the Ag substrate.

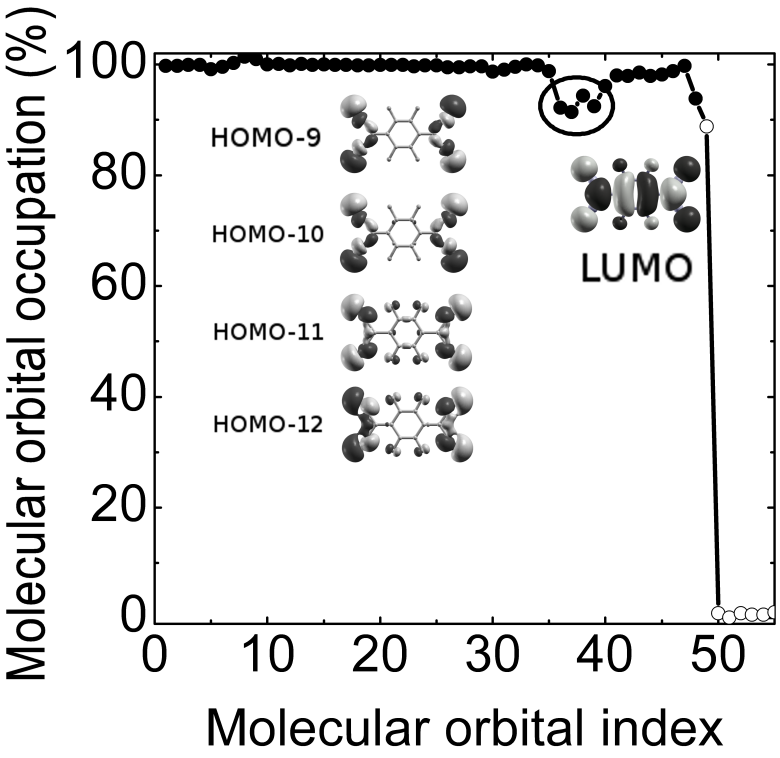

Figure 33: Molecular orbital population analysis for F4TCNQ adsorbed on Ag(111) in a dense monolayer. The bands derived from the isolated molecular system were taken as reference for the projection. The full (open) circles correspond to molecular orbitals occupied (unoccupied) prior to adsorption. The reason for some occupation numbers to be above 100% is a well known shortcoming of the adopted Mulliken population analysis.

This situation of charge forward and backward donation involving σ- and π-orbitals is reminiscent of the Blyholder model[188] applied, e.g., to the bonding of CO on various metals, such as Pt(111),[189,190] Cu(111),[190] Ag(111),[190] Au(111),[190] Al(111),[191] and Fe(100).[192]

6.4.3 Dependence of the electronic structure on the packing density

In this subsection, we analyze how the packing density of the F_4TCNQ layer influences the electronic properties of the Ag/F_4TCNQ interface. This is insofar interesting as, experimentally, a strong linear dependence of the F_4TCNQ induced work-function modification on the nominal coverage has been observed.[167,170] On the other hand, a

pronounced non-linear evolution with coverage has been discussed for $\Delta\phi$ and the level alignment for the adsorption of 4'-substituted 4-mercaptobiphenyls on Au(111).[111] Moreover, sub-monolayers of organic molecules on metals are interesting as they allow addressing the limiting case of isolated molecules on metals, an aspect of particular interest in the emerging field of molecular electronics.

Here, the effect of coverage is addressed by comparing the work-function modifications as well as its two contributions, BD and ΔE_{vac}, for the two unit cells shown in Figures 28b and 28c. Each unit cell contains one F_4TCNQ molecule. The unit cell for the loosely packed layer is nearly twice as big as in the densely packed case. $\Delta\phi$, ΔE_{vac}, and BD for the two packing densities are listed in Table 9. In addition to reporting the energies in eV, also the respective contributions to the z-components of the dipole moments per unit cell are given in Debye (D). The latter are useful, as they are independent of the unit cell size, and, therefore, ideal for addressing depolarization effects. The other values listed in Table 9 are the total transferred charge, Q_ρ, and the binding energy, E_{bind}, per molecule.[viii]

As far as the work-function modifications are concerned, one observes a slightly sub-linear increase with increasing the coverage (i.e., while the packing increases by a factor of 1.88, the work function increases by a factor of only 1.67). This also manifests itself in the dipole moment of the unit cell, which is $3.05\,D$ in the sub-monolayer coverage and is decreased to $2.59\,D$ (i.e., by 15%) for the monolayer coverage. This is a possible indication of depolarization effects in the densely packed layer; i.e., the neighboring bonding-induced dipoles reduce each other. Overall, this effect is relatively weak. To trace determine origin, it is useful to first analyze the evolutions of ΔE_{vac} and BD separately.

ΔE_{vac} changes only slightly (the ratio of the corresponding dipoles is computed to be 0.93). The reason for that lies in the almost identical geometrical structures in the monolayer and sub-monolayer cases on Ag(111). The nitrogen atoms of F_4TCNQ are located about $2.38\,\mathring{A}$ above the top metal surface in the monolayer setup. In the sub-monolayer case, they are located $2.39\,\mathring{A}$ above the metal surface. The central ring is located $1.19\,\mathring{A}$ above the nitrogen atoms in the former case and $1.20\,\mathring{a}$ in the latter case. Hence, the vertical adsorption distance and the bent are hardly affected by increasing the packing density.

BD, on the other hand, experiences slightly larger depolarization effects. The associated dipole moment decreases from $5.85\,D$ to $5.33\,D$ (i.e., by 9%) when going from sub-monolayer to monolayer coverage. Considering the origin of BD, this has to be a consequence of the adsorption-induced charge rearrangements, $\Delta\rho_{\text{bond}}(z)$. The total charge transferred, i.e., the maximum of Q_{bond}, is nearly the same for both packing densities; the shape of $\Delta\rho_{\text{bond}}(z)$, however, differs. Compared to the charge rearrangements shown for the densely packed case in Figure 31, at reduced coverage the electron accumulation is somewhat more pronounced in the area above the plane of the central ring and correspondingly reduced below the π-plane (plot not shown). As far as changes in the orbital population are concerned, the *MODOS* derived occupation of the *LUMO* is increased by about 10% in the sub-monolayer case. This is consistent with a shift

[viii] Here, the binding energy is calculated via subtraction of the metal slab energy and the F4TCNQ monolayer energy from the system energy in the same unit cells.

of the *LUMO* associated peak away from the metal Fermi level by $0.2\,eV$ as shown in Figure 34.

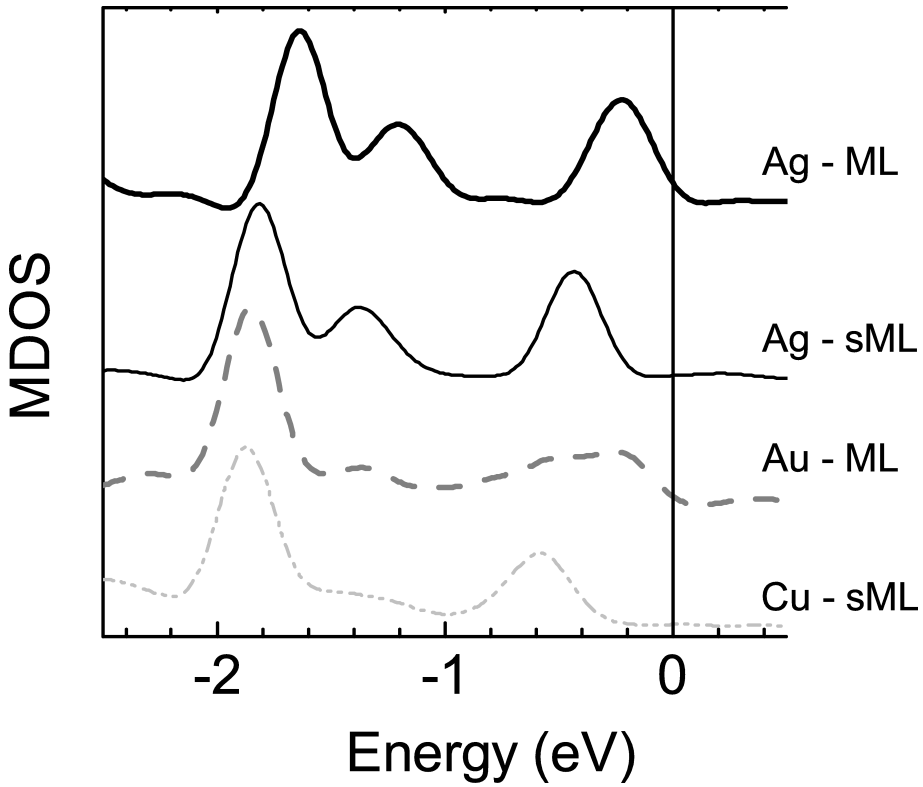

Figure 34: Calculated MDOS for F4TCNQ adsorbed on Ag(111) in the monolayer and sub-monolayer regimes, as well as for F4TCNQ on Au(111) at monolayer coverage and for a sub-monolayer F4TCNQ on Cu(111). The corresponding structures are chosen according to Figure 28b and 28c. The Fermi energy was chosen as the origin of the energy axis

A possible explanation for the relatively weak depolarization effects lies in the peculiar dipole distribution that arises due to the superposition of forward and backward donation processes. While the electron density is increased in the π-backbone, it is decreased on parts of the -CN groups (compare Figures 30 and 31). A simplified schematic representation of the resulting dipole structure is shown in Figure 35. A dipole pointing towards the metal surface can be associated locally with the -CN groups (σ-dipole). Another one pointing away from the metal will be delocalized over the whole π-system (π-dipole). At dense packing, the molecular rows are displaced with respect to each other on the surface. Therefore, the σ-dipoles pointing downwards in one row will come to lie close to the π-dipoles pointing upwards in the neighboring row. Therefore, the mutual depolarization of the π-dipoles is to some extent compensated by a dipole enhancement due to the interaction with the closer lying (albeit weaker) σ-dipoles.

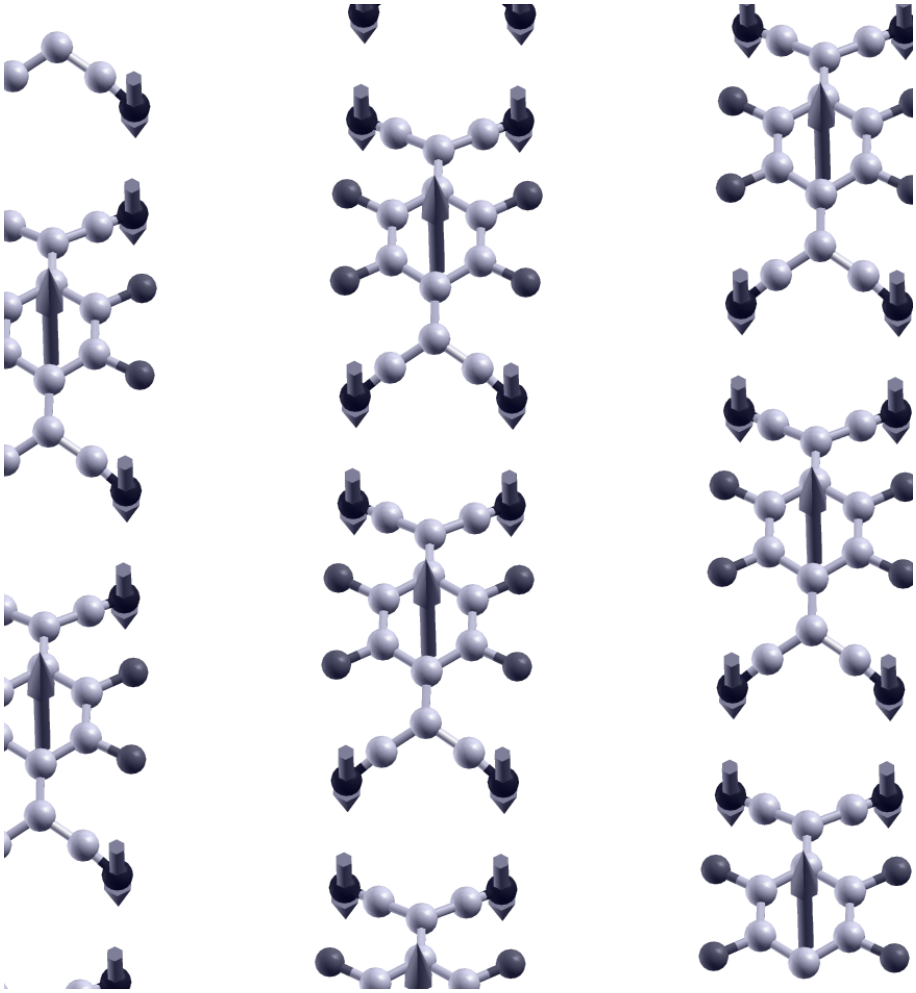

Figure 35: Dipole structure arising due to charge-transfer between F4TCNQ on Ag(111) at monolayer coverage. The metal atoms are not shown. The molecular rows are shifted relative to each other as observed experimentally.

What remains to be explained is why the biggest deviation from linear coverage dependence is observed for the work function modification: The reason for that is that $\Delta\Phi$ is obtained by subtracting ΔE_{vac} from the approximately twice as big *BD*. As the dipole moment associated with ΔE_{vac} remains nearly the same, an only slightly changing value is subtracted from the more strongly changing dipole associated with *BD*. Consequently, the relative changes in $\Delta\Phi$ are the strongest of all involved quantities.

6.4.4 Impact of the substrate metal

When comparing the role of different coinage metals as substrates, one has to distinguish between the low and high coverage case. The latter is accessible only for Au and Ag (see 6.3.2). The former is accessible for all coinage metals used in the present contribution including Cu(111). The (111) surfaces of those metals are characterized by significantly

different work functions. We calculated values of $5.25\,eV$ for Au(111) and $4.49\,eV$ for Ag (111), which are in excellent agreement with our measurements ($5.3\,eV$ [167] for pristine Au(111) and $4.5\,eV$ for Ag(111), our work]. The work function of Cu(111) is intermediate between Ag and Au and is calculated (measured) to be $\phi = 4.82\,eV$ ($4.9\,eV$) [193] for pristine Cu(111).

The work-function modification, $\Delta\Phi$, differs quite significantly for Ag and Au in the high-coverage regime and is distinctly bigger for Ag(111). The values are $+0.85\,eV$ for Ag and $+0.29\,eV$ for Au. This leads to both F4TNQ covered metals ending up with virtually identical work functions ($5.54\,eV$ for Au; $5.34\,eV$ for Ag). Such a trend is also observed both experimentally as well as theoretically for self-assembled thiolate monolayers on the same metals.[1,88,120] This means that F_4TCNQ exhibits a much greater influence on Ag, which again has to be related either to the monolayer contribution, ΔE_{vac} and/or differences in *BD* resulting from different interfacial charge rearrangements. From the corresponding values in Table 9, one can conclude that the monolayer contribution is, in fact, not responsible for the observed difference, as both ΔE_{vac} contributions differ only slightly ($-0.82\,eV$ for Ag and $-0.79\,eV$ for Au). This is again a consequence of very similar adsorption geometries: The nitrogen atoms are located $2.44\,\mathring{A}$ (Au), and, $2.38\,\mathring{A}$ (Ag) above the metal and also the adsorption distances of the central carbon atoms are very similar ($1.23\,\mathring{A}$ (Au) and $1.19\,\mathring{A}$ (Ag) above the nitrogen atoms). The charge rearrangements, however, differ to a much greater extent. The total charge transferred, Q_{bond}, is by more than 60% larger on Ag (111) (0.55 electrons on Ag versus 0.34 electrons on Au). As the arrangement of the molecules on the surface is assumed to be identical in both cases (see 6.3.2), considerations regarding dipole arrangements as discussed before for the packing-density dependence do not apply here.

Instead, as shown in Figure 36a, we find that more electron density is depleted between the top metal atoms and the plane of the nitrogen atoms in the Ag case. The extra electrons are, however, not shifted towards the top Ag layer, where they would give rise to an extra bond dipole that would decrease the metal work function. On the contrary, less electron density is accumulated in the top metal layer than in the Au(111) case. Instead, the electrons from the interfacial region of Ag/F_4TCNQ are to a distinctly larger extent transferred onto the F_4TCNQ acceptor layer than it is the case of the Au/F_4TCNQ system. This phenomenon is visualized in Figure 36b.

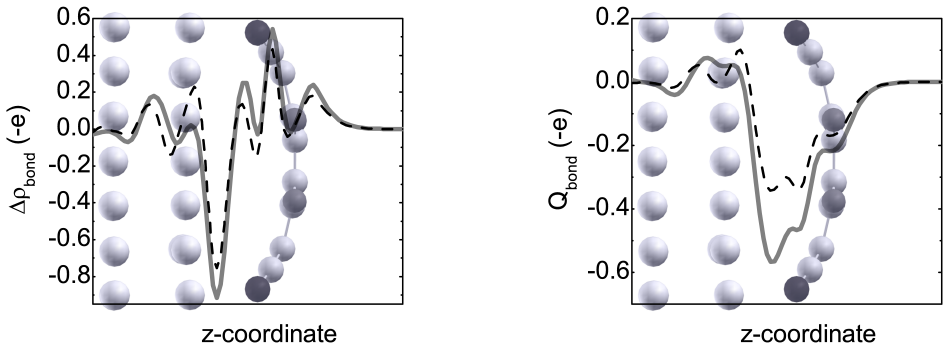

(a) (b)

Figure 36: a) Comparison of charge rearrangements, $\Delta, \rho_{\text{bond}}$, for densely packed layers of F4TCNQ adsorbed on Ag(111), (solid gray), and Au(111), (dashed black). b) Comparison of the total transferred charges, Q_{bond}. The structure of the molecules on Ag(111) is shown in the background as a guide to the eye. Note that e corresponds to the (positive) elementary charge. Hence, with the unit of the y-axis being (-e/$\AA$), positive y-values correspond to electron accumulation (i.e., charge depletion) and negative values to electron depletion (i.e., charge accumulation).

Interestingly, the difference between the work functions of the pristine substrates is compensated by the charge rearrangements also as far as the level alignments are concerned. Hence, the molecular LUMO derived peaks are pinned at about $0.3\,eV$ below the Fermi level in both cases (Figure 34). Another indication for the stronger interaction of F_4TCNQ with Ag(111) compared to Au(111) is the significantly larger binding energy in the former case ($2.6\,eV$ compared to $0.9\,eV$).[ix]

The situation is somewhat different for adsorption on Cu(111), which for the reasons discussed in the methodology section could only be studied in the low coverage regime.[x] The monolayer contribution, ΔE_{vac}, on Cu(111) distinctively differs from the two other metals. In fact, it is almost twice as big in the Cu case ($-0.82\,eV$) as in the corresponding Ag case ($-0.47\,eV$). This is the consequence of a stronger bend of the molecule on Cu(111). In this context it, however, needs to be mentioned that a comparison between DFT-based calculations and XSW experiments[176] indicates that the bent of F_4TCNQ on Cu(111) is somewhat overestimated by the calculations. To what extent this is a general shortcoming of local DFT functionals due to their inability to describe van der Waals interactions or a problem related to the description of the Cu surface cannot be clearly decided at the moment, as, to the best of our knowledge, no XSW data for F_4TCNQ adsorbed on other coinage metals are available. The *BD* associated with the F_4TCNQ sub-monolayer on Cu(111) is virtually the same as on Ag(111) ($1.01\,eV$ in the Cu case and $0.98\,eV$ for Ag), indicating that a similar amount of charge is transferred.

[ix] Here, the binding energy is calculated via subtraction of the metal slab energy and the F4TCNQ monolayer energy from the system energy in the same unit cells.

[x] Small numerical deviations compared to the numbers reported in Ref. [176] are due to the fact that here we described the substrate by five metal layers, compared to four layers in our previous study. This slightly changes the numbers but affects the qualitative conclusions in no way.

As far as the F_4TCNQ sub-monolayer on Au is concerned, the expected picture evolves for the charge transfer, i.e., the total transferred charge is very similar to the densely packed situation and the dipole moment of the unit cell hardly changes with coverage. The values of *BD* increase close to linearly with the packing density. The adsorption geometry, however, significantly differs from all other investigated cases: The bending is strongly reduced and, thus, ΔE_{vac} decreases with the net effect of $\Delta\Phi$ being slightly larger in the sub-monolayer than in the monolayer case. This behavior is quite unexpected and its origin is not fully understood. Bearing in mind that the calculated binding energy is very low, it also cannot be entirely excluded, that it is at least in part a consequence of the applied methodology that, for example, does not take into account van der Waals interactions.[xi]

6.4.5 Comparison between the theoretical predictions and experimental data

In this section physical observables derived from calculations, such as the adsorption induced work-function modifications, $\Delta\Phi$, and the energetic positions of the molecular levels, will be compared to experimental UPS data. We will primarily focus on F_4TCNQ on Ag(111) and present new experimental data. Experimental data for F_4TCNQ on (albeit polycrystalline) Au are taken from Ref. [167]. For the case of F_4TCNQ on Cu(111), a detailed comparison between theory and experiments can be found in Ref. [176].

[xi] Note that the here presented results stem from a local minimum in the energy, where the F4TCNQ is adsorbed flat, i.e., a slight perturbation results in a twist of the molecule along its long molecular axis which is an energetically favored configuration.

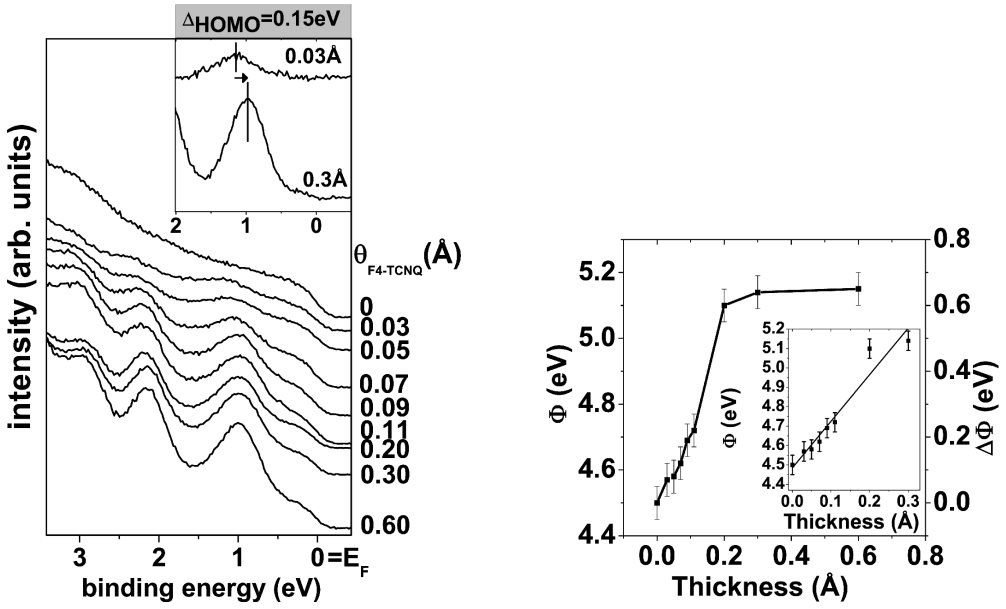

(a) (b)

Figure 37: a) Near Fermi energy region UPS spectra of pristine Ag(111) and after sequential deposition of F4TCNQ. Photoemission features induced by F4TCNQ are clearly visible are at ca. $1.0\,eV$ and $2.2\,eV$ binding energy. Monolayer coverage is expected to occur at a nominal coverage of ca. 0.3 to 0.6 $\AA$. The inset shows the LUMO-derived peak for 0.03 and 0.3 $\AA$ coverage after subtraction of appropriately weighted pristine Ag(111) spectra. b) Work function, Φ, and work-function modification, $\Delta\Phi$, upon adsorption of F4TCNQ on Ag(111). The inset shows the sub-monolayer regime in more detail. The line is a linear fit to the data points from 0.03 to 0.3 $\AA$ coverage.

Figure 37a contains valence-region UPS spectra of pristine Ag(111) and subsequently deposited F_4TCNQ for nominal coverages up to 0.6 $\AA$. Upon F_4TCNQ adsorption, a distinctive feature appears in the lowest coverage spectrum at $1.15\,eV$ binding energy (BE) at a coverage of 0.03 $\AA$. In analogy to the situation on Au[167] and Cu[176], it can be identified as the formerly unoccupied LUMO of the neutral molecule, which has been filled as a result of the interfacial charge transfer and thus lies now clearly below EF. With subsequent deposition of F_4TCNQ the LUMO-derived peak shifts towards lower BE, reaching a final position of $1.00\,eV$ at 0.3 $\AA$. This is in good agreement with the theoretical results presented above, where a shift of the LUMO-derived feature of $0.20\,eV$ towards lower BE was predicted at sub-monolayer coverages (6.4.3). The features at higher BE can be associated with the HOMO and HOMO-1 derived peaks from Figure 32 (using the nomenclature appropriate for the neutral molecule). The HOMO-derived peak exhibits the same shift as that derived from LUMO and reaches a final position at $2.15\,eV$ BE. Qualitatively, the agreement between the calculated density of states and the measured UPS spectra is reasonably good; the spacing between the peaks is, however, clearly larger in the experiments.[xii] This is not unexpected bearing in mind

[xii] Note that here especially the peak associated with the filled former LUMO is emerging too close to the Fermi energy in the calculation.

that gradient-corrected functionals typically yield a too small spacing between molecular orbitals. This can, e.g., be inferred from comparing Kohn-Sham eigenvalues with quasi-particle excitation energies.[194–196] It is, therefore, common practice to expand the calculated spectra by multiplying them with a constant factor.[197,198] Furthermore, variations in the experimental spectra are observed when recording them at different angles,[199–201] an effect that is not accounted for in the presented calculations, in which UPS cross-sections are not considered. Moreover, especially at sub-monolayer coverage the actual film-structure is not known and in the actually investigated samples deviations from the assumed ideal structure might play a prominent role.

As shown in Figure 37b, the sample work function Φ increases almost linearly with coverage from $4.5\,eV$ [pristine Ag(111)] to about $5.15\,eV$ at a nominal coverage of $0.3\,\mathring{A}$ [see inset in Figure 37b]. At higher coverages, the work function remains virtually constant. Based on this finding, a nominal coverage of around 0.3 to $0.6\,\mathring{A}$ can be associated with almost full monolayer coverage. The measured maximum work function increase of about $0.65\,eV$ for F_4TCNQ on Ag(111) agrees very well with the calculated $\Delta\Phi$ value of $0.85\,eV$ for the densely packed monolayer, especially considering that the calculations assume a completely covered and perfectly ordered layer.

As far as the linear coverage dependence is concerned, two scenarios can be envisioned: One would be a gradual decrease of the average spacing between the adsorbate molecules with increasing coverage in analogy to the observation for tetrathiofulvalene (TTF) on Au(111).[177] There the structure arises from mutual electrostatic repulsion of the adsorbate molecules, which are charged as a result of the molecule to metal electron transfer. In that case, a close to linear increase of $\Delta\Phi$ with the F_4TCNQ surface density can be rationalized on the basis of the results of 6.4.3. Alternatively, also the formation of (small) F_4TCNQ clusters, whose size and/or density increases with coverage would result in a close to linear work-function increase.

A linear evolution of $\Delta\Phi$ with coverage has also been observed on (polycrystalline) Au.[167] With $\Delta\Phi = 0.35\,eV$, the net effect is, however, much smaller than on Ag, again in excellent agreement with the calculations, which predict a work-function increase of only $0.29\,eV$ for a densely packed F_4TCNQ layer on Au(111) (cf. Table 9).

Table 9: Area of the unit cell, work function modification $\Delta\Phi$, distortion induced change in the electrostatic energy, ΔE_{vac}, bond dipole (BD), 'total' transferred charge, Q_{bond}, and binding energy, E_{bind}. The values for $\Delta\Phi$, ΔE_{vac}, and BD are given in eV as well as in Debye, where the former refers to the actual energy and latter denotes the corresponding unit cell dipole moment. All quantities are listed for F4TCNQ on Ag(111) and Au(111) in monolayer as well as sub-monolayer coverage (cf. Figure 28); for adsorption on Cu(111) only the values for sub-monolayer coverage have been calculated (cf., methodology section 6.3). The ratios of all values for different coverages are also given.

Metal	Area ($\AA$)	$\Delta\Phi$(eV)/(D)	ΔE_{vac}(eV)/(D)	BD (eV)/(D)	Q_{bond}(e)	E_{bind}(eV)
Ag_{ML}	120	**0.85**/2.59	**-0.82**/-2.62	**1.68**/5.33	0.55	2.61
Ag_{subML}	225	**0.51**/3.05	**-0.47**/-2.81	**0.98**/5.85	0.55	1.90
Ratio	1.88	**1.67**/0.85	**1.74**/0.93	**1.71**/0.91	1.00	1.37
Au_{ML}	121	**0.29**/0.93	**-0.79**/-2.55	**1.07**/3.46	0.34	0.90
Au_{subML}	226	**0.33**/1.98	**-0.33**/-1.98	**0.66**/4.01	0.38	0.75
Ratio	1.87	**0.88**/0.47	**2.39**/1.29	**1.62**/0.86	0.89	1.20
Cu_{subML}	172	**0.19**/1.13	**-0.82**/-4.88	**1.01**/6.00	0.44	2.70

6.5 Summary and conclusions

This section 6 provided a comprehensive theoretical description of the adsorption of the prototypical strong acceptor F_4TCNQ on coinage metals. Such systems are particularly interesting as electrodes in organic (opto)electronic devices, as their work functions can be continuously tuned over a wide range. We find that the work-function increase due to the F_4TCNQ layer originates from a subtle interplay between a molecular dipole resulting from bonding-induced distortions of the adsorbate and a bond dipole stemming from the interfacial charge transfer. The latter is a superposition of electron transfer from the metal into the π^*-LUMO and back-transfer from σ-states localized on the -CN substituents. This can be inferred, on the one hand, from an analysis of the real-space charge rearrangements and, on the other hand, from a projection of the molecular density of states onto the bands derived from the individual molecular orbitals (MODOS).

Comparing the electronic structure of a system with full- and ca. half-monolayer packing on Ag(111), cf. subsection 6.4.3, it is found that depolarization effects play an only minor role in the investigated system. A possible explanation for that is the peculiar arrangement of opposing dipoles as a result of the monolayer structure. Furthermore, weak depolarization is fully consistent with the experimentally observed linear dependence of the metal work function on F_4TCNQ coverage.

Another interesting observation is that when covered by a densely packed F_4TCNQ monolayer, the work functions of Au(111) and Ag(111) become similar despite the fact that the pristine work function of a pristine Au(111) surface is by ca. $0.7-0.8\,eV$ larger than that of a Ag(111) surface. This is found to be primarily a consequence of the much larger net electron transfer from Ag to F_4TCNQ, cf. subsection 6.4.4.

The results of the calculations agree well with new experimental data on Ag(111), cf. subsection 6.4.5, and also previously published experimental results. This supports the validity of the developed detailed microscopic model for the electronic properties of the

interfaces that is otherwise largely based on the quantum-mechanical modeling.

7 A particularly strong organic acceptor for tuning the hole-injection barriers in modern organic devices.

7.1 Foreword

A better understanding of metal/organic interfaces combined with means to control their properties is crucial for the further improvement of organic (opto)electronic devices. In this context, the use of organic acceptors is an efficient tool to modify metal work functions and hole-injection barriers (HIBs), which has the potential to considerably improve the performance of organic devices.

Here, we present a particularly potent acceptor suitable for that purpose, namely 3,5--difluoro-2,5,7,7,8,8-hexacyanoquinodimethane (F_2HCNQ). It clearly outperforms the frequently applied and in the meantime prototypical system 2,3,5,6-tetrafluoro-7,7,8,8-tetracyanoquinodimethane (F_4TCNQ), intensively studied in a previous chapter 6. This makes F_2HCNQ a highly promising candidate for applications in organic devices.

This part follows a submitted paper by Rangger Gerold M., Hofmann Oliver T., Bröker Benjamin, and Zojer Egbert. The paper has recently (Jan. 2010) been sent to Synthetic Metals.

7.2 Introduction

Modern organic devices play an ever increasing role in our daily life. The advantages of using organic semiconductors as alternatives to inorganic semiconductors include, amongst others, their mechanical flexibility, their low cost thin-film processability and their low weight. Hereby, the physical and chemical processes occurring at metal/organic interfaces crucially determine the device performance and have attracted considerable attention in recent years.[149,152–154] Successful strategies have been demonstrated to tune the alignment between the metal Fermi level and the molecular states and, thus, decisively influence the carrier-injection across metal-organic interfaces. These include the use of covalently bonded self-assembled monolayers,[123,131,144,162,202] redox-doping of the organic layers,[164,165] or the deposition of (sub)monolayers of strong electron acceptors[166,167,169,170,183,203] (or donors[159,171,172,204,205]), which are known to form charge transfer complexes with the underlying metal. In this part of the thesis, a particularly strong organic acceptor for tuning metal work functions is suggested. Hereby, it is found out that it has the potential to surpass all systems described so far.

A particularly potent and in the meantime a prototypical organic acceptor is F_4TCNQ. The structural formula is shown in Figure 38a. This potent acceptor and its affect on coinage metals has already been extensively reviewed within this thesis, see 6. Here, I want to summarize the literature dealing with F_4TCNQ used to somehow modify interfaces.

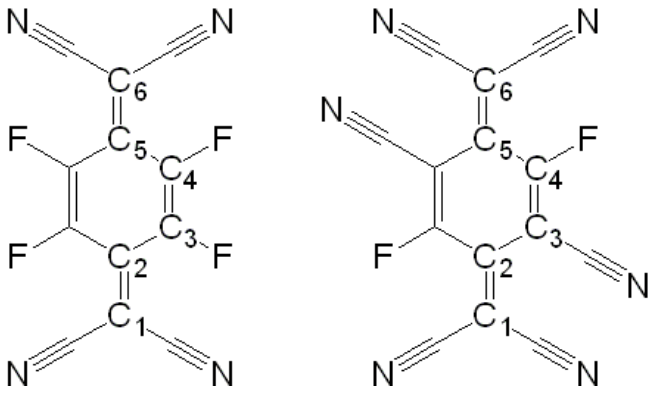

Figure 38: a) Chemical structure of F_4TCNQ (2,3,5,6-tetrafluoro-7,7,8,8-tetracyanoquinodimethane). b) Chemical structure of F_2HCNQ (3,5-difluoro-2,5,7,7,8,8-hexacyanoquinodimethane). The numbering of the bonds will be needed for Figure 40.

It has been shown that spontaneous charge transfer to a F_4TCNQ layer occurs from a variety of substrates, such as Au(111),[4,167] Ag(111),[4,183] Cu(111),[4,176] hydrogenated diamond (100),[206] and 2-methylpropene saturated Si(100)(2x1) surface.[207] Hence, by incorporation of F_4TCNQ a controlled tuning of the hole concentration of single-wall carbon nanotubes field effect transistors[208] and organic semiconductors using zinc-phthalocyanine[209,210] has been successfully demonstrated. Moreover, F_4TCNQ possesses the ability to significantly improve the efficiencies of organic light emitting diodes[211,212] A variation of the F_4TCNQ coverage even allows a continuous tuning of the HIB over a wide range.[4,167,170]

A common factor increasing the HIBs of the interface between the metal electrode and an organic semiconductor is Pauli repulsion,[149] as it always reduces the work function of the electrode. This can be quite significant; for example, for the adsorption of (inert) alkane chains on Au, Ag and Pb work-function reductions of up to about (0.7 ± 0.2) eV (Au), (0.5 ± 0.1) eV (Ag), (0.3 ± 0.1) eV (Ob) have been reported.[179] This effect can be avoided (or at least mitigated) by incorporating an interfacial layer consisting of a strong organic acceptor between the metal and the semiconductor.[166,167,175]

Also from a fundamental point of view an F_4TCNQ adsorbate layer is interesting. It has, for example, been shown recently in combined theoretical and experimental studies that the actually achieved work-function modification originates from a subtle interplay between charge forward and backward transfer processes combined with molecular dipole moments due to the adsorption induced distortion of the molecules.[4,176]

One of the complications encountered when using F_4TCNQ doped hole-injection layers is that F_4TCNQ molecules are relatively volatile and diffuse easily throughout organic layers.[166,213] In this context, a derivative of F_4TCNQ suggested by Gao et al.[214] appears as an interesting alternative, as it shows increased molecular weight and furthermore superior thermal stability as shown by thermal gravimetric analysis attributed to its asymmetric structure:[214] In F_2HCNQ, see Figure 38b, two of the fluorine atoms at the ring are replaced by cyano groups. Accordingly, the deposition temperatures

of F_4TCNQ and F_2HCNQ as a function of deposition rates were studied. There, the enhanced thermal stability of F_2HCNQ was approved as it shows increased deposition temperature per rate.[214] Cyclic voltametry measurements indicated an increased electron affinity (EA) of F_2HCNQ (see below). This furthermore indicates that also when deposited on surfaces the properties of F_2HCNQ should be superior to those of F_4TCNQ.

In the following, we use density functional theory (DFT) based quantum-mechanical calculations to first compare the molecular properties of individual F_4TCNQ and F_2HCNQ molecules. The main focus of the present work, however, lies on predicting and understanding the electronic structure of a densely packed F_2HCNQ monolayer on a Ag(111) surface. Ag as a substrate is of particular interest as, on the one hand it has the lowest work function amongst the coinage metals and is thus most "in need" of techniques that help reducing HIBs. On the other hand, the strong chemisorptions of 7,7,8,8--tetracyanoquinodimethane (TCNQ) based molecules on Ag(111)[4] reduces the impact of methodological shortcomings of DFT in the description of dispersion forces. Thus giving the most reliable results of our description (see below). To analyze the details of the interface electronic structure, the induced work-function modification is, as in the previous chapters, split into a contribution from interfacial charge transfer and the impact of the molecular distortion in the monolayer. Additionally, the interplay between charge forward and backward transfer processes will be briefly reviewed (cf. chapter 6 of this thesis and Refs. [176 and 4]). Particular emphasis will be put on understanding, why F_2HCNQ outperforms F_4TCNQ. A last point will discuss the impact of the monolayer packing density.

7.3 Methodology

7.3.1 Computational methodology

Basically, "the same" methodology was applied as previously 3.3 and 6.3.1. Nonetheless, I want to briefly write the computational details for the sake of completeness. As usual DFT based band structure calculations using the plane-wave code *VASP*[38,39] version 4.6.2636, within the framework of the generalized gradient approximation (GGA) using the Perdew-Wang 1991 (PW91) exchange-correlation functional[53,54] were applied. For all projections of the density of states onto atomic orbitals the atomic orbital based code *SIESTA* version 2.0.239 was used.[45] To model interfaces, a slab-type approach has been used, where the F_2HCNQ monolayer is put onto a 5 layer slab out of silver with a plane wave cutoff energy of 20 Ryd. Due to the periodic boundary conditions, this corresponds to a surface infinitely extended in the x- and y-directions (for unit cell specifications see below); in z-direction the slabs are separated by more than 20 $\AA$ of empty space. For the two different unit cell sizes (*vide supra*) two different Monkhorst pack[33] k-point grids were taken. Therefore, for the smaller a (4x4x1) and for the larger unit cell in real space a (3x3x1) k-point grid was applied. For calculations of the isolated molecules in a supercell the unit-cell size in real space was modified in a way to use a (1x1x1) k-point grid, i.e. the x and y axis were multiplied by 4 to avoid basis set superposition errors. For all calculations a second order Methfessel-Paxton occupation scheme[34] with a broadening of 0.2 eV was used. The systems were relaxed in a way that all atoms except the bottom three metal layers were allowed to relax until the

remaining forces were below $0.01\frac{eV}{\mathring{A}}$. Using *VASP*, to obtain the molecular density of states (MDOS) each Kohn-Sham orbital was projected onto spherical harmonics inside spheres surrounding each atom and weighted accordingly. All calculations were done spin unrestricted.

One general shortcoming of DFT calculations with local functionals that has to be kept in mind here is that such functionals cannot properly account for van der Waals type interactions, cf. 2.1.3 This primarily impacts adsorption geometries and binding energies. It has, however, been shown that for a given adsorption geometry, the choice of the functional has no significant impact on the charge transfer at the interface.[215] For a strongly chemisorbed systems (F_4TCNQ on Cu(111)) it has even been shown in a combined theoretical and experimental study[176] that the DFT calculations reasonably well reproduce the adsorption distances determined by the X-ray standing wave (XSW) method. However, as far as the adsorption energies are concerned, their absolute values are certainly underestimated. For example, using non-local functional to model the bonding of 3,4,9,10-perylene-tetracarboxylicdianhydride (PTCDA) on Ag(111) the van der Waals contributions to the binding energy have been estimated to amount to about 3 eV.[215] However, as we are here concerned only with binding energy differences between the relatively similar molecules F_4TCNQ and F_2HCNQ (i.e., we are dealing with molecules with similar numbers of electrons and comparable polarizabilities and thus very similar van der Waals attractions), this should be of only minor significance for the drawn conclusions. In fact, as F_2HCNQ is characterized by a larger π-system than F_4TCNQ, including van der Waals interactions would only increase the differences in binding energies; i.e., the stronger bonding of F_2HCNQ predicted here can be regarded a lower limit to the actual effect.

3D representations of the interface structures as well as charge rearrangement plots were produced using XCrysDen.[110] For calculating the properties of individual molecules including molecular vibrations Gaussian03[130] is used in conjunction with the PW91 and the B3LYP45 exchange-correlation functional with a 6-31+G* basis set.[180,181]

7.3.2 Structure of the system

To the best of our knowledge, no experimental characterization of F_2HCNQ on metal surfaces is available. In particular, no information on the experimental surface unit cell for F_2HCNQ on Ag(111) exists.[i] The most closely related system, for which an experimentally determined unit cell is available from low temperature scanning tunneling microscopy (STM) measurements is F_4TCNQ on Au(111).[183] There, a $\begin{pmatrix} 4 & -1 \\ 4 & 0 \end{pmatrix}$ unit cell has been determined.[183] Following the procedure from Ref. [4], we assumed the same packing as for F_4TCNQ on Au(111) also for F_2HCNQ on Ag(111) (see Figure 39a). This is necessary, as a periodic structure commensurate between metal surface and the adsorbate layer is needed as a consequence of the periodic boundary conditions in the band-structure calculations. The above assumption is, in fact, justified by the

[i] Ag(111) has proved itself to be the most reliable metal for analyzing metal/acceptor systems, adopting our theoretical approaches, in terms of agreement with the experiment.

relatively similar sizes of the molecules and the virtually identical lattice constants of Au and Ag.

To study the impact of coverage and to elucidate the role of depolarization effects in the closely packed film, F_2HCNQ was additionally put in a loose sub-monolayer packing considering one molecule in a $((3\sqrt{3} \times 5))$ unit cell as used previously in theoretical studies using F_4TCNQ[4,176], Figure 39b. This unit cell roughly corresponds to half a monolayer coverage. In both setups the long molecular axes are parallel to the $< 1\bar{1}0 >$ direction.[ii]

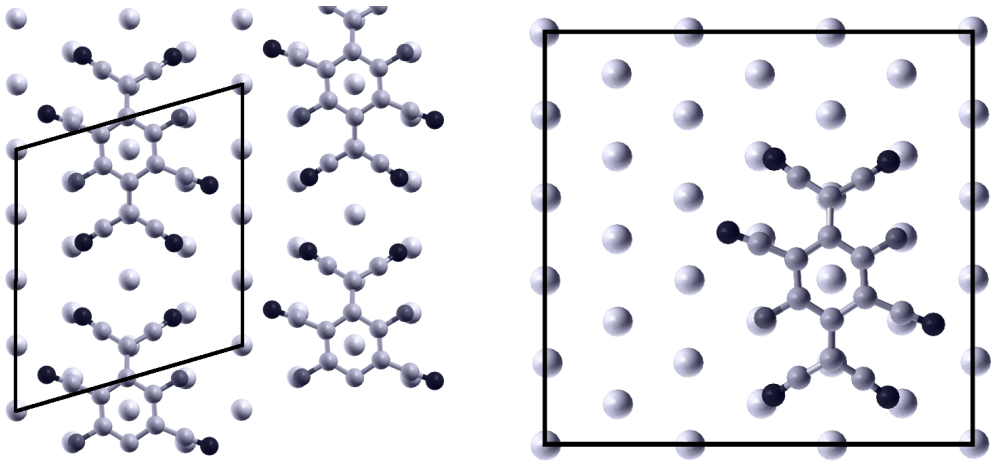

(a) (b)

Figure 39: a) Monolayer setup for F_2HCNQ on Ag (111). b) Sub-monolayer setup for F_2HCNQ on Ag(111). The black lines mark the respective unit-cells. Note, that only the top metal layer and the molecule are shown for reasons of clarity.

7.4 Results and discussion

7.4.1 Molecular properties

F_4TCNQ and F_2HCNQ possess the same core with two of the fluorine atoms of F_4TCNQ replaced by cyano groups in F_2HCNQ. The effect on the molecules' electronic structure can be estimated from the Swain-Lupton constants[216], which divide the total effect of substitution as given by Hammetts constant into a mesomeric (R) and an inductive (F) part. In fluorine, both constants are of similar size, but have opposite signs (R = -0.39, F = 0.45)[217]. Therefore, fluorine works as a moderate electron withdrawing group, with the effect being mitigated when the atom is strongly coupled to the π-system. For cyano groups both contributions are of electron withdrawing nature, and the inductive effect is stronger than that of fluorine (R= 0.15, F = 0.51)[217]. Consequently, the -CN groups possess a stronger electron withdrawing character and F_2HCNQ is a stronger electron acceptor. This is also evidenced by its electron affinity calculated to be 0.44

[ii] In Ref[4] the orientation in the loose sub-monolayer packing was $< 11\bar{2} >$. There, it was tested that the results and conclusions drawn therefore also hold for the $< 1\bar{1}0 >$ direction.

eV lower (F_4TCNQ: -4.12 eV; F_2HCNQ: -4.47 eV).[iii] This results are in very good agreement with the cyclovoltametry measurements of Gao et al,[214] which find the first reduction peak of F_2HCNQ at -5.59 V and hence distinctively deeper lying than the one of F_4TCNQ, -5.33V (the different absolute values between theory and experiment result primarily from the neglect of solvent effects in the calculations).[214]

The bond-length pattern of the molecular backbone in Figure 40 hints towards a quinoidal character of both molecules. This results in extra energy gain upon charge transfer due to an aromatic stabilization of the ring and is one of the reasons for both molecules' high potential as electron acceptors.[182] The bond-length changes are, however, only minor and confined to the bonds in direct proximity of the CN-substituents, which are both elongated.

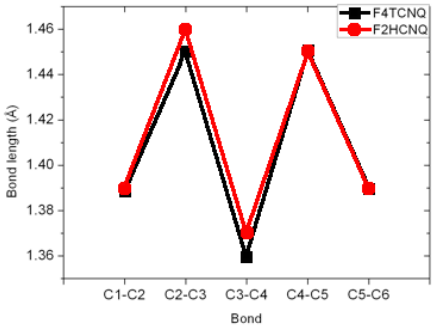

Figure 40: Differences in the bond-length alternation pattern of the two acceptor molecules in the isolated case; F_4TCNQ (black squares) and F_2HCNQ (red circles). For the numbering of the bonds refer to Figure 38.

7.4.2 The F_2HCNQ monolayer adsorbed on a Ag(111) surface

Upon contact between a strong acceptors and a metal, one typically observes electron transfer from the metal to the molecular layer.[149] This results in an at least partial filling of the lowest originally unoccupied band of the acceptor layer. For example, a nearly complete filling of the lowest unoccupied molecular orbital (LUMO)-derived band in F_4TCNQ has been observed experimentally on Ag,[4,170] Au[167] as well as Cu[176] and was backed up by theoretical studies[4,176]. Note that especially in Ref. [4] a detailed extensive study including an analysis of the origin of all the physical processes at the interface of F_4TCNQ and Ag(111) can be found. Common of F_4TCNQ on all coinage metals is that partial charge transfer into the molecular LUMO and important in that context, back transfer from deeper lying molecular orbitals was described (*vide infra*). These fractional occupations arise from the fact that, upon contact with the metal, the molecular bands hybridize with the metal states and only parts of the resulting states are occupied in the combined system. One strong argument in favor of

[iii] The corresponding Becke, Lee, Yang and Parr (B3LYP) values are F_4TCNQ: -4.12 eV; F_2HCNQ: -4.56 eV

fractional occupancies is that a completely filling the LUMO derived band (i.e., transferring two electrons per molecule from the metal to the F_2HCNQ layer) would result in an unrealistically high dipole moment of 29 Debye per molecule-metal charge transfer complex.[iv] According to the Helmholtz equation, for a densely packed layer such a dipole would result in a work-function increase by approximately 9 eV. This would shift the molecular levels up in energy in a way that the LUMO would lie far above the Fermi level again. This however, would be inconsistent with what is to be expected in thermodynamic equilibrium.

This puzzle has been first resolved for F_4TCNQ on Cu(111), for which it has been shown that the electron transfer from the metal to the molecular π-system is to a large extent compensated by local back transfer of σ-electrons from the four terminal -CN groups.[176]

For F_2HCNQ, due to its even stronger acceptor character and deeper lying LUMO level of the isolated molecule (*vide supra*), one might expect an even more pronounced charge transfer into the molecular LUMO compared to F_4TCNQ. At this point, however, the question arises to what extent this effect is compensated by stronger back transfer involving the additional -CN groups.

Work-function modification for the monolayer packing The potential energy change due charge rearrangements upon bond formation, ΔE_{BD}, is not the only contribution to the adsorbate-induced work-function modification. Additionally, the adsorption also results in a significant distortion of the molecule as it was shown for F_4TCNQ on Ag, Au and Cu previously.[4,176] This results in breaking its inversion symmetry and providing it with a dipole moment perpendicular to the metal surface as the -CN groups are bending towards the surface.[4,176] From the Helmholtz equation it follows that this results in an additional contribution to the work-function modification (ΔE_{vac}) that, actually, counteracts the impact of the interfacial charge rearrangements. Thus, the net-effect of the adsorbate layer can conceptually be partitioned into these two contributions, cf. equation 57, 47 or Refs. [89,131]

$$\Delta\phi = \Delta E_{\mathrm{BD}} + \Delta E_{\mathrm{vac}}, \tag{64}$$

where ΔE_{BD} is a consequence of the bond dipole, i.e., it reflects the energetic changes due to the charge rearrangements, and ΔE_{vac} refers to the impact of the bonding-induced geometric distortion of the molecule. The latter can be obtained from the distorted F_2HCNQ monolayer in the absence of the metal and the former is calculated from the difference of the charge densities of the systems before and after contact.

Interestingly, the emerging dipole moment perpendicular to the surface leading to ΔE_{vac} is almost identical for both molecules, namely -2.59 Debye for F_4TCNQ versus -2.58 Debye for F_2HCNQ (corresponding to ΔE_{vac}'s of -0.85 eV and -0.83 eV). This is insofar not straightforward as the geometry induced dipole moment in the adsorbed F_4TCNQ molecule originates from the downwards bent terminal cyano groups. Thus, one might have expected a similar contribution from the two additional cyano groups at the central ring. What is, however, observed in the calculations is that the latter substituents stay virtually in the plane of the ring 3.60 $\AA$ above the top Ag layer (compared

[iv] Here, we assume that the molecule and the metal are approximately 3 $\AA$ apart.

to 3.65 $\AA$ for the ring and 2.28 $\AA$ for the N atoms in the terminal cyano groups).[v]

The also experimentally observed bending down of the outer cyano groups [109] is a consequence of the interaction of the N-lone pairs with the metal surface. The bent is energetically favorable because it corresponds to a relatively soft geometric degree of freedom as can be inferred from an analysis of the vibrational eigenmodes of the isolated molecules (note that the actual distortion can be understood as a superposition of these eigenmodes): The out of plane vibration in F_4TCNQ with all -CN groups displaced in phase is calculated at only 33 cm^{-1}. In F_2HCNQ the low-energy vibrational spectrum is complicated by the lower symmetry of the molecule. Still, at 17 cm^{-1} a vibration is observed in which all terminal -CN groups move to one side of the ring (the central cyano groups are actually displaced to the other side of the ring for this vibration). Vibrations in which all six cyano groups oscillate in phase are found only at much higher energies, namely, at 74 cm^{-1} and 149 cm^{-1}. This indicates that displacing all cyano substituents to the same side of the molecular plane is energetically significantly more costly and rationalizes why such a bending conformation is not observed. A more quantitative explanation would require the calculation of the vibrational spectrum of the adsorbed molecule. This is, however, computationally extremely demanding.

As far as the charge rearrangements are concerned, a more pronounced impact of the extra -CN groups is observed for adsorbing F_2HCNQ. ΔE_{BD} is calculated to be 1.84 eV and thus by approximately 10% larger than the 1.68 eV for F_4TCNQ adsorption. A first impression of the charge transfer processes can be gained from the 3-dimensional charge density rearrangements shown for F_2HCNQ on Ag(111) in Figure 41 - the corresponding plots for F_4TCNQ can be found in an earlier chapter 6.4.2.

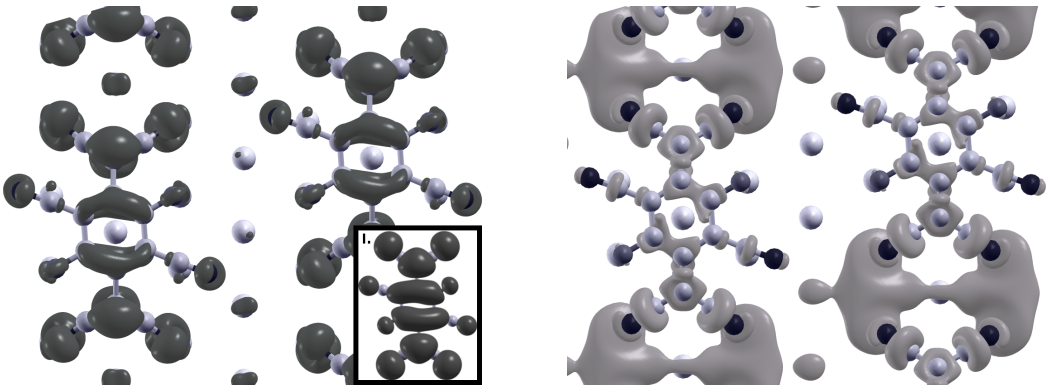

(a) (b)

Figure 41: Top view of the 3D charge-density rearrangements of F_2HCNQ on Ag(111). In a), the dark areas represent the area of electron accumulation. The inset I. shows the representation of the molecular LUMO. In b), the bright areas represent the area of electron depletion. (Iso-value 0.01 electrons per $\AA^3$)

Figure 41a shows the electron accumulation and 41b the areas of electron density

[v] A biased geometry optimization where the cyano groups of the ring were manually placed bent towards the metal returned in the optimized structure with the ring cyano groups almost perfectly in the plane of the ring.

depletion. Electron density is shifted from the regions depicted in Figure 41b to those of Figure 41a upon adsorption of F_2HCNQ. The region of electron density accumulation is reminiscent of the shape of the molecular LUMO shown as inset in Figure 41a. This finding is consistent with the filling of the LUMO already observed for F_4TCNQ. Hence, the π-electron system of the F_2HCNQ layer gains electron density (charge forward donation). Electron density depletion on the other hand affects both the π-region of the metal as well as the σ-system of F_2HCNQ. In particular, the electron density in the region of the -CN triple bond is decreased for the outer substituents. It is, however, not observed for the cyano groups directly attached to the ring indicating that the latter do not significantly contribute to the electron back-transfer that limits the work-function increase. This can be explained by the larger distance of the respective cyano orbitals from the metal surface as they do not bend towards the Ag(111) surface as discussed above.

The differences compared to the charge rearrangements for F_4TCNQ adsorption (cf., chapter 6.4.2) are shown in Figure 42. Hereby, Figures 42a, 42c and 42e display the regions to which more electrons are transferred in the case of F_2HCNQ compared to F_4TCNQ. Figures 42b, 42d and 42f highlight the areas where less electron density is transferred. These plots indicate that in F_2HCNQ there is slightly more electron transfer to the π-system below the plane of the molecule, while there is slightly less to the region directly above the molecular plane. There is also less electron transfer to the region below the nitrogen atoms in the terminal -CN groups and the electron transfer to the nitrogen atoms in the -CN groups attached to the central ring compensates the transfer to the replaced fluorine atoms.

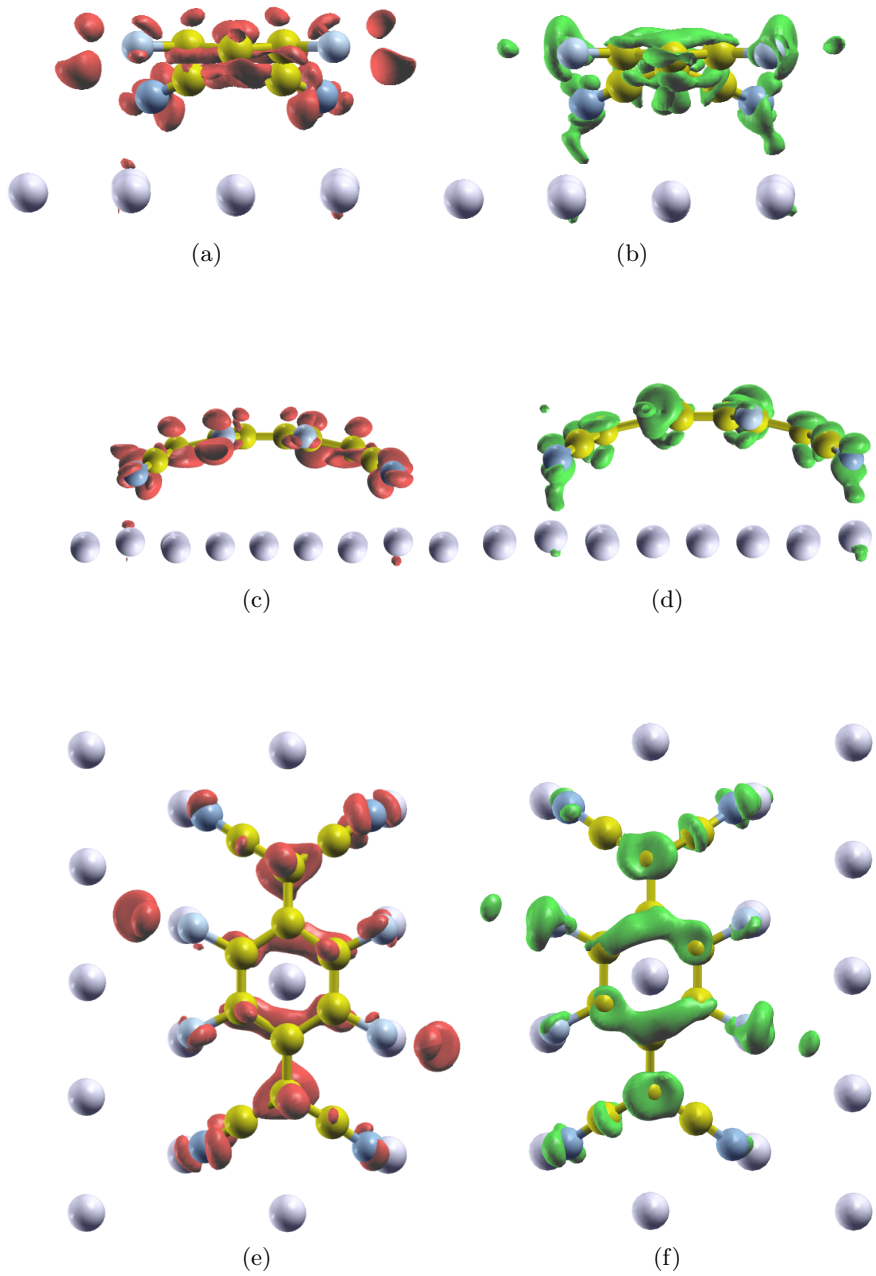

Figure 42: a, c and e show different views of increased electron accumulation for F_2HCNQ compared to F_4TCNQ on Ag(111). b, d and f show different views on areas of decreased electron accumulation for F_4TCNQ compared to F_2HCNQ on Ag(111). View angles from top to bottom: View along the long molecular axis; view along the short molecular axis, top view. (Iso-value for all plots 0.01 electrons per $\mathring{A}^3$) The F_4TCNQ molecule is also shown as guide to the eye indicating the position of the molecules.

All this is also seen in the differences of the charge densities rearrangements integrated over the xy-plane of the unit cell shown in Figure 43a. The main features can be identified herein. The depletion of electron density above the top metal layer being somewhat stronger for F_2HCNQ is visible. This indicates a slightly larger net transfer from the metal to the molecule. Furthermore, the electron accumulation in the π-planes above and below what roughly corresponds to the molecular plane, and a "dip" in the accumulation below the plane in the region of the outer cyano groups can be seen. In the region of the cyano substituents directly attached to the central ring, only a small shoulder is visible supporting the notion of no significant σ-back transfer from those -CN groups.

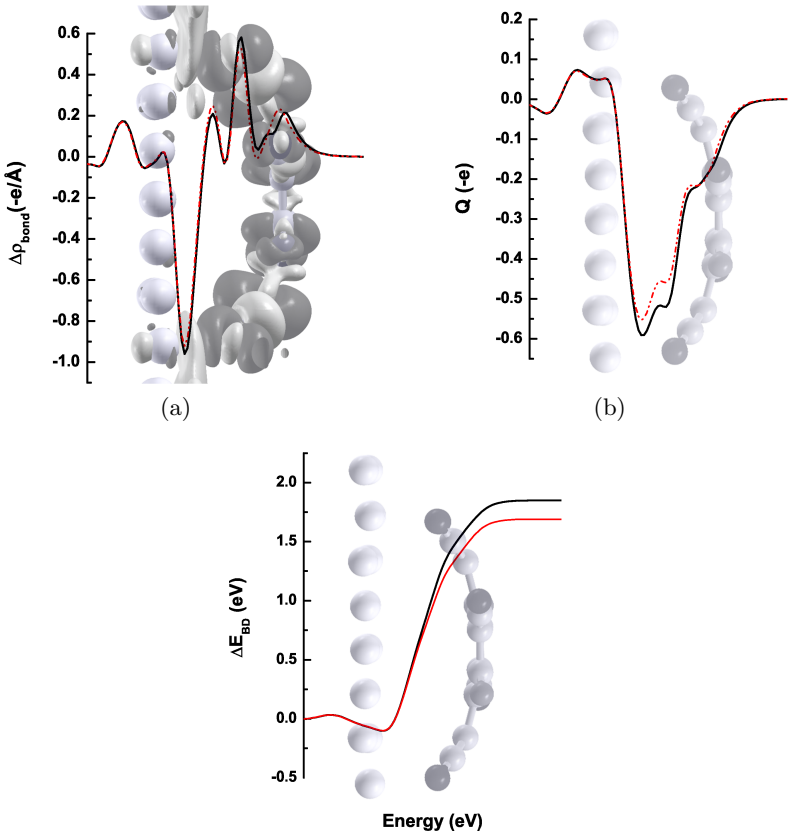

Figure 43: (a) Plane integrated charge density rearrangements of F_2HCNQ and F_4TCNQ on Ag(111). (b) Total charge transferred for both systems as a function of the position z. (c) Effect of the charge rearrangements onto the potential energy landscape of the electrons. In all cases, the solid (black) line represents the curves for F_2HCNQ and the dashed (red) line F_4TCNQ. In (a), the 3D charge rearrangements of F_2HCNQ are shown in the background as guide to the eye. Dark areas represent an area of electron accumulation and lighter areas of electron depletion. Note the F_2HCNQ monolayer with its outer cyano groups significantly bent down. The bent monolayer together with the uppermost metal layer is shown in (b) and (c).

When integrating these charge rearrangements up to a certain position z, one obtains the charge transferred from above to below a plane located at z, $Q(z)$, This quantity is shown in Figure 43b. Defining the negative maximum of $Q(z)$ as net amount of charge transferred from the metal to the molecule, one observes an only slight increase when going from F_4TCNQ (0.55 electrons) to F_2HCNQ (0.59 electrons). The most significant deviations between F_2HCNQ and F_4TCNQ occur between the region of electron depletion above the top metal layer and the π-lobe below the molecular plane.

Integrating the charge transferred once more, one obtains the effect of the charge rearrangements onto the potential energy of the electrons. This corresponds to ΔE_{BD} and can be seen in Figure 43c. Here, the effect of the collective slight changes of F_2HCNQ with respect to F_4TCNQ, discussed above, result in an increased potential increase of about 0.2 eV for F_2HCNQ. It can furthermore be seen that the derivation starts at an "area" where the additional cyano groups exert influence to.

An alternative way of analyzing charge rearrangements is in terms of molecular orbitals, the molecular orbital density of states (MODOS). Hereby, the total density of states is projected onto the molecular orbitals of the monolayer in its final position.[1,63,64,73,112] Such a partitioning scheme allows analyzing which molecular orbitals loose or gain electrons as a result of the molecule-metal interaction.[vi] As shown in Figure 44, this analysis reveals that upon interaction the molecular LUMO is nearly completely filled (91% occupation of the LUMO derived hybrid orbitals in F_2HCNQ vs. 89% for F_4TCNQ). As far as the back-donation is concerned, the simple picture seen for F_4TCNQ with 4 orbitals (HOMO-9 till HOMO-12) largely localized on the CN groups being partly emptied due to the back-donation,[109] is somewhat blurred for F_2HCNQ. The reason for that is that due to the coupling amongst the now six cyano groups a larger number of orbitals have significant contributions on the downward bent substituents. When summing up over all orbitals, also this analysis reveals that slightly more electrons are transferred from the Ag to F_2HCNQ than to F_4TCNQ.

[vi] Note that such changes can also be fractional.

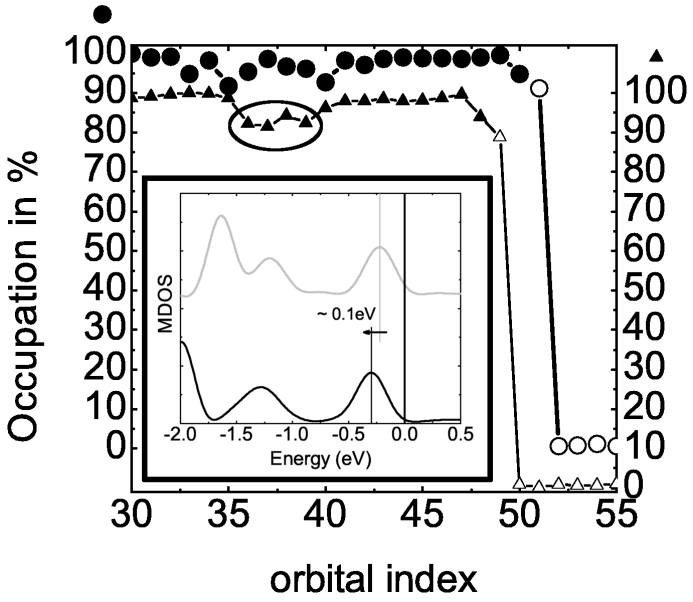

Figure 44: Comparison of the population analysis for F_2HCNQ (circles) and F_4TCNQ (triangles) on Ag(111). The values for F_4TCNQ have been consistently shifted to lower values for better visualization (right scale marked with the triangle above). The most striking difference is highlighted with the circle. Inset: Molecular contribution towards the density of states (MDOS) of top (light gray) F_4TCNQ and bottom (black) F_2HCNQ on Ag(111). The Fermi level of both spectra was aligned to 0. A clear shift towards lower energy is visible for F_2HCNQ.

The slightly increased electron transfer into the LUMO-derived states in F_2HCNQ manifests itself also in the occupied density of states, which usually can be well compared to ultra-violet photoemission spectroscopy (UPS) measurements. As shown in the inset of Figure 44 the calculated MDOS is shifted by 0.1 eV towards lower energies compared to the Fermi energy.

The values for ΔE_{vac} and ΔE_{BD} are summarized in Table 10. The net effect of adsorbing F_2HCNQ on Ag(111) is a pronounced increase of the work-function of pure Ag(111) from 4.47 eV to 5.50 eV (i.e., by 1.03 eV) in the metal-molecule system. This is by about 21% (0.18 eV) larger than the work-function increase obtained for F_4TCNQ on the same surface, which amounts to 0.85 eV. Considering the exponential dependence of the injected current at a metal-semiconductor contact on the barrier height, this difference can become very significant when using acceptor modified electrodes in organic devices. The quite large relative enhancement of $\Delta\Phi$ when using F_2HCNQ instead of F_4TCNQ (21% difference in $\Delta\Phi$ compared to only 10% for ΔE_{BD}) is a consequence of Eq. 64 and the different signs of ΔE_{vac} and ΔE_{BD}.

Table 10: Work-function modification $\Delta\Phi$, dipole as a consequence of the molecular distortions, ΔE_{vac}, dipole resulting from the charge transfer, ΔE_{BD}, as well as total charge transferred, $\mathrm{Q_{bond}(e)}$ of F_2HCNQ-ML and F_4TCNQ in the monolayer packing regime on Ag(111) and F_2HCNQ-sML in the sub-monolayer packing regime. Note that the ratio of the areas is 1.88 and that there is no unit cell size dependence of Q_{bond}.

molecule	$\Delta\Phi$(eV)/(D)	ΔE_{vac}(eV)	ΔE_{BD}(eV)	Q_{bond}(e)
F_2HCNQ-ML	1.03	-0.81	1.84	0.59
F_2HCNQ-sML	0.63	-0.45	0.63	0.62
Ratio	1.63	1.80	2.92	0.95
F_4TCNQ	0.85	-0.82	1.68	0.55

As a last aspect regarding the electronic structure of the F_2HCNQ monolayer, the impact of coverage should be briefly discussed. Depolarization effects have been shown in particular for self-assembled monolayers (SAMs) to limit the achievable work-function change in densely packed dipolar layers.[2,111,141,142] An look at the data in Table 10, where the electronic properties of a densely and a loosely packed F_2HCNQ layer on Ag(111) are compared, however, shows that mutual depolarization effects are only minor. For example, for the net effect $\Delta\Phi$, the charge transfer and bending induced dipole moment per molecule for full coverage is still nearly ninety percent of that in the approximately half monolayer regime. This is reminiscent of the situation in F_4TCNQ, where this behavior has been attributed at least in part to the interplay between opposing dipoles due to the charge forward and backward transfer.[4] It also shows that the impact of the additional cyano groups attached to the central ring of the molecule on depolarization is negligible.

Impact on the monolayer binding energy The binding energy between metal and monolayer is one of the critical factors determining the stability of the interface. It becomes crucially important when dealing with real world devices containing acceptor modified interfacial layers. Here, we partition the bonding into several processes (the corresponding energies per acceptor molecule are summarized in Table 11):

- distortion of the flat isolated molecule to the geometry it adopts when adsorbed on the metal, i.e., primarily the energy necessary to bend the molecules ($\Delta E_{\mathrm{bending}}$)

$$\Delta E_{\mathrm{bending}} = E_{\mathrm{straight}} - E_{\mathrm{bend_{isolated}}} \tag{65}$$

- formation of the monolayer from the individual bent molecules ($\Delta E_{\mathrm{ML-formation}}$)

$$\Delta E_{\mathrm{ML-formation}} = E_{\mathrm{bend\_isolated}} - E_{\mathrm{bend\_monolayer}} \tag{66}$$

- the reconstruction of the metal slab ($\Delta E_{\mathrm{reconstruct}}$)

$$\Delta E_{\mathrm{reconstruct}} = E_{\mathrm{reconst\_slab}} - E_{\mathrm{ideal\_slab}} \tag{67}$$

- and finally the bonding between the distorted monolayer and the reconstructed

slab (ΔE_{bond}).

$$\Delta E_{\mathrm{bond}} = E_{\mathrm{system}} - (E_{\mathrm{reconst\_slab}} + E_{\mathrm{bend\_monolayer}} \tag{68}$$

The net binding energy, $\Delta E_{\mathrm{binding}}$ is then given as the sum of the above contributions.

$$\Delta E_{\mathrm{binding}} = \Delta E_{\mathrm{bond}} + \Delta E_{\mathrm{reconstruct}} + \Delta E_{\mathrm{ML-formation}} + \Delta E_{\mathrm{bending}} \tag{69}$$

Table 11: Partitioning of the binding energy of F_4TCNQ and F_2HCNQ on Ag(111). $\Delta E_{\mathrm{bending}}$ is the energy necessary to bend the planar molecule. $\Delta E_{\mathrm{ML-formation}}$ is the monolayer formation energy of the individual bent molecules. $\Delta E_{\mathrm{reconstruct}}$ is the metal reconstruction energy. ΔE_{bond} is the binding energy of the molecules with the substrate, calculated via subtracting the reconstructed slab and the monolayer from the system. All values are given in eV.

molecule	$\Delta E_{\mathrm{bending}}$ (eV)	$\Delta E_{\mathrm{ML-formation}}$ (eV)	$\Delta E_{\mathrm{reconstruct}}$ (eV)	ΔE_{bond} (eV)	$\Delta E_{\mathrm{binding}}$ (eV)
F_2HCNQ	-0.52	-0.07	-0.04	-2.61	-3.23
F_4TCNQ	-0.59	0.17	-0.02	-2.78	-3.21

It needs to be stressed that analyzing only ΔE_{bond} can result in qualitatively wrong conclusions. It has, for example, been shown by Romaner et al. [215] that the negative $\Delta E_{\mathrm{binding}}$ for PTCDA on Ag(111) obtained by generalized gradient based DFT calculations by Du et al [218], was not a consequence of an actual bonding of the layer to the metal, which is not properly captured by DFT, but rather a manifestation of the energy gain upon layer formation.

Interestingly, $\Delta E_{\mathrm{bending}}$ is virtually identical for both molecules, i.e., the energy needed to bend the molecules is basically not influenced by the additional cyano groups. The monolayer formation energy
$\Delta E_{\mathrm{ML-formation}}$ is however depending on the presence of the additional -CN groups. It is energetically not favorable for F_2HCNQ to form the monolayer in contrast to F_4TCNQ. The metal reconstruction energy $\Delta E_{\mathrm{reconstruct}}$ does, not surprisingly, not differ. A difference between the two systems can be seen for the bonding of the monolayer to the metal. ΔE_{bond} is about 7% larger for the F_2HCNQ monolayer than for the F_4TCNQ monolayer at the same coverage (-2.78 eV versus -2.61 eV). This difference does not arise from different covalent contributions to the bonding energies, as can be inferred from the adsorption distances of F_4TCNQ and F_2HCNQ being the same (*vide supra*) and from the "ring" cyano groups hardly bending towards the surface. Quantitatively, this can be shown from virtually identical values obtained when integrating the crystal orbital overlap population (COOP) [64,73] up to the Fermi energy of the system. Thus, differences in ΔE_{bond} primarily arise from differences in the energy gained by the charge transfer between the metal and the monolayer. These, however, arise from the larger electron affinity of F_2HCNQ, the larger net charge transfer, and the somewhat smaller charge transfer distance.

7.5 Summary and conclusions

The aim of the present theoretical contribution is to suggest F_2HCNQ as an even stronger acceptor than the commonly employed F_4TCNQ to tune the interface energetics in modern organic optoelectronic devices.

The net modification of the work function of a Ag(111) electrode induced by a densely packed F_2HCNQ layer is found to arise from a subtle interplay between charge forward and backward donation as well as strong molecular distortions upon adsorption. The molecular LUMO (π^*) becomes largely filled, whereas several deeper lying molecular orbitals involving the terminal -CN groups loose charge. The latter is detrimental for the achievable net work-function increase.

Interestingly, the additional -CN groups attached to the central ring in F_2HCNQ do not participate in that back transfer, which can be explained by the geometric structure of the F_2HCNQ layer. As a net effect, F_2HCNQ allows for a work-function increase of the Ag(111) electrode by 1.04 eV, which is 27% larger than for F_4TCNQ. This can have significant consequences considering the exponential dependence of carrier injection at interfaces on the barrier height. Moreover, it is shown that the binding of the F_2HCNQ layer to the substrate is slightly affected by the enhanced acceptor properties.

Nonetheless, especially the high binding energy, the higher molecular weight and the somewhat larger molecular area hint towards an increased stability of such an interfacial layer when used in devices.

8 Investigation of a family of acceptor molecules on Ag(111).

8.1 Foreword

Organic devices can be divided mainly into three classes: organic light emitting diodes (OLEDs), organic photovoltaic cells (OPVCs) and organic field-effect-transistors (OFETs). Despite their different functionalities, all of them have interfaces between electrodes (made of metal, transparent conductive oxides, or conducting polymers) and conjugated organic materials in common. The improvment of the interface energetics, i.e. the reduction of injection barriers has attracted considerable interest in recent years and is of crucial importance for the device performance.[115–118,148–154]

Promising ways to reduce charge injection barriers are (i) self-assembled monolayers (SAMs) that carry an intrinsic dipole (discussed in earlier chapters 3, 4 and 5) or by molecules that undergo a charge transfer type reaction with the electrode materials (see chapters 6 and 7).

One prospective of the EU-project *ICONTROL* was to improve the energetics of such interfaces. Through collaboration with chemists or the Max Planck Institute for Polymer Research in Mainz and experimental physicists of the Humboldt university in Berlin the here investigated molecules were synthesized and measured. My contribution was to model the interface using standard density functional theory (DFT) methods. The here presentend molecules were syntesized by Ralf Rieger of the MPI-Mainz. He additonally performed cyclic voltammetry measurements. Ultra-violet photoemission spectroscopy (UPS) and x-ray photoelectron spectroscopy (XPS) measurements were carried out by Benjamin Bröker in Berlin. This part follows a draft of a publication by Bröker Benjamin, Rangger Gerold M., Blum Ralf-Peter, Rieger Ralf, Vollmer Antje, Müllen Klaus, Rabe Jürgen P., Zojer Egbert, and Koch Norbert.

Oliver T. Hofmann suggested a way of obtaining a qualitative guess for the areas of the here investigated molecules. This was insofar useful as it allowed better comparison of the theoretical low coverage work-function modification with the experimental work-function modification.

The following summarizes experimental and theoretical results for pyrenetetraone (PyT) and two derivatives, bromo-pyrenetetraone (Br-PyT) and nitro-pyrenetetraone (NO_2-PyT) as isolated entities as well as adsorbed on Ag(111). Theoretically, PyT was additionally calculated on Au(111). The herein presented data has not been published before as due to patent-issues the whole process has been delayed.

8.2 Introduction

The first molecular layers of an interface are especially important for the electronic properties (such as charge carrier injection) into subsequently deposited organic layers. The most promising ways to improve charge injection is by employing SAMs[119–123] or by molecules that undergo a charge transfer type reaction with the electrode materials.[113,168,173–177] In all cases, a dipole at the interface between the electrode and the SAM is formed. This is changing the electronic level alignment in a way that the hole-injection barrier (HIB) or electron-injection barrier (EIB) is significantly reduced into subsequently deposited conjugated organic materials. In that context, an in the mean-time prototypical acceptor used to tune the HIB is 2,3,5,6-tetrafluoro-7,7,8,8-tetra-

cyanoquinodimethane (F_4TCNQ).[4,167,170,176] An in depth analysis of this molecule can be found in the chapter 6 within this thesis. It has been shown that by inserting a thin layer of F_4TCNQ between the electrode and the organic material, the HIB into p-sexiphenyl (6P) can be lowered by as much as 1.2 eV.[167] In fact, even a continuous tuning of the HIB over a wide range could be achieved by changing the F_4TCNQ coverage on Au(111) or Ag(111).[167,170] Recently it has also been shown that the same concept can be used to reduce the electron injection barrier.[204] In both cases rather low weight molecules were used which might be prone to inter-layer diffusion as it has already been shown for F_4TCNQ.[166,213] Therefore, molecular electron acceptors with higher thermal stability (which means to a first approximation a higher molecular weight) are desired as it was previously discussed for 3,5-difluoro-2,5,7,7,8,8-hexacyanoquinodimethane (F_2HCNQ), see section 7.

In the present part PyT and two derivatives Br-PyT and NO_2-PyT are studied as possible strong electron accepting molecules with distinctive higher molecular weight than F_4TCNQ. Their chemical structures are shown in the inset of Figure 45. Prior to the extensive photoelectron spectroscopy characterization, their potential as acceptor was studied using cyclic voltammetry and DFT gas-phase calculations.

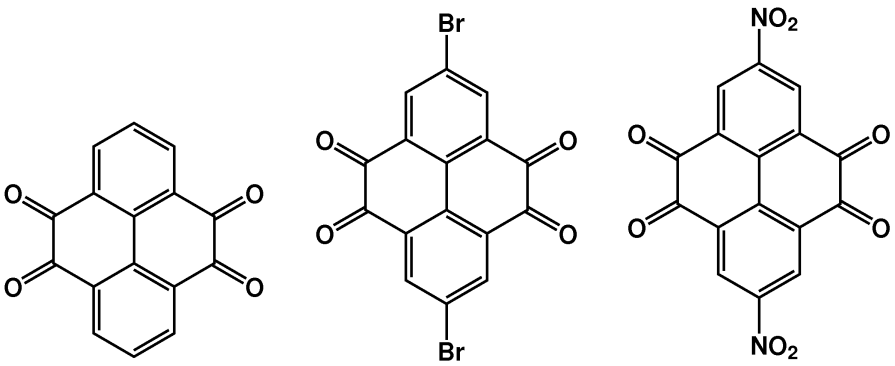

(a) PyT (b) Br-PyT (c) NO_2-PyT

Figure 45: Chemical structures of the here investigated molecules. (a) pyrenetetraone (PyT), (b) bromo-pyrenetetraone (Br-PyT), and (c) nitro-pyrenetetraone (NO_2-PyT).

Compared to F_4TCNQ and its measured electron affinity of -5.33 eV[214] the here investigated molecules show rather moderate electron accepting properties. PyT bears a measured electron affinity (EA) of -4.0 eV. As expected due to the substitutions with additional electron withdrawing groups the measured EAs of Br-PyT and NO_2-PyT are higher. -4.2 eV for the former and -4.3 eV for the latter. As a reference for the reduction peaks of all molecules the reduction of Ferrocene (Fe) to Fe+ was used.[219,220]

The calculated vertical EAs of the isolated molecules show qualitatively the same picture as the EA increases from -2.42 eV PyT to -2.79 eV Br-PyT and finally to -3.05 eV NO_2-PyT.[i] DFT approves the rather moderate, with respect to F_4TCNQ, electron accepting character of the here investigated molecules. Nevertheless, substitution with electron poor parts leads to increased electron affinities. However, the molecular weight

[i] Compare to the calculated electron affinity of F_4TCNQ of -3.68 eV

of NO_2-PyT and Br-PyT is higher than the one of F_4TCNQ, compare Table 12.

Table 12: Molecular weights of the here investigated systems.

molecule	molecular formula	weight
F_4TCNQ	$C_{12}F_4N_4$	276.15
PyT	$C_{16}H_6O_4$	262.22
Br-PyT	$C_{16}H_4Br_2O_4$	420.01
NO_2-PyT	$C_{16}H_4N_2O_8$	352.21

Therefore, in real-world devices this might lead to less inter-diffusion and an improved HIB into subsequent deposited organic materials. The improved HIB can be shown when analyzing the level alignment of subsequently deposited Fullerene (C_{60}) on Ag(111).[ii]

Concerning the adsorption process of the molecules themselves we will show that geometric distortions in addition to charge transfer, especially on Ag(111) will play an important role. For Ag(111) the work function increases for all molecules studied here whereas on Au(111), experimentally, the work function decreases for all canditates. Calculations confirm these observations for Ag(111) and for PyT on Au(111).

Based on the isolated properties of all molecules one can deduce the order of impact: PyT strongly decreases [moderately increases] the work function on Au(111) [Ag(111)], NO_2-PyT only moderately decreases [strongly increases] the work function on Au(111) [Ag(111)] and Br-PyT lies in between.

8.3 Methodology

8.3.1 Experimental methodology

Photoelectron spectroscopy experiments were performed at the endstation SurICat (beamline PM4) at the synchrotron light source BESSY II (Berlin, Germany).[221] Spectra were collected with a hemispherical electron energy analyzer (Scienta SES 100) using an excitation photon energy of 35 eV. The secondary electron cut-off (SECO) spectra were obtained with the samples biased at -10 V in order to clear the analyzer's work function. The error of all energy values reported here is estimated to be ± 0.05 eV.

The experimental setup consists of interconnected sample preparation (base pressure $< 7 \times 10^{-9}$ mbar) and analysis (base pressure 1×10^{-10} mbar) chambers, which enables sample transfer without breaking vacuum conditions. Metal single crystals were cleaned by repeated cycles of annealing (up to 550° C) and Ar-ion sputtering. Organic materials were sublimed from resistively heated Al_2O_3 crucibles or tantalum pinhole sources. The mass-thickness of the organic layers was monitored with a quartz crystal microbalance and all thickness readings are nominal ones. A density of 1.35 g/cm^3 was used in all experiments. Binding energy (BE) values are reported relative to the Fermi-energy for UPS spectra.

[ii] These results are not presented here as they do not include any theoretical modeling but they are essential to the whole story and are included in the paper-draft.

8.3.2 Computational methodology

DFT based band structure calculations using generalized gradient approximation (GGA) with the Perdew-Wang 1991 (PW91) functional were carried out using the plane-wave code *VASP* version 4.6.[38,39] To account for the broken symmetry along the z-direction as unavoidable when modeling interfaces, the periodic slab approach was used. Thereby, the different PyT monolayers (including the substituted ones) were put onto a 5 layer Ag(111) slab. In z-direction more than $20\,\mathring{A}$ of empty space divides the consecutive systems. A Monkhorst-Pack[33] k-point grid of $(3 \times 3 \times 1)$ was deployed in conjunction with a first order Methfessel-Paxton occupation scheme.[34] (broadening of $0.2\,eV$) All atoms of the molecule as well as the top two metal row atoms were fully relaxed using a damped molecular dynamics scheme until all remaining forces were below $0.01\frac{eV}{\mathring{A}}$. All calculations were done in a non spin-polarized manner.

For all calculations the same unit cell size was used corresponding to a loose setup, i.e. sub-monolayer coverage as no experimental unit cells are known. It is however expected that they vary due to the different size of the molecules. All molecules were put into a $(3\sqrt{3} \times 5)$ unit cell, cf. Figure 46. This was done as this unit cell was previously used in theoretical studies of F_4TCNQ on metal surfaces and hence allows a direct comparison.[4,176]

Note that only PyT was calculated on Au(111) as the systems on Au are physisorbed and DFT is known due to the lack of vdW to perform poorly for such system. For PyT on Au this resulted in slow convergence and poor results in comparison with the experiment. Additionally, the molecule was put at the 3,4,9,10-perylene-tetracarboxylic-dianhydride (PTCDA)-Au(111)[175] distance by hand and a single electronic relaxation step was performed, keeping the molecule fixed.

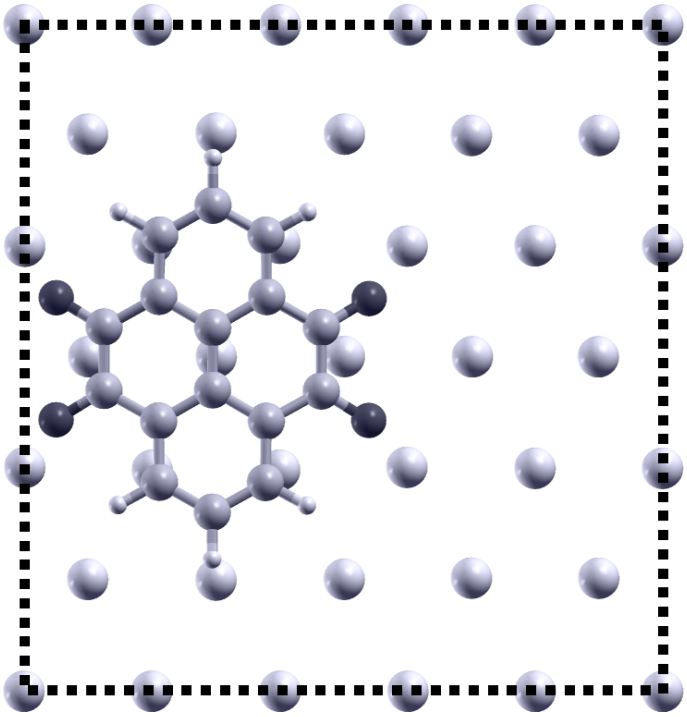

Figure 46: Top view on the theoretical unit cell (indicated as dashed black line) of PyT on Ag(111). For all other molecules the same setup was chosen. Note that only the top metal row is shown.

To obtain the special projections of the density of states (DOS) onto molecular orbitals of the monolayer molecular orbital density of states (MODOS) the atomic orbital based code *SIESTA* version 2.0.2 [45] was used. A more detailed description of the methodology applied in the *SIESTA* calculations can be found in Ref. [109]. Calculations of individual molecular properties were made using Gaussian03 [130] together with the B3LYP [30,31] exchange-correlation functional with a 6-31+G* basis set. [180,181]

Gaussian03 calculations using the *Volume* keyword were performed in order to obtain a qualitative guess of the area of the investigated molecules. The molecular volume is defined as being encompassed in a contour of 0.001 electrons/Bohr^3 density. To obtain the surface area of a molecule, one needs to (i) divide the volume by the "height" of a single carbon atom (given by the same volume calculation and assuming a spherical electron distribution, h(C)=1.98 $\AA$); (ii) second, a scaling factor needs to be introduced as the isodensity value of the volume calculation is too small to reflect densely packed layers. This simplistic approach underestimates the surface area per molecule by nearly 30%. Therefore, a scaling factor of 0.70, yielding reasonable agreement with experimental data for densely packed monolayers of PTCDA, [175] F_4TCNQ, [183] and hexaazatriphenylene-hexanitrile (HATCN) [222] was used.

The area of the unit cell is the same for all molecules and amounts to about 225 $\AA^2$ The areas of the molecules are reported in Table 13. Here the last column roughly shows the respective size of the molecules in percent of the unit-cell size, i.e. 100% would correspond to a perfect coverage.

Table 13: Areas of the unit cell, PyT, Br-PyT and NO_2-PyT in $\AA^2$. The last column shows the area of the molecules in % of the unit cell area, roughly indicating the coverage.

system	area $\AA^2$	%
unit cell	224.75	100
PyT	85.74	40
Br-PyT	122.56	55
NO_2-PyT	108.02	50

3D representations of the interface structures as well as charge rearrangements were produced using XCrysDen.[110]

8.4 Results and Discussion

All molecules on the two metals will be discussed. The ordering will reflect their acceptor strenght, i.e. PyT will be first, Br-PyT second and NO_2-PyT last. The results for the adsorption on Au(111) will be summarized as there except for PyT no calculations were made. The adsorption on Ag(111) will be discussed in great detail including the simulation results. However, all XPS results are summarized and only UPS will be discussed.

8.4.1 Characterization of pyrenetetraone adsorbed on Au(111) and Ag(111).

Pyrenetetraone on Au(111) Figures 47a (total energy range) and b (zoom into the near Fermi region) show the evolution of the UPS valence band (VB) spectra with respect to coverage for PyT on Au(111). Hereby, the decrease in Au 4d and 5s features as well as the vanishing of the Au surface state at 0.3 eV BE is accompanied by the appearance of molecular derived features in the region between 2 and 12 eV BE. The fact that no new molecular features at the vicinity of the Fermi edge emerge is a first indication of a weak interaction of the molecule with the substrate. This can be seen in the zoom into the near Fermi region of Figure 47b. There, it clearly shows that no new features, which would be reminiscent of charge transfer from the metal to the molecule as for instance reported for F_4TCNQ on Au(111),[167] appear.

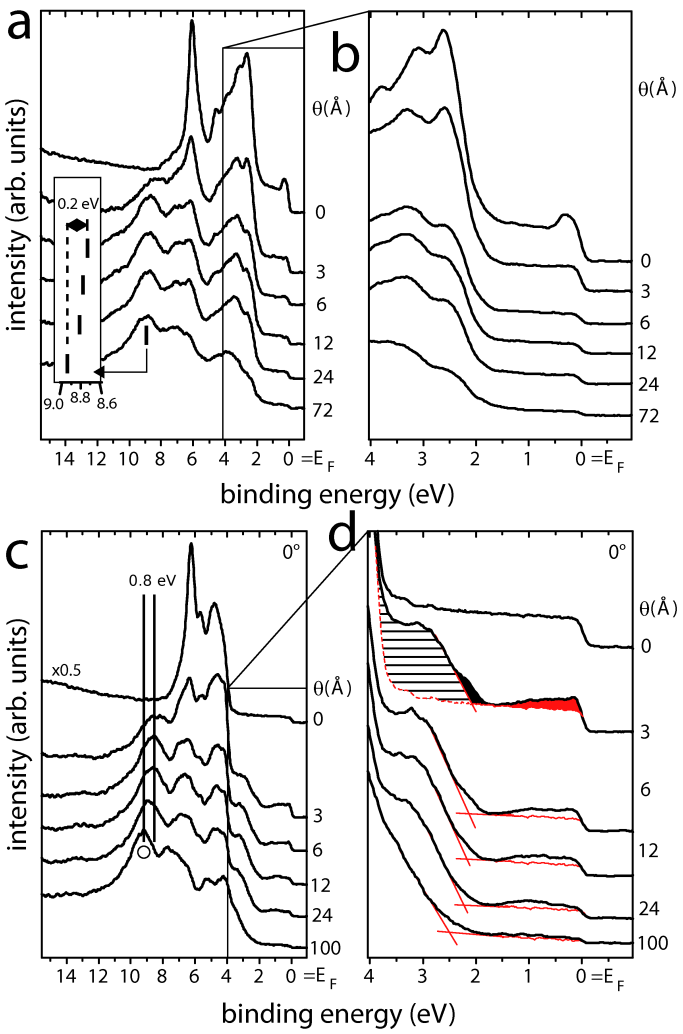

Figure 47: UPS valence-band spectra showing the sequential deposition of PyT on Au(111) (a and b) and Ag(111) (c and d). a and c show the full spectrum, whereas b and d show a zoom into the near Fermi-energy region. E_F denotes the Fermi-energy. The inset in a) depicts the shift of the peak position of a PyT molecular level in more detail. For the description of the filled areas in d please see text. Figure courtesy Benjamin Bröker.

Moreover, even at the highest deposition tested (72 Å) clearly substrate features are present in the spectrum as we still detect intensity from the gold 5s states at the Fermi-edge. This hinders the evaluation of "molecular" parameters (such as ionization energy) as the highest occupied molecular orbital (HOMO) derived band is convoluted with the substrate features. Nevertheless, for studying the evolution of molecular features one peak at ≈8 eV can be analyzed. This one is rather undisturbed as it lies at higher BE than the gold 4d features. Using this peak we can deduce a shift of the molecular valence band features with increasing deposition. It amounts to about 0.2 eV when going from

6 Å to 72 Å, shown as filled black circle on enlarged BE scale in the inset of Figure 47a. The whole situation suggests that the molecular lowest unoccupied molecular orbital (LUMO) of neutral PyT will not hybridize upon contact and that it will not be partly filled. This is not unexpected as the energetic difference of the molecular LUMO of the isolated molecule and the Fermi-level of Au(111) assuming Fermi-level alignment differs most compared to the other molecules and Au(111).[167]

The work-function change ($\Delta\Phi$), as obtained from the SECO is shown in Figure 48a (black squares), and it underlines the previous findings. Despite being an electron accepting molecule, PyT strongly decreases the work function of pristine Au ($\Phi_{\mathrm{Au(111)}}$ = 5.45 eV) by about 0.7 eV after depositing 6 Å of the molecule.

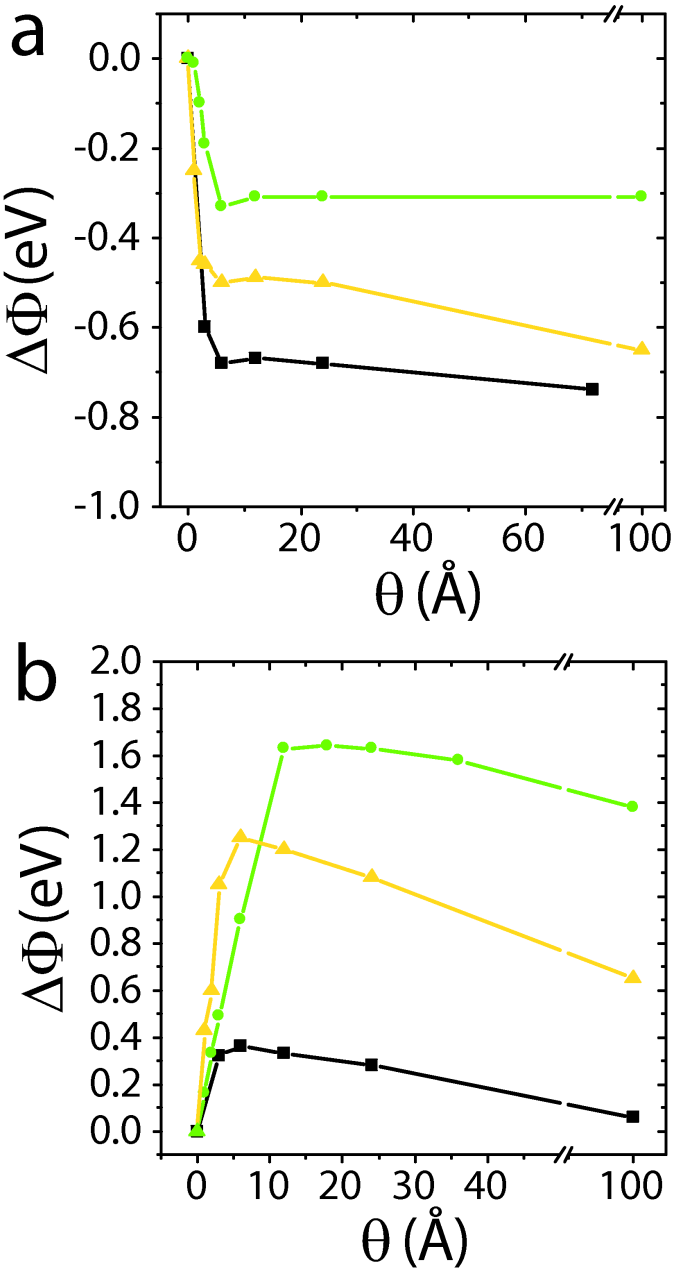

Figure 48: Work-function change ($\Delta\Phi$) for the sequential deposition of PyT (black squares), Br-PyT (yellow triangles), and NO_2-PyT (green circles) on Au(111) (a) and Ag(111) (b). The initial work function of the pristine substrates were $\Phi_{Au} = 5.45\,eV$ and $\Phi_{Ag} = 4.50\,eV$. The error bar of all data points is $\pm 0.05\,eV$. Figure courtesy Benjamin Bröker.

For higher depositions, Φ remains almost constant. Only for 72 $\AA$ coverage a slight

decrease of about 0.05 eV is observed. This total work-function decrease is reminiscent of molecules only weakly interacting with the substrate and can almost exclusively be attributed to the "Pauli-push back" effect, ever present when molecules approach the metal.[149,223]

However, purely physisorbed molecules on Au(111) like pentacene and α-NPD decrease the work function by as much as 1 eV.[167,224] The difference between the latter and the present measurement is that in our case the first molecular layer is not closed even at the highest deposition. Therefore, it would be possible that the work function would decrease even further in the present case to finally approach the values of pentacene and α-NPD if the first layer was fully closed.

Pyrenetetraone on Ag(111) In the case of PyT on Ag(111) the energetic difference of the Fermi-level of the metal and the neutral molecule assuming Fermi level alignment should be smaller compared to the situation on Au(111). Hence, possible charge transfer might occur.

The UPS spectra with respect to coverage are shown in Figure 47c and d. Hereby, Figure 47d is a zoom into the near Fermi-edge region. A similar attenuation behavior of the Ag substrate features as observed previously on Au can be identified. Nevertheless, a close inspection of the region <4 eV BE in Figure 47d reveals an increased intensity close to the Fermi-edge (red/gray filled area). Additionally visible is another distinctive broad peak at around 3.0 eV BE (black striped area). Furthermore, a shoulder at the low BE side of the latter (black filled area) is observed. All three features are maximized in their intensity between 3 $\AA$ and 6 $\AA$ PyT deposition and become partially attenuated at higher nominal coverages. But even at 100 $\AA$ some emission is still observed from these states together with emission from Ag 4s states. This is again a strong indication for island growths.

The intensity of these peaks is maximized at low coverages, i.e. confined to the region at the interface between silver and PyT. This resembles the case of other acceptor molecules such as F_4TCNQ and PTCDA on Ag(111).[193,204] Hereby in both cases charge is transferred from the substrate to the molecule upon adsorption. This, however, establishes a completely different picture than previously analyzed on Au(111).

Now, we propose charge transfer between the substrate and the PyT molecule, i.e. a partially filling of the formerly unoccupied molecular LUMO. Based on our measurements and on DFT calculations (*vide infra*) we assign the feature close to the Fermi-edge and the small shoulder at around 2 eV BE to hybrid orbitals between the former LUMO and HOMO of the neutral molecule and metal bands. The broad feature at around 3 eV as well as the feature at around 8.4 eV also originate from the negatively charged molecules (anions) in direct contact with the substrate.

The apparent shift of the latter feature by 0.8 eV to higher BE with increased coverage can result from four effects: (i) the anion species get attenuated and the spectral features of the neutral molecule appear (this can be quite gradual, particularly because the feature probably consists of several molecular orbitals). (ii) Different screening abilities of the created hole, when the distance between the probed molecule and the substrate is increased. (iii) Furthermore, the orientational dependence of the ionization energy, which can lead to a rigid shift of all molecular orbitals[225] needs to be considered here. (iv) Charging of the molecular film, which cannot be excluded, since even at 100 $\AA$

deposition the Fermi-edge of the substrate is still visible indicating possibly very high islands of the organic film.

The work-function evolution as a function of coverage is shown in Figure 48b (black squares) for PyT on Ag(111). Hereby, the maximum work-function increase of +0.35 eV evolves at the nominal coverage of 6 Å. Furthermore, from the decrease of the work function between 24 Å and 100 Å we can estimate an upper limit of 0.2 eV for the shift of a possibly charged molecular layer and the uncharged molecules.

XPS results confirm the weak interaction as no chemically shifted species is emerging.

DFT-modeling of pyrenetetraone on Au(111) and Ag(111) In the simulations of PyT on Au(111) the molecule is found planar at a distance of about 3.6 Å away from the Au(111) surface. This is reminiscent of weak interaction.[215] The theoretically obtained work-function change amounts to -0.08 eV and thus is in strong contrast to the experimental result. The values are shown in Table 14. Considering that the here applied DFT methodology does not account for van der Waals (vdW) interactions, which are the major interactions in such physisorbed systems the result is not a big surprise.[215] Due to the lack of vdW the "adsorption distance", i.e. distance molecule and metal surface is too large. As a consequense, the above mentioned ever present "Pauli push back" included in the work-function change is underestimated. The "Pauli push back" effect however, decreases the metal work function *per se* and can amount to about 1 eV and could hence be exclusively responsible for the work-function decrease.

On Ag(111), however, the molecule is found in a bent conformation with the outermost hydrogen atoms at a distance of 3.2 Å and the oxygen atoms at 2.3 Å away from the uppermost surface atoms as depicted in Figure 49. This is a first indication of a much stronger interaction.

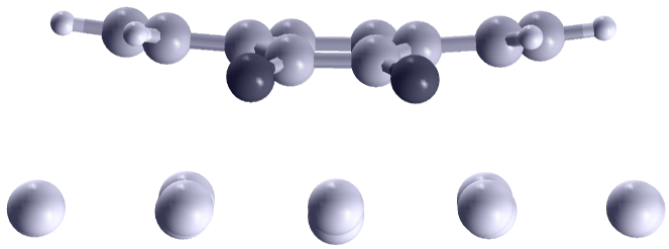

Figure 49: Side view on PyT on Ag(111). Only the top metal row is shown. Note the "saddle-like" conformation of the molecule resulting in an intrisic dipole moment of the molecule, see text.

In theoretical studies, the work-function change is usually divided into two parts:[iii] (i) the charge-transfer induced change in the potential energy landscape of the electrons, ΔE_{BD}, resulting in a bond-dipole, bond dipole (BD), and (ii) the intra-molecular dipole (ΔE_{vac}), which results solely from the geometric distortion of the molecule upon going from the isolated to the adsorbed state.[176] In the present case ΔE_{vac} accounts to -0.44 eV and ΔE_{BD} to +0.69 eV. Therefore, the final calculated work-function change,

[iii] This splitting of the work function was used priory in basically all chapters of this thesis, see 3, 4, 5, 6 and 7

the sum of both contributions, amounts to and increase of +0.25 eV. This is in decent agreement with the experiment (+0.35 eV). The values are shown in Table 14.

Table 14: Comparison of the DFT-calculated work-function modification, $\Delta\Phi_{\text{Theory}}$, and their parts, ΔE_{BD} and ΔE_{vac} with the experimental work-function modification at "monolayer coverage", $\Delta\Phi_{\text{exp.}}^{\text{ml-cov}}$, and the experimental work-function modification scaled to fit the theoretical coverage, $\Delta\Phi_{\text{exp.}}^{\text{scaled}}$. The value in the bracket indicates the corresponding coverage in percent with respect to full coverage, compare Table 13. The data for all derivatives on both metals are reported here. Note that theoretically only PyT on Au(111) was calculated.

Molecule-Metal	$\Delta\Phi_{\text{Theory}}$ eV	ΔE_{BD} (eV)	ΔE_{vac} (eV)	$\Delta\Phi_{\text{exp.}}^{\text{ml-cov}}$ (eV)	$\Delta\Phi_{\text{exp.}}^{\text{scaled}}$ (eV)
PyT-Au(111)	-0.08	-0.05	-0.03	-0.75	x
Br-PyT-Au(111)	x	x	x	-0.50	x
NO_2-PyT-Au(111)	x	x	x	-0.29	x
PyT-Ag(111)	0.25	0.69	-0.44	0.35	0.32 (40%)
Br-PyT-Ag(111)	0.35	0.71	-0.37	1.25	1.05 (55%)
NO_2-PyT-Ag(111)	0.73	1.07	-0.33	1.65	0.90 (50%)

Accounting the theoretically assumed low packing regime, assuming a linear dependence of the experimental work function in the sub-monolayer regime, one needs to specify which theoretical coverage "corresponds" to the experiments. For that purpose the area of the molecule was determined as described in the methodology section and the corresponding coverage was calculated. The area of the unit cell is 225 $\mathring{A}^2$ and the area of PyT is calculated to be 85.74 $\mathring{A}^2$. Hence the theoretical sub-monolayer setup for PyT corresponds to about 40% coverage. Note that this coverage is an actual upper limit. The experimental value corresponding to the theoretical coverage can be found in Table 14 and amounts to approximately 0.32 eV.

Analyzing the charge rearrangements in greater detail, it is found that pronounced electron accumulation occurs in the π-system of the molecule. This can be seen in Figure 50, left column. Generally the shape of the area of electron accumulation is reminiscent of the molecular LUMO of the isolated molecule, compare inset of Figure 50 (L). The area of electron depletion however is mainly located on the oxygen atoms, cf. right column of Figure 50. This suggests that the bond to the surface is largely established through them, which is in agreement with the found geometry and the XPS results. The latter show chemically shifted species indicating the charge transfer and show evidence for strong 3D growth, where the molecules rather dewet the surface and built islands than close the second layer.

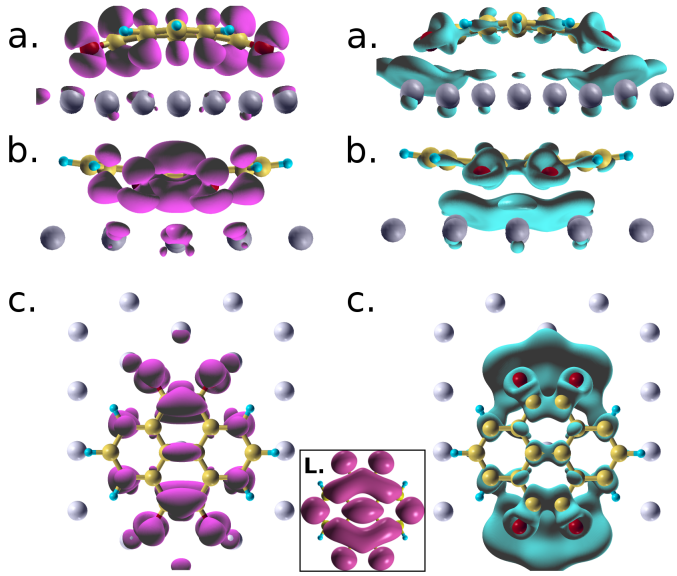

Figure 50: 3D charge rearrangements for PyT on Ag(111). Both columns show, going from top to bottom, a side view along the short molecular axes, a side view along the long molecular axes, and a top view. The left column shows areas of charge accumulation and the right column shows the area of charge depletion. At the bottom, marked with L, a representation of the molecular LUMO of the isolated molecule is shown. The iso-values for all plots were 0.01 electrons per $\AA^3$ and for the LUMO 0.01 electrons per Bohr^3.

8.4.2 Characterization of Br-PyT and NO_2-PyT adsorbed on Au(111) and Ag(111).

After the characterization of PyT on Au(111) and Ag(111) we will now turn to the substituted molecules. In a first part we will analyze the "medium" acceptor Br-PyT as judged from cyclic voltammetry and DFT gas-phase calculations and afterwards the strongest acceptor of the investigated row, NO_2-PyT. First of all the results on Au(111) will be summarized and then the one for Ag(111) are presented including the DFT results. The XPS results are summarized.

Bromo-pyrenetetraone on Au(111) Similar to the findings for PyT on Au(111) no emission from intra-gap states in the UPS is observed for Br-PyT on the same substrate indicating no strong chemical interaction, i.e. no significant charge transfer from the metal to the substrate. This is addionally backed up by the XPS results. The XPS results additonally show when studying the bromine signal that the molecules remain intact on the surface. However, the work-function decrease, compare Figure 48, is less pronounced for Br-PyT on Au(111) hinting to the conclusion that the interaction is not as weak as for PyT on Au(111).

Bromo-pyrenetetraone on Ag(111) For the deposition of Br-PyT on Ag(111) three features appear close to the Fermi-level as Figure 51 proves. The first one is located

directly at the Fermi-level (red in Figure 51d), the second one is appearing as shoulder at approximately 2 eV (black) of a larger feature (third one) found at approximately 3 eV (black striped).

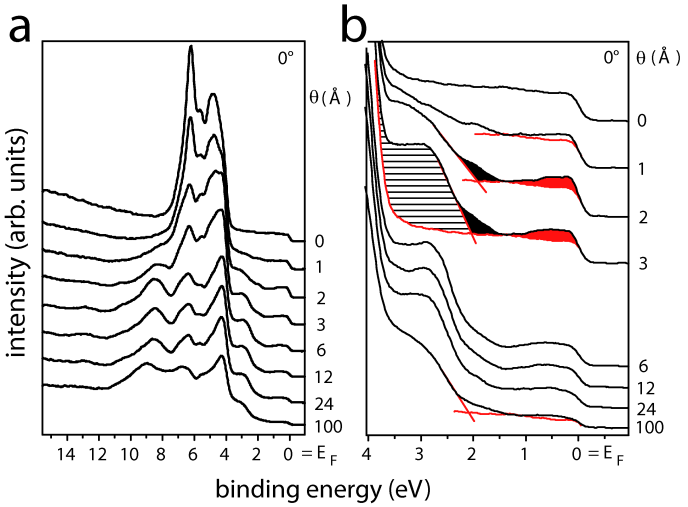

Figure 51: UP valence band spectra showing the sequential deposition of Br-PyT on Ag(111). a shows the full spectrum, whereas b shows a zoom into the near Fermi-energy region. The inset in a) shows the Fermi-edge of the 6 Å (full line) and 24 Å (dashed line) spectrum. E_F denotes the Fermi-energy. Figure courtesy Benjamin Bröker.

This is equivalent to the findings for PyT on Ag(111). In analogy, we assign the two lower BE peaks to a partially filled LUMO-metal hybrid state (red) and a HOMO-metal hybrid state (black). This is additionally approved by the corresponding DFT results (*vide infra*). The black striped feature stems from deeper lying orbitals of the negatively charged Br-PyT anion species.

Work-function measurement further support this charge-transfer type interaction between silver and Br-PyT, compare Figure 48. Hereby, a rapid linear increase is observed from 0 Å to 6 Å by +1.25 eV (absolute $\Phi = 5.75$ eV). Surprisingly, the work-function change decreases strongly, -0.65 eV, upon further deposition to $\Phi = 5.15$ eV at 100 Å.

Noteworthy in that context is, that once again even at the highest coverage the onset of the metal Fermi edge is visible. This hints again to island growth and suggests that the first monolayer is not closed. The apparent shift of the molecular features in the valence band is of similar magnitude (approximately 0.6 eV) as it was for the unsubstituted PyT molecule (0.8 eV).

However, as already stated for PyT on Ag(111) different effects can play a role here: (i) the change from the charged Br-PyT to the neutral molecule with increasing coverage, (ii) different screening, (iii) change in molecular orientation, and (iv) charging. At present, none of the latter three effects can be excluded since all of them can lower the work function *per se*.

Furthermore, the bromine core level spectra show clear evidence for decomposition of the Br-PyT molecule when adsorbed on Ag(111). This of course influences the valence

band spectra accordingly. However, the observed charge-transfer peaks, similar to the ones of PyT on Ag(111), cannot stem from Ag-Br bond, because the lowest feature has its onset at 1.3 eV.[226]

DFT-modeling of bromo-pyrenetetraone on Ag(111) The calculations confirm the last statement insofar as the molecule carbonyl groups are bent *towards* the surface (distance = 2.35 $\mathring{A}$) while the bromine atoms are bent *away* from the surface (distance = 3.40 $\mathring{A}$), compare Figure 52. There, the two parts of the total work-function modification amount to $\Delta E_{\mathrm{vac}} =$ -0.37 eV, the dipole due to geometric distortions, and $\Delta E_{\mathrm{BD}} = 0.71$ eV.

Therefore, the finally calculated work-function change, the sum of both contributions, amounts to and increase of +0.35 eV. Noticable here is that due to the more electronegative Br-atoms, at an increased distance from the substrate, the "intrinsic" dipole of the molecule due to the geometric distortions is reduced compared to the parent molecule PyT. Note that also ΔE_{BD} is reduced, i.e. the substitution did not lead to an increased charge transfer. Only because the geometric effect outweights the charge transfer effect, the total work-function modification is slightly increased with respect to PyT in the calculations.

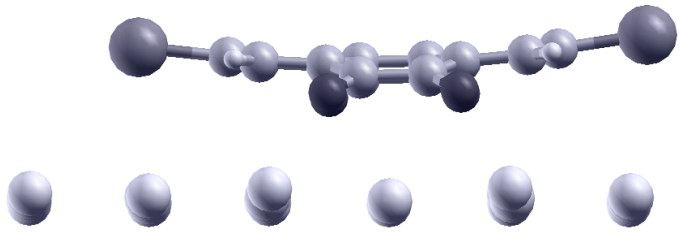

Figure 52: Side view on Br-PyT on Ag(111). Only the top metal row is shown. Note the "saddle-like" conformation of the molecule resulting in an intrisic dipole moment of the molecule itself, see text.

As far as the charge rearrangements are concerned, as seen for the unsubstituted molecule on Ag(111), significant electron depletion occurrs on the carbonyl groups, indicating strong participation in the bonding process. On the other side the bromine atoms do not hold significant electron density, i.e. do not participate in the bonding process, compare Figure 53. Furthermore, charge accumulation mainly affects the π-system of the molecule.

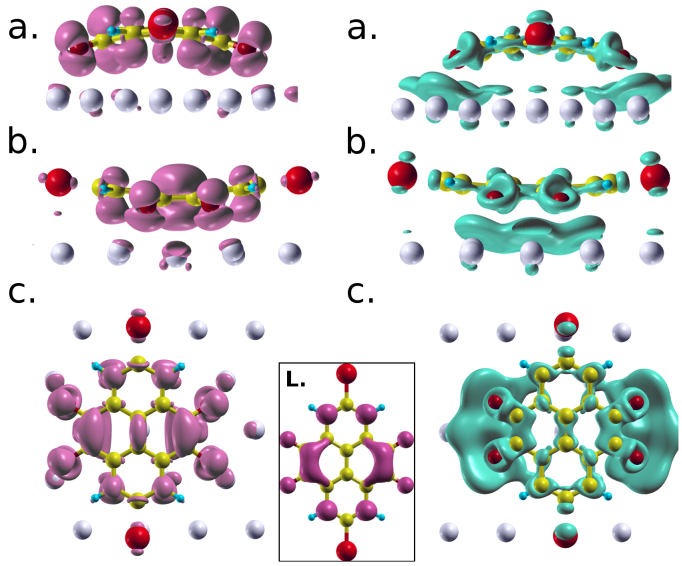

Figure 53: 3D charge rearrangements for Br-PyT on Ag(111). Both columns show, going from top to bottom, a side view along the short molecular axes, a side view along the long molecular axes, and a top view. The left column shows areas of charge accumulation and the right column shows the area of charge depletion. At the bottom, middle, marked with L, a representation of the molecular LUMO of the isolated molecule is shown. The iso-values for all plots were 0.01 electrons per $\AA^3$ and for the LUMO 0.01 electrons per Bohr^3.

Comparing $\Delta\Phi$ of the calculations ($\Delta\Phi = +0.35\,\text{eV}$) with the experimental work-function modification ($\Delta\Phi = 1.25\,\text{eV}$) at a coverage of 6 $\AA$, one does not obtain a good agreement, cf. yellow triangles in Figure 48b and Table 14. In the present case, the experimental work function, Figure 48, shows a pronounced dependence on to coverage. This strong dependence goes in hand with increased polarization effects occurring when Br-PyT molecules approach each other as the Br-atoms are with respect to the hydrogens of PyT more polar. Experimentally, this can only happen within the first layers as the bromine core level spectra shows that the molecules do only remain intact within the first layers and afterwards the molecules loose its bromine atoms. Furthermore, strong island growth similar to PyT on Ag(111) occurs as UPS and XPS measurements show. Therefore, the experimental work-function modification needs to be taken with care as the experiments hint towards strong islanding and losening of the Br-atoms. Therefore, this would correspond to the measured work-function modification not being comparable to the theoretical calculations. Note, that the measured work-function modification considering the theoretical coverage would be 1.05 eV, see Table 14.

8.4.3 Characterization of NO_2-PyT adsorbed on Au(111) and Ag(111).

After characterization of PyT and Br-PyT we will now analyze the strongest acceptor within the investigated ones, namely NO_2-PyT. The experimental results for Au(111) will be summarized and the results for Ag(111) will be discussed.

Nitro-pyrenetetraone on Au(111) UPS results again show a rather weak interaction, especially at low coverages and strong molecular features at higher nominal coverages.

XPS results confirm that the molecule adsorbs intact and that the interaction on Au(111) is rather weak.

The work function during the deposition of NO_2-PyT on Au(111) changes from 5.45 eV to 5.15 eV (6 Å NO_2-PyT coverage), i.e. $\Delta\Phi$= -0.4 eV. Afterwards it remains constant for all higher nominal coverages, cf. Figure 48a, green circles. This however, is in contrast to the results of the valence-band spectra, where no charge-transfer intra-gap states have been observed. It has to be stated here, that the partial compensation of the "push back" effect could be also supported by a slight bend of the molecule creating a permanent dipole (ΔE_{vac} in the calculations) itself counteracting the push-back. This might also hold true for Br-PyT on Au(111) but due to the even stronger electron negative groups of NO_2-PyT this should be enhanced here.

Nitro-pyrenetetraone on Ag(111) The valence-band spectrum of NO_2-PyT on Ag(111), Figure 54c, shows similar features as observed for all molecules previously on Ag(111). Hence, they are assigned accordingly to a now partially filled LUMO-metal hybrid state (red), a HOMO-metal hybrid state (black, at approximately 2 eV), and higher orbitals of the negatively charged species at ≈3 eV, all indicated in Figure 54d. The work function changes strongly and linear and amounts to $\Delta\Phi$= +1.65 eV (absolute value of Φ = 6.15 eV) at 12 Å deposition as shown in Figure 48b, green. With higher deposition it decreases slightly by about -0.2 eV to +1.4 eV (Φ = 5.9 eV) at 100 Å, which is a much smaller reduction than for Br-PyT on Ag(111).

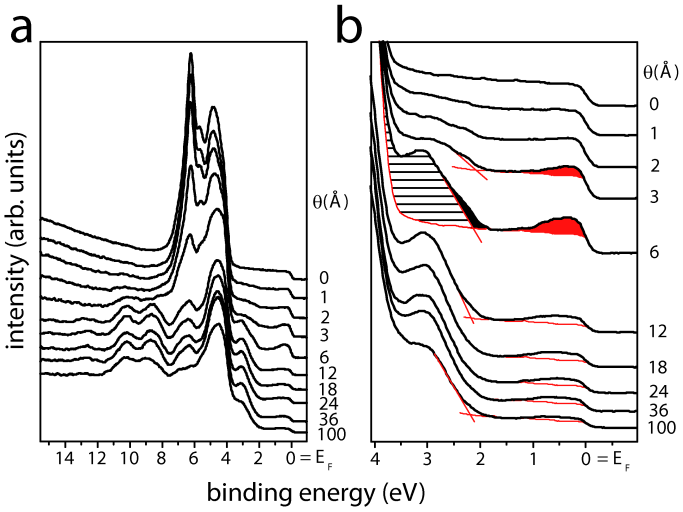

Figure 54: UP valence band spectra showing the sequential deposition of NO_2-PyT Ag(111). a shows the full spectrum, whereas b shows a zoom into the near Fermi-energy region. E_F denotes the Fermi-energy.

DFT-modeling of NO_2-pyrenetetraone on Ag(111) DFT-calculations confirm the strongest impact of NO_2-PyT on Ag(111) with a calculated net work-function increase

of $\Delta\Phi = 0.73\,\mathrm{eV}$.

Analyzing its theoretical origin one obtains an increase due to the charge rearrangements ($\Delta E_{\mathrm{BD}} = 1.07\,\mathrm{eV}$), and a decrease due to the geometric distortions ($\Delta E_{\mathrm{vac}} = -0.33\,\mathrm{eV}$), cf. Table 14. Taking the experimental work-function modification "fitting" the calculated work-function modification one obtains $\Phi_{\mathrm{exp}}^{\mathrm{scaled}} = 0.9\,\mathrm{eV}$ which shows good agreement with the calculations.

Once again, the final geometry of the calculations feature the saddle-like conformation, cf. Figure 55. With the same argument as before one can understand the smaller decrease of ΔE_{vac} as a result of these distortions, see discussion for Br-PyT.

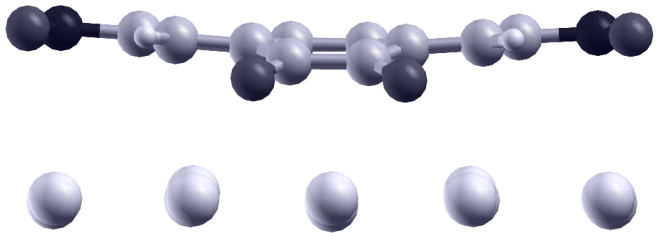

Figure 55: Side view on NO_2-PyT on Ag(111). Only the top metal row is shown. Note the "saddle-like" conformation of the molecule resulting in an intrisic dipole moment of the molecule itself, see text.

The 3D charge rearrangements show once more accumulation in the π-area of the molecule and depletion at the interface and the carbonyl groups. Comparison with the inset (L) in Figure 56 proves once more that the shape of the charge-accumulation area is strongly reminiscent of the shape of the molecular LUMO. Once more the carbonyl groups feature electron depletion, hinting to their importance in the bonding process.

On the other side the NO_2 groups, being part of the π-system, now do hold significant electron density, i.e. they do enhance bonding to the surface in the calculations, compare Figure 56. Especially the oxygen atoms are bearing electron density, i.e. they particularly enhance bonding, as the XPS results confirm.

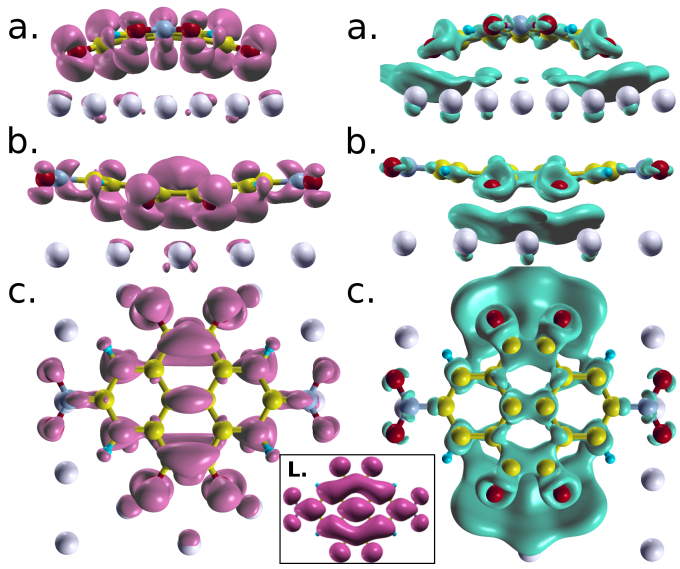

Figure 56: 3D charge rearrangements for NO_2-PyT on Ag(111). Both columns show, going from top to bottom, a side view along the short molecular axes, a side view along the long molecular axes, and a top view. The left column shows areas of charge accumulation and the right column shows the area of charge depletion. At the bottom, middle, marked with L, a representation of the molecular LUMO of the isolated molecule is shown. The iso-values for all plots were 0.01 electrons per $\AA^3$ and for the LUMO 0.01 electrons per Bohr^3.

8.4.4 Comparison of the calculated charge rearrangements

Figure 57 shows a comparison of the plane integrated charge rearrangements, $\Delta, \rho_{\text{bond}}$, upon adsorption, the total charge transferred, Q_{bond}, and the effect of the charge rearrangements onto the potential energy landscape of the electrons, ΔE_{BD}, for all molecules on Ag(111).

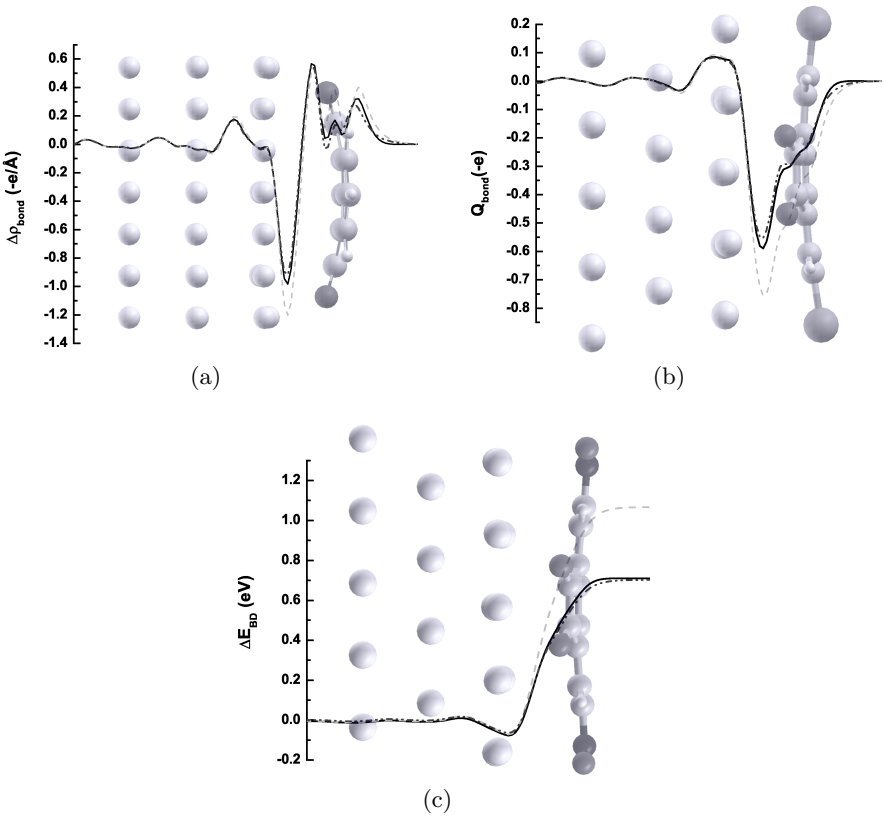

Figure 57: (a) Plane integrated charge density rearrangements of PyT, Br-PyT and NO_2-PyT on Ag(111). (b) Total charge trasferred for all systems as a function of the position z. (c) Effect of the charge rearrangements onto the potential energy landscape of the electrons, shown for all three systems. In all cases the dark gray, dash-dot-dotted, thicker line represents the result for PyT, the black, solid line represents Br-PyT and the light gray, dashed line NO_2-PyT. In (a) the adsorption of PyT, in (b) the adsorption of Br-PyT and in (c) the adsorption of NO_2-PyT is shown in the background as guide to the eye. Note the bent conformation of all of the systems

It clearly can be seen that all the described quantities hardly differ for PyT and Br-PyT, compare Figure 57a for $\Delta, \rho_{\text{bond}}$, 57b for Q_{bond}, and 57c for E_{BD}. This confirms that the substitution with Bromine hardly effects the charge rearrangements and obviously does not enhance the charge rearrangements occuring upon adsorption. This is insofar not surprising as the charge rearrangements are related to changes in the molecular LUMO (π-system) and the Br atoms do not affect LUMO, compare Figure 50 and 53.

Contrary the effect of NO_2 substitution strongly participate in the molecular π-system, compare LUMO in Figure 56. Therefore, it is not surprising that the more charge is depleted above the top metal row and shifted into the π-system. This can be seen in Figures 57a. Therefore, more charge is transferred, i.e. deeper minima in Figure 57b. Consequently, the effect on the potential is enhanced as can be seen in Figure 57c.

8.5 Summary and Conclusion

In this part of the thesis, the potential of the electron acceptors PyT, Br-PyT, and NO_2-PyT was analyzed by means of UPS and XPS studies as well as by DFT calculations. The choice of molecules was motivated by cyclic voltammetry measurements and DFT screening of the isolated molecules. They showed low lying LUMO levels, which are comparable to other electron accepting molecules. Nonetheless, they are not comparable to previous results such as F_4TCNQ or F_2HCNQ, also analyzed in great detail in this thesis.

On Au(111) the interaction between molecules and the surface was found to be rather weak in all three cases, which is manifested by the absence of new emissions in the valence band (originating from molecule/metal hybrid stares) and chemically shifted species in the core level spectra. Additional, calculations for PyT on Au(111) revealed weak interaction and it could be concluded that one encounters van-der Waals interaction rather than chemisorption. Furthermore, experimentally the work function was observed to decrease in all three cases, but not as much as expected for purely physisorbed systems. Besides, the work-function decrease was compensated the deeper the LUMO of the respective derivative was found in the cyclic voltammetry measurements and in the calculations. For NO_2-PyT a maximum work-function decrease of only 0.3 eV was obtained, which indicates some stronger chemical interaction between the substrate and molecule than pure physisorption.

In contrast a strong chemical interaction between PyT, Br-PyT, and NO_2-PyT on Ag(111) was found in the calculations as well as in the experiment. In the case of Br-PyT even a cleavage of the C-Br bonds is observed in the XPS measurements.

In all three cases new molecule/metal hybrid states emerge close to the Fermi-edge in the UPS, which is reminiscent of charge tansfer between the substrate and the molecules. This leads to an increase of the work function. The strongest increase is observed for NO_2-PyT, where a maximum absolute work function of 6.15 eV is obtained. In all three cases the new states in the valence spectra are very similar, despite the differences in molecular termination. The same is true for the core level spectra, where the evolution of the C_{1s} and the O_{1s} spectra closely resemble each other. DFT modeling suggests that carbonyl groups are bent towards the surface while the terminal hydrogen, bromine, and the nitro-group atoms are bent away from the surface. This explains the similar core level spectra evolution, because in all three cases the bonding to the surface is mediated by the carbonyl groups. This is also manifested spectroscopically, where the $C_{=O}$ peak is strongly chemically shifted by more than 1 eV in all three cases. Furthermore, the bromine atoms and nitro groups are almost found at the same binding energy as they are observed on Au(111), without exhibiting chemically shifted species. Here, DFT modeling confirms that the charge rearrangements in the region of the substituted atoms are almost negligible for Br-PyT. For NO_2-PyT, however, as being part of the π-system, they also indicate the role of NO_2 and here especially of the oxygen atoms and leave the conclusion that the effect must be strongest for this derivative.

By evaluating the bromine core levels, evidence for a decomposition of the Br-PyT molecule and the formation of Ag-Br is found. However, at present it is not clear whether the affected molecules only partly or fully loose their bromines. As a result the experimental and theoretical work-function modification differ significantely as they

do describe different systems. No indication for decomposition of NO_2-PyT on the Ag(111) surface is observed. All three cases on all substrates commonly show that the attenuation of the metal features is not completed even at 100 $\AA$. This shows that all three molecules rather build islands than close a second or even first layer on the two investigated surfaces.

Experimentally, by depositing several layers of C_{60} onto Br-PyT and NO_2-PyT modified surfaces, the HIB ends up at ≈1 eV in both cases. This corresponds to a decrease of 0.8 eV compared to the value for bare metal C_{60} deposition. Despite the large difference between the starting work functions of 0.5 eV after pre-deposition of Ag(111) with Br-PyT and NO_2-PyT, the work function drops to 5.5 eV in both cases after C_{60} deposition. This evidences that the C_{60} molecular features are pinned with respect to the Fermi-level, which hinders a further decrease of the HIB in both cases. As the pinning levels are a materials property of C_{60}, one should be able by using other materials (with lower pinning levels) to fully exploit the potential of Br-PyT and NO_2-PyT. The linear increase of the work function with coverage as observed in all three cases on Ag(111) should even permit to adjust the work function depending on the active organic material. The observed decomposition of Br-PyT does not influence the decrease in HIB into C_{60} negatively, but future studies needed to show that diffusion of Ag-Br are not an issue.

9 STM and XPS simulations using F_4TCNQ and F_2HCNQ.

9.1 XPS simulations for F_4TCNQ on Au(111)

In this part the simulated x-ray photoelectron spectroscopy (XPS) N 1s core level shift for the acceptor 2,3,5,6-tetrafluoro-7,7,8,8-tetracyanoquinodimethane (F_4TCNQ) on Au(111) within the final state approximation (see section 2.2.4) will be compared to the experiment. The latter has been carried out by N. Koch et al.[167] on polycrystalline Au. As described previously, only relative core level shifts can be calculated (cf. 2.2.4). Therefore, one needs two systems to compare. One system is the adsorbed F_4TCNQ on Au(111) and the other one the F_4TCNQ crystal. The latter corresponding to a multilayer XPS in the experiment. The N 1s core-level shift was analyzed. The following table shows the total energies for the respective calculations.

Table 15: Total energies for the XPS core-level shifts of the N 1s for F_4TCNQ on Au(111). As second system, representing the multilayer XPS signal, serves the F_4TCNQ crystal. The first column indicates the kind of calculation done; normal - corresponding to a single-point calculation of the system and N 1s corresponding to the calculation with modified pseudopotentials. The first part includes the values obtained using soft pseudopotentials and the second part using hard pseudopotentials. The "difference" line is N 1s energy minus normal energy for the crystal and the system. The resulting shift is calculated via subtracting the system difference of the crystal difference. All values are in eV.

soft PP	crystal	system	shift
normal	-594.41	-394.93	
N 1s	-685.54	-485.58	
difference	-91.13	-90.65	**-0.48**
hard PP	crystal	system	shift
normal	-594.85	-394.15	
N 1s	-685.53	-484.58	
difference	-90.68	-90.43	**-0.25**

The values in table 15 indicate a shift of the N 1s signal from monolayer to multilayer of -0.48 eV (soft pseudopotentials) or -0.25 eV (hard pseudopotentials). This shift is superimposed to the shift due to the intrinsic dipole moment of the bent molecule which is -0.79 eV for F_4TCNQ on Au(111), cf. Table 9 within the F_4TCNQ part (6) of this thesis. In total it adds up to either a -1.27 eV (soft pseudopotentials) or a -1.04 eV (hard pseudopotentials) shift towards higher binding energy in the multilayer setup.

In the experiment even at low coverage $5\mathring{A}$ two N 1s peaks are visible. The higher binding energy peak has been assigned to the neutral F_4TCNQ molecule and the lower binding energy peak to the anion species.[167] Anion species in that context is the terminology used for the adsorbed molecule. At high coverage ($60\mathring{A}$) a strong increase in the higher binding energy component was seen.[167] This gives rise to a relative shift of about 1.35 eV towards higher binding energy.

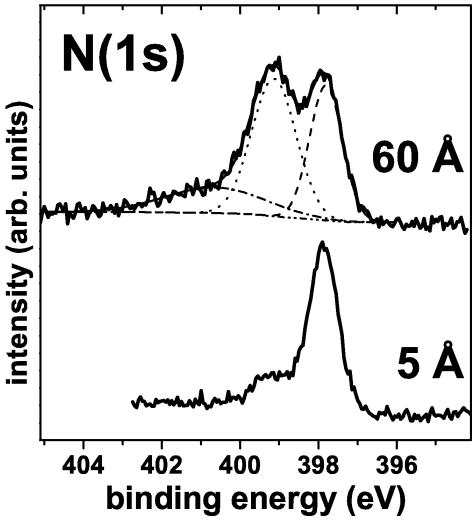

Figure 58: Experimental N 1s XPS spectra (photon energy, 630 eV) of 5Å F_4TCNQ on Au and 60Å F_4TCNQ on Au. For the latter the peak components and the background obtained by the fitting routine are indicated. The Figure is part of a Figure of Ref. [167].

Noticeable here is that the theoretical shift with the soft pseudopotentials agrees well with the experimental shift. Moreover, astonishing is that the hard pseudopotentials did not improve the result in that case. The difference between theory and experiment might even be smaller considering the fact that the experimental data was obtained from polycrystalline Au whereas for the calculations a perfectly oriented Au(111) surface was assumed. Additonally, the orientation of the molecule in the thick layer is distinctively influencing the experimental shift as the ionization energy is dependent on the orientation.[225]

9.2 STM simulations

Crucial for all surface problems is the determination of a unit cell. Most of the time, no experimental information about it is accessible. Hence assumptions are made.

For instance, for F_4TCNQ on Cu(111) no experimental information about the packing was/is available. Due to that, Lorenz Romaner assumed a low packing setup ensuring that there is no artificial interaction between adjacent molecules.[176] The simulated scanning tunneling microscopy (STM) image of this setup can be found in sub-section 9.2.3.

In general I made STM images for almost all systems I calculated throughout my thesis. In the following three sub-sections only simulations for the monolayer setup of F_4TCNQ on Au(111) and 3,5-difluoro-2,5,7,7,8,8-hexacyanoquinodimethane (F_2HCNQ) on Ag(111) as well as the submonolayer setup of F_4TCNQ on Cu are shown.

9.2.1 F_4TCNQ monolayer STM

In the previous chapter, 6, about the adsorption of F_4TCNQ on Au(111), Ag(111) and Cu(111) two different unit cells were used. The monolayer setup for Au and Ag was based on an experimentally low temperature STM image of F_4TCNQ on Au(111).[183]. Unfortunately, the published STM image is not the monolayer STM-image.[i] The published STM image is shown in Figure 59. It shows most likely the STM of a double-layer F_4TCNQ on Au(111).

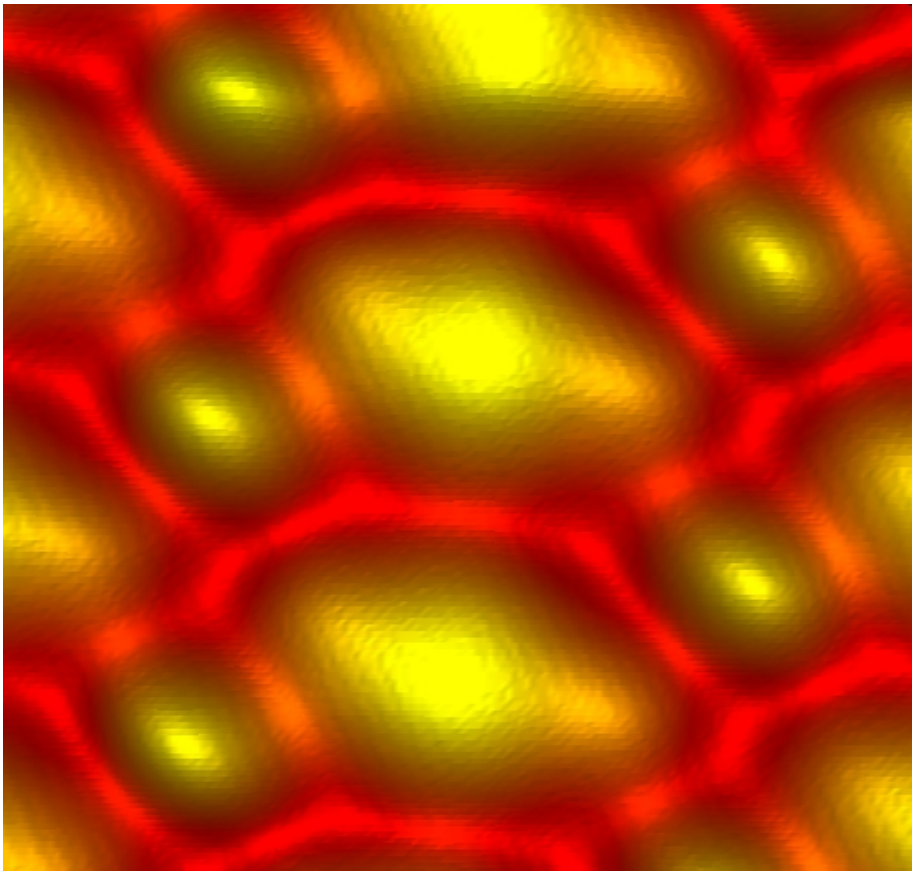

Figure 59: Published STM image of a single F_4TCNQ on Au(111).[183] [Image parameters: 0.22 nA, -1.5 V] - The picture here shows most likely a STM of the double layer.

The true STM image, based on the figures of a draft of the paper 183, of the monolayer is shown in Figure 60.

[i] This is based on private communications with Saw-Wai Hla during at the 254th Wilhelm und Else Hareaus Seminar in Bad Honnef (26.01.2009 till 30.01.2009) and private communications with Norbert Koch.

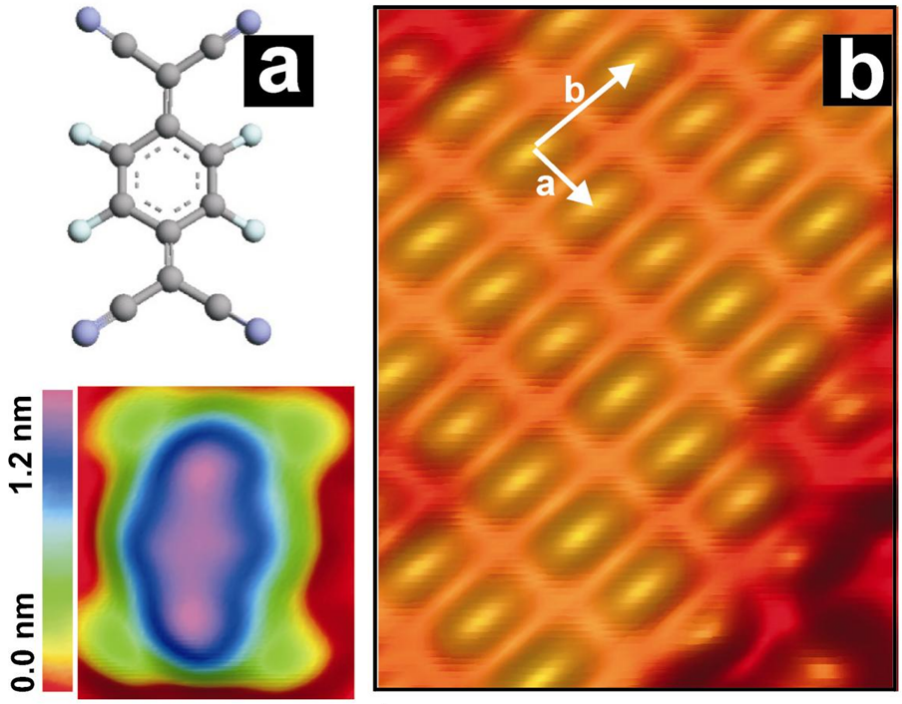

Figure 60: Structure and electronic properties of the F_4TCNQ-Au(111) complex. (a) STM image of a single F_4TCNQ on Au(111) [Image parameters: 0.22 nA, -1.5 V] together with a chemical model. (b) Self-assembled F_4TCNQ on Au(111). [Image parameters: 0.35 nA, 0.4 V, 5 nm x 7.5 nm scan]. Note: The electron tunneling is from the HOMO-1 and HOMO level to the tip in (a), and from the tip into a hybrid surface-LUMO state in (b).

Based on that images a $\begin{pmatrix} 4 & -1 \\ 4 & 0 \end{pmatrix}$ unit cell was determined.[183] This unit cell has been taken for the simulation of the dense packed setup for F_4TCNQ on Au(111) and Ag(111) as well as for F_2HCNQ on Ag(111). The former can be affirmed by the virtual identical lattice constants and latter can be rationalized by comparison of the dimensions of the molecule which are basically identical.

Here, simulated STM images of all setups should underline the chosen setups (The chosen interval was from the Fermi energy to -1.5 eV below the Fermi edge, i.e. the same as in the experiment.). Additionally, visible is that the comparison with Figure 60 shows and excellent agreement whereas the comparison with the published STM image, Figure 59, shows a decisive difference. Hereby, the additional spots visible in the "experiment" are missing. They attracted my attention and the first guess was that there might be ad-atoms. Nonetheless, after unsuccessfully trying to reproduce the published STM images, the explanation was simple.

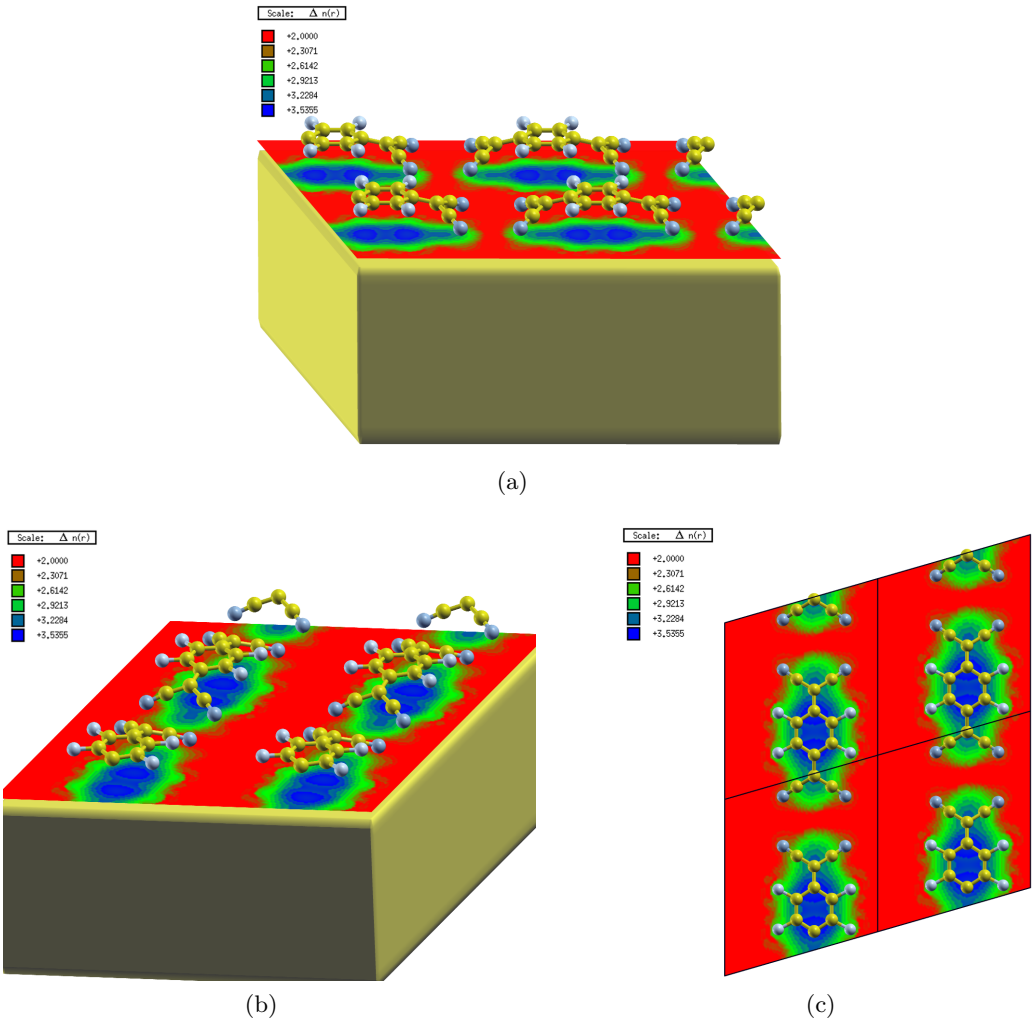

(a)

(b)

(c)

Figure 61: Simulated STM-images of F_4TCNQ on Au(111). a) and b) Side view of the system. c) Top view on the system. The molecules are shown in their arrangement and in c) the unit cell is also indicated with black lines. The Au bulk is represented as golden bullion. In all subfigures the height scale is plotted in $\AA$ with the top metal layer as zero.

9.2.2 F_2HCNQ monolayer STM

In the previous chapter about the interface modification with the acceptor F_2HCNQ the same unit cell as for the adsorption of F_4TCNQ on Ag(111) was assumed for the densely packed monolayer setup. This was motivated in two ways. First of all the lattice constants of Au and Ag are virtually identical (calculated values are Ag: 2.94 $\AA$ and Au: 2.95 $\AA$). A second point is the virtually identical molecular area.

This assumption of the same unit cell can be further rationalized with the help of simulated STM images of the monolayer packing for F_2HCNQ. Figure 62 shows three different views of a STM image of the F_2HCNQ-lowest unoccupied molecular orbital (LUMO). The chosen interval was from the Fermi energy to -1.5 eV below the Fermi

edge.

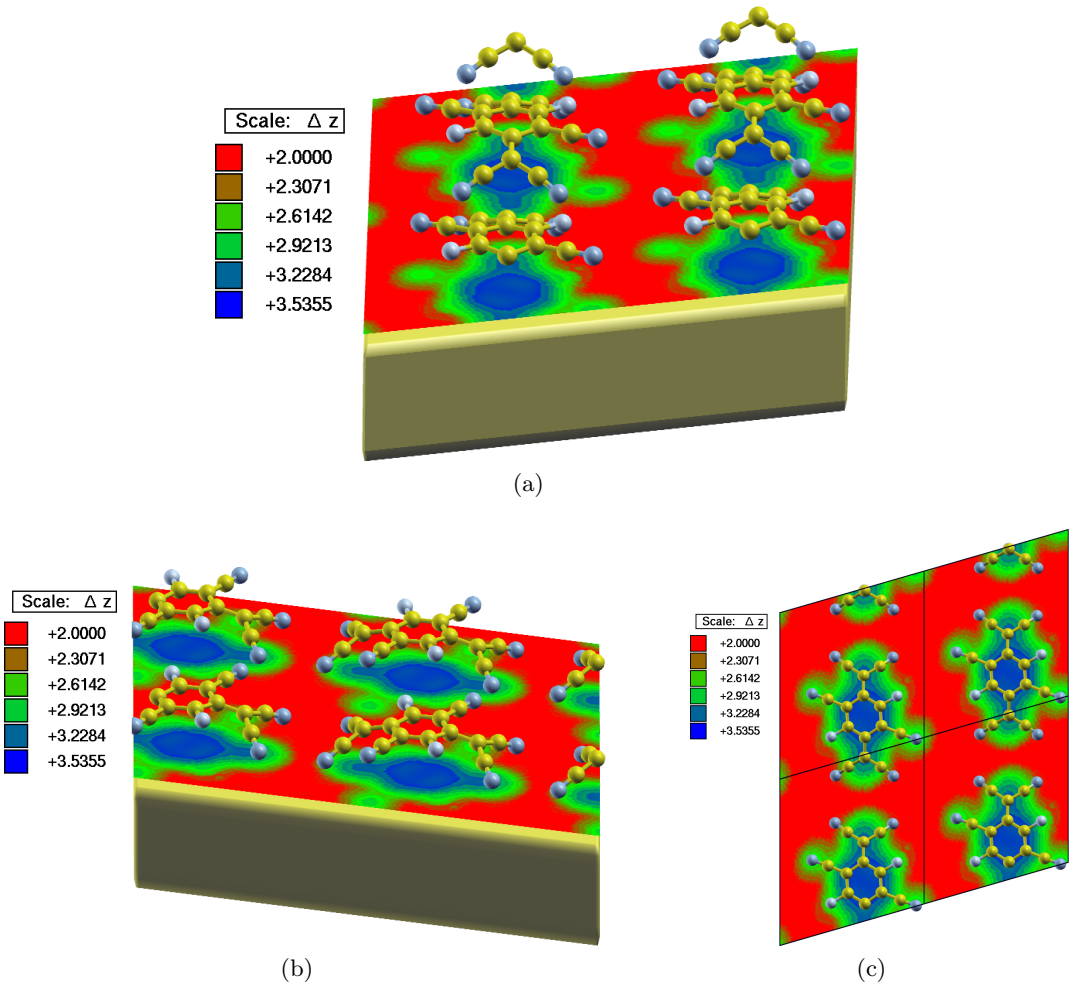

Figure 62: Simulated STM-images of F_2HCNQ on Ag(111). a) and b) Side view of the system. c) Top view on the system. The molecules are shown in their arrangement and in c) the unit cell is also indicated with black lines. The Ag bulk is represented as golden bullion. In all subfigures the height scale is plotted in $\mathring{A}$ with the top metal layer as zero.

9.2.3 F_4TNQ sub monolayer STM

In this part a simulated STM image of the sub-monolayer setup of F_4TCNQ on Cu(111) is shown in Figure 63. The image clearly shows that there is no interaction between adjacent molecules and confirms that the chosen setup is indeed a low coverage regime ensuring no artificial interactions.

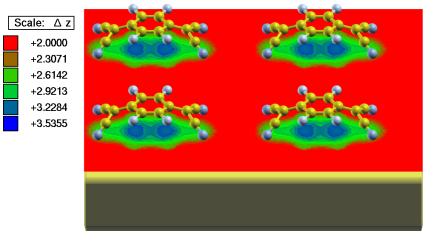

(a)

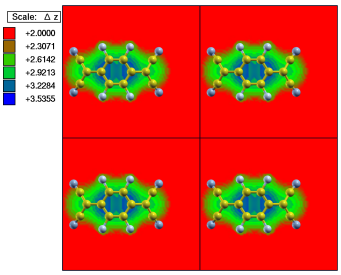

(b)

Figure 63: Simulated STM-images of F_4TCNQ on Cu(111). a) Side view of the system. b) Top view of the system. The molecules are shown in their arrangement and in b) the unit cell is also indicated with black lines. The Cu bulk is represented as golden bullion. In all subfigures the height scale is plotted in $\mathring{A}$ with the top metal layer as zero.

10 Back to life: An analysis of the covalent bond with the help of the COOP and the MOOP

10.0.4 Foreword

The immense development in organic-electronic devices over the last decades has convinced more and more scientists to turn towards the field of organic devices. Crucial in this context is the understanding of metal/organic interfaces. Using organic acceptors or donors is an efficient tool to modify metal work functions.[116] This can considerably improve the performance of organic devices.

This part of the thesis deals with an unconventional approach of analyzing the bonding mechanism between a molecule and the underlying metal. Therefore, the strong acceptor 2,3,5,6-tetrafluoro-7,7,8,8-tetracyanoquinodimethane (F_4TCNQ) as first example and the donor 1H,1'H-[4,4']bipyridinylidene (HV0) as second example will be used to demonstrate the purpose of the applied methodology. Prior to that, the used computational methodology will be shortly revised as it is basically the same for both molecules. The outline for the discussion of both molecules is used as a first draft for upcoming publications about this issue and therefore the whole setup is "paper"-like.

For both molecules the general results of our standard methods to describe such chemisorbed systems are shortly revised as this eases understanding of the upcoming analyzes.

10.0.5 Methodology

All calculations presented here are based on the optimized adsorption geometry obtained from the plane wave density functional theory (DFT) code *VASP* version 4.6.[38,39] Precise details on the computational details used to obtain this geometry (F_4TCNQ on Ag(111)) can be found in the respective theoretical contributions, for F_4TCNQ on Ag(111) see Ref. [4] and for HV0 on Au(111) see Ref. [205]. Here, the same Monkhorst-Pack[33] k-point grid of (3x3x1) was used for a single electron relaxation step in the atomic orbital based code *SIESTA*[45] version 2.0. This code was used because it eases projections onto molecular and atomic orbitals mainly used in the present contribution. Hereby, the Perdew, Burke and Ernzerhof (PBE) exchange correlation functional and norm-conserving pseudo-potentials based on relativistic calculations using the Troullier-Martins scheme and a linear core correction were used. Calculations for orbital representations were made using Gaussian03[130] and the Becke, Lee, Yang and Parr (B3LYP) exchange-correlation functional with a 6-31+G* basis set.[180,181] XCrysDen[110] was used to generate all orbital representations.

For the analysis of the crystal orbital overlap population (COOP) we follow the process described in 2.2.3 and define the projections onto atomic orbitals as (compare Equation 50)

$$COOP_{X,Y}(E) = \sum_{m\in X, l\in Y, i,k} c^*_{im\mathbf{k}}\, c_{il\mathbf{k}}\, S_{ml\mathbf{k}}\, \delta(E-\epsilon_{i\mathbf{k}}). \tag{70}$$

Here, X and Y denote a set of atomic orbitals, the $c_{il\mathbf{k}}$ correspond to the linear combination of atomic orbitals (LCAO) coefficients and the $S_{ml\mathbf{k}}$ is the overlap matrix. This

definition resolves the bonding (positive) and anti-bonding (negative) contributions of specific atomic orbitals on the energy scale. This enabling us to investigate the impact of specific atoms on the adsorption process.

Conceptually, the basis set in which the COOP is carried out is not restricted to atomic orbitals (AOs). One might as well use the basis of molecular orbitals (MOs) to see where, on the energy scale, a specific MO gives bonding or anti-bonding contributions. Therefore, we here use our previous definition of the molecular orbital overlap population (MOOP) (cf: equation 37):

$$MOOP_{X,Y}(E) = \sum_{m\in X, l\in Y, i,k} c^{M*}_{im\mathbf{k}}\, c^{M}_{il\mathbf{k}}\, S^{M}_{ml\mathbf{k}}\, \delta(E-\epsilon_{i\mathbf{k}}) \tag{71}$$

Now, the $c^{M}_{il\mathbf{k}}$ correspond to the linear combination of molecular orbitals (LCMO) coefficients and $S^{M}_{ml\mathbf{k}}$ is the overlap matrix of the molecular orbitals with the metal bands. For an in depth description refer to the previous chapter about COOP and MOOP in the Theory part of the thesis, see 2.2.3. Now for calculation of the MOOP of a specific molecular orbital with the metal one takes the LCMO coefficients for the molecule and the LCAO coefficients for the metal and the overlap matrix of the molecular orbitals with the metal.

Recall that positive areas in both curves represent bonding and negative areas anti-bonding interactions. Additionally, for both quantities one can define a total overlap population (ToP) as integration up to the Fermi energy. This reflects the bonding strength and theoretically scales with the covalent bonding energy. However, our applied generalized gradient approximation (GGA) formalism is known to underestimate van der Waals (vdW) interactions. This however implies that our values for the total overlap population are lower limits for bonding strength as the vdW contributions will always enhance binding.

10.1 Inspection of the covalent bond between the acceptor F_4TCNQ and Ag(111)

10.1.1 Introduction

In chapter 6 about the adsorption of F_4TCNQ we saw that a strong chemical interaction is occurring for F_4TCNQ on Ag(111), Au(111) and Cu(111).[4,167,170,176,213,227] Hereby, the formerly unoccupied lowest unoccupied molecular orbital (LUMO) of the isolated molecule gets largely filled upon adsorption.[4,168,176] Furthermore, the whole bonding process is connected to strong molecular distortions in a way that the in gas-phase planar molecule gets an intramolecular dipole moment in the bonded system.[4,176] This in conjunction with charge transfer leads to a calculated work-function increase of Ag(111) covered with F_4TCNQ of 0.85 eV. Such a value is a first indication of a strong covalent bond that will be formed when the molecule gets chemisorbed. Another, yet even stronger indication is the calculated binding energy[i] of F_4TCNQ on Ag(111), which amounts to 2.10 eV.[4] Such strong chemisorption goes in hand with the appearance of partial bonds to the surface. At the same time, bonds within the adsorbed, distorted

[i] Hereby, the calculated binding energy does not include van der Waals interaction as such interactions are not described in the applied methodology (DFT-with PW91 functional).

molecule are weaker or stronger with respect to the same bonds in the planar, isolated molecule. A theoretical indicator for the description of such bonding processes was first introduced by Hoffmann et al.[64,73,228]. They defined a crystal orbital overlap population COOP to interrogate the bonding and anti-bonding behavior of the atomic orbitals and their overlap with the metal band. In such a way they could visualize the bonding and anti-bonding contributions of the covalent bond established between atoms of the adsorbate and the substrate.

In the present contribution, we will highlight the advantages of such a descriptive analysis as parts of, yet even more precisely, even atomic orbitals of F_4TCNQ responsible for the strong bond can be identified. Additionally, the role of the metal bands is analyzed. Moreover, we present an enhancement of this analysis method as we expand the analysis of bonding and anti-bonding contributions on molecular orbitals and their interaction with the substrate, naming that quantity MOOP. Prior to analyzing our molecules with the help of the COOP and the MOOP we revise results based on a projection of the density of states onto molecular orbitals of the isolated monolayer (molecular orbital density of states (MODOS)) which enables to identify those molecular orbitals strongly hybridizing and participating in the bonding process.

10.1.2 Results and discussion

Before the bonding process of F_4TCNQ is analyzed with the help of the MODOS, we are going to have a look at what we intuitively expect to happen when we put a strong acceptor onto the metal surface. Afterwards using the COOP, the focus will first of all be laid on the analysis of the changes within the molecular backbone itself occurring upon bonding. By doing so an already quite intuitive picture of the whole bonding process evolves. Then, the bond between the molecule and the metal is analyzed including the role of the metal in the whole process. In a final step, the molecular orbital overlap population is included into our considerations and special orbital overlaps of the molecule with the metal are pointed out.

F_4TCNQ, Figure 64, possesses four strong electron withdrawing groups (-CN) at its end.

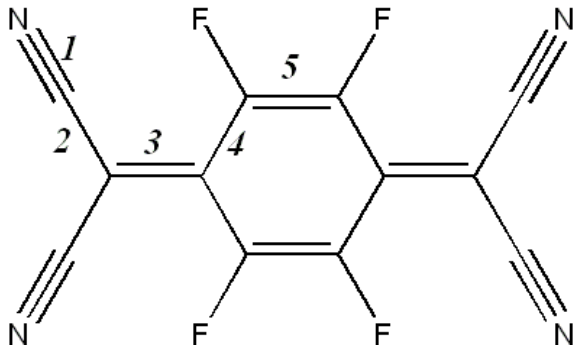

Figure 64: Structural formula of F_4TCNQ. The numbering is needed for Figure 65.

From the electron affinity (EA) of the isolated molecule it is known that F_4TCNQ

is a strong acceptor. When aligning a strong acceptor with a suitable metal, where the metal Fermi energy is close to the respective LUMO position prior to contact a strong chemical bond is expected to form after bringing the two partners in contact. When thinking about the latter situation, i.e., molecule and metal in contact, it can be easily deduced that F_4TCNQ will accept electrons from the underlying substrate as the LUMO is located below the Fermi level of the metal when simply considering vacuum alignment. Hence, when incorporating electrons into its backbone the molecular levels will shift upward in energy and broaden until thermodynamically equilibrium is reached.

It has been shown in chapter 6, that this is however not the ultimate truth as in the case of F_4TCNQ it was theoretically shown, with the help of the MODOS, that accepting electrons, i.e. an almost totally filling of the LUMO is not the only thing that happens.[4,176] This filling results in a too large shift of the molecular levels up in energy. As a consequence, the molecular LUMO would again come to lie above the Fermi level, due to an exaggerated bond-dipole. It was shown that a non-negligible amount of electrons are transferred back into the substrate from the molecule.[4,176]

In that context, noteworthy is that in contrast to the common "textbook"-picture, i.e. the "frontier molecular orbital bonding picture"[ii], here rather uncommonly deeper lying orbitals significantly contribute within the bonding process (*vide infra*).

Integration of the MODOS of a particular molecular orbital up to the Fermi edge enables us to identify all orbitals strongly hybridizing and interacting with the metal. At this point I do not want to revise the detailed analysis given in chapter 6. Nevertheless, for better readability of this chapter I want to quickly recall that upon the bonding process of F_4TCNQ on Ag(111) the molecular LUMO gets largely filled (89%). Important in the present context is that four deeper lying orbitals (HOMO-9 till HOMO-12) significantly donate charge back to the metal. When visualizing these MOs of the isolated molecule one notices that they have a σ-type feature located on the outer cyano groups in common whereas the molecular LUMO is a π-orbital.[iii]

F_4TCNQ: Intramolecular changes We now want to go a step further and analyze the bonds within our molecule and the changes occurring upon bonding, with the help of the COOP. Strong chemisorption together with strong molecular distortions as it is the case for F_4TCNQ (6) affect the molecular backbone in a very distinctive way. Thereby, partial bonds to the surface will form and bonds within the molecule will be weakened or strengthened. Consequently bond length will change as well. The molecular backbone undergoes an aromatic stabilization upon adsorption in a sense that carbon-carbon double bonds of the former, in gas-phase, quinoidal backbone will get longer and carbon-carbon single bonds will get shorter upon bonding including the change in the

[ii] Here, the "frontier molecular orbital bonding picture" represents the common picture of frontier molecular orbitals being the only ones interacting with the substrate upon the adsorption process.

[iii] An additional short-come of our considerations in this part might be the neglect of self-interaction error. A recent theoretical study[229] of 3,4,9,10-perylene-tetracarboxylicdianhydride (PTCDA) showed that its impact might even lead to wrong ordering of molecular orbitals and artificial shifts in energy of up to 1 eV for localized electron density. Here, especially the molecular orbital representations of these four deeper lying molecular orbitals with densities on their terminating cyano groups might be affected. Hence, this might effect the ordering but nonetheless the general conclusions drawn here are not affected.

carbon-nitrogen bond that will get longer in the adsorbed geometry. Such an aromatic stabilization upon adsorption is known to be a driving force of electron transfer. [187]

Let us in a first step analyze such changes in the backbone in terms of bond-order (bond-strength). When shortening a bond, the overlap of the atomic orbitals will be enlarged and hence the total COOP, scaling with the bond-order and as a result with the bond-strength, will be larger and *vice versa*.[iv] The expected behavior can be seen in Figure 65 as there the bond-length change is compared to the change in the ToP of the atoms along the path indicated with numbers in Figure 64. The ToP is the integration of the COOP with respect to energy up until the Fermi energy. A zig-zag alternation pattern, yet of different signs, for both quantities is observed along the molecular backbone. What is remarkable in that context is that when studying the "COOP alternation pattern" of F_4TCNQ the relative changes are especially strong for the carbon-nitrogen bond. This however, provides us with valuable information that in this part of the molecule strong changes upon adsorption within the molecule will occur and successively bonds to the metal can be expected to form here. The bond-order at this position of the molecule is shifted to forming bonds between the N-atoms an the metal (*vide infra*).

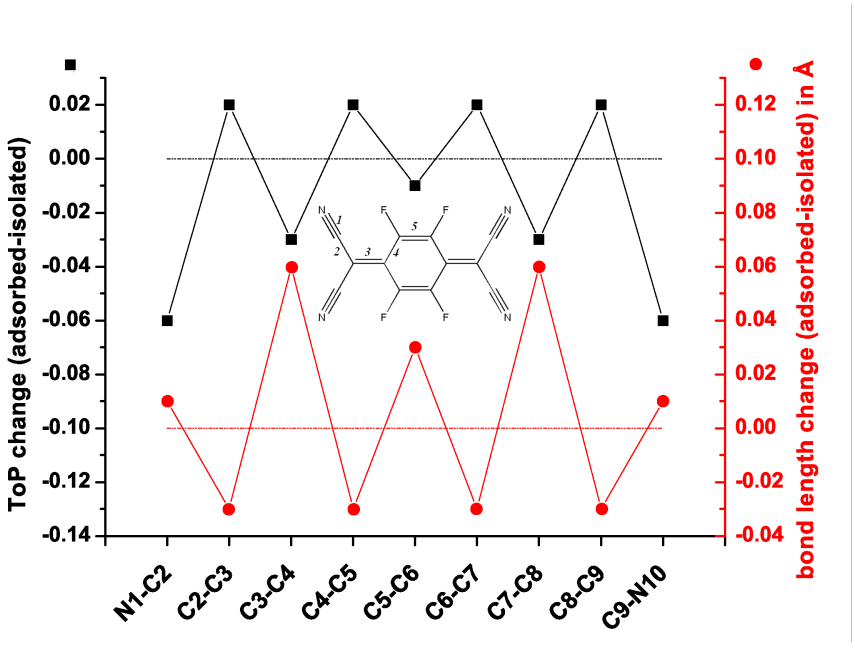

Figure 65: Bottom, right y-axis: Bond- length changes (adsorbed - isolated) - gray or red - of F_4TCNQ on Ag(111) along a selected path of atoms. Top, left y-axis: Total overlap population changes (adsorbed - isolated) of F_4TCNQ on Ag(111) along a selected path of atoms. The horizontal lines indicate zero change and are a guide to the eye to easily see positive or negative changes. For the labeling of the x-axis see inset.

[iv] Note, that Hoffmann states that the COOP scales with the bond-order in his original papers. [64] The bond-order however, is related to the bond-length and consequently it is also an index of bond-strength. In the latter context it is mainly used within this chapter.

In a next step the molecular backbone change and its effect onto the "ToP of the total molecule" is characterized. The "ToP of the total molecule", molecular total overlap population (mToP), is the sum of the ToP of all adjacent atom-pairs of the molecule, i.e. the integration of the COOP of all nearest neighbor atom-pairs of the molecule up to the Fermi edge. It is expected that it is energetically not favorable for the isolated molecule to bent, as found in the adsorbed case. The mToP of the gas-phase planar molecule is expected to be maximized and every distortion should weaken bonds, i.e. lower the intramolecular bonding strength. Therefore, the mToPs of the planar and the distorted molecule are compared. As expected the mToP of the isolated molecule is greater than the one of the distorted molecule. The corresponding values can be found in Table 16.

Table 16: Molecular total overlap population (mToP) of the isolated molecule, the molecule in the distorted, i.e. adsorbed setup and the metal-molecule total overlap population (mmToP) due to the bond with the metal. The last column is the sum of the mToP of the adsorbed (distorted) molecule and the mmToP due the bond. For the definitions of the mToP and the mmToP refer to the main text. The values for F_4TCNQ are reported in this table.

	mToP: isolated	mToP: distorted	mmToP: bond	sum (distorted+bond)
F_4TCNQ	5.16	4.90	0.26	5.16

However, the question yet arising is, why do the molecules bend and bond to the surface when it is energetically more favorable for them to stay planar. To answer that question we have to include the "total overlap population of the molecule and the underlying substrate" as out of that the molecule gains "bonding strength" due to the new bonds formed with the substrate. The "total overlap population of the molecule and the underlying substrate", molecular-metal total overlap population (mmToP), is a direct result of the bond and is defined as the sum of all ToPs of all pairs of atoms consisting of one atom of the molecule and the other one of the top-two metal rows. A total overlap population of pairs consisting of molecular atoms and atoms of deeper lying metal rows is essentially not existing. Table 16 shows that it is indeed favorable for the molecule to bent and bond with the metal, compare mToP and the "sum"-column.[v]

The distortions of F_4TCNQ lead to particularly distinct deviations of the intramolecular COOP, named molecular crystal orbital overlap population (mCOOP), when comparing the isolated and the adsorbed part. Figure 66a shows the mCOOP, i.e. the sum of the COOP of all possible pairs of atoms belonging to the molecule for the adsorbed and the isolated case. A strong shift of the molecular features is visible and especially remarkable are the strong changes in the shape and intensity and the diminishing strong bonding features around 2 eV of the isolated molecule. Previously, it has been seen that an exceptionally larger derivation of the "COOP bond-pattern profile" is found for the carbon-nitrogen bond (*vide supra*). It is reasonable to assume that this will reflect itself in the mCOOP as well. Therefore, in Figure 66b only the contributions of the carbon-nitrogen bonds to the intramolecular COOP of F_4TCNQ are shown, i.e. the sum of

[v] Note that non-covalent bonds would theoretically enhance the mmToP of the molecule metal bond. They are not considered in the here applied analysis.

the COOP of all four C-N pairs. Here, it is clearly visible that this distinctive double feature in the isolated case is due to the carbon-nitrogen COOP that is vanishing in the adsorbed case. This is an additional indication that the bond of the molecule and the metal will be primarily established there.

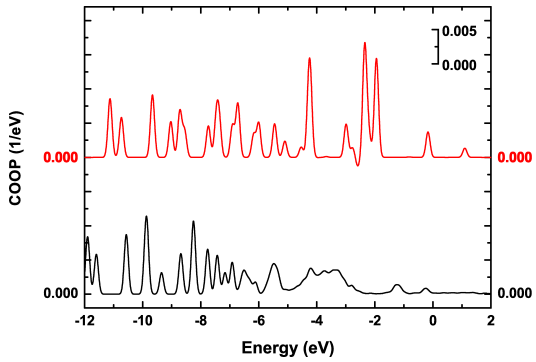

(a)

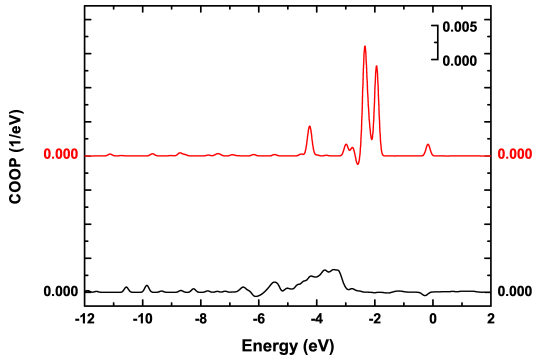

(b)

Figure 66: a): "Intramolecular COOP" (molecular COOP - mCOOP), i.e. the sum of the COOP of all possible combinations of atomic pairs of F_4TCNQ on Ag(111), bottom black, and the isolated F_4TCNQ molecule, top gray/red. b): Contribution of the carbon-nitrogen COOP, i.e. the sum of the COOP of all C-N pairs, to the mCOOP of F_4TCNQ on Ag(111), bottom black, and the isolated F_4TCNQ molecule, top gray/red.

The last finding can be analyzed in greater detail as the "C-N COOP" can be split up into specific interactions of atomic orbitals with each other. In a second step these specific interactions are studied in the adsorbed case.

Figure 67a shows the C≡N bonding feature (black thick line) and specific interactions of atomic orbitals of the carbon and the nitrogen atoms in the isolated case. Figure 67b shows the corresponding analysis for the adsorbed case. Especially, the p-p orbital interaction, i.e. the sum of all px, py and pz overlaps, of both atoms prove to be the major contribution to this characteristic double-bonding feature in the range of -1.5 and -3 eV. As expected for the "high" energy range analyzed, the s-s COOP of the two atoms contributes little. When this analysis is repeated for the carbon-nitrogen bond in the bonded, bent F_4TCNQ molecule (Figure 67b) the p-p orbital COOP is more or less exclusively responsible for the change in shape and the shift in energy of the

analyzed feature. All other orbital-interactions play only an insignificant role as they vanish almost completely for both cases.

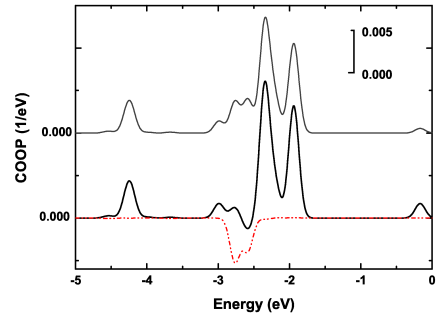

(a)

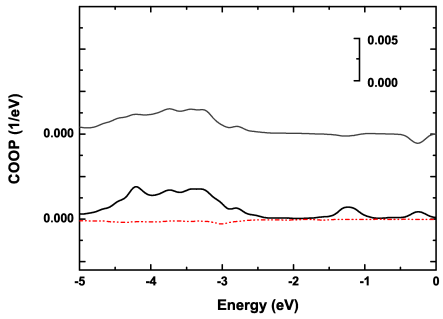

(b)

Figure 67: A detailed analysis of the carbon-nitrogen COOP, i.e. the sum of all individual C-N pairs, of the isolated a) and adsorbed b) F_4TCNQ on Ag(111). The thick black line represents the total carbon-nitrogen atom COOP in both cases. The dash-dotted line (red/gray) represents the s-s overlap and the gray displaces line the p-p COOP.

COOP: Molecule to metal bond In this part we analyze the molecule to metal bond in greater detail with the help of the COOP. We will identify preferred areas of the molecule that act as docking groups and in a next step analyze the role of the different metal bands in the bonding process.

The total COOP of F_4TCNQ with the underlying metal, molecule-metal crystal orbital overlap population (mmCOOP), is shown in Figure 68a. The mmCOOP is defined as sum of the individual COOP of all pairs of atoms with one atom belonging to the molecule and the other one the metal, more precisely to the atoms within the top two metal rows.[vi] In Figure 68a, it is most remarkable that neither strong bonding nor

[vi] The overlap of the molecular atomic functions with the metal atomic functions of atoms belonging to the three deeper lying rows is essentially zero, i.e. the corresponding COOP is zero and hence they are neglected when calculating the mmCOOP.

anti-bonding features occur right at the Fermi edge indicating that the frontier molecular orbital interactions of F_4TCNQ with the metal are not the ones responsible for the strong bond. Nevertheless, three very distinct features can be found, indicated with arrows in Figure 68a. Unexpectedly in this case the first feature closest to the Fermi edge at about -3.2 eV is anti-bonding. It is followed by two prominent bonding peaks when going to lower energies. Tracing down the origin of these features suggests based on our previous considerations studying the role of the outer cyano groups first. Therefore, it is more than reasonable to assume that these specific areas of the molecule will also be strongly entangled in the bond with the metal. This is clearly confirmed in Figure 68a. Here, the gray curve in corresponds to the mmCOOP of the cyano groups with the underlying metal, which is virtually identical to the total mmCOOP. This implies that the covalent bond formed between F_4TCNQ and the metal is exclusively formed due to the interaction of the cyano-groups with the metal states.

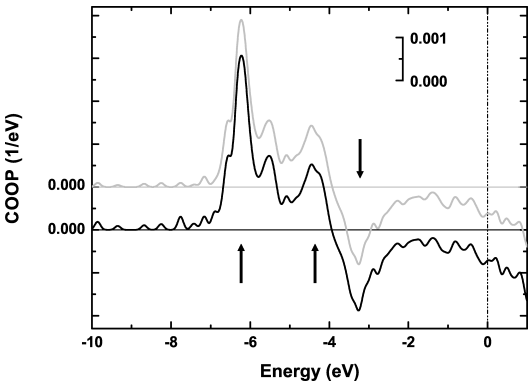

(a)

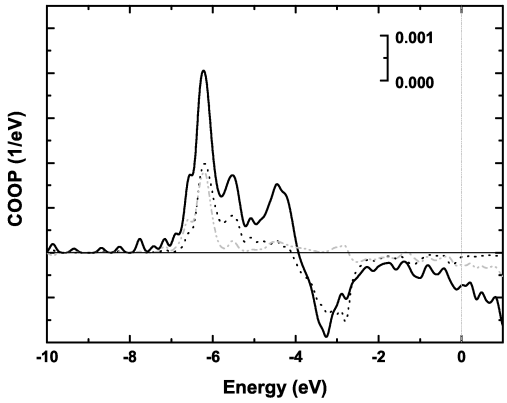

(b)

Figure 68: a) Black: molecule-metal COOP (mmCOOP) of F_4TCNQ with Ag(111). The arrows indicate prominent features that are discussed in the main text. The gray curve is the mmCOOP of only the cyano groups with the underlying metal. b) Contributions of the metal s (gray, dash-dot-dotted line) and d (black, dotted line) band towards the total mmCOOP (black, solid line). The vertical line (dash-dot-dot) at zero indicates the Fermi energy and the horizontal line indicate the division between bonding (positive) and anti-bonding (negative) features.

The cyano-metal bond can be further split up into interactions of the cyano s, p with the metal. The first interesting finding here is that the lowest peak (bonding) in energy is due to N_s and N_{pz} COOP with the metal whereas the N_{px}, N_{py} and N_{pz} COOP with the metal is responsible for the other features (the transition from bonding to anti-bonding).

Additional insight into the metal-molecule bond can be gained when investigating the role of the metal (Figure 68b). Hereby, the mmCOOP of the molecule with the metal s and d band is treated separately. Astonishingly, the metal s-band and molecule mmCOOP is responsible for about half of the major bonding feature lowest in energy (-6.5 eV) whereas for the higher lying bonding to anti-bonding transition it is essentially not contributing. The "other" half of the contribution to this major bonding feature stems from the metal d-band. The diffuse metal orbitals, bearing p-character, used

in *SIESTA* contribute bonding for all three features and are not shown in Figure 68b. They together with the metal d-band are responsible for the bonding peak at -4.5 eV whereas the anti-bonding feature at around -3 eV is essentially due to the metal d-band. Considering the latest finding the metal d-band is essentially not contributing in an overall bonding way as its bonding are canceled with its anti-bonding features. Therefore, in the end of the day the bonding contribution results from metal s-band and molecule interaction.

MOOP: Molecule to metal bond In this part we will introduce a modification of the COOP which will be based on MOs and their "bonding proclivities"[64] with the underlying metal bands.

It was shown previously that as a result of the adsorption, the former, i.e. prior to the adsorption, LUMO is getting largely filled and that a couple of deeper lying orbitals (HOMO-9 till HOMO-12) bearing electron density on the terminating cyano groups significantly loose charge.[4,111] Hence, now, when analyzing the bonding contributions of MOs, as a first rough guess these molecular orbitals are expected to be mainly responsible for the strong covalent bond that is emerging when F_4TCNQ adsorbs on Ag(111).

Figures 69 and 70 show the total MOOP curve, bottom-solid black line, and specific MOOP curves of selected MOs with the underlying metal. The total MOOP curve is the sum of all MOOP curves of all individual molecular orbitals with the underlying metal.

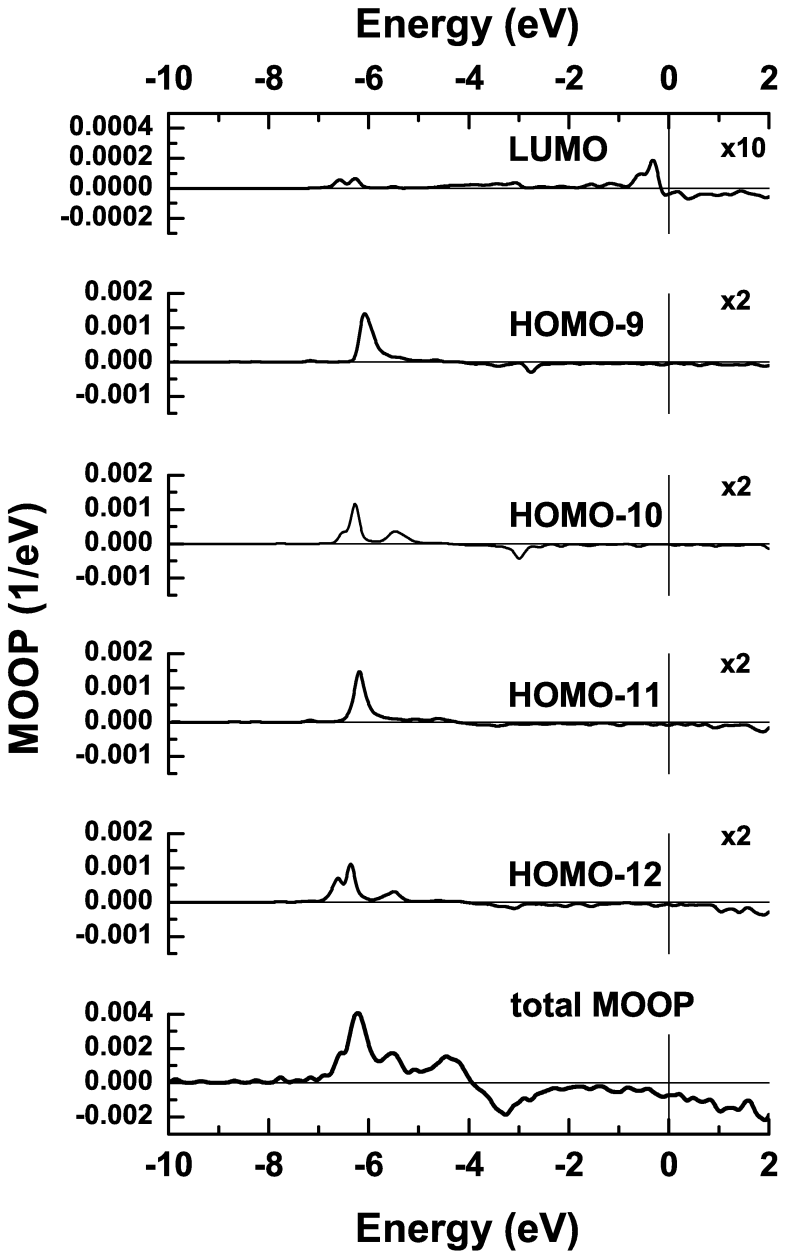

Figure 69: MOOP analysis of F_4TCNQ on Ag(111). Starting from the top: MOOP of the LUMO, MOOP of the HOMO-9, the HOMO-10, the HOMO-11 and the HOMO-12. The bottom shows the total MOOP as sum of all individual MOOPs of all individual molecular orbitals with the metal. The Fermi edge has been aligned to zero for all plots. The $x10$ or $x2$ indicates that the y-axis has been magnified ten times or two times with respect to the total MOOP axis.

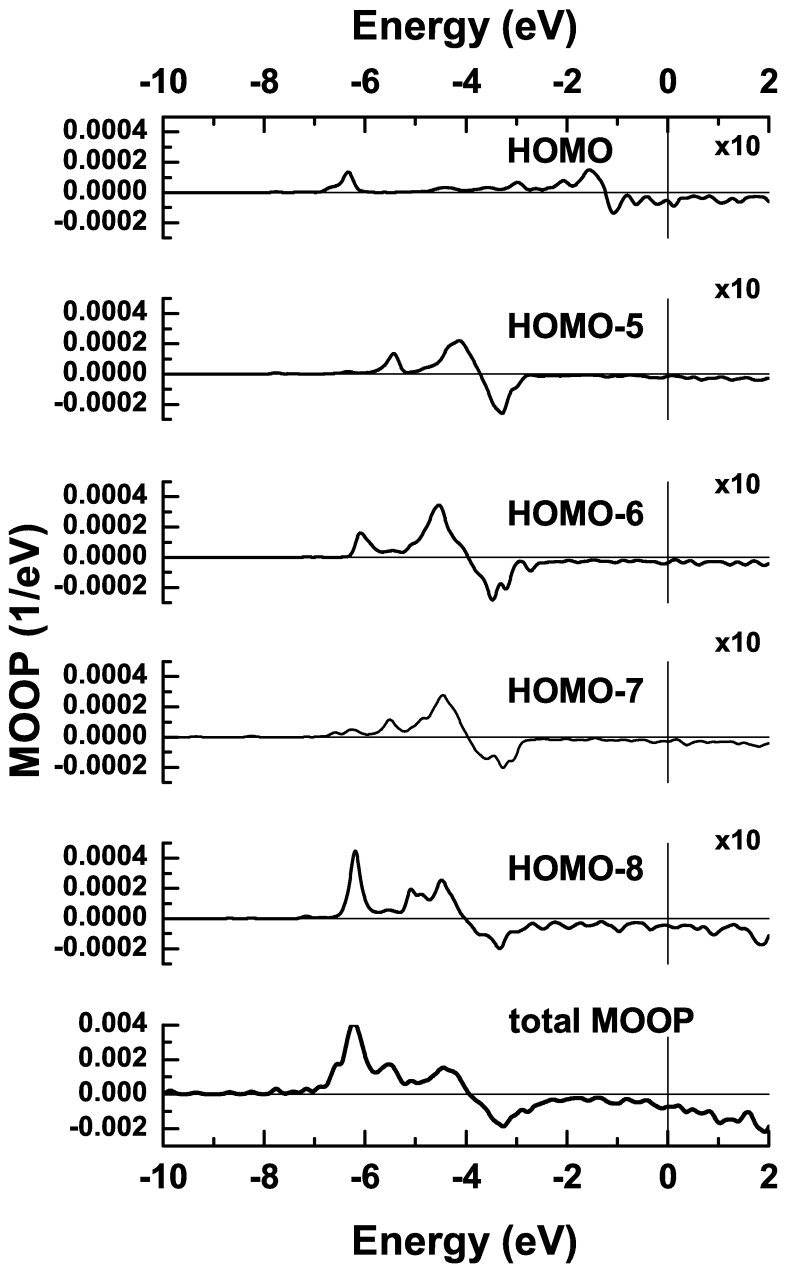

Figure 70: MOOP analysis of F_4TCNQ on Ag(111). Starting from the top: MOOP of the HOMO, MOOP of the HOMO-5, the HOMO-6, the HOMO-7 and the HOMO-8. The bottom shows the total MOOP as sum of all individual MOOPs of all individual molecular orbitals with the metal. The Fermi edge has been aligned to zero for all plots. The $x10$ indicates that the y-axis has been magnified ten times with respect to the total MOOP axis.

The respective molecular orbitals of the depicted MOOP-curves of the previous Fig-

ures are shown in Figure 71.[vii]

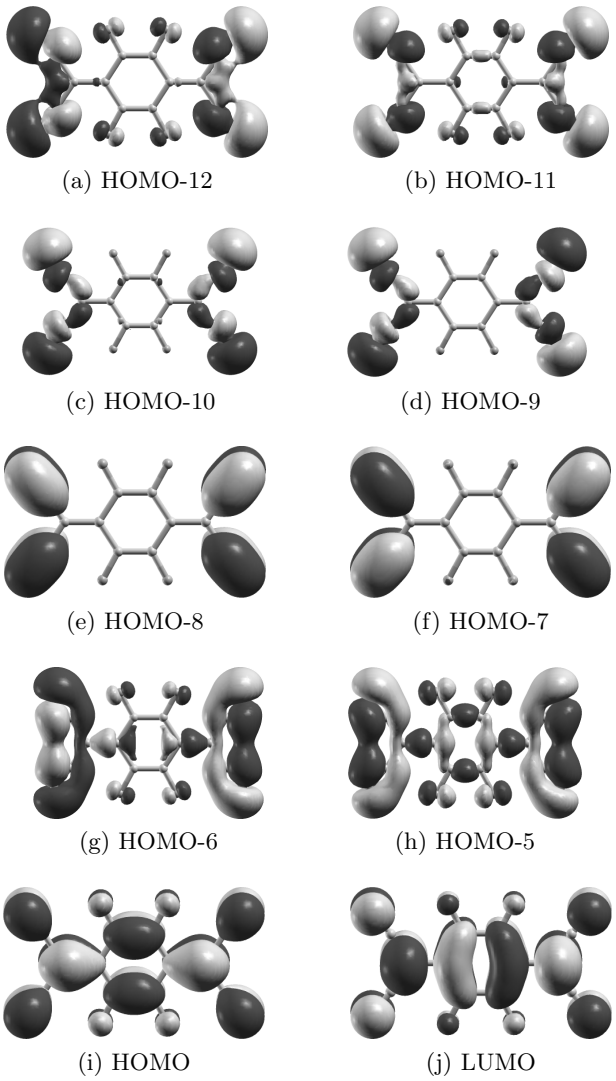

(a) HOMO-12 (b) HOMO-11

(c) HOMO-10 (d) HOMO-9

(e) HOMO-8 (f) HOMO-7

(g) HOMO-6 (h) HOMO-5

(i) HOMO (j) LUMO

Figure 71: Molecular orbitals of the isolated F_4TCNQ molecule.

The collaborative effect of the MOOP of the depicted molecular orbitals as well as one additional selected MOOP of the HOMO-17 can be seen in Figure 72.

[vii] They have been obtained via a separate Gaussian03 calculation (RB3LYP/6-31G(d,p)) and the isodensity value of 0.01 electrons per $Bohr^3$

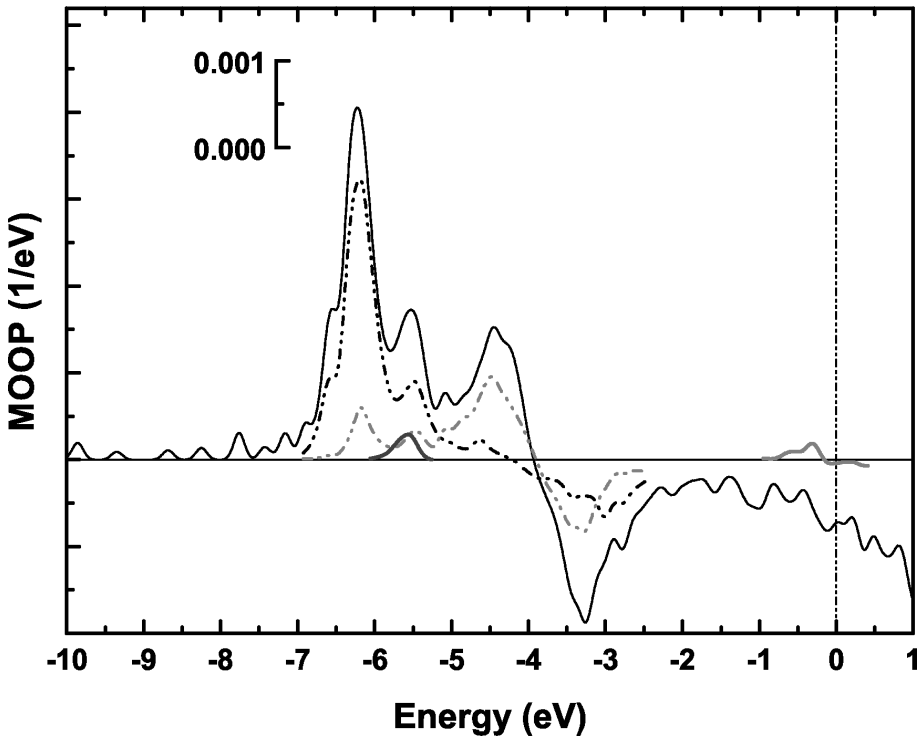

Figure 72: MOOP analysis of F_4TCNQ on Ag(111). The MOOP of the LUMO is seen as weak intensity peak with a transition from bonding to anti-bonding at the Fermi edge (vertical line) in gray. The MOOP of the HOMO-5 till HOMO-8 is shown as gray dash dot dot line, mainly responsible for the transition of bonding to anti-bonding in the range of (-5 to -2.5) eV. The sum of the MOOP of specific molecular orbitals (HOMO-9 till HOMO-12) is shown as black dash dot dot line, mainly responsible for the strongest feature lowest in energy. Furthermore, an additional contribution to the bonding feature at -5.5 eV energy the MOOP of HOMO-17 is shown (dark gray line).

Interestingly, the MOOP of the LUMO, Figure 69 or 72, does not lead to the remarkable features marked with the arrows in Figure 68a as its interaction is located at the Fermi edge and is comparably small. Analyzing it in more detail, the hybridization of the molecular LUMO, iso density representation in Figure 71, with the metal bands lead to exclusively bonding contributions below the Fermi energy and turns anti-bonding around the Fermi edge. Nonetheless, the hybridization of the molecular LUMO shifts its main contribution below the Fermi edge and it contributes "in a bonding way" as can be seen in Figure 73 where the MODOS curve of the LUMO and the MOOP are shown. Note, that the amplitude of the bonding part of the LUMO interaction is by a factor of *20 smaller* than the strongest bonding contribution (around -6 eV), which can additionally be seen in Figure 74 where the integrated MOOP of the LUMO can be seen in comparison to the integrated total MOOP.

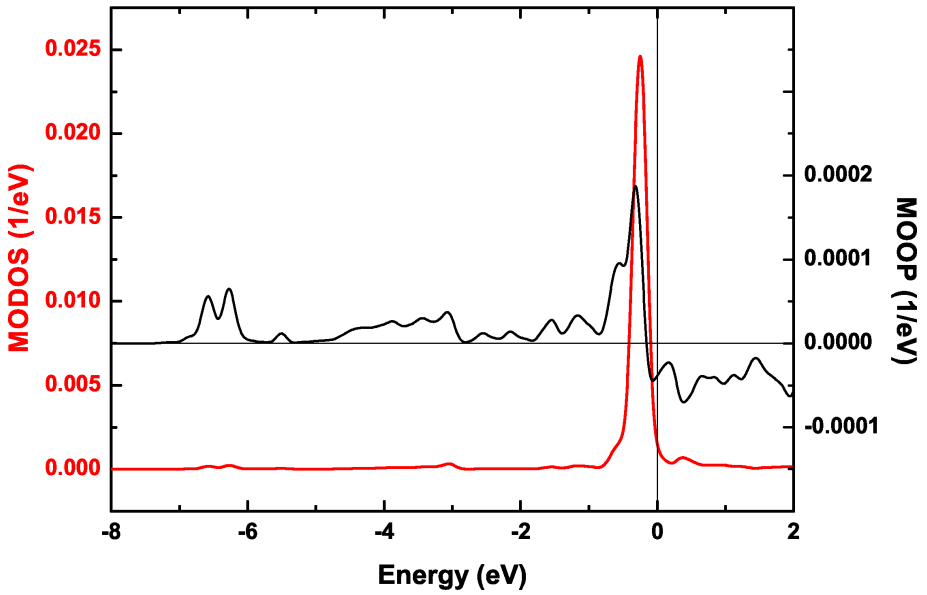

Figure 73: MODOS and MOOP of the LUMO of F_4TCNQ on Ag(111). The Fermi edge is at zero. Note that the main contribution of the LUMO (MODOS-curve) is below the Fermi edge, leading to an almost complete filling after adsorption.

Therefore, other molecular orbitals must be responsible for the three prominent features and in the end of the day also for the strong bond. Also shown in Figure 72 are collaborative MOOP-curves of the 4 deeper lying orbitals (HOMO-12 till HOMO-9, iso-density representations in Figure 71). Comparing the black dash-dot-dotted curve (collaborative effect of the HOMO-9 till HOMO-12) with the total MOOP/COOP (black solid line) one notices immediately that the strongest bonding feature lowest in energy is almost exclusively stemming from these molecular orbital - metal interactions. Nevertheless, they cannot explain the pronounced transition from bonding to anti-bonding following that strong bonding feature when going towards the Fermi energy on the energy scale (between -5.5 and -2 eV). The integrated MOOP of these molecular orbitals interacting with the metal can be seen in Figure 74 as dashed, blue line. Their broad maximum is lowest in energy and the integrated MOOP decreases when going towards the Fermi energy.

However, additional molecular orbitals, different from the once previously identified as important ones within the bonding process,[4,111] must interact in the energy range of -5.5 to -2 eV to explain this transition. An interplay of several molecular orbitals (HOMO-8 till HOMO-5, iso-density representations in Figure 71) with the metal band is necessary to obtain the basic shape of this transition. Herby, the HOMO-5 and 6 both feature a kind of σ-shape electron density on the terminating cyano groups as well, whereas the HOMO-7 and 8 are π-orbitals with their electron density exclusively lying on the cyano groups, representations can be seen in Figure 71. Their integrated MOOP (purple, dash-dotted line in Figure 74) features a narrow maximum at slightly higher binding energies and declines drastically towards the Fermi edge.

Noteworthy here is that the slight increase the MOOP at around -5.5 eV is also due to the MOOP of the HOMO-17 which shows a bonding peak in this range. Note that it is of the same magnitude as the contribution of the molecular LUMO MOOP.

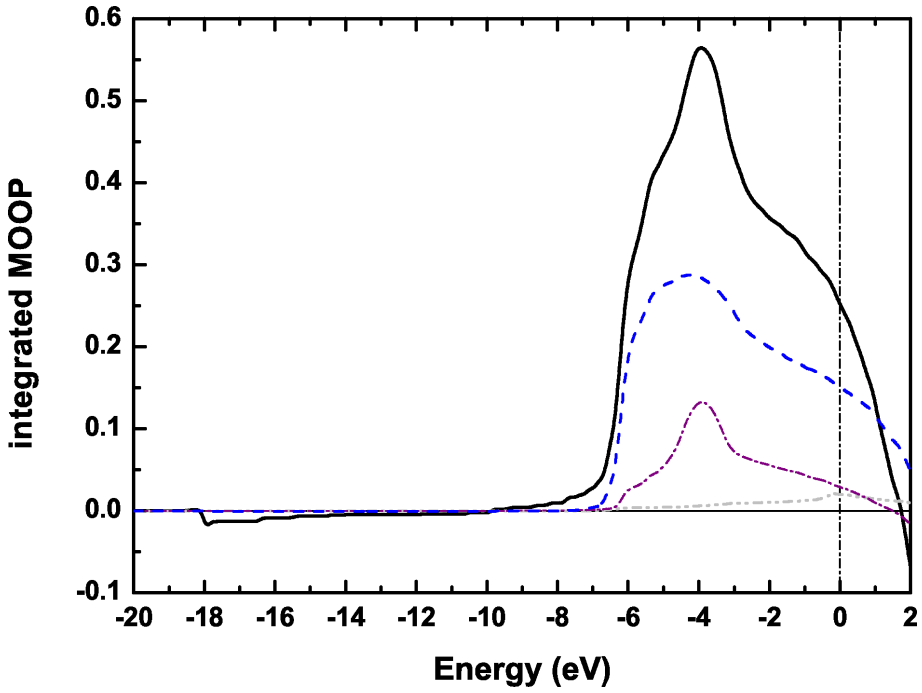

Figure 74: Integrated MOOP of F4TCNQ on Ag(111) - black thick line, and integrated MOOP of the same selected molecular orbital-metal interactions as in Figure 72. The integrated MOOP of the sum of the MOOPs of the (HOMO-12 till HOMO-9, blue dashed line) and (HOMO-8 till HOMO-5, purple dashed-dotted line) as well as the integrated MOOP of the LUMO (gray dash-dot-dotted line). The vertical line indicates the Fermi edge.

Figure 74 shows drastically that all the MOOPs of the different molecular orbitals with the metal contribute in a bonding way as they all are positive at the Fermi edge. Noteworthy, is furthermore that the contribution of the molecular "LUMO-MOOP" (gray, dash dot-dotted line in Figure 74) is comparably small, especially when compared to the impact of the MOOP of the HOMO-12 to HOMO-9. Yet, even previously unrecognized molecular orbital interactions (HOMO-8 till HOMO-5) are precious in terms of bonding as their overlap population is even stronger than the one for the LUMO, compare Figure 74.

Influence of the molecular distortions onto the covalent molecule-metal bond This part will show that the molecular distortions developing upon bond formation are essential for the covalent bond. Thus, we will compare the bent molecule with a straight molecule at the same distance on the same metal. Therefore, the bent "outer" parts of the molecule were forced planar in a way that all atoms had the same height as the

central atoms.

Figure 75 shows the total COOP curve of a straight and a bent F_4TCNQ molecule on Ag(111). The total COOP curve is the sum of all possible combinations of COOP curves with one atom belonging to the molecule and the other one belonging to the top two metal rows.

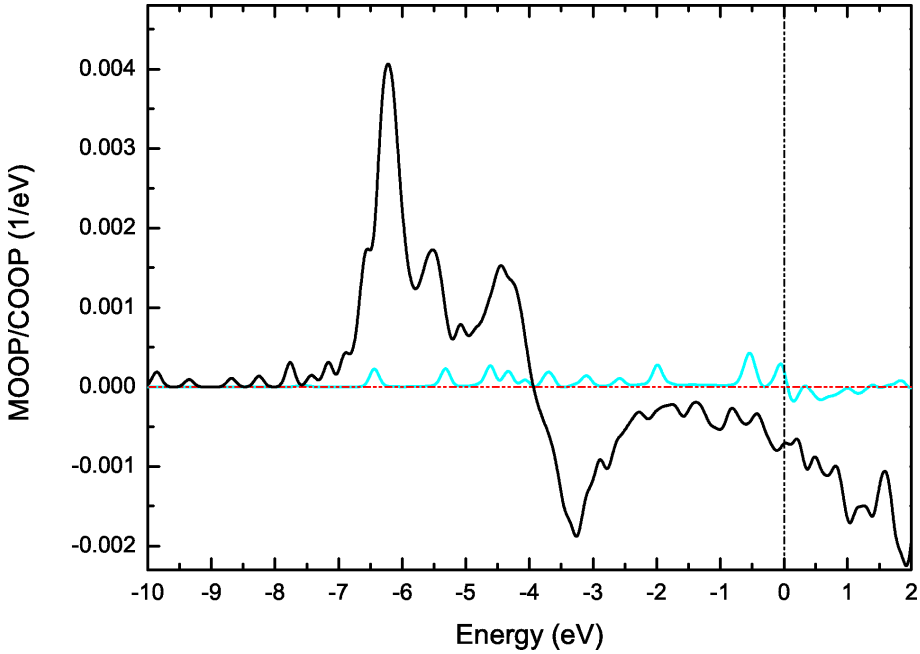

Figure 75: Total COOP/MOOP curves of a bent (solid black line) and a straight (gray, cyan line) F_4TCNQ molecule on Ag(111). The vertical line at zero indicates the Fermi edge and the horizontal line at zero indicates the boarder between bonding and anti-bonding.

Note that the amplitude of the COOP is *reduced* by more than a factor of *10* for the straight adsorption case. This clearly proves that the bent is *crucial* for the development of the strong covalent bond. The mmToP changes from 0.26 for the bent to 0.09 for the straight F_4TCNQ on Ag(111) signaling that the bonding strength is about 3 times smaller for the straight F_4TCNQ. Thus, in the end of the day it is indeed preferable for the former planar F_4TCNQ to bend and bond on the Ag(111) surface as can be seen in Figure 76 where the mmCOOP is shown for both setups.

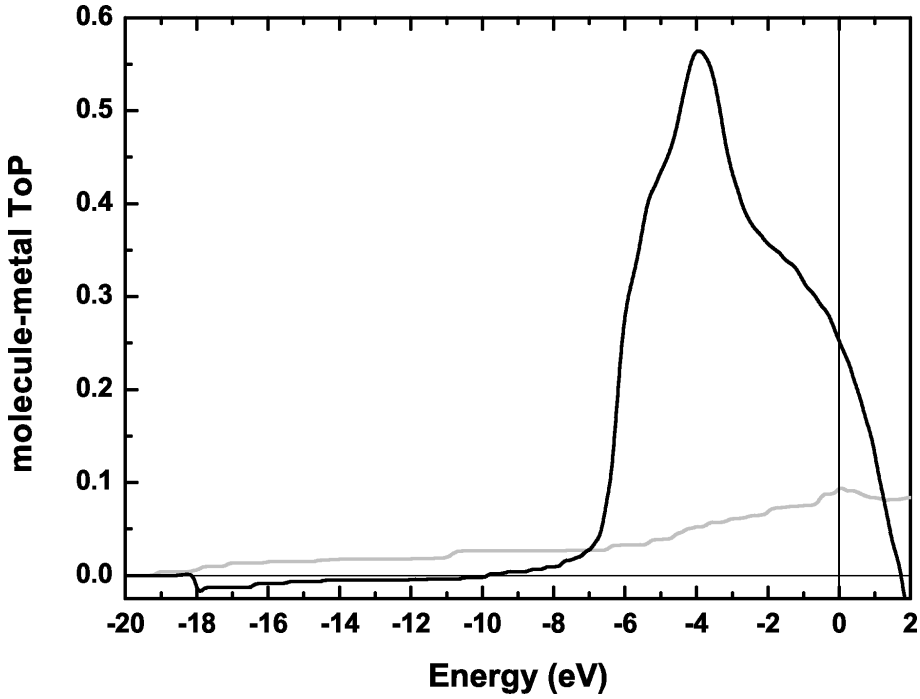

Figure 76: Molecular-metal total overlap population (mmCOOP) for the straight F_4TCNQ molecule (gray) and the bent F_4TCNQ molecule (black) on Ag(111). The vertical line at zero indicates the Fermi edge.

10.1.3 Summary and conclusions

This part of the thesis was aiming to explain the complicated processes occurring upon bonding of organic molecules on metal surfaces on a descriptive way for the broad audience. Therefore, a well characterized model molecule, namely F_4TCNQ was chosen and investigated on Ag(111). By applying the COOP and the MOOP molecular orbitals, regions of the molecule and even atoms as well as metal bands involved in the bonding process were identified.

These results however, might lead to reconsider our knowledge about bonding of molecules on surfaces as the common textbook frontier molecular orbital bonding picture proves misleading in our cases. Here, the "main-actual bonding contributions" result from molecular orbitals bearing electron density at the terminating cyano groups (HOMO-5 till HOMO-12). Nonetheless, it *clearly disproves* the frontier molecular orbital picture as the role of the HOMO and LUMO in terms of bond-strength is secondary. Additionally, formerly overlooked MOs (HOMO-5 till HOMO-8) were found to decisively participate in the bonding process. Hence, in our case mainly the interactions of deep lying molecular orbitals are responsible for the strong bond.

Furthermore the cyano-groups were unambiguously identified as docking groups. It was shown that the geometric distortions of the molecule introduced upon the adsorption is crucial for the strong covalent bond established between the molecule and the substrate.

Last but not least an additional important implication of this present study is that the calculations prove crucial for a concise understanding of the complex bonding picture as conclusions merely drawn from photo-spectroscopy experiments might be misleading. This can be seen for the case of F_4TCNQ where based on experiments a filling of the LUMO was claimed.[167] Additionally, theoretical studies[4,176] highlighted the importance of deep lying orbitals (HOMO-9 till HOMO-12). Nonetheless, the impact of other deep lying orbitals could only be discovered using the COOP and the MOOP. In conclusion for a fundamental description of all the processes governing the adsorption a broad variety of theoretical and experimental techniques is necessary.

10.2 Forgotten orbitals within the bonding process of HV0.

This part deals with the adsorption of a strong donor HV0 on Au(111). The whole process will be analyzed with the help of the COOP and the MOOP. Theoretically, it has been shown that the adsorption of HV0 results in a work-function reduction of up to -1.6 eV on pristine Au(111).[205] Experimentally, a derivative of HV0, the extraordinary strong organic donor 1,1'-dimethyl-1H,1'H-[4,4']bipyridinylidene (MV0) on Au(111) has been shown to decrease the electron injection barrier into subsequently deposited organic electron transport layers such as Fullerene (C_{60}) and Aluminium-tris-(8-hydroxychinolin) (Alq3) by as much as 0.65 eV and 0.80 eV as it strongly reduces the work function of the Au electrode.[204]

Hence, a precise understanding of the interface properties governing this behavior is highly desired. Thereby, theoretical modeling of the interface is of crucial importance. For HV0 it has been shown that when analyzing the molecular orbitals of the molecule and their role within the bonding process the main effect is an emptying of the highest occupied molecular orbital (HOMO).[205] Based on that result it is expected that only the molecular HOMO is responsible for the established bond. The corresponding bonding energy is reported to be 1.25 eV for HV0 on Au(111).[205] The present contribution, however, will highlight that more is hidden within the bonding process and that former unidentified molecular orbitals will play a decisive role.

Before the focus is turned to the results of the the bonding process of HV0 is analyzed with the help of the MODOS we want to recall what one intuitively expects to happen when a strong donor is put on a surface.

HV0 is a strong donor with a calculated vertical ionization potential (IP) of 4.85 eV in gas phase.[205] When aligning such a donor with a suitable metal, where the metal Fermi energy is close to or below the respective HOMO position prior to contact, a strong chemical bond is expected to establish upon contact. Considering the latter situation, i.e. molecule and metal in contact, it can be easily deduced that the donor HV0 is *donating* its electrons to the underlying substrate as the HOMO comes to lie above the metal Fermi energy when simply considering vacuum level alignment. As a result, the molecular levels shift downwards in energy and broaden until finally thermodynamically equilibrium is reached. Thereby, for Au(111) the interactions at the Fermi edge will be with the metal s-band and interactions lower in energy will be preferably with

the metal d-band as the metal s-band cuts the Fermi edge whereas the metal d-band is located deeper down in energy.

10.2.1 Results and discussion

Before the covalent bond is investigated with the COOP and afterwards with the MOOP the results based on the MODOS analysis is presented. Afterwards, the changes within the molecular backbone occurring upon adsorption will be studied with the COOP. In a next step the bond between the molecule and the metal is analyzed and especially important areas of the molecule will be pointed out. Here, also the influence of the metal bands will be highlighted. Then this picture is widened as then the molecular orbitals and their role within bonding are critically considered. In the end, the impact of the slight bent of the molecule is studied.

Via integrating the MODOS for every molecular orbital separately up to the Fermi edge one gets a number for the occupation of a specific orbital after bonding. Herby, a computational study of the adsorption of HV0 on Au(111) revealed that only the molecular HOMO looses charge (60% filling after adsorption).[205] Besides, that study shows that upon adsorption the molecular backbone undergoes a partial transition from a quinoidal to a benzoidic geometry,[205] which reflects itself in bond-order changes of the individual atom-pairs within the backbone. This however, can be analyzed with the COOP as it was previously done for the acceptor F_4TCNQ (see 10.1.2). The adsorption of HV0 gives rise to a reasonably large adsorption energy -1.25 eV.[205] Overall, the dipole as a result of interfacial charge transfer is calculated to be $\mu_{\text{bond}} = 7.25\,\text{Debye}$.[205] The dipole arising from geometric distortion of the molecule upon adsorption amounts to $\mu_{\text{bond}} = 1.3\,\text{Debye}$.[205] As a result the overall work-function modification turns out to be $\Delta\Phi = -1.20\,\text{eV}$.[205]

HV0: Intra-molecular changes In this part, the bonds within the molecule are analyzed with the help of the COOP. Thereby, the changes within the molecule resulting from the adsorption process will be studied. Recall the general feature of a COOP curve, i.e. bonding contributions are positive and anti-bonding negative. The establishment of a strong bond with the substrate as well as molecular distortions affect the molecular backbone. This can be analyzed when comparing the backbone of the isolated planar with the backbone of the adsorbed molecule. As a matter of fact, partial bonds to the surface will form and bonds within the molecule will weaken. Consequently, the bond length of the separate atoms in the molecular backbone will change. As stated in the introduction, the molecular backbone undergoes an aromatic stabilization upon adsorption in a sense that carbon-carbon double bonds of the former, in gas-phase, quinoidal backbone will get longer and carbon-carbon single bonds will get shorter upon bonding. This should reflect itself in the COOP as this quantity scales with the bond-order (bond-strength).[64] The expected behavior can be seen in Figure 77 together with the chemical structure of HV0. A zig-zag alternation pattern for both quantities, the bond-length and the COOP, is observed along the molecular backbone. The numbering of the

atoms, i.e. the path along the backbone is indicated in the inset of Figure 77. Remarkable in that context is that the central double bond of the isolated molecule is changing most. This, however might indicate a possible braking position of the molecule when for example thermal desorption spectra (TDSs) are recorded.

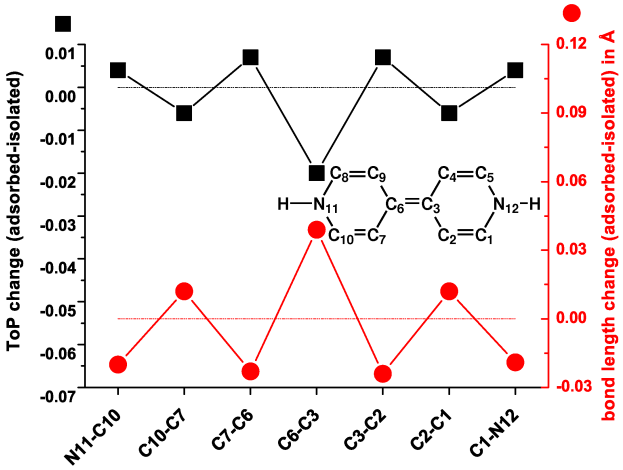

Figure 77: Right y-axis: Bond length changes (adsorbed - isolated) -red points - of HV0 on Au(111). Left y-axis: Corresponding total overlap population (ToP) changes (adsorbed - isolated) - black squares of the selected atom pairs. The horizontal lines indicate zero change and are a guide to the eye to easily see positive or negative changes. The inset shows the structural formula of HV0. For the labeling of the x-axis see inset.

A comparison of the calculated mCOOPs, i.e. the sum of the COOP of all possible pairs of atoms for the isolated and the adsorbed case, are seen in Figure 78. One notices no qualitative change, neither in shape nor in intensity for HV0 on Au(111). This is in strong contrast to the adsorption of the acceptor F_4TCNQ on Ag(111), compare Figure 66a in section 10.1.2. Nevertheless, also for HV0 the effect of the bond with the metal is visible. Especially in the energy range between -10 eV and -2 eV. Here, some double features of the isolated molecule vanish and emerge as a single feature after bonding. Overall it can be concluded that the molecular backbone does not strongly change its bonding properties. This indicates that only a few atoms, molecular orbitals, will participate in the bonding process.

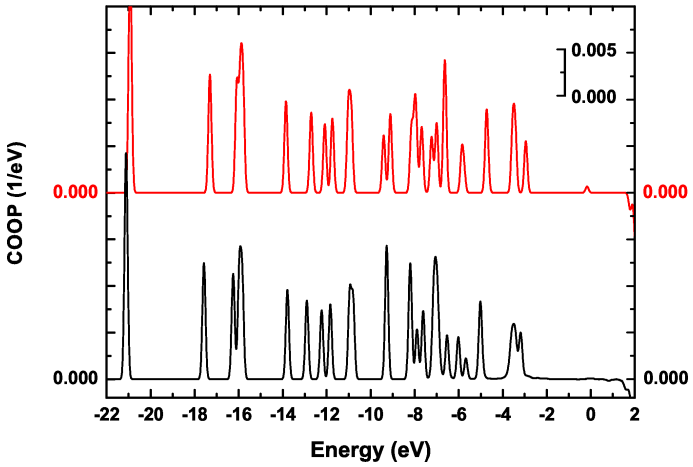

Figure 78: "Intramolecular COOP" (molecular COOP - mCOOP), i.e. the sum of the COOP of all possible combination of atomic pairs of HV0 on Au(111), bottom black, and mCOOP of the isolated HV0 molecule, top red.

Investigating the "intramolecular bond strength", i.e. mToP, the same trend becomes clear. To obtain this quantity one has to integrate the COOPs in energy up to the Fermi edge for all possible combinations of atoms of the molecule.[64] The so obtained number reflects the binding strength. As expected, the relative change is weak - it changes from 4.99 for the isolated molecule to 4.95 in the adsorbed case. What is reflected however is that it is indeed energetically not favorable for the isolated molecule to change its minimum position, i.e. leave planarity as in the adsorbed case the molecule features a slight bent.[205] The mToP of the gas-phase planar molecule is maximized and every distortion weakens bonds, i.e. lowers the intra-molecular bonding strength and hence is not desired. At this point a the question arises, why the molecule eventually bends and bonds to the surface. Overall, it must be energetically favorable for the molecule to do so as the adsorption of MV0 on Au(111) proves.[204] The newly formed bonds with the surface prove to be crucial and they have to be considered in this simple equation to answer the question. The mmToP, as defined as the sum of the ToP of all pairs of atoms with one atom belonging to the molecule and the other one to the top two metal rows, being a direct consequence of these new formed bonds is 0.09. Hence the sum of the mToP in the adsorbed case and the mmToP amount to 5.04. This value is now larger than the mToP of the isolated molecule, 4.99. Table 17 summarizes this result as it lists the mToP of the isolated and adsorbed molecule as well as the mmToP and the sum of the mToP and mmToP for the adsorbed case.

Table 17: Molecular total overlap population (mToP) of the isolated molecule, the molecule in the distorted, i.e. adsorbed setup and the metal-molecule total overlap population (mmToP) due to the bond with the metal. The last column is the sum of the mToP of the adsorbed (distorted) molecule and the mmToP due the bond. For the definitions of the mToP and the mmToP refer to the main text. The values for HV0 are reported in this table.

	mToP: isolated	mToP: distorted	mmToP: bond	sum (distorted+bond)
HV0	4.99	4.95	0.09	5.04

HV0: Molecule to metal bond - COOP In this part, the molecule to metal bond is analyzed in greater detail with the help of the mmCOOP. As it has been seen, new bonds will emerge, leading to an mmToP between the metal and the molecule. The mmCOOP is defined as sum of the COOP of all pairs of atoms with one atom of the molecule and the other one being from the top two metal rows.

The mmCOOP of HV0 with the underlying metal is shown in Figure 79.

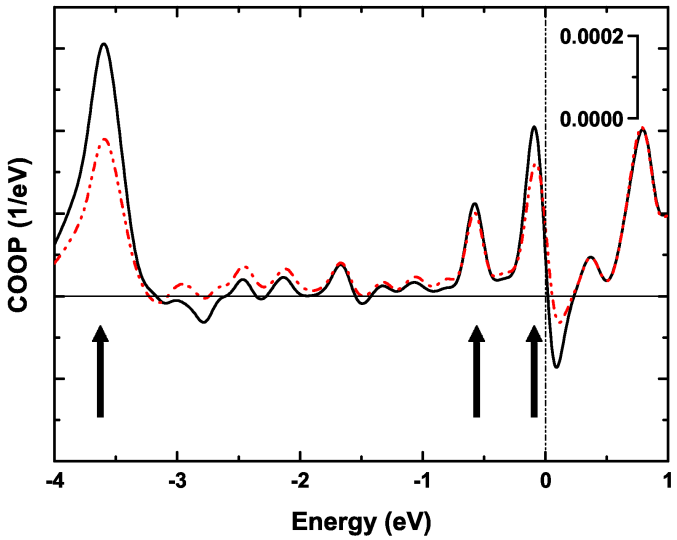

Figure 79: Molecular-metal COOP (mmCOOP) of HV0 on Au(111), black, solid curve, and the sum of the COOP of the secondary amines with the adjacent C atoms, including their H-atoms and the top two metal rows (gray/red, dash-dot-dot line). The vertical line (dash-dot-dot) at zero indicates the Fermi energy and the horizontal line indicate the division between bonding (positive) and anti-bonding (negative) features.

Remarkable on first sight is the transition from bonding to anti-bonding right at the Fermi edge, marked with an arrow. Two additional distinctive peaks are marked with an arrow in Figure 79 indicating specific areas of strongly bonding features. These are the bonding contributions right below this bonding to anti-bonding transition at the Fermi edge at about -0.6 eV and the prominent bonding peak at lower energy (about -3.6 eV). Here it becomes obvious that the "frontier molecular" orbital bonding picture

partially holds true. Nonetheless, some deeper lying molecular orbitals seem to be involved in the bonding process as well. For the donor it is expected that the molecular HOMO is mainly responsible for the bond. Therefore, these strong features at the Fermi edge should somehow be linked with interactions of the HOMO with the metal. When additionally considering the molecular distortions,[205] i.e. the secondary amine groups are slightly closer to the metal surface than the central part, it is expected that the bond is established in that region of the molecule. A part of the mmCOOP, namely the sum of the COOP with the atoms of the molecule being the secondary amine groups and their surrounding carbon atoms (including the saturating hydrogen atoms) with the metal, is shown in Figure 79 as red dotted curve. It reproduces all prominent mmCOOP features. Some of them are even enhanced when just considering these atoms whereas the bonding feature at about -0.6 eV binding energy is almost perfectly reproduced.

Figure 80 decomposes the mmCOOP of the HV0 with the underlying metal into contributions of the different metal bands.

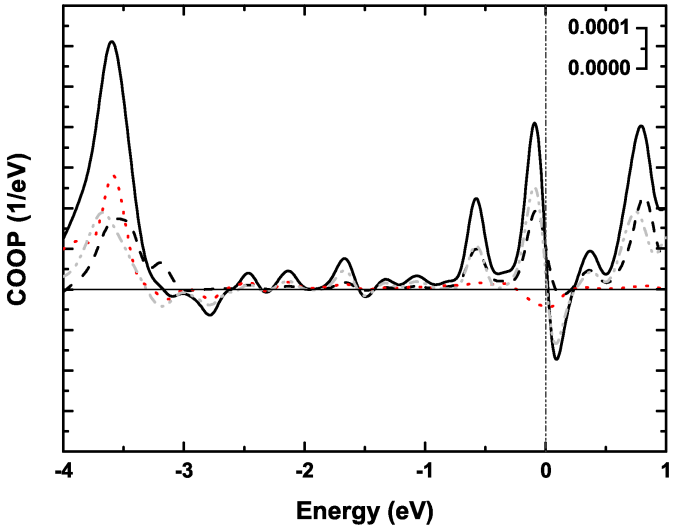

Figure 80: Analysis of the influence of the metal bands on the bond. Black solid in is the mmCOOP of HV0 on Au(111). The gray, dash-dot-dotted line corresponds to the metal s-band - HV0 mmCOOP. The red, dotted line is the metal d-band viologen interaction and the black, dashed line the interaction of *SIESTA* specific diffuse orbitals, bearing p-character, with the molecule. The vertical line (dash-dot-dot) at zero indicates the Fermi energy and the horizontal line indicate the division between bonding (positive) and anti-bonding (negative) features.

Here, it is clearly revealed that metal d-band interactions do not play a role at all at the Fermi edge, as intuitively expected (*vide supra*). At the Fermi edge, metal s-band and diffuse metal orbital molecule interactions are the ones responsible for the shape of the curve. For the most prominent feature at -3.5 eV the interaction of HV0 with all three metal components (s-band, d-band and "diffuse p-band") contribute equally. Therefore, for the molecule metal interaction in that case the metal d-band contributes in a strongly bonding way deeper down in energy and at the Fermi energy the metal

s-band and "diffuse p-band" contribute equally.

HV0: Molecule to metal bond - MOOP In this part, the molecular orbitals and their role within the bonding process are analyzed. As previously discovered the molecular HOMO is expected to be a key orbital within the bonding process.

Based on the theoretical study of Hofmann et al. [205] it is reasonable to assume that the strong connection of the HOMO with the charge transfer will reflect itself in bonding contributions in the MOOP. The "half empty" HOMO, calculated to be around 60% occupied after adsorption,[205] being the frontier orbital in that case, should be visible as an almost perfectly "symmetric" transition from bonding to anti-bonding at the Fermi edge within the MOOP. Figures 81 and 82 show the total MOOP curve as being the sum of all MOOPs of all molecular orbitals with the underlying metal (black solid line) and MOOPs of selected molecular orbitals with the metal.

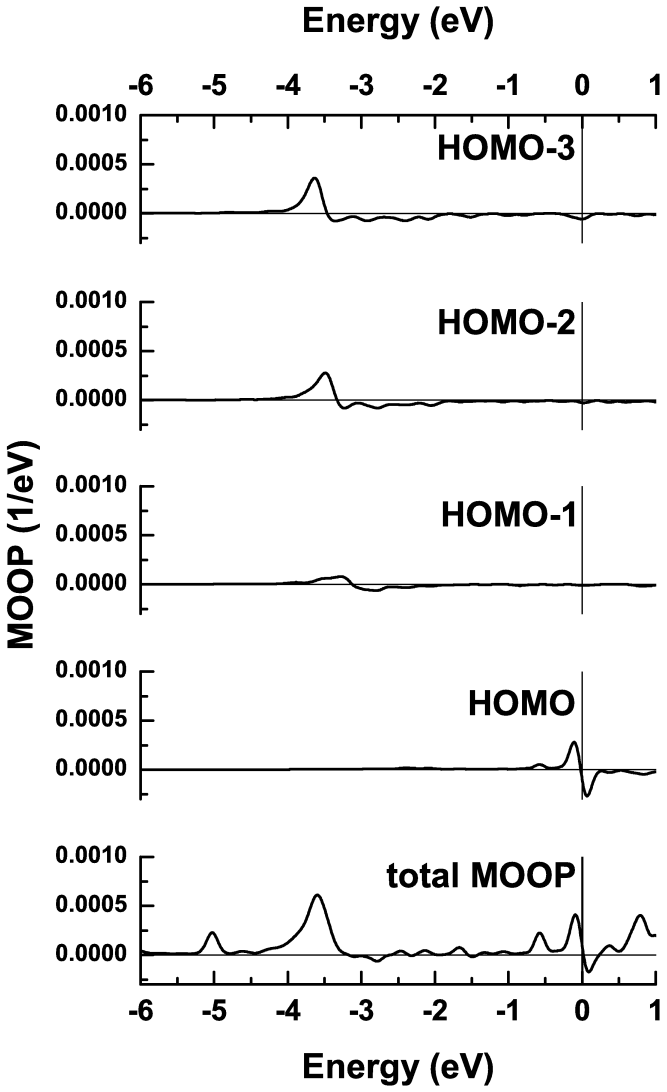

Figure 81: MOOP analysis of HV0 on Au(111). The bottom curve shows the total MOOP of HV0 on Au(111), i.e. the sum of all MOOPs of all individual molecular orbitals and the metal. The "HOMO", "HOMO-1", "HOMO-2" and the "HOMO-3" MOOP are shown explicitly. The Fermi edge is set to zero and all curves are aligned.

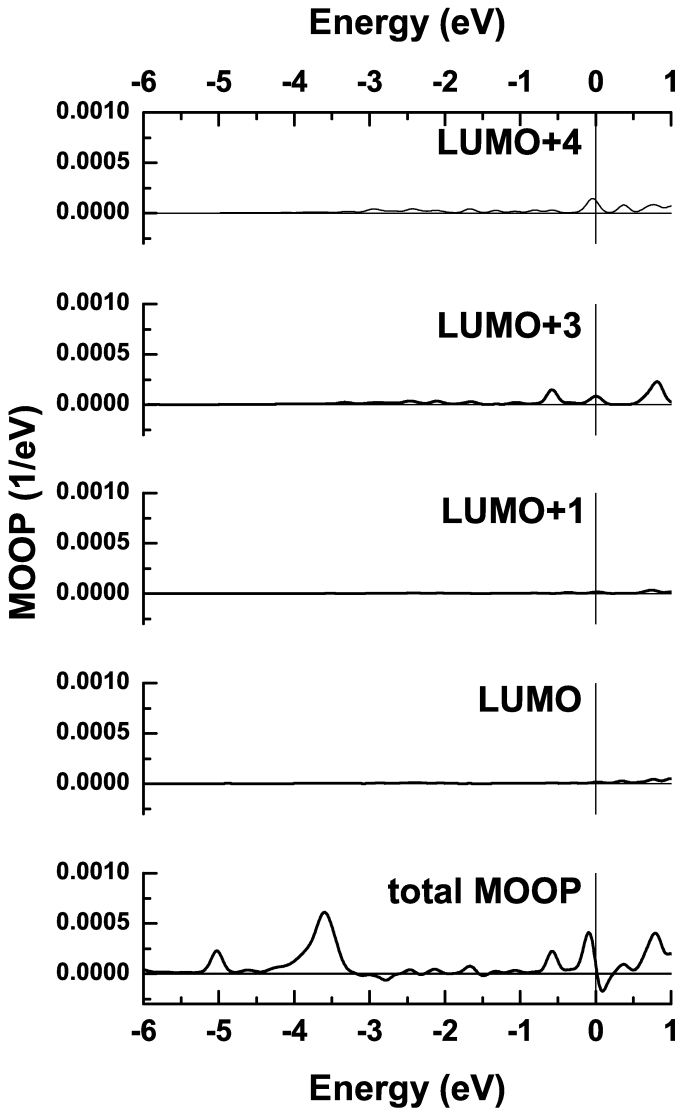

Figure 82: MOOP analysis of HV0 on Au(111). The bottom curve shows the total MOOP of HV0 on Au(111), i.e. the sum of all MOOPs of all individual molecular orbitals and the metal. The "LUMO", "LUMO+1", "LUMO+3" and the "LUMO+4" MOOP are shown explicitly. The Fermi edge is set to zero and all curves are aligned.

As expected the "HOMO curve", Figure 81, is responsible for the transition from bonding to anti-bonding right at the Fermi edge. An easy way of understanding this is that due to the bond formation and the loss of electrons the" molecular HOMO" position was shifted towards higher energy, i.e. closer to the Fermi level of the metal. Hence, the Fermi edge cuts through the contribution of the HOMO-hybrid state. This leads to bonding and anti-bonding states at the Fermi edge. However, in that context the expected almost symmetrical contribution is disturbed. Therefore, other molecular orbitals must disturb in that energy window as well.

An obvious guess, as there are additional bonding peaks right below the HOMO peak as well, are deeper lying molecular orbitals. Therefore, the MOOP curves of deeper lying molecular orbitals were analyzed, Figure 81. Astonishingly the MOOP of the HOMO-1 does not contribute significantly at all, i.e. it is essentially non-bonding. Hence, it is not responsible for the asymmetry observed at the Fermi edge and the bonding contribution just below the HOMO feature. The MOOPs of the HOMO-2 and HOMO-3 (gray, dotted lines at around -3.5 eV) lead to the strong bonding feature at around -3.5 eV. Now, when continuing to analyze deeper lying orbitals one would essentially get the major impacts even further down in energy. As a matter of fact, the assumption that deeper lying orbitals cause the asymmetry at the Fermi edge transition is wrong. Therefore, the puzzle of asymmetry and of the bonding contribution at around -0.8 eV remains to be solved.

As deeper lying molecular orbital interactions did not explain their existence the only possibility is to look into previously unoccupied states, Figure 82. These states however, did not attract much attention in the previous study as they do not significantly gain electron density upon adsorption.[205] In terms of establishing the covalent bond, however, they need to be considered. More precisely, the MOOPs of the LUMO+2 and LUMO+3 (dark-gray, dash dot dotted lines in the interval -1 to 1 eV) are responsible for the asymmetry and the bonding peak at -0.8 eV. An orbital representation of these two reveals increased σ-character around the secondary amine parts of the molecule. The molecular orbital representations of all important orbitals within the bonding process are shown in Figure 83.

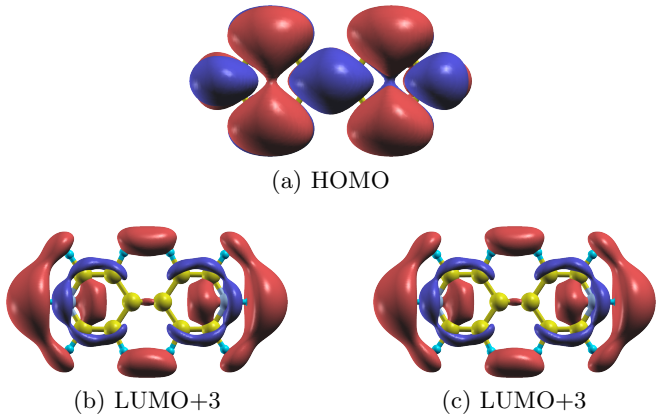

(a) HOMO

(b) LUMO+3

(c) LUMO+3

Figure 83: Selected molecular orbitals of the isolated HV0 molecule.

The integrated MOOP of the discussed molecular orbitals and the underlying metal is shown in Figure . The value of this quantity at the Fermi edge is connected to the "bonding strength" as the sum for all integrated MOOPs for all molecular orbitals with the metal equals the mmToP. Astonishingly, the HOMO-2 and HOMO-3 among others are in fact important to explain the general shape of the MOOP curve, cmp. Figure 81, but do not significantly contribute to the mmToP. The most important contributions to the mmToP result from the LUMO+3 and LUMO+4 interactions with the metal, see Figure . This is insofar surprising as they do not bear significant electron density,

around 2%.[205] The contribution of the HOMO to the mmToP is by a factor of 2 smaller than the contributions of the former unoccupied molecular orbitals. As a result, the previously unrecognized, former empty molecular orbitals gain increased importance when analyzing the metal//molecule bond in terms of the MOOP.

Influence of the molecular distortions onto the covalent molecule-metal bond The aim of this paragraph is to show that the molecular distortions developing upon bond formation are essential for the covalent bond. Therefore, the ToP of the bent molecule is compared with the ToP of a straight molecule at the same distance on Au(111).

Therefore, the bent "outer" parts of the molecule were forced planar at the height of the central atoms. Comparing the total overlap population of the two systems (bent and straight HV0) a reduction from 0.09 for the bent, to 0.01 for the straight molecule on Au(111) is observed. The latter is essentially non-bonding, indicating the importance of the bent, as all the bonding features actually vanish in the straight setup (curve not shown). This effect is not so pronounced as previously noted when analyzing F_4TCNQ on Ag(111) but it nonetheless shows that the bent is crucial.

10.2.2 Summary and conclusions

The present part was aiming to explain the complicated processes occurring upon bonding of the strong donor HV0 on Au(111) using descriptive, "easy-to-understand" methods. Therefore, by applying a rarely used and one new analysis methods, namely the COOP and the MOOP, previously unidentified molecular orbitals, regions of the molecule and even atoms particularly strong involved in the bonding process were identified. Such analysis methods, hence, help gaining a comprehensive view of bonding process, i.e. our knowledge about bonding of molecules on surfaces is completing. For HV0 it was discovered that the most significant bonding contributions result of former unoccupied and so far not considered molecular orbitals (LUMO+2 and LUMO+3). Besides, the expected impact of the molecular HOMO was confirmed. Interesting in that case was that the HOMO-1 was essentially non-bonding and that the contribution of the HOMO-2 and the HOMO-3 have significant influence onto the shape of the MOOP curve but are essentially non-bonding when summing up their contribution till the Fermi edge.

An interesting aspect comes along when analyzing the influence of the metal. Here, the molecular HOMO and the LUMO+2,3 impacts are exclusively due to interaction with the metal s-band. On the other hand, the HOMO-2,3 impacts are essentially due to metal-d band interactions.

Furthermore, the geometric distortions of the molecule proved to enhance the bonding. Yet, in terms of covalent/ionic bonding strength the donor HV0 is rather moderate, especially when compared to the previously analyzed acceptor F_4TCNQ on Ag(111), see 10.1.

Glossary

6P p-sexiphenyl.

AE all electron.

Alq3 Aluminium-tris(8-hydroxychinolin).

AO atomic orbital.

B3LYP Becke, Lee, Yang and Parr.

BD bond dipole.

BE binding energy.

Br-PyT bromo-pyrenetetraone.

C_{60} Fullerene.

CG conjugate gradient.

COOP crystal orbital overlap population.

CP Cole-Perdew.

DFT density functional theory.

DOS density of states.

DZP double-ζ polarized.

EA electron affinity.

EIB electron-injection barrier.

F_2HCNQ 3,5-difluoro-2,5,7,7,8,8-hexacyanoquinodimethane.

F_4TCNQ 2,3,5,6-tetrafluoro-7,7,8,8-tetracyanoquinodimethane.

GGA generalized gradient approximation.

HATCN hexaazatriphenylene-hexanitrile.

HIB hole-injection barrier.

HOMO highest occupied molecular orbital.

HOPS highest occupied π-state.

HV0 1H,1'H-[4,4']bipyridinylidene.

IP ionization potential.

IR infrared.

LCAO linear combination of atomic orbitals.

LCMO linear combination of molecular orbitals.

LDA local density approximation.

LDOS local density of states.

LEED low energy electron diffraction.

LUMO lowest unoccupied molecular orbital.

LUPS lowest occupied π-state.

mCOOP molecular crystal orbital overlap population.

MDOS molecular density of states.

mmCOOP molecule-metal crystal orbital overlap population.

mmToP molecular-metal total overlap population.

MO molecular orbital.

MODOS molecular orbital density of states.

MOOP molecular orbital overlap population.

mToP molecular total overlap population.

MV0 1,1'-dimethyl-1H,1'H-[4,4']bipyridinylidene.

NO_2-PyT nitro-pyrenetetraone.

OFET organic field-effect-transistor.

OLED organic light emitting diode.

OPVC organic photovoltaic cell.

PAW projector augmented wave.

PBE Perdew, Burke and Ernzerhof.

PDOS projected density of states.

PS pseudopotential.

PTCDA 3,4,9,10-perylene-tetracarboxylicdianhydride.

PW91 Perdew-Wang 1991.

PW92 Perdew-Wang.

PyT pyrenetetraone.

PZ81 Perdew-Zunger.

revPBE revised Perdew, Burke and Ernzerhof.

RMM residual minimization method.

SAM self-assembled monolayer.

SCF self-consistent field.

SECO secondary electron cut-off.

SOMO singly unoccupied molecular orbital.

STM scanning tunneling microscopy.

STS scanning tunneling spectroscopy.

TCNQ 7,7,8,8-tetracyanoquinodimethane.

TDS thermal desorption spectroscopy.

ToP total overlap population.

TTF tetrathiofulvalene.

UHV ultra high vacuum.

UPS ultra-violet photoemission spectroscopy.

USPP ultra-soft pseudopotential.

VB valence band.

vdW van der Waals.

VWN Vosko-Wilk-Nusair.

XC exchange correlation.

XPS x-ray photoelectron spectroscopy.

XSW X-ray standing wave.

References

[1] Gerold M. Rangger, Lorenz Romaner, Georg Heimel, and Egbert Zojer. Understanding the properties of interfaces between organic self-assembled monolayers and noble metals - a theoretical perspective. *Surface and Interface Analysis*, 40: 371–378, 2008. doi: 10.1002/sia.2645.

[2] LinJun Wang, Gerold M. Rangger, Lorenz Romaner, Georg Heimel, Tomáš Bučko, ZhongYun Ma, QiKai Li, Zhigang Shuai, and Egbert Zojer. Electronic Structure of Self-Assembled Monolayers on Au(111) Surfaces: The Impact of Backbone Polarizability. *Advanced Functional Materials*, 19:3766 – 3775, 2009. doi: 10.1002/adfm.200901152.

[3] LinJun Wang, Gerold M. Rangger, ZhongYun Ma, QiKai Li, Zhigang Shuai, Egbert Zojer, and Georg Heimel. Is there a Au-S bond dipole in self-assembled monolayers on gold? *Physical Chemistry Chemical Physics*, page accepted, 2010. doi: 10.1039/B924306.

[4] Gerold M. Rangger, Oliver T. Hofmann, Lorenz Romaner, Georg Heimel, Benjamin Bröker, Ralf-Peter Blum, Robert L. Johnson, Norbert Koch, and Egbert Zojer. F4TCNQ on Cu, Ag, and Au as prototypical example for a strong organic acceptor on coinage metals. *Phys. Rev. B*, 79(16):165306, 2009. doi: 10.1103/PhysRevB.79.165306.

[5] A. Gross. *Theoretical Surface Science* . Springer, Berlin, 2003.

[6] Frank Jensen. *Introduction to Computational Chemistry*. Wiley, 2006.

[7] H. Sormann and E. Schachinger. *Theoretische Festkörperphysik*. Script, 2009.

[8] H. Sormann and E Schachinger. *Bandstrukturmethoden*. Script, 2009.

[9] David S. Sholl and Janice A. Steckel. *Density Functional Theory - A Practical Introduction*. Wiley, 2009. ISBN: 978-0-470-37317-0.

[10] Daniel Joubert. *Density Functionals: Theory and Applications Proceedings, Meerensee, near Cape Town, South Africa 1997*. Springer, 1998.

[11] M. Born and R. Oppenheimer. Zur Quantentheorie der Molekülen. *Ann. Phys.*, 84:457–484, 1927. doi: DOI:10.1002/andp.19273892002.

[12] R. P. Feynman. Forces in Molecules. *Phys. Rev.*, 56(4):340, Aug 1939. doi: 10.1103/PhysRev.56.340.

[13] Hans Hellmann. *Einführung in die Quantenchemie*. Deucke, Leipzig, 1937.

[14] John A. Pople. Nobel Lecture: Quantum chemical models. *Rev. Mod. Phys.*, 71 (5):1267–1274, Oct 1999. doi: 10.1103/RevModPhys.71.1267.

[15] W. Kohn. Nobel lecture: Electronic structure of matter - wave functions and density functionals. *Reviews of Modern Physics*, 71:1253–1266, 1999.

[16] L.H. Thomas. The calculation of atomic fields. *Proc. Camb. Phil. Soc*, 23:542–548, 1927.

[17] E. Fermi. A statistical method for the determination of some atomic properties and the application of this method to the theory of the periodic system of elements. *Z. Phys.*, 48:73–79, 1928.

[18] E. H. Lieb. Thomas-Fermi and related theories of atoms and molecules. *Reviews of Modern Physics*, 53:603–641, 1981.

[19] P. Hohenberg and W. Kohn. Inhomogeneous Electron Gas. *Phys. Rev.*, 136(3B): B864–B871, Nov 1964. doi: 10.1103/PhysRev.136.B864.

[20] M. C. Payne, M. P. Teter, D. C. Allan, T. A. Arias, and J. D. Joannopoulos. Iterative minimization techniques for ab initio total-energy calculations: molecular dynamics and conjugate gradients. *Rev. Mod. Phys.*, 64(4):1045–1097, Oct 1992. doi: 10.1103/RevModPhys.64.1045.

[21] S. H. Vosko, L. Wilk, and M. Nusair. Accurate spin-dependent electron liquid correlation energies for local spin density calculations: a critical analysis. *Canadian Journal of Physics*, 58:1200–1211, 1980.

[22] J. P. Perdew and Alex Zunger. Self-interaction correction to density-functional approximations for many-electron systems. *Phys. Rev. B*, 23(10):5048–5079, May 1981. doi: 10.1103/PhysRevB.23.5048.

[23] Lee A. Cole and J. P. Perdew. Calculated electron affinities of the elements. *Phys. Rev. A*, 25(3):1265–1271, Mar 1982. doi: 10.1103/PhysRevA.25.1265.

[24] John P. Perdew and Yue Wang. Accurate and simple analytic representation of the electron-gas correlation energy. *Phys. Rev. B*, 45(23):13244–13249, Jun 1992. doi: 10.1103/PhysRevB.45.13244.

[25] John P. Perdew and Yue Wang. Accurate and simple density functional for the electronic exchange energy: Generalized gradient approximation. *Phys. Rev. B*, 33(12):8800–8802, Jun 1986. doi: 10.1103/PhysRevB.33.8800.

[26] J. P. Perdew, K. Burke, and M. Ernzerhof. Generalized gradient approximation made simple. *Physical Review Letters*, 77(18):3865–3868, 1996.

[27] Yingkai Zhang and Weitao Yang. Comment on "Generalized Gradient Approximation Made Simple". *Phys. Rev. Lett.*, 80(4):890, Jan 1998. doi: 10.1103/PhysRevLett.80.890.

[28] J. P. Perdew, J. A. Chevary, S. H. Vosko, K. A. Jackson, M. R. Pederson, D. J. Singh, and C. Fiolhais. Atoms, Molecules, Solids, and Surfaces - Applications of the Generalized Gradient Approximation for Exchange and Correlation. *Physical Review B*, 46(11):6671–6687, 1992.

[29] John P. Perdew, Adrienn Ruzsinszky, Jianmin Tao, Viktor N. Staroverov, Gustavo E. Scuseria, and Gábor I. Csonka. Prescription for the design and selection of density functional approximations: More constraint satisfaction with fewer fits. *The Journal of Chemical Physics*, 123(6):062201, 2005. doi: 10.1063/1.1904565.

[30] Axel D. Becke. Density-functional thermochemistry. III. The role of exact exchange, journal = The Journal of Chemical Physics. 98(7):5648–5652, 1993.

[31] Chengteh Lee, Weitao Yang, and Robert G. Parr. Development of the Colle-Salvetti correlation-energy formula into a functional of the electron density. *Physical Review B*, 37(2):785, 1988.

[32] Georg Kresse and Jürgen Furthmüller. *VASP the Guide*. Institut für Materialphysik, Universität Wien, Sensengasse 8, A-1130 Wien, Austria. URL http://cms.mpi.univie.ac.at/VASP/.

[33] H. J. Monkhorst and J. D. Pack. Special points for Brillouin-zone integrations. *Physical Review B*, 13(12):5188–5192, 1976.

[34] M. Methfessel and A. T. Paxton. High-precision sampling for Brillouin-zone integration in metals. *Physical Review B*, 40(6):3616–3621, 1989.

[35] Peter E. Blöchl, O. Jepsen, and O. K. Andersen. Improved tetrahedron method for Brillouin-zone integrations. *Phys. Rev. B*, 49(23):16223–16233, Jun 1994. doi: 10.1103/PhysRevB.49.16223.

[36] Harald Ibach and Hans Lüth. *Solid-State Physics: An Introduction to Principles of Materials Science*. Springer, 3 edition, 2002.

[37] G. Kresse and J. Hafner. Abinitio Molecular-Dynamics for Liquid-Metals. *Physical Review B*, 47(1):558–561, 1993.

[38] G. Kresse and J. Furthmüller. Efficient iterative schemes for ab initio total-energy calculations using a plane-wave basis set. *Physical Review B*, 54(16):11169–11186, 1996.

[39] G. Kresse and J. Furthmüller. Efficiency of ab-initio total energy calculations for metals and semiconductors using a plane-wave basis set. *Computational Materials Science*, 6(1):15–50, 1996.

[40] Peter Pulay. Convergence acceleration of iterative sequences. the case of scf iteration. *Chem. Phys. Lett.*, 73:393, 1980. doi: doi:10.1016/0009-2614(80)80396-4.

[41] D. D. Johnson. Modified Broyden's method for accelerating convergence in self-consistent calculations. *Phys. Rev. B*, 38(18):12807–12813, Dec 1988. doi: 10.1103/PhysRevB.38.12807.

[42] Michael P. Teter, Michael C. Payne, and Douglas C. Allan. Solution of Schrödinger's equation for large systems. *Phys. Rev. B*, 40(18):12255–12263, Dec 1989. doi: 10.1103/PhysRevB.40.12255.

[43] D. M. Bylander, Leonard Kleinman, and Seongbok Lee. Self-consistent calculations of the energy bands and bonding properties of $B_{12}C_3$. *Phys. Rev. B*, 42(2): 1394–1403, Jul 1990. doi: 10.1103/PhysRevB.42.1394.

[44] D M Wood and A Zunger. A new method for diagonalising large matrices. *Journal of Physics A: Mathematical and General*, 18(9):1343–1359, 1985.

[45] J. M. Soler, E. Artacho, J. D. Gale, A. Garcia, J. Junquera, P. Ordejon, and D. Sanchez-Portal. The SIESTA method for ab initio order-N materials simulation. *Journal of Physics-Condensed Matter*, 14(11):2745–2779, 2002.

[46] Emilio Artacho, E Anglada, O Dieguez, J D Gale, A Garcia, J Junquera, R M Martin, P Ordejon, J M Pruneda, D Sanchez-Portal, and J M Soler. The SIESTA method; developments and applicability. *Journal of Physics: Condensed Matter*, 20(6):064208 (6pp), 2008.

[47] Emilio Artacho, José María Cela, Julian D. Gale, Alberto García, Javier Junquera, Richard M. Martin, Pablo Ordejón, Daniel Sanchez-Portal, and José M. Soler. *User's Guide: SIESTA 3.0-beta*. Universidad Autónoma de Madrid, 1996-2009. URL http://www.uam.es./siesta.

[48] S. Huzinaga, J. Andzelm, M. Klobukowski, E. Radzio-Andzelm, Y. Sakai, and H. Tatewak. *Gaussian Basis Sets for Molecular Calculations (Physical Sciences Data)*. Elsevier Publishing Company, 1985.

[49] Javier Junquera, Óscar Paz, Daniel Sánchez-Portal, and Emilio Artacho. Numerical atomic orbitals for linear-scaling calculations. *Phys. Rev. B*, 64(23):235111, Nov 2001. doi: 10.1103/PhysRevB.64.235111.

[50] Emilio Artacho, Daniel Sánchez-Portal, A. García, and J. M. Soler. Linear-Scaling ab-initio Calculations for Large and Complex Systems. *physica status solidi (b)*, 215:809–817, 1999.

[51] Otto F. Sankey and David J. Niklewski. Ab initio multicenter tight-binding model for molecular-dynamics simulations and other applications in covalent systems. *Phys. Rev. B*, 40(6):3979–3995, Aug 1989. doi: 10.1103/PhysRevB.40.3979.

[52] D. R. Hamann, M. Schluter, and C. Chiang. Norm-Conserving Pseudopotentials. *Physical Review Letters*, 43(20):1494–1497, 1979.

[53] Peter E. Blöchl. Projector augmented-wave method. *Physical Review B*, 50(24): 17953–17979, 1994.

[54] G. Kresse and D. Joubert. From ultrasoft pseudopotentials to the projector augmented-wave method. *Physical Review B*, 59(3):1758–1775, 1999.

[55] D. Vanderbilt. Optimally Smooth Norm-Conserving Pseudopotentials. *Physical Review B*, 32(12):8412–8415, 1985.

[56] N. Troullier and José Luriaas Martins. Efficient pseudopotentials for plane-wave calculations. *Phys. Rev. B*, 43(3):1993–2006, Jan 1991. doi: 10.1103/PhysRevB.43.1993.

[57] N. Troullier and José Luriaas Martins. Efficient pseudopotentials for plane-wave calculations. II. Operators for fast iterative diagonalization. *Phys. Rev. B*, 43(11):8861–8869, Apr 1991. doi: 10.1103/PhysRevB.43.8861.

[58] García Alberto. *ATOM User Manual*. ICMAB-CSIC, Barcelona, Spain, 3.2.8 edition, April 2008.

[59] A De Vita and M J Gillan. The ab initio calculation of defect energetics in aluminium. *Journal of Physics: Condensed Matter*, 3(33):6225–6237, 1991.

[60] F. Ample, D. Curulla, F. Fuster, A. Clotet, and J. M. Ricart. Adsorption of CO and CN- on transition metal surfaces: a comparative study of the bonding mechanism. *Surface Science*, 497(1-3):139–154, 2002.

[61] Paul S. Bagus and Francesc Illas. Decomposition of the chemisorption bond by constrained variations: Order of the variations and construction of the variational spaces. 96:8962–8970, 1992.

[62] D. Curulla, A. Clotet, J. M. Ricart, and F. Illas. Ab Initio Cluster Model Study of the Chemisorption of CO on Low-Index Platinum Surfaces. *Journal of Physical Chemistry B*, 103(25):5246–5255, 1999.

[63] C. J. Nelin, P. S. Bagus, and M. R. Philpott. The Nature of the Bonding of Cn to Metals and Organic-Molecules. *Journal of Chemical Physics*, 87(4):2170–2176, 1987.

[64] Roald Hoffmann. A chemical and theoretical way to look at bonding on surfaces. *Reviews of Modern Physics*, 60(3):601, Jul 1988. doi: 10.1103/RevModPhys.60.601.

[65] Lorenz Romaner. *Modelling of organic semiconductors and their interaction with metal surfaces*. PhD thesis, Graz University of Technology, 2007.

[66] R. S. Mulliken. Electronic Population Analysis on LCAO[Single Bond]MO Molecular Wave Functions. I. *Journal of Chemical Physics*, 23(10):1833–1840, 1955.

[67] Per-Olov Löwdin. On the Non-Orthogonality Problem Connected with the Use of Atomic Wave Functions in the Theory of Molecules and Crystals. *The Journal of Chemical Physics*, 18(3):365–375, 1950. doi: 10.1063/1.1747632.

[68] Per-Olov Löwdin. On the Nonorthogonality Problem. *Advances in Quantum Chemistry*, 5:185–199, 1970. doi: 10.1016/S0065-3276(08)60339-1.

[69] R.F.W. Bader. *Atoms in Molecules*. Clarendon Press, Oxford, 1990.

[70] Richard F. W. Bader. A quantum theory of molecular structure and its applications. *Chemical Reviews*, 91:893–928, 1991. doi: 10.1021/cr00005a013.

[71] Alan E. Reed, Larry A. Curtiss, and Weinhold Frank. Intermolecular interactions from a natural bond orbital, donor-acceptor viewpoint. *Chemical Reviews*, 88: 899–926, 1988.

[72] Roald Hoffmann. *Solids and Surfaces: A Chemist's View of Bonding in Extended Structures*. Wiley-VCH, 1989.

[73] T. Hughbanks and R. Hoffman. Molybdenum chalcogenides: clusters, chains and extended solids. The approach to bonding in three dimensions. *J. Am. Chem. Soc.*, 105(5):Pages: 1150–1162, 1983.

[74] G. Binnig, H. Rohrer, Ch. Gerber, and E. Weibel. Tunneling through a controllable vacuum gap. *Applied Physics Letters*, 40(2):178–180, 1982. doi: 10.1063/1.92999.

[75] G. Binnig, H. Rohrer, Ch. Gerber, and E. Weibel. Surface Studies by Scanning Tunneling Microscopy. *Phys. Rev. Lett.*, 49(1):57–61, Jul 1982. doi: 10.1103/PhysRevLett.49.57.

[76] G. Binnig, K. H. Frank, H. Fuchs, N. Garcia, B. Reihl, H. Rohrer, F. Salvan, and A. R. Williams. Tunneling Spectroscopy and Inverse Photoemission: Image and Field States. *Phys. Rev. Lett.*, 55(9):991–994, Aug 1985. doi: 10.1103/PhysRevLett.55.991.

[77] Julian C. Chen. *Introduction to Scanning Tunneling Microscopy*. Oxford University Press, 2nd edition edition, 2008.

[78] K. Oura, V. G. Lifshits, A. A. Saranin, A. V. Zotov, and M. Katayama. *Surface Science - An Introduction*. Springer, 2003.

[79] J. Tersoff and D. R. Hamann. Theory of the Scanning Tunneling Microscope. *Physical Review B*, 31(2):805–813, 1985. doi: 10.1103/PhysRevB.31.805.

[80] J. Bardeen. Tunnelling from a Many-Particle Point of View. *Phys. Rev. Lett.*, 6 (2):57–59, Jan 1961. doi: 10.1103/PhysRevLett.6.57.

[81] J. Tersoff and D. R. Hamann. Theory and Application for the Scanning Tunneling Microscope. *Physical Review Letters*, 50(25):1998–2001, 1983. doi: 10.1103/PhysRevLett.50.1998.

[82] Marek Gajdoš, Andreas Eichler, Jürgen Hafner, Gerhard Meyer, and Karl-Heinz Rieder. CO adsorption on a Cu(211) surface: First-principle calculation and STM study. *Phys. Rev. B*, 71(3):035402, Jan 2005. doi: 10.1103/PhysRevB.71.035402.

[83] G. Heimel, L. Romaner, J. L. Brédas, and E. Zojer. Organic/metal interfaces in self-assembled monolayers of conjugated thiols: A first-principles benchmark study. *Surface Science*, 600(19):4548–4562, 2006. doi: 10.1016/j.susc.2006.07.023.

[84] Lukas Köhler and Georg Kresse. Density functional study of CO on Rh(111). *Phys. Rev. B*, 70(16):165405, Oct 2004. doi: 10.1103/PhysRevB.70.165405.

[85] S. Lizzit, A. Baraldi, A. Groso, K. Reuter, M. V. Ganduglia-Pirovano, C. Stampfl, M. Scheffler, M. Stichler, C. Keller, W. Wurth, and D. Menzel. Surface core-level shifts of clean and oxygen-covered Ru(0001). *Phys. Rev. B*, 63(20):205419, May 2001. doi: 10.1103/PhysRevB.63.205419.

[86] Gerold M. Rangger and Anna M. Track. *Manual for VASP*. Institute for solid state physics, Petersgasse 16, 8010 Graz, 2009.

[87] F. M. Hoffmann and et al. Infrared reflection-absorption spectroscopy of adsorbed molecules. *Surf. Sci. Rep.*, 3:107, 1983.

[88] G. Heimel, L. Romaner, E. Zojer, and J. L. Brédas. Toward Control of the Metal-Organic Interfacial Electronic Structure in Molecular Electronics: A First-Principles Study on Self-Assembled Monolayers of -Conjugated Molecules on Noble Metals. *Nano Letters*, 7(4):932, 2007.

[89] G. Heimel, L. Romaner, J. L. Brédas, and E. Zojer. Interface energetics and level alignment at covalent metal-molecule junctions: pi-conjugated thiols on gold. *Physical Review Letters*, 96(19):196806, 2006. doi: 10.1103/PhysRevLett.96.196806.

[90] J. C. Love, L. A. Estroff, J. K. Kriebel, R. G. Nuzzo, and G. M. Whitesides. Self-assembled monolayers of thiolates on metals as a form of nanotechnology. *Chemical Reviews*, 105(4):1103–1169, 2005.

[91] G. E. Poirier. Characterization of organosulfur molecular monolayers on Au(111) using scanning tunneling microscopy. *Chemical Reviews*, 97(4):1117–1127, 1997.

[92] F. Schreiber. Structure and growth of self-assembling monolayers. *Progress in Surface Science*, 65(5-8):151–256, 2000.

[93] Frank Schreiber. Self-assembled monolayers: from 'simple' model systems to biofunctionalized interfaces. *Journal of Physics: Condensed Matter*, 16:R881–R900, 2004.

[94] Daniel K. Schwartz. Mechanismn and kinetics of self-assembled monolayer formation. *Annual Review of Physical Chemistry*, 52(1):107–137, 2001.

[95] A. Ulman. Formation and structure of self-assembled monolayers. *Chemical Reviews*, 96(4):1533–1554, 1996.

[96] J. Genzer and K. Efimenko. Creating long-lived superhydrophobic polymer surfaces through mechanically assembled monolayers. *Science*, 290(5499):2130–2133, 2000.

[97] G. K. Jennings and P. E. Laibinis. Self-assembled monolayers of alkanethiols on copper provide corrosion resistance in aqueous environments. *Colloids and Surfaces a-Physicochemical and Engineering Aspects*, 116(1-2):105–114, 1996.

[98] D. Cahen, R. Naaman, and Z. Vager. The cooperative molecular field effect. *Advanced Functional Materials*, 15(10):1571–1578, 2005.

[99] X. F. Guo, M. Myers, S. X. Xiao, M. Lefenfeld, R. Steiner, G. S. Tulevski, J. Y. Tang, J. Baumert, F. Leibfarth, J. T. Yardley, M. L. Steigerwald, P. Kim, and C. Nuckolls. Chemoresponsive monolayer transistors. *Proceedings of the National Academy of Sciences of the United States of America*, 103(31):11452–11456, 2006.

[100] B. de Boer, A. Hadipour, M. M. Mandoc, T. van Woudenbergh, and P. W. M. Blom. Tuning of metal work functions with self-assembled monolayers. *Advanced Materials*, 17(5):621, 2005.

[101] D. M. Alloway, M. Hofmann, D. L. Smith, N. E. Gruhn, A. L. Graham, R. Colorado, V. H. Wysocki, T. R. Lee, P. A. Lee, and N. R. Armstrong. Interface dipoles arising from self-assembled monolayers on gold: UV-photoemission studies of alkanethiols and partially fluorinated alkanethiols. *Journal of Physical Chemistry B*, 107(42):11690–11699, 2003.

[102] J. Chen, M. A. Reed, A. M. Rawlett, and J. M. Tour. Large on-off ratios and negative differential resistance in a molecular electronic device. *Science*, 286(5444): 1550–1552, 1999.

[103] L. A. Bumm, J. J. Arnold, M. T. Cygan, T. D. Dunbar, T. P. Burgin, II Jones, L., D. L. Allara, J. M. Tour, and P. S. Weiss. Are Single Molecular Wires Conducting? *Science*, 271(5256):1705–1707, 1996. doi: 10.1126/science.271.5256.1705.

[104] J. G. Kushmerick, D. B. Holt, J. C. Yang, J. Naciri, M. H. Moore, and R. Shashidhar. Metal-Molecule Contacts and Charge Transport across Monomolecular Layers: Measurement and Theory. *Phys. Rev. Lett.*, 89(8):086802, Aug 2002. doi: 10.1103/PhysRevLett.89.086802.

[105] Sungil Kim, Kyuwook Ihm, Tai-Hee Kang, Sungu Hwang, and Sang-Woo Joo. Binding property and structure of aromatic isocyanide self-assembly monolayers on Ag and Au surfaces. *Surface and Interface Analysis*, 37(3):294–299, 2005. 10.1002/sia.2019.

[106] J. Gottschalck and B. Hammer. A density functional theory study of the adsorption of sulfur, mercapto, and methylthiolate on Au(111). *Journal of Chemical Physics*, 116(2):784–790, 2002.

[107] G. Kresse and J. Hafner. Ab initio molecular dynamics for open-shell transition metals. *Physical Review B*, 48(17):13115, 1993.

[108] G. Kresse and J. Hafner. Ab-Initio Molecular-Dynamics Simulation of the Liquid-Metal Amorphous-Semiconductor Transition in Germanium. *Physical Review B*, 49(20):14251–14269, 1994.

[109] L. Romaner, G. Heimel, M. Gruber, J. L. Brédas, and E. Zojer. Stretching and breaking of a molecular junction. *Small*, 2(12):1468–1475, 2006.

[110] A. Kokalj. Computer graphics and graphical user interfaces as tools in simulations of matter at the atomic scale. *Computational Materials Science*, 28(2):155–168, 2003. Code available from http://www.xcrysden.org/.

[111] Lorenz Romaner, Georg Heimel, and Egbert Zojer. Electronic structure of thiol-bonded self-assembled monolayers: Impact of coverage. *Physical Review B*, 77(4): 045113, 2008.

[112] I. H. Campbell, S. Rubin, T. A. Zawodzinski, J. D. Kress, R. L. Martin, D. L. Smith, N. N. Barashkov, and J. P. Ferraris. Controlling Schottky energy barriers in organic electronic devices using self-assembled monolayers. *Physical Review B*, 54(20):14321–14324, 1996.

[113] A. Hauschild, K. Karki, B. C. C. Cowie, M. Rohlfing, F. S. Tautz, and M. Sokolowski. Molecular distortions and chemical bonding of a large pi-conjugated molecule on a metal surface. *Physical Review Letters*, 94(3):036106, 2005.

[114] David R. Lide. *CRC: Handbook of Chemistry and Physics 1999-2000: A Ready Reference Book of Chemical and Physical Data (81st edn)*. CRC Press: USA, 2000.

[115] G. S. Tulevski, C. Nuckolls, A. Afzali, T. O. Graham, and C. R. Kagan. Device scaling in sub-100 nm pentacene field-effect transistors. *Applied Physics Letters*, 89(18):183101, 2006. doi: 10.1063/1.2364154. URL http://link.aip.org/link/?APL/89/183101/1.

[116] Norbert Koch. Organic Electronic Devices and Their Functional Interfaces. *ChemPhysChem*, 8(10):1438–1455, 2007.

[117] Dario Natali, Luca Fumagalli, and Marco Sampietro. Modeling of organic thin film transistors: Effect of contact resistances. *Journal of Applied Physics*, 101(1): 014501, 2007. doi: 10.1063/1.2402349.

[118] Jana Zaumseil and Henning Sirringhaus. Electron and Ambipolar Transport in Organic Field-Effect Transistors. *Chemical Reviews*, 107:1296–1323, 2007. doi: DOI:10.1021/cr0501543.

[119] I. H. Campbell, J. D. Kress, R. L. Martin, D. L. Smith, N. N. Barashkov, and J. P. Ferraris. Controlling charge injection in organic electronic devices using self-assembled monolayers. *Applied Physics Letters*, 71(24):3528–3530, 1997.

[120] Christopher D. Zangmeister, Laura B. Picraux, Roger D. van Zee, Yuxing Yao, and James M. Tour. Energy-level alignment and work function shifts for thiol-bound monolayers of conjugated molecules self-assembled on Ag, Cu, Au, and Pt. *Chemical Physics Letters*, 442(4-6):390–393, 2007.

[121] K. Demirkan, A. Mathew, C. Weiland, Y. Yao, A. M. Rawlett, J. M. Tour, and R. L. Opila. Energy level alignment at organic semiconductor/metal interfaces: Effect of polar self-assembled monolayers at the interface. *The Journal of Chemical Physics*, 128(7):074705, 2008. doi: 10.1063/1.2832306.

[122] Patrick Marmont, Nicolas Battaglini, Philippe Lang, Gilles Horowitz, Jaehyung Hwang, Antoine Kahn, Claire Amato, and Patrick Calas. Improving charge injection in organic thin-film transistors with thiol-based self-assembled monolayers. *Organic Electronics*, 9:419–424, 2008. doi: doi:10.1016/j.orgel.2008.01.004.

[123] C. Bock, D. V. Pham, U. Kunze, D. Kafer, G. Witte, and Ch Woll. Improved morphology and charge carrier injection in pentacene field-effect transistors with thiol-treated electrodes. *Journal of Applied Physics*, 100(11):114517–7, 2006.

[124] D. J. Wold and C. D. Frisbie. Fabrication and characterization of metal-molecule-metal junctions by conducting probe atomic force microscopy. *Journal of the American Chemical Society*, 123(23):5549–5556, 2001.

[125] Abraham Nitzan and Mark A. Ratner. Electron Transport in Molecular Wire Junctions. *Science*, 300(5624):1384–1389, 2003. doi: 10.1126/science.1081572.

[126] Y. Q. Xue and M. A. Ratner. Microscopic study of electrical transport through individual molecules with metallic contacts. II. Effect of the interface structure. *Physical Review B*, 68(11):1154067, 2003.

[127] G. Heimel, L. Romaner, J. L. Brédas, and E. Zojer. Odd-Even Effects in Self-Assembled Monolayers of ω-(Biphenyl-4-yl)alkanethiols: A First-Principles Study. *Langmuir*, 24(2):474–482, 2008.

[128] Lorenz Romaner, Georg Heimel, Claudia Ambrosch-Draxl, and Egbert Zojer. The Dielectric Constant of Self-Assembled Monolayers. *Advanced Functional Materials*, 18(24):3999–4006, 2008. 10.1002/adfm.200800876.

[129] Tomas Bucko, Jurgen Hafner, and Janos G. Angyan. Geometry optimization of periodic systems using internal coordinates. *The Journal of Chemical Physics*, 122(12):124508–10, 2005.

[130] M. J. Frisch, G. W. Trucks, H. B. Schlegel, G. E. Scuseria, M. A. Robb, J. R. Cheeseman, V. G. Zakrzewski, J. A. Montgomery, Jr., R. E. Stratmann, J. C. Burant, S. Dapprich, J. M. Millam, A. D. Daniels, K. N. Kudin, M. C. Strain, O. Farkas, J. Tomasi, V. Barone, M. Cossi, R. Cammi, B. Mennucci, C. Pomelli, C. Adamo, S. Clifford, J. Ochterski, G. A. Petersson, P. Y. Ayala, Q. Cui, K. Morokuma, P. Salvador, J. J. Dannenberg, D. K. Malick, A. D. Rabuck, K. Raghavachari, J. B. Foresman, J. Cioslowski, J. V. Ortiz, A. G. Baboul, B. B. Stefanov, G. Liu, A. Liashenko, P. Piskorz, I. Komaromi, R. Gomperts, R. L. Martin, D. J. Fox, T. Keith, M. A. Al-Laham, C. Y. Peng, A. Nanayakkara, M. Challacombe, P. M. W. Gill, B. Johnson, W. Chen, M. W. Wong, J. L. Andres, C. Gonzalez, M. Head-Gordon, E. S. Replogle, and J. A. Pople. Gaussian 98. 2001.

[131] Georg Heimel, Lorenz Romaner, Egbert Zojer, and Jean-Luc Brédas. The Interface Energetics of Self-Assembled Monolayers on Metals. *Accounts of Chemical Research*, 41(6):721–729, 2008. 0001-4842.

[132] Georg Heimel, Lorenz Romaner, Egbert Zojer, and Jean-Luc Brédas. A theoretical view on self-assembled monolayers in organic electronic devices. volume 6999, page 699919. SPIE, 2008. doi: 10.1117/12.785122.

[133] Qiang Sun and Annabella Selloni. Interface and Molecular Electronic Structure vs Tunneling Characteristics of CH3- and CF3-Terminated Thiol Monolayers on Au(111). *The Journal of Physical Chemistry A*, 110(40):11396–11400, 2006.

[134] Q. Sun, A. Selloni, and G. Scoles. Electronic Structure of Metal/Molecule//Metal Junctions: A Density Functional Theory Study of the Influence of the Molecular Terminal Group. *The Journal of Physical Chemistry B*, 110:3493–3498, 2006. doi: doi:10.1021/jp053673i.

[135] Ralph G. Pearson. Acids and Bases. *Science*, 151:172–177, 1966. doi: 10.1126/science.151.3707.172.

[136] Robert G. Parr and Ralph G. Pearson. Absolute hardness: companion parameter to absolute electronegativity. *Journal of American Chemical Society*, 105:7512–7516, 1983. doi: 10.1021/ja00364a005.

[137] Michael Malicki, Zelei Guan, Sieu D. Ha, Georg Heimel, Stephen Barlow, Mariacristina Rumi, Antoine Kahn, and Seth R. Marder. Preparation and Characterization of 4'-Donor Substituted Stilbene-4-thiolate Monolayers and Their Influence on the Work Function of Gold. *Langmuir*, 25:7967–7975, 2009. doi: 10.1021/la9004104.

[138] Nicholas Camillone III, Christopher E. D. Chidsey, Gang-yu Liu, and Giacinto Scoles. Superlattice structure at the surface of a monolayer of octadecanethiol self-assembled on Au(111). *The Journal of Chemical Physics*, 98(4):3503–3511, 1993.

[139] G. E. Poirier and M. J. Tarlov. The c(4x2) Superlattice of n-Alkanethiol Monolayers Self-Assembled on Au(111). *Langmuir*, 10:2853–2856, 1994. doi: 10.1021/la00021a001.

[140] W. Azzam, C. Fuxen, A. Birkner, H. T. Rong, M. Buck, and C. Wöll. Coexistence of different structural phases in thioaromatic monolayers on Au(111). *Langmuir*, 19(12):4958–4968, 2003.

[141] A. Natan, L. Kronik, H. Haick, and R. T. Tung. Electrostatic properties of ideal and non-ideal polar organic monolayers: Implications for electronic devices. *Advanced Materials*, 19(23):4103–4117, 2007. doi: 10.1002/adma.200701681.

[142] D. Cornil, Y. Olivier, V. Geskin, and J. Cornil. Depolarization Effects in Self-Assembled Monolayers: A Quantum-Chemical Insight. *Advanced Functional Materials*, 17(7):1143–1148, 2007. doi: 10.1002/adfm.200601116.

[143] A. Natan, Y. Zidon, Y. Shapira, and L. Kronik. Cooperative effects and dipole formation at semiconductor and self-assembled-monolayer interfaces. *Phys. Rev. B*, 73:193310, 2006. doi: 10.1103/PhysRevB.73.193310.

[144] Robert W. Zehner, Parsons Bradley F., Hsung Richard P., and Sita Lawrence R. Tuning the Work Function of Gold with Self-Assembled Monolayers Derived from X-[C6H4-C⁝C-]nC6H4-SH(n=0,1,2;X=H,F,CH3, and OCH3). *Langmuir*, 15: 1121–1127, 1999.

[145] Paul C. Rusu and Geert Brocks. Work functions of self-assembled monolayers on metal surfaces by first-principles calculations. *Physical Review B (Condensed Matter and Materials Physics)*, 74(7):073414–4, 2006.

[146] P. C. Rusu and G. Brocks. Surface Dipoles and Work Functions of Alkylthiolates and Fluorinated Alkylthiolates on Au(111). *Journal of Physical Chemistry B*, 110 (45):22628–22634, 2006. 1520-6106.

[147] V. De Renzi, R. Rousseau, D. Marchetto, R. Biagi, S. Scandolo, and U. del Pennino. Metal work-function changes induced by organic adsorbates: A combined experimental and theoretical study. *Physical Review Letters*, 95(4):046804, 2005.

[148] H. Ishii, K. Sugiyama, D. Yoshimura, E. Ito, Y. Ouchi, and K. Seki. Energy-level alignment at model interfaces of organic electroluminescent devices studied by UV photoemission: trend in the deviation from the traditional way of estimating the interfacial electronic structures. *Selected Topics in Quantum Electronics, IEEE Journal of*, 4(1):24–33, 1998. 1077-260X.

[149] H. Ishii, K. Sugiyama, E. Ito, and K. Seki. Energy level alignment and interfacial electronic structures at organic/metal and organic/organic interfaces. *Advanced Materials*, 11(8):605–625, 1999.

[150] H. Ishii, H. Oji, E. Ito, N. Hayashi, D. Yoshimura, and K. Seki. Energy level alignment and band bending at model interfaces of organic electroluminescent devices. *Journal of Luminescence*, 87-89:61–65, 2000.

[151] X. Crispin, V. Geskin, A. Crispin, J. Cornil, R. Lazzaroni, W. R. Salaneck, and J. L. Bréedas. Characterization of the Interface Dipole at Organic/ Metal Interfaces. *Journal of the American Chemical Society*, 124(27):8131–8141, 2002.

[152] A. Kahn, N. Koch, and W. Y. Gao. Electronic structure and electrical properties of interfaces between metals and π-conjugated molecular films. *Journal of Polymer Science Part B-Polymer Physics*, 41(21):2529–2548, 2003. doi: DOI:10.1002/polb.10642. 732VY Times Cited:103 Cited References Count:48.

[153] David Cahen and Antoine Kahn. Electron Energetics at Surfaces and Interfaces: Concepts and Experiments. *Advanced Materials*, 15(4):271–277, 2003.

[154] Norbert Koch. Energy levels at interfaces between metals and conjugated organic molecules. *Journal of Physics: Condensed Matter*, 20(18):184008, 2008. 0953-8984.

[155] Henning Sirringhaus, Nir Tessler, and Richard H. Friend. Integrated Optoelectronic Devices Based on Conjugated Polymers. *Science*, 280(5370):1741–1744, 1998.

[156] R. H. Friend, R. W. Gymer, A. B. Holmes, J. H. Burroughes, R. N. Marks, C. Taliani, D. D. C. Bradley, D. A. Dos Santos, J. L. Brédas, M. Logdlund, and W. R. Salaneck. Electroluminescence in conjugated polymers. *Nature*, 397 (6715):121–128, 1999. 0028-0836 10.1038/16393 10.1038/16393.

[157] Annica Crispin, Xavier Crispin, Mats Fahlman, Magnus Berggren, and William R. Salaneck. Transition between energy level alignment regimes at a low band gap polymer-electrode interfaces. *Applied Physics Letters*, 89(21):213503–3, 2006.

[158] Carl Tengstedt, Wojciech Osikowicz, William R. Salaneck, Ian D. Parker, Che-H. Hsu, and Mats Fahlman. Fermi-level pinning at conjugated polymer interfaces. *Applied Physics Letters*, 88(5):053502–3, 2006.

[159] Linda Lindell, Mikael Unge, Wojciech Osikowicz, Sven Stafstrom, William R. Salaneck, Xavier Crispin, and Michel P. de Jong. Integer charge transfer at the tetrakis(dimethylamino)ethylene/Au interface. *Applied Physics Letters*, 92(16): 163302–3, 2008.

[160] J. Morgado, A. Charas, and N. Barbagallo. Reduction of the light-onset voltage of light-emitting diodes based on a soluble poly(p-phenylene vinylene) by grafting polar molecules onto indium–tin oxide. *Applied Physics Letters*, 81(5):933–935, 2002.

[161] E. L. Bruner, N. Koch, A. R. Span, S. L. Bernasek, A. Kahn, and J. Schwartz. Controlling the Work Function of Indium Tin Oxide: Differentiating Dipolar from Local Surface Effects. *Journal of the American Chemical Society*, 124(13):3192–3193, 2002. 0002-7863.

[162] H. Yan, Q. Huang, Cui J., J.G.C. Veinot, Kern M.M., and Marks T.J. High-Brightness Blue Light-Emitting Polymer Diodes via Anode Modification Using a Self-Assembled Monolayer. *Advanced Materials*, 15:835–838, 2003. doi: 10.1002/adma.200304585.

[163] K. Asadi, F. Gholamrezaie, E. Smits, P. W. M. Blom, and Bert de Boer. Manipulation of charge carrier injection into organic field-effect transistors by self-assembled monolayers of alkanethiols. *Journal of Materials Chemistry*, 17:1947 – 1953, 2007.

[164] M. Pfeiffer, A. Beyer, T. Fritz, and K. Leo. Controlled doping of phthalocyanine layers by cosublimation with acceptor molecules: A systematic Seebeck and conductivity study. *Applied Physics Letters*, 73(22):3202–3204, 1998.

[165] M. Pfeiffer, K. Leo, X. Zhou, J. S. Huang, M. Hofmann, A. Werner, and J. Blochwitz-Nimoth. Doped organic semiconductors: Physics and application in light emitting diodes. *Organic Electronics*, 4(2-3):89–103, 2003.

[166] W. Y. Gao and A. Kahn. Controlled p doping of the hole-transport molecular material N,N '-diphenyl-N,N '-bis(1-naphthyl)-1,1(')-biphenyl-4,4 '-diamine with tetrafluorotetracyanoquinodimethane. *Journal of Applied Physics*, 94(1):359–366, 2003.

[167] Norbert Koch, Steffen Duhm, J. P. Rabe, Antje Vollmer, and Robert L. Johnson. Optimized hole injection with strong electron acceptors at organic-metal interfaces. *Physical Review Letters*, 95(23):237601, 2005.

[168] Norbert Koch, Georg Heimel, Jishan Wu, Egbert Zojer, Robert L. Johnson, Jean-Luc Brédas, Klaus Müllen, and Jürgen P. Rabe. Influence of molecular conformation on organic/metal interface energetics. *Chemical Physics Letters*, 413(4-6): 390–395, 2005. doi: DOI: 10.1016/j.cplett.2005.08.004.

[169] Steffen Duhm, Hendrik Glowatzki, Valentin Cimpeanu, J. Klankermayer, J. P. Rabe, Robert L. Johnson, and Norbert Koch. Weak Charge Transfer between an Acceptor Molecule and Metal Surfaces Enabling Organic/Metal Energy Level Tuning. *The Journal of Physical Chemistry B*, 110(42):21069–21072, 2006. doi: 10.1021/jp0644715.

[170] S. Duhm, H. Glowatzki, J. P. Rabe, N. Koch, and R. L. Johnson. Spontaneous charge transfer at organic-organic homointerfaces to establish thermodynamic equilibrium. *Applied Physics Letters*, 90(12):122113–3, 2007.

[171] A. G. Werner, F. Li, K. Harada, M. Pfeiffer, T. Fritz, and K. Leo. Pyronin B as a donor for n-type doping of organic thin films. *Applied Physics Letters*, 82(25): 4495–4497, 2003.

[172] C. K. Chan, E. G. Kim, J. L. Brédas, and A. Kahn. Molecular n-Type Doping of 1,4,5,8-Naphthalene Tetracarboxylic Dianhydride by Pyronin B Studied Using Direct and Inverse Photoelectron Spectroscopies. *Advanced Functional Materials*, 16(6):831–837, 2006.

[173] E. Umbach. Characterization of organic overlayers on well-defined substrates. *Progress in Surface Science*, 35(1-4):113–127, 1990.

[174] Y. Zou, L. Kilian, A. Schöll, Th Schmidt, R. Fink, and E. Umbach. Chemical bonding of PTCDA on Ag surfaces and the formation of interface states. *Surface Science*, 600(6):1240–1251, 2006. doi: 10.1016/j.susc.2005.12.050.

[175] F. S. Tautz. Structure and bonding of large aromatic molecules on noble metal surfaces: The example of PTCDA. *Progress in Surface Science*, 82(9-12):479–520, 2007.

[176] Lorenz Romaner, Georg Heimel, Jean-Luc Brédas, Alexander Gerlach, Frank Schreiber, Robert L. Johnson, Jorg Zegenhagen, Steffen Duhm, Norbert Koch, and Egbert Zojer. Impact of Bidirectional Charge Transfer and Molecular Distortions on the Electronic Structure of a Metal-Organic Interface. *Physical Review Letters*, 99(25):256801, 2007.

[177] I. Fernandez-Torrente, S. Monturet, K. J. Franke, J. Fraxedas, N. Lorente, and J. I. Pascual. Long-Range Repulsive Interaction between Molecules on a Metal Surface Induced by Charge Transfer. *Physical Review Letters*, 99(17):176103, 2007. doi: 10.1103/PhysRevLett.99.176103.

[178] C. Huckstadt, S. Schmidt, S. Hufner, F. Forster, F. Reinert, and M. Springborg. Work function studies of rare-gas/noble metal adsorption systems using a Kelvin probe. *Physical Review B*, 73(7):075409, 2006.

[179] Eisuke Ito, Hiroshi Oji, Hisao Ishii, Kazuyoshi Oichi, Yukio Ouchi, and Kazuhiko Seki. Interfacial electronic structure of long-chain alkane/metal systems studied by UV-photoelectron and metastable atom electron spectroscopies. *Chemical Physics Letters*, 287(1-2):137–142, 1998.

[180] R. Krishnan, J. S. Binkley, R. Seeger, and J. A. Pople. Self-consistent molecular orbital methods. XX. A basis set for correlated wave functions. *The Journal of Chemical Physics*, 72(1):650–654, 1980.

[181] Peter M. W. Gill, Benny G. Johnson, John A. Pople, and Michael J. Frisch. The performance of the Becke–Lee–Yang–Parr (B–LYP) density functional theory with various basis sets. *Chemical Physics Letters*, 197(4-5):499–505, 1992.

[182] Seth R. Marder, Bernard Kippelen, Alex K. Y. Jen, and Nasser Peyghambarian. Design and synthesis of chromophores and polymers for electro-optic and photorefractive applications. *Nature*, 388(6645):845–851, 1997. 0028-0836.

[183] F. Jackel, U. G. E. Perera, V. Iancu, K. F. Braun, N. Koch, J. P. Rabe, and S. W. Hla. Investigating Molecular Charge Transfer Complexes with a Low Temperature Scanning Tunneling Microscope. *Physical Review Letters*, 100(12):126102–4, 2008.

[184] R. L. Johnson and J. Reichardt. FLIPPER II – a new photoemission system in HASYLAB. *Nuclear Instruments and Methods in Physics Research*, 208(1-3): 791–796, 1983.

[185] R. E. Long, R. A. Sparks, and K. N. Trueblood. The crystal and molecular structure of 7,7,8,8-tetracyanoquinodimethane. 18(5):932–939, 1965.

[186] T. J. Emge, M. Maxfield, D. O. Cowan, and T. J. Kistenmacher. Solution and Solid-State Studies of Tetrafluoro-7,7,8,8-Tetracyano-P-Quinodimethane, Tcnqf4 - Evidence for Long-Range Amphoteric Intermolecular Interactions and Low-Dimensionality in the Solid-State Structure. *Molecular Crystals and Liquid Crystals*, 65(3-4):161–178, 1981.

[187] M. S. Khatkale and J. P. Devlin. Vibrational and Electronic-Spectra of the Monoanion, Dianion, and Trianion Salts of Tcnq. *Journal of Chemical Physics*, 70(4):1851–1859, 1979.

[188] George Blyholder. Molecular Orbital View of Chemisorbed Carbon Monoxide. *The Journal of Physical Chemistry*, 68:2772–2777, 1964. doi: 10.1021/j100792a006.

[189] Hideaki Aizawa and Shinji Tsuneyuki. First-principles study of CO bonding to Pt(111): validity of the Blyholder model. *Surface Science*, 399(2-3):L364–L370, 1998.

[190] B. Hammer, Y. Morikawa, and J. K. Nørskov. CO Chemisorption at Metal Surfaces and Overlayers. *Physical Review Letters*, 76(12):2141, 1996.

[191] T. C. Chiang, G. Kaindl, and D. E. Eastman. Photoemission from physisorbed Co on clean and Xe-covered Al(111). *Solid State Communications*, 36(1):25–28, 1980.

[192] G. Blyholder and M. Lawless. A theoretical study of the site of CO dissociation on Fe(100). *Surface Science*, 290(1-2):155–162, 1993.

[193] S. Duhm, A. Gerlach, I. Salzmann, B. Bröker, R. L. Johnson, F. Schreiber, and N. Koch. PTCDA on Au(1 1 1), Ag(1 1 1) and Cu(1 1 1): Correlation of interface charge transfer to bonding distance. *Organic Electronics*, 9(1):111–118, 2008.

[194] Stephan Kümmel and Leeor Kronik. Orbital-dependent density functionals: Theory and applications. *Reviews of Modern Physics*, 80(1):3–58, 2008.

[195] Mark S. Hybertsen and Steven G. Louie. Electron correlation in semiconductors and insulators: Band gaps and quasiparticle energies. *Physical Review B*, 34(8): 5390, 1986.

[196] R. O. Jones and O. Gunnarsson. The density functional formalism, its applications and prospects. *Reviews of Modern Physics*, 61(3):689, 1989.

[197] Lior Segev, Adi Salomon, Amir Natan, David Cahen, Leeor Kronik, Fabrice Amy, Calvin K. Chan, and Antoine Kahn. Electronic structure of Si(111)-bound alkyl monolayers: Theory and experiment. *Physical Review B*, 74(16):165323–6, 2006.

[198] J. Hwang, E. G. Kim, J. Liu, J. L. Brédas, A. Duggal, and A. Kahn. Photoelectron Spectroscopic Study of the Electronic Band Structure of Polyfluorene and Fluorene-Arylamine Copolymers at Interfaces. *Journal of Physical Chemistry C*, 111(3):1378–1384, 2007.

[199] S. Berkebile, P. Puschnig, G. Koller, M. Oehzelt, F. P. Netzer, C. Ambrosch-Draxl, and M. G. Ramsey. Electronic band structure of pentacene: An experimental and theoretical study. *Physical Review B*, 77:115312, 2008.

[200] G. Koller, S. Berkebile, J. Ivanco, F. P. Netzer, and M. G. Ramsey. Device relevant organic films and interfaces: A surface science approach. *Surface Science*, 601(24): 5683–5689, 2007.

[201] M. Oehzelt, L. Grill, S. Berkebile, G. Koller, F. P. Netzer, and M. G. Ramsey. The molecular orientation of para-sexiphenyl on Cu(110) and Cu(110) p(2x1)O. *ChemPhysChem*, 8:1707–1712, 2007.

[202] C. Bock, D. V. Pham, U. Kunze, D. Kafer, G. Witte, and A. Terfort. Influence of anthracene-2-thiol treatment on the device parameters of pentacene bottom-contact transistors. *Applied Physics Letters*, 91(5):052110–3, 2007.

[203] G. Witte and Ch Wöll. Molecular beam deposition and characterization of thin organic films on metals for applications in organic electronics. *physica status solidi (a)*, 205(3):497–510, 2008. doi: 10.1002/pssa.200723433.

[204] B. Bröker, R. P. Blum, J. Frisch, A. Vollmer, O. T. Hofmann, R. Rieger, K. Mullen, J. P. Rabe, E. Zojer, and N. Koch. Gold work function reduction by 2.2 eV with an air-stable molecular donor layer. *Applied Physics Letters*, 93(24):243303–3, 2008.

[205] Oliver T. Hofmann, Gerold M. Rangger, and Egbert Zojer. Reducing the Metal Work Function beyond Pauli Pushback: A Computational Investigation of Tetrathiafulvalene and Viologen on Coinage Metal Surfaces. *The Journal of Physical Chemistry C*, 112(51):20357–20365, 2008. doi: 10.1021/jp806834g.

[206] Dongchen Qi, Wei Chen, Xingyu Gao, Li Wang, Shi Chen, Kian Ping Loh, and Andrew T. S. Wee. Surface Transfer Doping of Diamond (100) by Tetrafluorotetracyanoquinodimethane. *Journal of the American Chemical Society*, 129(26): 8084–8085, 2007.

[207] Kozo Mukai and Jun Yoshinobu. Observation of charge transfer states of F4-TCNQ on the 2-methylpropene chemisorbed Si(1 0 0)(2x1) surface. *Journal of Electron Spectroscopy and Related Phenomena*, 174:55–58, 2009. doi: DOI: 10.1016/j.elspec.2009.04.006.

[208] T. Takenobu, T. Kanbara, N. Akima, T. Takahashi, M. Shiraishi, K. Tsukagoshi, H. Kataura, and Y. Aoyagi Y. Iwasa. Control of Carrier Density by a Solution Method in Carbon-Nanotube Devices. *Advanced Materials*, 17(20):2430–2434, 2005. doi: 10.1002/adma.200500759.

[209] J. Blochwitz, T. Fritz, M. Pfeiffer, K. Leo, D. M. Alloway, P. A. Lee, and N. R. Armstrong. Interface electronic structure of organic semiconductors with controlled doping levels. *Organic Electronics*, 2(2):97–104, 2001. doi: DOI: 10.1016/S1566-1199(01)00016-7.

[210] Weiying Gao and Antoine Kahn. Electronic structure and current injection in zinc phthalocyanine doped with tetrafluorotetracyanoquinodimethane: Interface versus bulk effects. *Organic Electronics*, 3(2):53–63, 2002. doi: DOI: 10.1016/S1566-1199(02)00033-2.

[211] J. Blochwitz, M. Pfeiffer, T. Fritz, and K. Leo. Low voltage organic light emitting diodes featuring doped phthalocyanine as hole transport material. *Applied Physics Letters*, 73(6):729–731, 1998.

[212] X. Zhou, M. Pfeiffer, J. Blochwitz, A. Werner, A. Nollau, T. Fritz, and K. Leo. Very-low-operating-voltage organic light-emitting diodes using a p-doped amorphous hole injection layer. *Applied Physics Letters*, 78(4):410–412, 2001.

[213] Steffen Duhm, Ingo Salzmann, Benjamin Bröker, Hendrik Glowatzki, L. Johnson, Robert, and Norbert Koch. Interdiffusion of molecular acceptors through organic layers to metal substrates mimics doping-related energy level shifts. *Applied Physics Letters*, 95(9):093305, 2009.

[214] Z. Q. Gao, B. X. Mi, G. Z. Xu, Y. Q. Wan, M. L. Gong, K. W. Cheah, and C. H. Chen. An organic p-type dopant with high thermal stability for an organic semiconductor. *Chemical Communications*, (1):117–119, 2008.

[215] L. Romaner, D. Nabok, P. Puschnig, E. Zojer, and C. Ambrosch-Draxl. Theoretical study of PTCDA adsorbed on the coinage metal surfaces, Ag(111), Au(111) and Cu(111). *New Journal of Physics*, 11(5):053010, 2009.

[216] C. Gardner Swain and Lupton E. C. Field and resonance components of substituent effects. *J. Am. Chem. Soc.*, 90:4328–4337, 1968.

[217] Corwin Hansch, A. Leo, and R. W. Taft. A survey of Hammett substituent constants and resonance and field parameters. *Chemical Reviews*, 91(2):165–195, 1991. doi: 10.1021/cr00002a004.

[218] S. X. Du, H. J. Gao, C. Seidel, L. Tsetseris, W. Ji, H. Kopf, L. F. Chi, H. Fuchs, S. J. Pennycook, and S. T. Pantelides. Selective Nontemplated Adsorption of Organic Molecules on Nanofacets and the Role of Bonding Patterns. *Physical Review Letters*, 97(15):156105–4, 2006. doi: 10.1103/PhysRevLett.97.156105.

[219] A. J. Bard and L. R. Faulkner. *Electrochemical Methods. Fundamentals and Applications.* J. Wiley& Sons, 1980.

[220] W.C. Barrette, H. W. Johnson, and Sawyer D. T. Voltammetric evaluation of the effective acidities (pKa) for Broensted acids in aprotic solvents. *Analytical Chemistry*, 56:1890–1898, 1984. doi: DOI:10.1021/ac00275a030.

[221] A. Vollmer, O. D. Jurchescu, I. Arfaoui, I. Salzmann, T. T. M. Palstra, P. Rudolf, J. Niemax, J. Pflaum, J. P. Rabe, and N. Koch. The effect of oxygen exposure on pentacene electronic structure. *European Physical Journal E*, 17(3):339–343, 2005.

[222] H. Glowatzki, B. Bröker, R-P. Blum, Hofmann O.T., A. Vollmer, R. Rieger, K. Müllen, E. Zojer, J.P. Rabe, and N. Koch. "Soft" Metallic Contact to Isolated C_{60} Molecules. *Nano Letters*, 8:3825–3829, 2008. doi: 10.1021/nl8021797.

[223] Paul S. Bagus, Volker Staemmler, and Christof Wöll. Exchangelike Effects for Closed-Shell Adsorbates: Interface Dipole and Work Function. *Physical Review Letters*, 89(9):096104, 2002.

[224] N. Koch, A. Vollmer, Y. Sakamoto, and T. Suzuki. The Effect of Fluorination on Pentacene/Gold Interface Energetics and Charge Reorganization Energy. *Advanced Materials*, 19:112–116, 2007. doi: DOI:10.1002/adma.200601825.

[225] S. Duhm, G. Heimel, I. Salzmann, H. Glowatzki, R. L. Johnson, A. Vollmer, J. P. Rabe, and N. Koch. Orientation-dependent ionization energies and interface dipoles in ordered molecular assemblies. *Nature Materials*, 7(4):326–332, 2008.

[226] Kazuhiko Seki, Hiroshi Yanagi, Yasushi Kobayashi, Toshiaki Ohta, and Tadaaki Tani. UV photoemission study of dye/AgBr interfaces in relation to spectral sensitization. *Phys. Rev. B*, 49(4):2760–2767, Jan 1994. doi: 10.1103/PhysRevB.49.2760.

[227] Norbert Koch, Steffen Duhm, Jurgen P. Rabe, Stephan Rentenberger, Robert L. Johnson, Jurgen Klankermayer, and Frank Schreiber. Tuning the hole injection barrier height at organic/metal interfaces with (sub-) monolayers of electron acceptor molecules. *Applied Physics Letters*, 87(10):101905–3, 2005.

[228] Sunil D. Wijeyesekera and Roald Hoffmann. Transition metal carbides. A comparison of bonding in extended and molecular interstitial carbides. *Organometallics*, 3(7):949–961, 1984. doi: 10.1021/om00085a001.

[229] T. Körzdorfer, S. Kümmel, N. Marom, and L. Kronik. When to trust photoelectron spectra from Kohn-Sham eigenvalues: The case of organic semiconductors. *Physical Review B (Condensed Matter and Materials Physics)*, 79(20):201205–4, 2009.